amU
Aix Marseille Université

NNT : 2024AIXM0451

THÈSE DE DOCTORAT

Soutenue à AMU — Aix-Marseille Université
le 27 novembre 2024 par

Thomas KRONLAND-MARTINET

GéoPol

Géolocalisation sans GPS grâce à la lumière polarisée du ciel en bande spectrale UV et visible

Discipline
Sciences du Mouvement Humain
Sciences pour l'Ingénieur

École doctorale
ED 463 Sciences du Mouvement Humain
ED 353 Sciences pour l'Ingénieur : Mécanique, Physique, Micro et Nanoélectronique

Laboratoire/Partenaires de recherche
UMR 7287 - Insitut des Sciences du Mouvement Etienne-Jules Marey
UMR 7334 - Institut Matériaux Microélectronique Nanosciences de Provence

Composition du jury

Pascal VASSEUR Professeur des Universités, Université de Picardie Jules Verne	Rapporteur
Yann BATTIE Professeur des Universités, Université de Lorraine	Rapporteur
Simon BENHAMOU Directeur de Recherche, Université de Montpellier	Examinateur
Anne SENTENAC Directrice de Recherche, Aix-Marseille Université	Présidente du jury
Stéphane VIOLLET Directeur de Recherche, Aix-Marseille Université	Directeur de thèse
David DUCHÉ Maître de Conférences, Aix-Marseille Université	Co-directeur de thèse
Julien SERRES Professeur des Universités, Aix-Marseille Université	Invité
Marcel PASQUINELLI Professeur Émérite, Aix-Marseille Université	Invité

cnrs
INSTITUT DES SCIENCES ETIENNE DU MOUVEMENT JULES MAREY
imnp Institut Matériaux Microélectronique Nanosciences de Provence

Affidavit

I, undersigned, Thomas Kronland-Martinet, hereby declare that the work presented in this manuscript is my own work, carried out under the scientific supervision of Stéphane Viollet and David Duché, in accordance with the principles of honesty, integrity and responsibility inherent to the research mission. The research work and the writing of this manuscript have been carried out in compliance with both the french national charter for Research Integrity and AMU charter on the fight against plagiarism.

This work has not been submitted previously either in this country or in another country in the same or in a similar version to any other examination body.

Marseille 02/08/2024



This work is licensed under Creative Commons Attribution-NonCommercial-NoDerivatives 4.0 International Public License

Liste de publications et participation aux conférences

Liste des publications et/ou brevets réalisées dans le cadre du projet de thèse :

Publications :

1. Kronland-Martinet, T., Poughon, L., Pasquinelli, M., Duché, D., Serres, J. R., & Viollet, S. (2023). SkyPole—A method for locating the north celestial pole from skylight polarization patterns. Proceedings of the National Academy of Sciences, 120(30), e2304847120. DOI : 10.1073/pnas.2304847120. URL : https://www.pnas.org/doi/abs/10.1073/pnas.2304847120
2. Serres, J. R., Lapray, P. J., Viollet, S., Kronland-Martinet, T., Moutenet, A., Morel, O., & Bigué, L. (2024). Passive Polarized Vision for Autonomous Vehicles : A Review. Sensors (Basel, Switzerland), 24(11). DOI : 10.3390/s24113312. URL : https://www.mdpi.com/1424-8220/24/11/3312
3. Kronland-Martinet, T., Poughon, L., Moutenet, A., Pasquinelli, M., Duché, D., Serres, J. R., & Viollet, S. (2024). Locating the North Celestial Pole from Skylight Polarization Patterns and Solar Declination. Under review at IEEE Transactions on Instrumentation and Measurement.

Brevet :

1. Kronland-Martinet, T., Pasquinelli, M., Duché, D., Serres, J. R., & Viollet, S. (2023). Procédé de détermination des invariances temporelles du degré de polarisation linéaire dans le ciel (being extended internationally)

Participation aux conférences et écoles d'été au cours de la période de thèse :

Présentations orales :

1. Kronland-Martinet, T., Poughon, L., Pasquinelli, M., Duché, D., Serres, J. R., & Viollet, S. (2024, June). SkyPole : a geolocation algorithm based on polarized vision without using astronomical ephemerides. In Polarization : Measurement, Analysis, and Remote Sensing XVI (Vol. 13050, pp. 74-79). SPIE. DOI : https://doi.org/10.1117/12.3013560. URL : https://hal.science/hal-04607780

2. Thomas Kronland-Martinet, Léo Poughon, Marcel Pasquinelli, David Duché, Julien Serres, Stéphane Viollet. SkyPole -A bio-inspired polarimetric compass for GPS-denied navigation. Journée des Jeunes Chercheurs en Robotique (JJCR 2023), GDR Robotique ; Franck Ruffier ; Maan El Badaoui El Najjar, Oct 2023, Moliets, France. URL : https://hal.science/hal-04496952

Posters :

1. Thomas Kronland-Martinet, Léo Poughon, Marcel Pasquinelli, David Duché, Julien R Serres, Stéphane Viollet. SkyPole - Méthode de localisation du pôle Nord céleste par traitement d'images polarimétriques du ciel. ORASIS 2023, Laboratoire LIS, UMR 7020, May 2023, Carqueiranne, France. URL : https://hal.science/hal-04219358
2. Thomas Kronland-Martinet, Léo Poughon, Marcel Pasquinelli, David Duché, Julien Serres, Stéphane Viollet. SkyPole - A bio-inspired method to locate the north celestial pole. 18ème Journée de l'École Doctorale Sciences du Mouvement Humain ED463 (JEDSMH 2023), May 2023, Montpelier, France. , 2023, 18ème Journée de l'École Doctorale Sciences du Mouvement Humain ED463 (JEDSMH 2023). URL : https://hal.science/hal-04232445
3. Thomas Kronland-Martinet, Léo Poughon, Marcel Pasquinelli, David Duché, Julien Serres, Stéphane Viollet. SkyPole -A bio-inspired polarimetric compass for GPS-denied navigation. Journée des Jeunes Chercheurs en Robotique (JJCR 2023), Oct 2023, Moliets et Maâ, France. , 2023. URL : https://hal.science/hal-04496956
4. Julien Serres, Antoine Moutenet, Léo Poughon, Thomas Kronland-Martinet, Stéphane Viollet. Tour d'horizon des capteurs polarimétriques dédiés à la robotique mobile. 18èmes journées Imagerie Optique Non-Conventionnelle, Mar 2023, Paris, France. , 2023. URL : https://hal.science/hal-04109732

Résumé et mots clés

Les systèmes de navigation par satellite permettent de se géolocaliser avec précision et de manière simple. Cependant, ces dispositifs peuvent voir leurs signaux détériorés, volontairement ou non, par exemple suite à un brouillage des signaux. La fusion de données satellitaires avec des données issues de divers dispositifs de navigation, tels que les centrales inertielles ou lidars, permettent de pallier ces inconvénients. Néanmoins, malgré ces améliorations, les systèmes de navigation actuels restent vulnérables. La redondance d'information est essentielle pour assurer la fiabilité des systèmes de navigation, de plus en plus autonomes. Cette redondance est présente également chez les animaux migrateurs utilisant des informations issues du champ magnétique terrestre, des étoiles, ou encore du motif de polarisation du ciel pour naviguer. Ce dernier, encore peu utilisé, permet la navigation céleste de jour sans nécessiter une vue directe du soleil, le rendant ainsi compatible avec la navigation en milieu urbain, par exemple.
Dans ce manuscrit de thèse, nous nous proposons d'étudier le motif de polarisation du ciel, afin de développer un système de géolocalisation sans satellite. Cette possibilité a pu être envisagée car le motif de polarisation est lié à la position du soleil dans le ciel, dont la mesure, pouvant être obtenue grâce à un sextant, permet de se géolocaliser en mer. Le sextant reste aujourd'hui un instrument obligatoire dans certains navires. Dans le cadre de cette thèse, une méthode de géolocalisation, permettant d'obtenir de jour la position du pôle nord céleste donc le nord géographique mais aussi sa latitude sur Terre, a été développée, en s'inspirant de la perception des oiseaux migrateurs calibrant leur compas magnétique de nuit à partir de la rotation céleste des étoiles. En étudiant les variations temporelles du degré de polarisation dans le ciel, nous sommes capables d'obtenir la position du pôle céleste à partir d'images successives du ciel prises par une caméra polarimétrique. Plus précisément, nous cherchons les points dont le degré de polarisation est invariant entre deux instants. Cela fait apparaître deux cercles, appelés cercles d'invariance, et liés aux symétries du motif de polarisation. Le pôle céleste peut être localisé simplement, car il se situe sur une de ces deux invariances, et il est le seul point dans le ciel à avoir un degré de polarisation constant à tout moment de la journée, ce qui signifie qu'il est le seul point du ciel contenu dans une invariance à tout moment. Cette méthode à l'avantage de ne nécessiter que des mesures de la polarisation du ciel, aucune autre information telle que l'heure, la date, ou des éphémérides solaires n'étant requise contrairement aux méthodes préexistantes. Elle a également l'avantage d'être extrêmement simple, nécessitant uniquement des calculs pouvant être plausiblement réalisés par des animaux. Nous montrons aussi comment la déclinaison et l'heure solaire peuvent être extraites du motif de polarisation du ciel. L'heure solaire peut, dans un second temps,

permettre d'estimer sa longitude. Nous avons testé notre méthode en simulation et expérimentalement, à l'aide d'une caméra polarimétrique à division de plan focal. Nous proposons ensuite des améliorations de notre méthode, à travers des outils de traitement d'images, tels que des réseaux de neurones, ayant montré de remarquables performances pour le traitement d'images polarisées.
En parallèle de cette méthode, un banc de caractérisation permettant de contrôler le degré et l'angle de polarisation d'une source de lumière ultraviolette, basée sur la combinaison de deux faisceaux de lumière polarisées orthogonalement et d'intensité relative variable, a été mise en œuvre. La caractérisation d'un capteur polarimétrique par une source dont le degré de polarisation peut être contrôlé est particulièrement utile pour l'étude des performances de la méthode de navigation développée dans cette thèse.

Mots clés : compas céleste, vision polarisée, géolocalisation, environnement sans GPS, diffusion de Rayleigh, caractérisation de capteur polarimétrique.

Abstract and keywords

Satellite navigation systems (GNSS) allow for precise and simple geolocation. However, these devices can see their signals degraded, either voluntarily or not, by blurring of their signals, for example. The fusion of satellite data with data from various navigation devices, such as inertial measurement units or lidars, helps to mitigate these disadvantages. Nevertheless, despite these improvements, current navigation systems still have flaws. Redundancy of information is essential to ensure the reliability of increasingly autonomous navigation systems. This redundancy is also present in migratory animals, using information from the Earth's magnetic field, stars, or the skylight polarization pattern. The latter, still poorly used, allows for celestial navigation, during day, without requiring a direct view of the Sun, making it compatible with urban navigation, for instance.
In this thesis manuscript, we propose to study the skylight polarization pattern to develop a geolocation system without GNSS. This possibility was envisaged because the polarization pattern is related to the sun's position in the sky, whose measurement, obtainable using a sextant, allows to geolocate at sea. The sextant is still a mandatory instrument on some ships today. In this thesis, a geolocation method, inspired by the perception of migratory birds calibrating their magnetic compass at night based on the celestial rotation of stars, has been developed to obtain the position of the north celestial pole during the day, thus the geographical north and also its latitude on Earth. By studying the temporal variations of the degree of polarization in the sky, we can obtain the position of the celestial pole from successive images of the sky taken by a polarimetric camera. More precisely, we seek points whose degree of polarization is invariant between two moments. This reveals two great circles, called invariance circles, linked to the symmetries of the polarization pattern. The celestial pole can be located simply because it is always on one of the invariances and is the only point in the sky with a constant degree of polarization at all times of the day, meaning it is the only point in the sky contained in an invariance at all times. This method has the advantage of requiring only measurements of the skylight polarization, with no other information such as time, date, or solar ephemeris needed, unlike existing methods. It also has the advantage of being extremely simple, requiring only calculations that could be performed by animals. We also show how the solar declination and solar time can be extracted from the skylight polarization pattern. Solar time measurements can then be used to estimate longitude. We have tested our method in simulation and experimentally using a division of focal plane polarimetric camera. We then propose various ways to improve our method, through image processing tools, such as neural networks, which have shown remarkable performance for processing polarized images.

In parallel to this method, a characterization setup, allowing to control independently the degree and angle of polarization of an ultraviolet light source, and based on the combination of two light beams with orthogonal state of polarization and variable relative intensity, was implemented. Characterizing a polarimetric sensor with a source having a controllable degree of polarization is particularly useful for studying the performances of the navigation method developed in this thesis.

Keywords: celestial compass, polarized vision, geolocation, Rayleigh scattering, GPS-denied environment, polarimetric sensor characterization.

Remerciements

Avant de présenter les travaux réalisés au cours de ma thèse de doctorat, je commencerai par quelques remerciements.

Tout d'abord, je tiens à exprimer ma profonde reconnaissance à mes encadrants de thèse, Stéphane Viollet, David Duché, Julien Serres et Marcel Pasquinelli, qui ont accepté ma candidature il y a trois ans et m'ont accompagné tout au long de ce projet. Leur confiance, leur bienveillance, et leur sympathie ont joué un rôle crucial dans mon développement professionnel et ont largement contribué au bon déroulement de cette thèse.

Je suis également très reconnaissant envers mes collègues Léo Poughon et Antoine Moutenet, avec qui j'ai eu le plaisir de partager cette aventure doctorale. Leur aide précieuse m'a permis de gagner un temps considérable. Je remercie aussi mes stagiaires pour leur travail assidu et leur engagement tout au long de leurs stages respectifs. Mes remerciements vont également à Jean-Marc Ingargiola pour ses précieux conseils en électronique, à Carmen Ruiz et Johann Toudert pour leur conseils en caractérisation optique, ainsi qu'à Tomas Fiorido et Olivier Margeat pour leur assistance dans la fabrication de capteurs à base d'oxyde de zinc. Je souhaite également exprimer ma gratitude envers l'équipe du CEDRE (CEntre de formation et de soutien aux Données de la REcherche) d'Aix-Marseille Université, en particulier Youssef Trardi et Nicolas Grevet, pour leur soutien en apprentissage profond.

Je remercie chaleureusement Gilles Montagne, Nathalie Perrin, Marie-Eve Cadenel, Annie Gibert, et Wilfried Meozzi pour leur réactivité et leur aide dans les démarches administratives. Je suis également reconnaissant à Patrick Decherchi, Guillaume Rao et Julien Fade pour leur participation à mon CSI et leurs conseils. Un grand merci à Ludovic Escoubas et Delphine Sturma pour m'avoir offert l'opportunité de participer au programme doctoral défense et sécurité intérieure ainsi qu'à Franck Buloup et Remy Casanova pour m'avoir permis d'enseigner dans leurs cours respectifs. Enfin, je remercie Franck Orsatti, Dien Vinh Hoang-Dinh ainsi que le cabinet ATOUT PI LAPLACE pour leur assistance dans la rédaction et le dépôt du brevet.

Je tiens également à exprimer ma reconnaissance aux rapporteurs et examinateurs de cette thèse, Pascal Vasseur, Yann Battie, Simon Benhamou, et Anne Sentenac pour avoir accepté de participer à mon jury de thèse et pour le temps consacré à la lecture de ce manuscrit.

Je souhaite remercier plus largement tous les collègues de l'ISM et de l'IM2NP (et de 3L-Optronics) avec qui j'ai partagé ces trois années de travail, dans la bonne humeur, et grâce à qui j'ai toujours pris plaisir à venir travailler.

Enfin, je veux remercier ma famille, qui m'a toujours soutenu et su me conseiller.

Contents

Affidavit 2

Liste de publications et participation aux conférences 3

Résumé et mots clés 5

Abstract and keywords 7

Remerciements 9

Contents 11

List of Figures 14

List of Acronyms 17

Introduction 19

1. Polarization and scattering of light 22
- 1.1. History of polarization . . . 22
- 1.2. Polarization definition . . . 24
  - 1.2.1. The wave equation . . . 25
  - 1.2.2. The ellipse of polarization and the Poincaré sphere . . . 28
  - 1.2.3. The Stokes formalism . . . 30
  - 1.2.4. The Mueller matrix . . . 37
- 1.3. Skylight polarization . . . 40
  - 1.3.1. Rayleigh scattering . . . 40
  - 1.3.2. Scattering in the atmosphere . . . 44
    - 1.3.2.1. Rayleigh single scattering model . . . 44
    - 1.3.2.2. Real skylight polarization, and alternative skylight polarization models . . . 48
  - 1.3.3. Advantages of the UV light for skylight polarization based navigation . . . 52

2. Polarimetric sensor : design and calibration 55
- 2.1. Polarization sensors . . . 55
  - 2.1.1. Division of time polarimeter . . . 57
  - 2.1.2. Instantaneous measurements . . . 58
    - 2.1.2.1. Divison of amplitude polarimeter . . . 59

2.1.2.2. Division of wavefront polarimeter 59
2.2. Skylight polarization sensors 61
2.2.1. Non-imaging sensors 61
2.2.2. Imaging sensors 63
2.3. Calibration 67
2.3.1. Geometric calibration 68
2.3.2. Radiometric calibration 69
2.3.3. Polarimetric calibration 71
2.3.4. Polarized light generation for DoLP measurement characterisation 76
2.3.4.1. Generation of partially polarized light 76
2.3.4.2. Experimental setup for controlling the AoP and DoLP of a light beam, independently 77
2.3.4.2.1. Conceptual explanation 77
2.3.4.2.2. Implementation of the source 79
2.3.4.2.3. Results 81
2.3.4.2.4. Discussion 84
2.4. Conclusion 84

3. Geolocation **86**
3.1. Skylight polarization navigation 86
3.1.1. Spherical astronomy definitions 86
3.1.2. Insect-inspired navigation 90
3.1.3. Geolocation using skylight polarization 95
3.2. Migratory birds inspired navigation 99
3.2.1. Skypole : locating the celestial pole from temporal variations of the skylight polarization pattern 102
3.2.1.1. Sun trajectory 103
3.2.1.2. DoLP variations at the celestial pole 103
3.2.1.2.1. DoLP invariance condition 104
3.2.1.2.2. DoLP invariance at the celestial pole 104
3.2.1.3. DoLP invariances in the celestial dome 104
3.2.1.3.1. First Set, radial invariance 105
3.2.1.3.2. Second Set, plane invariance 106
3.2.1.4. Variations of the DoLP invariances during a whole day 107
3.2.1.4.1. The NCP is the only point included in the radial invariance set at any time 107
3.2.1.4.2. There is no point included in the plane invariance set at any time 109
3.2.2. Polendar : Measuring the solar declination from skylight polarization patterns 110
3.2.2.1. Lemmas 111
3.2.2.1.1. Intersection of the plane and radial invariances is located at 90° from the positions of Sun . . . 111
3.2.2.1.2. Plane and radial invariances are great circles . 112

3.2.2.2. Relation between the solar declination and the intersection of the radial and plane invariances 113
3.2.2.2.1. Demonstration 113
3.2.2.2.2. Difference between the solar declination and the great circle distance between I and P_N . . . 114
3.2.3. Measuring time from skylight polarization patterns, the Wheatstone polar clock and the polar chronometer 116
3.3. Methodological approach to skylight navigation using the time invariances of the skylight polarization patterns 118
3.3.1. Measurement device 118
3.3.2. The SkyPole method 120
3.3.2.1. Algorithm 120
3.3.2.2. Experimentation 121
3.3.2.2.1. Methodology 121
3.3.2.2.2. Results 122
3.3.3. The SkyPole method with machine learning 122
3.3.3.1. Deep learning models for polarization image processing 123
3.3.3.2. Algorithm 127
3.3.3.3. Simulation results 128
3.3.3.4. Experimental results 129
3.3.4. The Polendar method 130
3.3.4.1. Algorithm 131
3.3.4.2. Simulation results 132
3.3.4.3. Experimental results 134
3.4. Discussion 135
3.4.1. Navigation algorithms 135
3.4.2. Animals navigation 140

Conclusion **143**

Bibliographie **145**

APPENDIX **170**

A. Matching of a simulated image to a real image **171**

B. Mueller matrices of the characterization setup's components **172**

C. Descriptif détaillé de la thèse **174**

List of Figures

1.1. Monochromatic electromagnetic plane wave . . . 27
1.2. Electric field and the polarization ellipse . . . 28
1.3. Parameters of the polarization ellipse . . . 29
1.4. The Poincaré sphere and the polarization ellipse's parameters . . . 30
1.5. Polarization ellipse examples . . . 35
1.6. The Poincaré sphere and the Stokes parameters . . . 35
1.7. Effect of a linear polarizer on a monochromatic elliptically polarized wave 39
1.8. Spherical and Cartesian coordinates . . . 42
1.9. Rayleigh scattering of a particle subject to an incident unpolarized light 44
1.10. Scattering angle . . . 46
1.11. Scattering plane. . . . 46
1.12. Distribution of the E-vectors in the sky . . . 47
1.13. False color patterns of angle and degree of the skylight's linear polarization simulated based on Rayleigh single scattering model . . . 47
1.14. Skylight DoLP variations under a clear sky, experimental and simulated data . . . 48
1.15. Skylight DoLP under cloudy skies, experimental and simulated data . . . 49
1.16. The four neutral point in the celestial dome . . . 49
1.17. Skylight DoLP under clear skies, experimental data . . . 51
1.18. Schematic representation of scattering in cloudy sky . . . 53
1.19. Skylight DoLP under cloudy skies, experimental data . . . 54

2.1. Anatomy of a mantis shrimp polarization sensitive compound eye . . . 56
2.2. Division of time polarimeters . . . 59
2.3. Effect of a polarizing beam splitter on an incident unpolarized light . . . 60
2.4. Division of wavefront polarimeter . . . 60
2.5. Structure of the camera eye . . . 62
2.6. Pol-neuron representation and output signal . . . 63
2.7. Schematic representation of four types of non-imaging sensors . . . 64
2.8. Schematic representation of the projection of light ray by a lens, onto the image plane . . . 65
2.9. Schematic representation of four types of imaging sensors . . . 66
2.10. An injection-molded lens with stress birefringence . . . 68
2.11. Geometric calibration of a fish-eye camera with a checkerboard . . . 69
2.12. DoFP sensor's response to an homogeneous light as a function of the exposure time . . . 70
2.13. Radiometric calibration setup of a polarized monochromatic camera . . . 71

2.14. Radiometric calibration of a polarized monochromatic DoFP sensor . 72
2.15. Misalignment between the polarizing filters and the photodiodes of a DoFP sensor . . . 72
2.16. Response variations of the pixels of a DoFP sensor, illuminated by a uniform unpolarized light source . . . 73
2.17. Cross-talk effect of a DoFP sensor . . . 73
2.18. Setup of the partially polarized light source . . . 80
2.19. Steps for determining the orientation of the rotating optical components of the setup . . . 82
2.20. Results obtained from the characterization setup . . . 83

3.1. Representation of a great circle and a small circle . . . 87
3.2. Coordinates of an observer O located at the Earth surface . . . 87
3.3. Sun equatorial coordinates . . . 88
3.4. Observer's meridian and a vertical circle . . . 89
3.5. Horizontal coordinate system . . . 89
3.6. Sun equatorial coodinates represented in the ENU frame . . . 89
3.7. Compass orientation and inertial navigation strategies . . . 91
3.8. Robot AntBot . . . 92
3.9. Methods for measuring the Sun's position . . . 92
3.10. Simulated angle of polarization in the local and global frame . . . 94
3.11. Simulated local angle of polarization . . . 94
3.12. Sun zenith angle for an observer O located at an angle ζ from the Sun's geographical position GP . . . 96
3.13. Circle of position centered on the geographic position of the Sun . . . 96
3.14. Geopositioning methods using a sextant . . . 97
3.15. Equation of time . . . 98
3.16. Navigational triangle . . . 99
3.17. Circumpolar startrails over the Atacama . . . 101
3.18. Zenith angle ζ of the NCP, as seen by an observer O, at a latitude ϕ . . . 102
3.19. The trajectory of the sun in the ENU frame . . . 103
3.20. Symmetries of skylight DoLP pattern . . . 105
3.21. Invariance circles on the celestial sphere . . . 107
3.22. Invariance circles on the celestial sphere . . . 108
3.23. Plot of equation . . . 110
3.24. Invariance circles on the celestial sphere, and the solar declination . . . 111
3.25. Intersection of the plane and radial invariance circles on the celestial sphere . . . 112
3.26. Demonstration declination and intersection of polarization invariances 115
3.27. Approximation error induced by the hypothesis $\alpha \ll 1$ . . . 116
3.28. Sun hour angle from the direction of polarization at the NCP . . . 117
3.29. Principle of the polar chronometer . . . 118
3.30. Four neighboring color-polarization super pixels of the DoFP measurement device . . . 119

3.31. Global view and mechanical layout of the measurement device 119
3.32. Method for finding the NCP based on the skylight's DoLP pattern . . . 121
3.33. Multiple intersections of invariances 122
3.34. SkyPole algorithm applied to experimental data for finding the NCP . . 123
3.35. NCP coordinates computed with the SkyPole algorithm from experimental data versus ground truth NCP coordinates 124
3.36. Schematic representation of a perceptron 124
3.37. Schematic representation of a multi-layer perceptron 125
3.38. Schematic representation of a convolution layer, with a 4x4 kernel . . . 127
3.39. Method for finding the NCP based on the skylight's DoLP pattern . . . 129
3.40. Celestial Pole coordinates estimation error 130
3.41. North Celestial Pole coordinates estimation error 131
3.42. Variation of the relative position between the NCP and the intersection of the radial and plane invariances as a function of the declination . . . 132
3.43. Method for finding the NCP based on the skylight's DoLP pattern and the solar declination 133
3.44. Celestial pole coordinates computed from simulated data with the Polendar algorithm 134
3.45. NCP coordinates estimation error 135
3.46. DoLP invariance patterns for varying maximum of DoLP 137
3.47. Representation of 1° error in latitude and true north on a map, for the camera's position 138
3.48. Artistic view of the celestial rotation of stars during night and of skylight polarization during day 141

List of Acronyms

AoP
Angle of Polarization.

CNN
Convolutional Neural Network.

CP
Celestial Pole.

DoAmp
Division of Amplitude.

DoFP
Division of Focal Plane.

DoLP
Degree of Linear Polarization.

DoP
Degree of Polarization.

DRA
Dorsal Rim Area.

EASA
European Union Aviation Safety Agency.

ENU
East, North, Up.

GMT
Greenwich Mean Time.

GNSS
Global Navigation Satellite System.

GPS
Global Positioning System.

INS
Inertial Navigation Sensors.

LCVR
Liquid Crystal Variable Retarder.

LIDAR
Laser Imaging, Detection And Ranging.

MAE
Mean Absolute Error.

MLP
Multi-Layer Perceptron.

NCP
North Celestial Pole.

POLDER
POLarization and Directionality of the Earth's Reflectances.

RADAR
RAdio Detection And Ranging.

RNN
Recurrent Neural Network.

SCP
South Celestial Pole.

UV
Ultraviolet.

Introduction

Global navigation satellite systems (GNSS) are widely used due their great navigation performance. In fact, GNSS can provide a position on Earth almost instantaneously and with a precision of a few meters [1]. However, GNSS systems are subject to disturbances. Those perturbations can be involuntary, due to multipath reception [2], occurring, for instance, when signals are reflected from buildings, or due to masking of the GNSS signals by obstacles located between the receiver and the transmitter [3]. GNSS signals can also be threatened voluntarily by malicious attacks, such as blurring [4], which consists in making the satellite signals unusable, or spoofing [5, 6], for which fake satellite signals are sent to a receiver in order to provide an incorrect position or bearing. The European Union Aviation Safety Agency (EASA) reported in 2023 that "GNSS jamming and/or spoofing has shown further increase in the severity of its impact, as well as an overall growth of intensity and sophistication of these events".
To ensure reliable positioning, GNSS can be combined with other sensors, such as inertial navigation sensors (INS), cameras, lidars (laser imaging, detection and ranging) or radars (radio detection and ranging) [7]. INS can provide a position with respect to an initial position through a robust estimation of the orientation and acceleration of the system. However, INS are subject to a signal drift in time leading to an error accumulation and, therefore, require to be calibrated regularly. A way of calibrating an INS is by means of GNSS positioning information [8]. Nevertheless, if a GNSS is spoofed, without being detected, the INS may be calibrated by a corrupted signal, making the system unreliable. Other systems were developed to add robustness to navigation, such as lidars, radars and cameras, but those systems require a prior knowledge or learning of the environment to provide a position on Earth.
Due to the limitations of those technological navigation methods, old fashioned navigation tools are still of interest. A magnetic compass provide the direction of the Earth's magnetic poles, different from the geographic poles and drifting in time, thus requiring compensation for the magnetic declination [9]. Moreover, magnetic compasses are sensitive to ferromagnetic metals, distorting the magnetic field. The sextant, a celestial navigation device invented in the 1730s by John Hadley and Thomas Godfrey, allowing to geolocate based on the measurement of a star's elevation [10], remains mandatory onboard merchant or French Navy's vessels [11]. However, sextants require a view of a star, such as the Sun, making it unsuitable for urban navigation or under cloudy weathers.
Alternatively, solutions to the navigation challenges may lie in the animal world. Some animals, such as migratory birds are known for their incredible navigation skills. However, the underlying mechanisms explaining those capabilities remain poorly understood [12]. Decades of research on animal navigation have yet made it pos-

sible to identify some strategies and cues used for this means. As reviewed in [12], various orientation and navigation strategies can be adopted with more or less complexity. A basic strategy, known as taxis, consists of orienting towards or away from a cue. Hatchling sea turtles, for instance, use a phototaxis strategy, moving towards the Sun, when leaving their breeding place [13]. Another basic strategy, adopted by dung-beetles, is known as compass orientation. It consists of maintaining a constant bearing with respect to a cue, such as the Milky Way [14] or skylight polarization [15], invisible to the human eye, for example. Similarly, vector navigation consists of using a sequence of bearings to reach a goal. Juvenile birds were shown to use this strategy when migrating, following the same direction for an known distance or time, based on celestial cues, such as the Sun, stars or skylight polarization, and the Earth magnetic field, and repeating this process, probably using an innate program [16]. This strategy differs from that of adult birds, that are able to optimize their travelled distance, compared to first-time migrants [17, 18]. An alternative strategy, known as piloting, consists of moving randomly until a known landmark is found, and then, going from landmark to landmark until the goal is reached. This strategy is employed by desert ants, using visual landmarks, such as trees, to find a known path [19]. A strategy comparable to using an INS, and adopted by desert ants, is known as path integration, or inertial navigation. This method consists of estimating a current position with respect to an initial position, through the estimation of intermediate positions found by combining distance and heading information. *Cataglyphis* desert ants are known to use the skylight pattern of polarization as a compass [20, 21]. The last and least understood strategy is known as true navigation. It supposes that some animals, such as migratory birds, can geolocate themselves using a bi-coordinate grid, not necessarily latitude and longitude, based on global stimuli such as the magnetic field or celestial cues [12, 22, 23].
As illustrated through those strategies, navigation cues used by animals, such as landscapes, stars or magnetic fields, are similar to those used by humans to navigate. However, the skylight polarization pattern has been introduced only recently as a celestial cue for navigation [24]. The use of this pattern for animal navigation was discovered in 1949 by Karl Von Frisch, while studying how bees navigate [25]. This pattern, related to the position of the Sun, allows the use of celestial cues for navigation during the day even when overcast, or when only a small patch of the sky is visible. Skylight polarization was found to be used by a wide variety of animals to navigate. Insects such as desert ants, desert locusts, monarch butterflies, crickets, or fruit-flies, and also some migrating birds navigate using this pattern [15].

Those studies on animal navigation led to the implementation of the AntBot robot, designed at the Institute of Movement Science, in Marseille, to mimic the inertial navigation behavior of the *Cataglyphis* desert ant [26]. This experiment was successful, but, as ants are only capable of locating with respect to their nest, the developed method could only provide a relative position. The aim of this thesis was to study the use of skylight polarization as an absolute navigation cue, allowing to geolocate, without using a GNSS. This task was known achievable, since the skylight polarization

pattern allows to measure the position of the Sun, which, as depicted through the sextant, can be used for positioning. Moreover, as the main advantage of sensing skylight polarization, rather than the direct sunlight, is the redundancy of available information and, therefore, the possibility of using skylight information in complex and noisy situations, when the sky is cloudy, or when only a small patch of the sky is visible, this thesis was also aimed at optimizing the skylight polarization acquisition and processing. As shown in the previous Antbot study [27], and inspired from *Cataglyphis* desert ant's spectral sensitivity to polarization, the use of ultraviolet (UV) sensors for navigation can improve the robustness of this task to perturbations such as clouds. This optimization step was thus addressed through UV sensing.

In this manuscript, the implementation of a characterization setup for UV sensors is presented as a preliminary step for the study of UV measurements. Due to a lack of time, UV sensing was not further studied. A geolocation method based on skylight polarization is also presented, inspired from the perception of migratory birds, considered true navigators, and calibrating their magnetic compass from the celestial rotation of stars. This method allows to obtain true north and the latitude, but also the time and date, related to longitude, by using only the skylight polarization pattern. The estimation of longitude was not implemented in this thesis, but only discussed.

This manuscript is organized as followed:
In chapter 1, the theory of polarization and skylight polarization is introduced, and the advantage of UV sensing is discussed.
Chapter 2 reviews the developed skylight polarization sensors and calibration methods. Then, the implementation of a setup aimed at characterizing a UV sensor is presented.
Chapter 3 reviews the existing skylight polarization navigation methods, mostly based on solar coordinates estimation. A navigation method based on time variations of the skylight polarization is then explained.
Those chapters are finally followed by the conclusion of this manuscript.

1. Polarization and scattering of light

In this chapter, we briefly introduce the polarization of light from an historical perspective. Starting from Maxwell's equations, we then define the polarization ellipse from the electric field of an electromagnetic plane wave. We next introduce the Stokes parameters and Mueller matrices used to describe polarized light and the influence of an optical component on the polarization state of light. Thereafter, we describe the polarization of light scattered by particles in the atmosphere based on Rayleigh scattering theory, and discuss the use of this model to describe the skylight polarization. We finally discuss the seemingly paradoxical sensitivity of animals to polarization in the ultraviolet.

1.1. History of polarization

Light, as we perceive it, varies in intensity and color. However, we are blind to a fundamental property of light named polarization. Due to this blindness, the polarization property of light was discovered in the 17th century. The first known observation of polarization was made in 1669, by Erasmus Bartholin, observing two images when looking through calcite, a crystal, from Island [28]. When turning the crystal, one ray remained fixed, and the other turned with the crystal. The rays where named ordinary and extraordinary rays, respectively, linked to intrinsic properties of the crystal. Crystals are birefringent materials, meaning they refract light differently depending on its polarization. Introducing the polarization property of light required to consider light as a wave. In 1690, Huygens proposed a wave theory of light through his book "Traité de la lumière" [29]. However, in 1703, Newton published his corpuscular theory of light [30] casting doubt upon the wave theory. The wave property of light was confirmed through Young's interference experiment in 1803 [31], which played a major role in the acceptance of the wave theory of light. Étienne Louis Malus was then the first to use the term polarization as a property of a light wave, and introduced the Malus law in 1809 [32], describing the intensity of light after coming out of a polarizer. In 1809, Dominique François Jean Arago discovered that skylight was polarized and observed a neutral point in the sky, meaning a point with unpolarized light, above the antisolar point [33]. Then, in 1840, Jacques Babinet discovered a second neutral point above the sun when observing the skylight polarization [34]. Sir David Brewster, aware of the discovery of the Babinet neutral point, and in accordance with his theory supposing that skylight polarization was due to reflections and refractions of sunlight, searched

for a third neutral point below the Sun, which he found in 1842 [35]. It was only in 2002, that Gabor Horváth observed the "fourth" neutral point, from high altitude, by using a hot air balloon [36]. The existence of four neutral points in the sky helped understanding skylight polarization. Sir David Brewster published in 1815 the Brewster law, showing the relation between polarization and the refractive index of a material [37]. In the meantime, Augustin-Jean Fresnel gave a general description of the refraction and reflection of polarized light, and analyzed the interference of polarized light [38]. In 1844, Wilhelm Karl von Haidinger discovered, even though humans do not perceive polarized light, some sensitivity of the human eye to polarization, enabling to see a pattern known as Haidinger's brushes [39]. In 1852, Sir George Gabriel Stokes defined the Stokes parameters [40], a set of four parameters used to describe the state of polarization of a light beam, followed by Jules Henri Poincaré, who, in 1892, represented polarization through a 3D sphere named the Poincaré sphere [41], which was later shown useful to represent the Stokes parameters. In 1861 and 1862, James Clerk Maxwell published a set of equations proving the electromagnetic nature of light [42]. In 1869, John Tyndall [43] conjectured that skylight was due to scattering of sunlight by particles, followed by Lord Rayleigh [44] which proposed a model to describe skylight scattering by small particles in the atmosphere, describing skylight polarization and explaining the blue color of the sky. In 1928, Edwin Herbert Land invented the sheet polarizer [45], much less expensive than crystal polarizers, allowing for the development of affordable polarization optics. The Jones formulation [46], a mathematical formalism to describe polarization, was introduced in the 1940s, and Hans Mueller used matrix multiplication to describe the state of polarization of light coming out of an optical system in 1943 [47]. Those formalism greatly simplified the description of polarized light. Between 1946 and 1950, Subrahmanyan Chandrasekhar gave practical applications of the Stokes parameters [48].

While polarization was given increasing attention from the scientific community, studies in ethology witnessed the use of polarization by animals. In 1914, by studying ants, Felix Santschi was the first to observe that the insects' compass was influenced by the scattered skylight [49]. It was only in 1947 that Karl von Frisch, unaware of Santschi's discovery, produced a similar experiment, and concluded, advised by the physician Hans Benndorf, that bees are sensitive to the skylight polarization [25]. His discovery was followed by similar findings on ants [20], flies [50], beetles [51] or spiders [52]. In the 1950s, insects' eye were studied, highlighting the intrinsic sensitivity of their compound eye to polarization due to the dichroism of molecules in their eyes [53]. In the 1970s-1980s, some vertebrates, such as birds, were shown to sense polarization [54]. During this period, multiple hypotheses were made on the use of polarization by animals to navigate. Kirschfeld suggested that animals use the state of polarization from two points in the sky to detect the position of the Sun, by referring to Rayleigh's sky polarization model [55]. Next, Brines suggested that the celestial pole was detected through polarized light by animals, giving access to navigation information such as True North [56]. Alternatively, Van der Glas suggested that polarization was coded through a trichromatic color pattern [57]. However, those hypothesis were put aside due to a lack of evidence and especially after the discovery of the dorsal rim area

(DRA) [58], the area of the compound eye looking towards the sky and only area of the insect's eye sensitive to the polarization, sufficient and necessary to detect the skylight polarization. This discovery allowed for new behavioral studies leading to hypothesize that insects use the symmetry of the skylight polarization pattern to navigate [59]. In parallel to those studies, Thorkild Ramskou suggested, in 1967, that Vikings navigated by using the skylight polarization [60]. This hypothesis originates from a story about a viking king Olaf II Haraldsson (995-1030), in which Sigurour, a viking, is able to find the position of the Sun even through clouds, using a stone. Nowadays, this stone is supposed to be a calcite crystal, but no "Sun stone" has been found yet. This hypothesis is however still subject to controversy [61, 62, 63, 64, 65, 66, 67].

Research on polarization led to the development of a wide range of applications. Sir Charles Wheatstone designed in 1848 a polar clock, providing the solar time based on the skylight polarization [68]. Ellipsometry was reported in 1888 by Paul Drude [69], enabling the analysis of materials through reflection or transmission of polarized light. After Edwin Herbert Land invented lightweight and inexpensive sheet polarizers, he developed the first polarized sunglasses. In 1948, August Herman Pfund created a device, the Pfund sky compass [70], based on skylight polarization to find the direction of the Sun, and used for transpolar flights. From 1996 the POLarization and Directionality of the Earth's Reflectances (POLDER) instrument was embarked onboard satellites for remote sensing of the Earth's atmosphere including polarization sensing [71]. The SkyPASS, a device to find True North and geolocate from skylight polarization without using global positioning system (GPS) was designed by Polaris sensor, a company founded in 2003, mainly for military applications [72].

This historical introduction of research on polarization and its use by animals to navigate shows the important progress made over time on their understanding. Knowledge acquired over time on polarization made and will make possible the development of new remote sensing applications. Animal navigation, even though increasingly understood, still remains mysterious, especially when it comes to vertebrates, much harder to study than insects.

This historical introduction was mostly written from elements introduced in Horváth's book on "Polarized Light and Polarization Vision in Animal Sciences" [15], Coulson's book on "Polarization and Intensity of Light in the Atmosphere" [73], and in Goldstein's book on "Polarized light" [74].

1.2. Polarization definition

In this section, we define the polarization property of light starting from Maxwell's equations which establish fundamental properties of electric and magnetic fields. From those equations, we derive the wave equations of an electromagnetic wave. Solutions of the electric wave equation are taken as a basis to introduce the polarization

of light through the so-called polarization ellipse.

1.2.1. The wave equation

Maxwell's equations are a set of four equations describing the variations in space and time of an electromagnetic field in presence of charges and currents. They were introduced in the 1860s by James Clerk Maxwell.
The Maxwell microscopic equations in the International System of Units, for non magnetic, linear, homogeneous and isotropic materials, are expressed as [75]:

$$\begin{cases} \operatorname{div}\vec{B} &= 0 \\ \overrightarrow{\operatorname{rot}}\,\vec{E} &= -\frac{\partial \vec{B}}{\partial t} \\ \operatorname{div}\vec{E} &= \frac{\rho}{\epsilon_0 \epsilon_r} \\ \overrightarrow{\operatorname{rot}}\,\vec{B} &= \mu_0 \vec{j} + \epsilon_0 \epsilon_r \mu_0 \frac{\partial \vec{E}}{\partial t} \end{cases} \tag{1.1}$$

Where $\vec{B}$ is the magnetic field, $\vec{E}$ is the electric field, div is the divergence and $\overrightarrow{\operatorname{rot}}$ the rotational operators, ρ is the electric charge volume density, $\vec{j}$ is the current volume density, ϵ_0 is the vacuum permittivity, μ_0 is the vacuum permeability, ϵ_r is the relative permittivity of the medium and $\frac{\partial}{\partial t}$ is the time derivative. In the following, we assume $\epsilon_r = 1$, which is a reasonable approximation for air. The $\vec{\cdot}$ symbol designates a vector. The electric and magnetic fields are both functions of space and time, such as $\vec{E} = \vec{E}(\vec{r}, t)$, and $\vec{B} = \vec{B}(\vec{r}, t)$, $\vec{r}$ being the position vector of a point in space and t the time. However, for readability, we omit those dependencies in our notations, when not ambiguous. Same remark for the electric charge volume density and the current volume density.
This formulation differs from the formulation using the Gaussian units convention, as employed in [76], but is equivalent.
From these equations, we can write:

$$\overrightarrow{\operatorname{rot}}\left(\overrightarrow{\operatorname{rot}}\,\vec{E}\right) = -\frac{\partial}{\partial t}(\overrightarrow{\operatorname{rot}}\,\vec{B}) = -\frac{\partial}{\partial t}\left(\mu_0 \vec{j} + \epsilon_0 \mu_0 \frac{\partial \vec{E}}{\partial t}\right) \tag{1.2}$$

Combining this equation with the following vector identity:

$$\overrightarrow{\operatorname{rot}}\left(\overrightarrow{\operatorname{rot}}\,\vec{E}\right) = \overrightarrow{\operatorname{grad}}\left(\operatorname{div}\vec{E}\right) - \vec{\Delta}\vec{E} \tag{1.3}$$

Where $\overrightarrow{\operatorname{grad}}$ is the gradient operator and $\vec{\Delta}$ is the vector laplacian operator.
We obtain the wave equation for the electric field:

$$\vec{\Delta}\vec{E} - \epsilon_0 \mu_0 \frac{\partial^2 \vec{E}}{\partial t^2} = \overrightarrow{\operatorname{grad}}\left(\frac{\rho}{\epsilon_0}\right) + \mu_0 \frac{\partial \vec{j}}{\partial t} \tag{1.4}$$

In vacuum, ρ and $\vec{j}$ being null, this equation comes down to:

$$\vec{\Delta}\vec{E} - \frac{1}{c^2}\frac{\partial^2 \vec{E}}{\partial t^2} = 0 \tag{1.5}$$

Where $c = \frac{1}{\sqrt{\epsilon_0 \mu_0}}$ is the speed of light in vacuum.
More generally, it can be shown that the equation is similar for a wave propagating in an homogeneous medium, free from charges and currents. In this case, the speed of light in vacuum is replaced by the speed of light in the medium $v = \frac{1}{\sqrt{\epsilon \mu}}$, where ϵ and μ are the permittivity and permeability, respectively, of the medium [76].
To solve equation 1.5, we can consider the Fourier transform of the electric field [76]:

$$\vec{E}(\vec{r}, t) = \frac{1}{\sqrt{2\pi}} \int_{-\infty}^{\infty} \vec{E}(\vec{r}, \omega) e^{-i\omega t} \mathrm{d}\omega \tag{1.6}$$

Where $i = \sqrt{-1}$ and ω is the pulsation, linked to the frequency f by $\omega = 2\pi f$.
By applying the second order time derivative to the Fourier transform, we get:

$$\frac{\partial^2 \vec{E}(\vec{r}, \omega)}{\partial t^2} = \omega^2 \vec{E}(\vec{r}, \omega) \tag{1.7}$$

Therefore the wave equation in vacuum (Eq. 1.5) becomes:

$$\vec{\Delta}\vec{E}(\vec{r}, \omega) - \frac{\omega^2}{c^2}\vec{E}(\vec{r}, \omega) = 0 \tag{1.8}$$

In the following, we consider plane wave solutions of the wave equation in vacuum. As precise in section 1.3.1, this hypothesis is acceptable when sensing skylight polarization.
A plane wave solution of the wave equation is of the form (cf. [74]):

$$\vec{E} = \vec{E}\left(\vec{r} \cdot \vec{s}, t\right) \tag{1.9}$$

Where $\vec{s}$ is a unit vector in a fixed direction, and $\cdot$ is the scalar product. For all points associated to a vector $\vec{r}$, and located on a same plane orthogonal to $\vec{s}$, we have:

$$\vec{r} \cdot \vec{s} = \text{constant} \tag{1.10}$$

Therefore, for a given time, $\vec{E}$ will be constant on this plane.
From the plane wave assumption, we can show that the 3D wave equation reduces to a 1D equation (cf. [74]). Let us suppose that the plane wave propagates in the z direction of a Cartesian frame, Eq. 1.8 will reduce to:

$$\frac{\partial^2 \vec{E}(z, \omega)}{\partial z^2} - \frac{\omega^2}{c^2}\vec{E}(z, \omega) = 0 \tag{1.11}$$

This equation is the harmonic oscillator equation, which has for solution:

$$\vec{E}(z,\omega) = \vec{E_0}(\omega) \cdot e^{i(kz+\varphi)} \tag{1.12}$$

where $k = \frac{\omega}{c}$.
For a monochromatic plane wave of pulsation ω_0, from Fourier transform (Eq. 1.6) and Eq. 1.12, we get:

$$\vec{E}(z,t) = \overrightarrow{E_{0m}} \cdot e^{ik_0 z} \cdot e^{-i\omega_0 t} \tag{1.13}$$

Where $k_0 = \frac{\omega_0}{c}$.
More generally, a monochromatic plane wave propagating in the $\vec{s}$ direction will have the form [74]:

$$\vec{E}(\vec{r},t) = \overrightarrow{E_{0m}} \cdot e^{i(k_0 \vec{s}\cdot\vec{r} - \omega_0 t)} \tag{1.14}$$

The vector $\vec{k} = k_0 \vec{s}$ is named the wave vector. The wavelength λ_0 is defined as $\lambda_0 = \frac{2\pi}{k_0} = \frac{2\pi c}{\omega_0}$.
Here, we only considered the electric field of an electromagnetic wave. It is worth noting that for a monochromatic plane wave, the magnetic field can be deduced from the electric field and the wave vector (cf. [74]). Moreover, the electromagnetic field is transverse in vacuum, meaning that the electric and magnetic fields are orthogonal to the wave vector (also true in an homogeneous medium free from charges and currents [74]). Finally, it can be shown, from Maxwell's equations for a monochromatic plane wave, that $\left(\vec{k}, \vec{E}, \vec{B}\right)$ forms a direct trihedron. In this case, the magnetic field can be deduced from the electric field through the relation:

$$\vec{B}(\vec{r},t) = \frac{\vec{s} \times \vec{E}(\vec{r},t)}{c} \tag{1.15}$$

Were $\times$ is the cross product. A visualization of a monochromatic electromagnetic plane wave is given in figure 1.1.

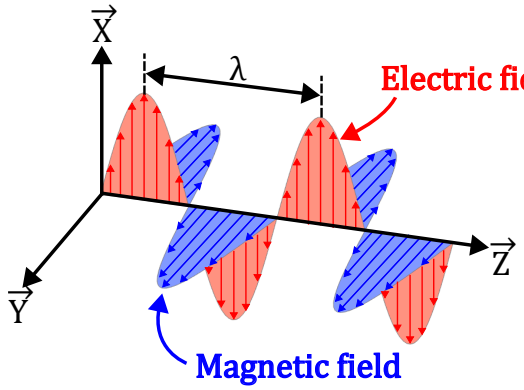

FIGURE 1.1. – Representation of a monochromatic electromagnetic plane wave propagating along the $\vec{Z}$ direction. The electric field is such as $\vec{E} = E\vec{X}$, and λ is the wavelength.

1.2.2. The ellipse of polarization and the Poincaré sphere

Polarization describes the electric field of an electromagnetic wave. As presented previously, the electric field of a monochromatic plane wave, propagating in the z direction of a cartesian frame, is transverse (meaning no component in the direction of propagation) and therefore can be expressed, taking the real part of Eq. 1.13, as:

$$\vec{E}(z,t) = E_{0x} \cdot \cos\left(k_0 z - \omega_0 t + \varphi_x\right) \vec{X} + E_{0y} \cdot \cos\left(k_0 z - \omega_0 t + \varphi_y\right) \vec{Y} \tag{1.16}$$

Were E_{0x} and E_{0y} are the amplitudes of the electric field in the $\vec{X}$ and $\vec{Y}$ directions respectively, and φ_x and φ_y are the origin phases of the electric field in the $\vec{X}$ and $\vec{Y}$ directions respectively, such as:

$$\overrightarrow{E_{0m}} = E_{0x} e^{i\varphi_x} \vec{X} + E_{0y} e^{i\varphi_y} \vec{Y} \tag{1.17}$$

We can deduce from this equation that the electric field draws an ellipse described by the following parametric equation:

$$\begin{cases} x = E_{0x} \cdot \cos\left(k_0 z - \omega_0 t + \varphi_x\right) \\ y = E_{0y} \cdot \cos\left(k_0 z - \omega_0 t + \varphi_y\right) \end{cases} \tag{1.18}$$

This ellipse is called the polarization ellipse (cf. figure 1.2).

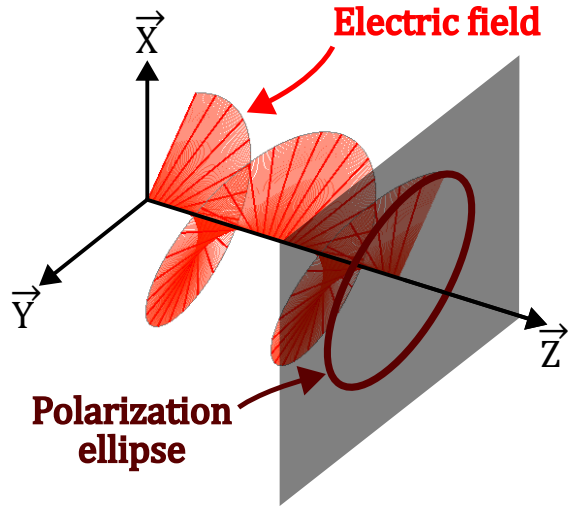

FIGURE 1.2. – Representation of a monochromatic electromagnetic plane wave propagating along the $\vec{Z}$ direction. The electric field vector draws an ellipse on a plane perpendicular to the $\vec{Z}$ axis.

The polarization ellipse can be characterized by its ellipticity angle χ, orientation angle ψ and direction of rotation represented in figure 1.3. Polarization rotates clockwise or counterclockwise depending on the sign of $\varphi = \varphi_y - \varphi_x$, the phase difference, and the convention used (discussed in [74]).

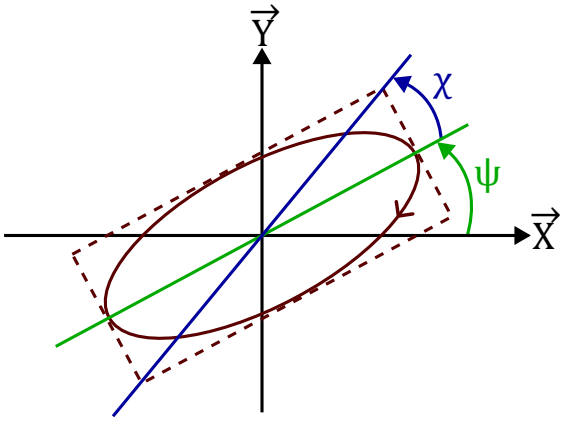

FIGURE 1.3. – Representation of the polarization ellipse. χ is the ellipticity angle, and ψ is the orientation angle of the ellipse. The direction of rotation is represented by an arrow on the ellipse.

Using trigonometric calculus, we can show:

$$\begin{aligned} \tan 2\psi &= \frac{2E_{0x} \cdot E_{0y} \cdot \cos\varphi}{E_{0x}^2 - E_{0y}^2} \\ \sin 2\chi &= \frac{2E_{0x} \cdot E_{0y} \cdot \sin\varphi}{E_{0x}^2 + E_{0y}^2} \end{aligned} \tag{1.19}$$

Two special cases for polarization can be considered, circular and linear polarization. A monochromatic plane wave is circularly polarized when its electric field draws a circle. A circle is an ellipse having an ellipticity of $\pm\pi/4$ radians. Therefore, a circularly polarized electric field must verify $E_{0x} = E_{0y}$, and $\varphi = \frac{\pi}{2} + k\pi, k \in \mathbb{Z}$. As for general elliptic polarization, we can distinguish left and right circular polarizations.
Linear polarization corresponds to an ellipticity of 0 degree. Linear polarization occurs when $\varphi = k\pi, k \in \mathbb{Z}$. For linear polarization the direction of rotation is not defined. A linearly polarized wave is represented in figure 1.1.
In the following sections, we will focus on linear polarization, since skylight polarization is mostly linearly polarized (cf. section 1.3.2.1).

The polarization ellipse can be described through the Jones formalism. In Jones formalism, the state of polarization is given by a 2D vector, named Jones vector:

$$\begin{bmatrix} E_{0x} \\ E_{0y} \cdot e^{i\varphi} \end{bmatrix} \tag{1.20}$$

However, as discussed in the next section, Jones formalism is not convenient for describing partially or unpolarized light. Jones formalism can be used for instance to study interference of polarized light, or for optical ray tracing [77]. The state of polarization of light can be represented on a sphere of unit radius, called the Poincaré

sphere [74]. The position of a point on this sphere is defined by two polar angles (cf. figure 1.4):

— its azimuth, which is equal to twice the orientation angle ψ of the ellipse

— its elevation, which is equal to twice the ellipticity angle χ of the ellipse

The Poincaré sphere is convenient to represent the evolution in time of the state of polarization of a wave. As discussed in the following section, the Poincaré sphere can be generalized to unpolarized or partially polarized light.

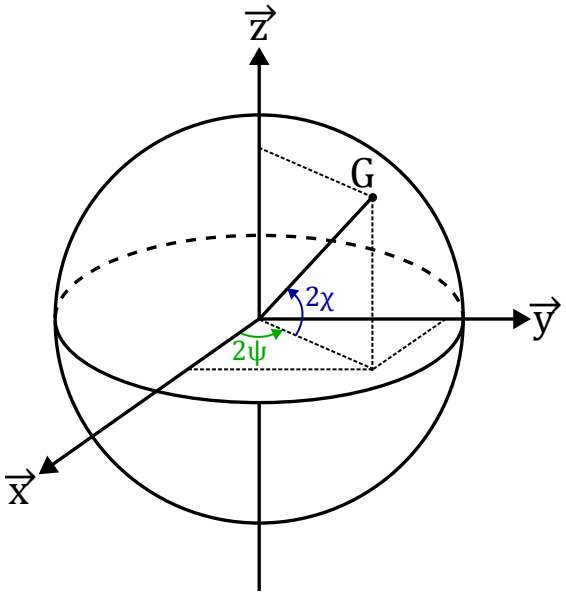

FIGURE 1.4. – The Poincaré sphere. The point G represents a purely polarized light defined by an ellipse of orientation ψ and ellipticity χ.

1.2.3. The Stokes formalism

Describing polarized light though the polarization ellipse is not convenient for remote sensing since the electric field varies with periods of about 10^{-15} second. Those periods are too short for being observed with a regular sensor. The human eye, and existing sensors are usually sensitive to irradiance since they integrate the wave energy over time. Moreover, the polarization ellipse is only defined for purely polarized light. However, in nature, light is mostly unpolarized or partially polarized [15]. Unpolarized light refers to light with an electric field varying randomly, with no preferred direction of oscillation. Partially polarized light can be considered as a combination of polarized light and unpolarized light.

When light is purely polarized, the electric field associated with the light is deterministic. When considering partially polarized light or unpolarized light, the electric field is described as a random vector. In this case, we can express the electric field for a plane wave propagating in the z direction as:

$$\vec{E}(z,t) = \overrightarrow{E_{xy}}(z,t) \cdot e^{-i\omega t} \tag{1.21}$$

Where $\overrightarrow{E_{xy}}$ is a random variable. ω is the "central" pulsation. As $\overrightarrow{E_{xy}}$ also varies in time, the signal has a spectral bandwidth Δf.
Therefore, when studying a partially polarized light, we must consider 3 time scales. The first one is the "central" period $T = \frac{1}{f} = \frac{2\pi}{\omega}$, which corresponds to the fastest variations of the electric field. The second time scale corresponds to typical time variations of $\overrightarrow{E_{xy}}$. Those variations are associated with periods of about $\frac{1}{\Delta f}$, which is slower than the previous. Finally, the sensor integrates the input signal with a slow integration time compared to the two first time scales.
The two components of a transverse electric wave propagating along the z direction can be expressed as [48]:

$$\begin{cases} E_x = E_{0x}(t) \cdot \cos(\omega t) \\ E_y = E_{0y}(t) \cdot \cos\left(\omega t - \varphi(t) - \epsilon\right) \end{cases} \tag{1.22}$$

Where $\varphi(t)$ is the instantaneous phase difference between the components of the electric field along the $\overrightarrow{X}$ and $\overrightarrow{Y}$ directions and ϵ is a constant retardation. $E_{0x}(t)$ and $E_{0y}(t)$ are the instantaneous amplitudes of the electric field in the $\overrightarrow{X}$ and $\overrightarrow{Y}$ direction, respectively. E_{0x}, E_{0y}, and φ are random variables.
Taking the electric field along a direction making an angle ξ with the $\overrightarrow{X}$ direction, we get:

$$\begin{aligned} E(\xi,\epsilon) &= E_{0x}(t)\cos(\omega t)\cos(\xi) + E_{0y}(t)\cos\left(\omega t - \varphi(t) - \epsilon\right)\sin(\xi) \\ &= \left[E_{0x}(t)\cos(\xi) + E_{0y}(t)\cos\left(\varphi(t)+\epsilon\right)\sin(\xi)\right]\cos(\omega t) \\ &\quad - E_{0y}(t)\sin\left(\varphi(t)+\epsilon\right)\sin(\xi)\sin(\omega t) \end{aligned} \tag{1.23}$$

When analyzing a light beam, we measure the irradiance, often referred to as the intensity. The irradiance of an electromagnetic wave is given by the time average of its squared Poynting vector [76]. Here, for a plane wave, we consider a relative irradiance, which corresponds to the time average of its squared electric field. This relative irradiance is proportional to the irradiance. Assuming a relative irradiance is generally not considered being an issue for skylight polarization remote sensing applications. It can however be an issue for some applications [78].
The relative intensity for the observation angle ξ and fixed retardance ϵ is given by:

$$I(\xi,\epsilon) = \langle E(\xi,\epsilon)^2 \rangle \tag{1.24}$$

Where $\langle\cdot\rangle$ represents the time average on one or multiple "central" periods of the signal (related to ω).
By taking the square of Eq. 1.23, we have:

$$\begin{aligned} E(\xi,\epsilon)^2 &= \left[E_{0x}(t)\cos(\xi) + E_{0y}(t)\cos\left(\varphi(t)+\epsilon\right)\sin(\xi)\right]^2\cos^2(\omega t) \\ &\quad + E_{0y}^2(t)\sin^2\left(\varphi(t)+\epsilon\right)\sin^2(\xi)\sin^2(\omega t) - 2\left[\ldots\right]\cos(\omega t)\sin(\omega t) \end{aligned} \tag{1.25}$$

Last term is not detailed since it will disappear when applying the time average.
When applying the time average to Eq. 1.25, we obtain:

$$\begin{aligned} I(\xi,\epsilon) &= \left\langle E(\xi,\epsilon)^2 \right\rangle \\ &= \frac{1}{2}E_{0x}^2(t)\cos^2(\xi) + \frac{1}{2}E_{0y}^2(t)\sin^2(\xi) \\ &\quad + \left[E_{0x}(t)E_{0y}(t)\cos\left(\varphi(t)\right)\cos(\epsilon) - E_{0x}(t)E_{0y}(t)\sin\left(\varphi(t)\right)\sin(\epsilon)\right]\cos(\xi)\sin(\xi) \\ &= \frac{1}{4}\left\{\left[E_{0x}^2(t) + E_{0y}^2(t)\right] + \left[E_{0x}^2(t) - E_{0y}^2(t)\right]\cos(2\xi)\right. \\ &\quad \left. +2\left[E_{0x}(t)E_{0y}(t)\cos\left(\varphi(t)\right)\cos(\epsilon) - E_{0x}(t)E_{0y}(t)\sin\left(\varphi(t)\right)\sin(\epsilon)\right]\sin(2\xi)\right\} \end{aligned} \tag{1.26}$$

Here, we applied the time average to one or multiple "central" periods of the wave. By supposing that other variables do not vary during the integration time (cf. time scale discussion above), we used the following equation:

$$\left\langle E_0^2(t)\cdot\cos^2(\omega t)\right\rangle = \frac{1}{2}E_0^2(t) \tag{1.27}$$

Similar equations where used for other variables. If considering irradiance measured with a sensor, the time integration will be much longer than the typical time variations of $\overrightarrow{E_{xy}}$. Therefore, we would have to consider also the mean values of the all time varying parameters of Eq. 1.26.
By setting:

$$\begin{cases} S_0 = \frac{1}{2}\left(E_{0x}^2(t) + E_{0y}^2(t)\right) \\ S_1 = \frac{1}{2}\left(E_{0x}^2(t) - E_{0y}^2(t)\right) \\ S_2 = E_{0x}(t)\cdot E_{0y}(t)\cdot\cos\left(\varphi(t)\right) \\ S_3 = E_{0x}(t)\cdot E_{0y}(t)\cdot\sin\left(\varphi(t)\right) \end{cases} \tag{1.28}$$

Eq. 1.26 becomes:

$$I(\xi,\epsilon) = \frac{1}{2}\left\{S_0 + S_1\cos(2\xi) + \left[S_2\cos(\epsilon) - S_3\sin(\epsilon)\right]\sin(2\xi)\right\} \tag{1.29}$$

The four parameters introduced in Eq. 1.28 are called the instantaneous Stokes parameters [79]. Usually, Stokes parameters are defined as the average, over the integration time of a sensor, of the instantaneous Stokes vector. The Stokes parameters are generally represented in a vector:

$$\overrightarrow{S} = \begin{pmatrix} S_0 \\ S_1 \\ S_2 \\ S_3 \end{pmatrix} \tag{1.30}$$

$\overrightarrow{S}$ is called the Stokes vector. This appellation is commonly used even though the Stokes vector is not a vector in a mathematical sense [77].

The Stokes parameters can be used to describe partially polarized or unpolarized light. Stokes parameters are very useful since they allow to describe polarized light by using observable quantities. Indeed, Eq. 1.29 links intensity to the Stokes parameters, as a function of the direction in which the field is measured, and a fixed retardance imposed to one component of the electric field. The two last parameters can be tuned by using two optical elements, a linear polarizer and a retarder. A linear polarizer is a filter that blocks light except in one direction named transmission axis. By using a linear polarizer, we can tune the direction parameter ξ. A retarder, or waveplate, adds a constant phase shift between two orthogonal electric field component of a light wave. By using a wave plate, we can tune the fixed retardance parameter ϵ.
To determine the four Stokes parameters of a light beam, we can proceed in the following way. By measuring light intensity through a polarizer oriented at 0°, 45° and 90°, we get:

$$\begin{aligned} I(0^\circ,0^\circ) &= \frac{1}{2}\left[S_0 + S_1\right], \\ I(45^\circ,0^\circ) &= \frac{1}{2}\left[S_0 + S_2\right], \\ I(90^\circ,0^\circ) &= \frac{1}{2}\left[S_0 - S_1\right] \end{aligned} \tag{1.31}$$

Then, by using a quarter wave plate, which introduces a 90° phase shift between the x and y axes, and a polarizer oriented at 45°, we get:

$$I(45^\circ,90^\circ) = \frac{1}{2}\left[S_0 + S_3\right] \tag{1.32}$$

We finally obtain the Stokes parameters from the measured intensities by the following:

$$\begin{aligned} S_0 &= I\left(0^\circ,0^\circ\right) + I\left(90^\circ,0^\circ\right), \\ S_1 &= I\left(0^\circ,0^\circ\right) - I\left(90^\circ,0^\circ\right), \\ S_2 &= 2I\left(45^\circ,0^\circ\right) - I\left(0^\circ,0^\circ\right) - I\left(90^\circ,0^\circ\right), \\ S_3 &= 2I\left(45^\circ,90^\circ\right) - I\left(0^\circ,0^\circ\right) - I\left(90^\circ,0^\circ\right) \end{aligned} \tag{1.33}$$

Interestingly, the Stokes parameters can be expressed with respect to the polarization ellipse parameters. Indeed, for a totally polarized light, by expressing Eq. 1.19 using Stokes parameters, we found that the angle ψ (also known as angle of polarization (AoP)) and the ellipticity χ of the polarization ellipse are given by:

$$\begin{aligned} \tan 2\psi &= \frac{S_2}{S_1} \\ \sin 2\chi &= \frac{S_3}{S_0} \end{aligned} \tag{1.34}$$

Therefore, the Stokes vector for a purely polarized light can be expressed as [74]:

$$\overrightarrow{S} = S_0 \begin{pmatrix} 1 \\ \cos 2\chi \cos 2\psi \\ \cos 2\chi \sin 2\psi \\ \sin 2\chi \end{pmatrix} \tag{1.35}$$

The Stokes parameters describe polarization as follows, S_0 corresponds to the total intensity of light. When measuring a beam of light with a photo-detector which is not sensitive to polarization, we only measure the S_0 parameter. The three other parameters describe the polarization state of light. S_1 and S_2 describe the angle of the polarization ellipse, and S_3 the ellipticity of the polarization ellipse.
For completely polarized light, we have the equation:

$$S_0^2 = S_1^2 + S_2^2 + S_3^2 \tag{1.36}$$

Here are some examples of Stokes vectors for purely polarized light:

— linear horizontally polarized light

$$\overrightarrow{S} = S_0 \begin{pmatrix} 1 \\ 1 \\ 0 \\ 0 \end{pmatrix} \tag{1.37}$$

— linear vertically polarized light

$$\overrightarrow{S} = S_0 \begin{pmatrix} 1 \\ -1 \\ 0 \\ 0 \end{pmatrix} \tag{1.38}$$

— linear +45° polarized light

$$\overrightarrow{S} = S_0 \begin{pmatrix} 1 \\ 0 \\ 1 \\ 0 \end{pmatrix} \tag{1.39}$$

— circular polarized light (sign of S_3 depends on the convention for direction of rotation)

$$\overrightarrow{S} = S_0 \begin{pmatrix} 1 \\ 0 \\ 0 \\ 1 \end{pmatrix} \tag{1.40}$$

The corresponding polarization ellipse are represented in figure 1.5.

We remark that polarization can be totally described from linear and circular pola-

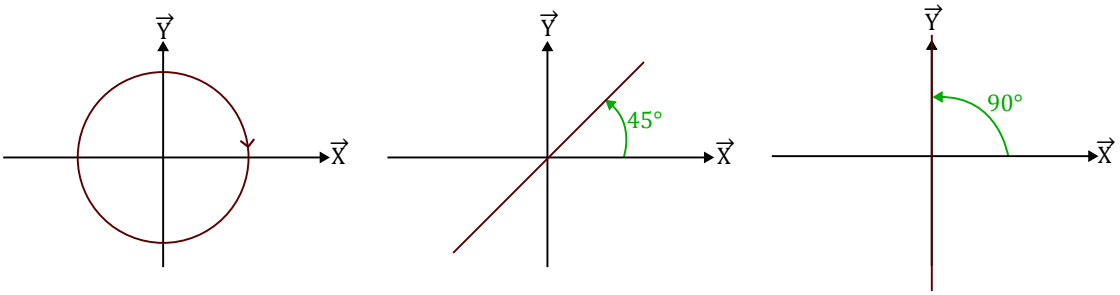

FIGURE 1.5. – Polarization ellipse for (left to right) circular polarized light, linear +45° polarized light and linear vertically polarized light.

rization states. Going back to the Poincaré sphere, we can express any point on the sphere from three coordinates. For this, we consider the reduced Stokes vector :

$$\overrightarrow{S_r} = \begin{pmatrix} S_1/S_0 \\ S_2/S_0 \\ S_3/S_0 \end{pmatrix} \tag{1.41}$$

Those parameters can be used to express the state of polarization independently of the light intensity. Those three parameters correspond to the Cartesian coordinates of a point in the Poincaré sphere, as shown in figure 1.6.

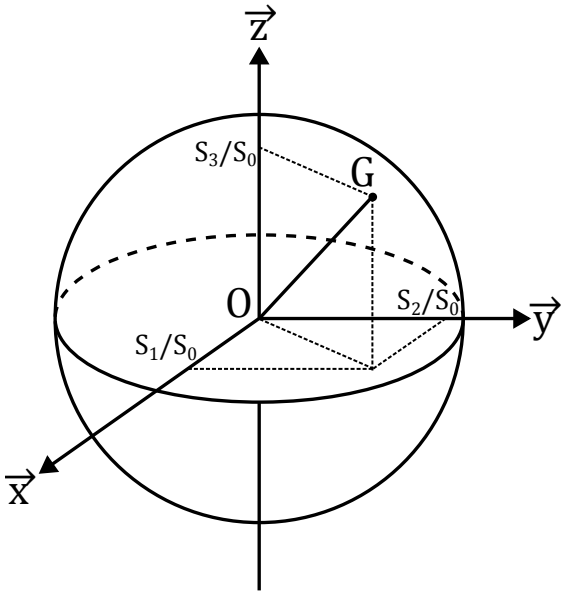

FIGURE 1.6. – The Poincaré sphere. The point G represents a purely polarized light defined by the Stokes parameters S_0, S_1, S_2, and S_3. The distance from the point G to the center of the sphere O corresponds to the degree of polarization of light.

For unpolarized light, the average amplitude over time of the electric field along

the $\overrightarrow{X}$ and $\overrightarrow{Y}$ directions is considered equal. Moreover, the phase difference can be considered as a uniform random variable. Therefore, by taking the time average, for an unpolarized light, of the Stokes parameters given in Eq. 1.28, considering the integration time of a photo-detector, we obtain:

$$\overrightarrow{S} = S_0 \begin{pmatrix} 1 \\ 0 \\ 0 \\ 0 \end{pmatrix} \tag{1.42}$$

which is the Stokes vector for unpolarized light.
We see here that we do no longer have the relation given in Eq. 1.36. In the Poincaré sphere, unpolarized light is represented as a point at the center of the sphere.
Partially polarized light of Stokes vector S_{pp} can be considered as a linear combination of a purely polarized light of Stokes vector S_p and of unpolarized light of Stokes vector S_u [74], such as:

$$\overrightarrow{S_{pp}} = (1-P)\overrightarrow{S_u} + P\overrightarrow{S_p} = (1-P)\begin{pmatrix} S_0 \\ 0 \\ 0 \\ 0 \end{pmatrix} + P\begin{pmatrix} S_0 \\ S_{p1} \\ S_{p2} \\ S_{p3} \end{pmatrix} = \begin{pmatrix} S_0 \\ PS_{p1} \\ PS_{p2} \\ PS_{p3} \end{pmatrix}, \quad 0 \leq P \leq 1 \tag{1.43}$$

P is named the degree of polarization (DoP) and is defined as the ratio of polarized light intensity to total light intensity. The DoP is obtained using Stokes parameters by:

$$P = \frac{\sqrt{S_1^2 + S_2^2 + S_3^2}}{S_0} \tag{1.44}$$

For linearly polarized light, we also define the degree of linear polarization (DoLP) as the ratio of linearly polarized light intensity to total light intensity, which in terms of Stokes parameters is given by:

$$P_l = \frac{\sqrt{S_1^2 + S_2^2}}{S_0} \tag{1.45}$$

For purely polarized light $P = 1$, and for unpolarized light $P = 0$.
For unpolarized or partially polarized light, we have the following equation:

$$S_0^2 > S_1^2 + S_2^2 + S_3^2 \tag{1.46}$$

The Stokes vector for a partially polarized light can finally by expressed as:

$$\mathbf{S} = S_0 \begin{pmatrix} 1 \\ P\cos 2\chi \cos 2\psi \\ P\cos 2\chi \sin 2\psi \\ P\sin 2\chi \end{pmatrix} \tag{1.47}$$

On the Poincaré sphere, the degree of polarization is encoded as the distance between the center of the sphere and the point representing the state of polarization of a given light beam. Light with a degree of polarization of P will therefore be located on a sphere of radius P (cf. figure 1.6).

1.2.4. The Mueller matrix

In the previous section, we described polarized light using the Stokes formalism. When light interacts with matter, the polarization is modified from this interaction. To describe those interaction, a very convenient formalism was introduced by Hans Mueller in the 1940s. By noticing that the Stokes parameters of light coming out of a polarizing component can be given as a linear combination of the incident light's Stokes parameters, we can represent polarizing components by a matrix filled with the linear combinations' coefficients, such as:

$$\overrightarrow{S_{out}} = \mathbf{M}\overrightarrow{S_{in}} \tag{1.48}$$

Where $\overrightarrow{S_{in}}$ is the incident light's Stokes vector, $\overrightarrow{S_{out}}$ is the Stokes vector of the light coming out of the polarizing component, and $\mathbf{M}$ is a 4 rows and 4 columns matrix representing the effect of the polarizing element on the incident light. $\mathbf{M}$ is called the Mueller matrix of the polarizing component.
As stated in [74], we can distinguish 4 ways of modifying the polarization of light, by changing the amplitude of electric field components, or the relative phase of the components, rotating the electric field, or depolarizing light. Those behavior can be represented through 4 optical filters, a linear polarizer, a retarder, a rotator and a depolarizer, respectively. Real optical components can be considered as a combinations of those 4 types of filters.
A linear polarizer, also called diattenuator, attenuates the amplitude of the electric field depending on its direction. It is characterized by two parameters, the orthogonal transmission axes coefficients p_x and p_y through the directions $\overrightarrow{X}$ and $\overrightarrow{Y}$, respectively, of the filter. When light goes through a diattenuator, the amplitudes of the two orthogonal components of the electric field are changed such as:

$$\begin{aligned} E_x^{out} &= p_x \cdot E_x^{in} \\ E_y^{out} &= p_y \cdot E_y^{in} \end{aligned} \tag{1.49}$$

Where E_x^{in} and E_y^{in} are the components of the input electric field along the $\overrightarrow{X}$ and $\overrightarrow{Y}$ directions, and E_x^{out} and E_y^{out} are the components of the output electric field along the $\overrightarrow{X}$ and $\overrightarrow{Y}$ directions.
From Eq. 1.28 and Eq. 1.48, we can show that the diattenuator's Mueller matrix is given

by:

$$\mathbf{M} = \frac{1}{2}\begin{pmatrix} p_x^2 + p_y^2 & p_x^2 - p_y^2 & 0 & 0 \\ p_x^2 - p_y^2 & p_x^2 + p_y^2 & 0 & 0 \\ 0 & 0 & 2p_x p_y & 0 \\ 0 & 0 & 0 & 2p_x p_y \end{pmatrix}, \quad 0 \leq p_{x,y} \leq 1 \tag{1.50}$$

The transmission axes coefficients of a linear diattenuator are sometimes expressed as follows:

$$\begin{aligned} p_x &= p \cdot \cos\iota \\ p_y &= p \cdot \sin\iota \end{aligned} \tag{1.51}$$

Where $0° \leq \iota \leq 90°$, and p defined such as $p^2 = p_x^2 + p_y^2$. The linear diattenuator's Mueller matrix can then be expressed from Eq. 1.50 as:

$$\mathbf{M} = \frac{p^2}{2}\begin{pmatrix} 1 & \cos 2\iota & 0 & 0 \\ \cos 2\iota & 1 & 0 & 0 \\ 0 & 0 & \sin 2\iota & 0 \\ 0 & 0 & 0 & \sin 2\iota \end{pmatrix} \tag{1.52}$$

A perfect polarizer keeps light unchanged in one direction, the transmission axis, and totally blocks the light in the orthogonal direction (cf. figure 1.7). Therefore, the amplitude attenuation coefficients of a perfect linear polarizer which outputs light polarized in the $\overrightarrow{X}$ direction are $p_x = 1$ and $p_y = 0$. The Mueller matrix thus becomes:

$$\mathbf{M} = \frac{1}{2}\begin{pmatrix} 1 & 1 & 0 & 0 \\ 1 & 1 & 0 & 0 \\ 0 & 0 & 0 & 0 \\ 0 & 0 & 0 & 0 \end{pmatrix} \tag{1.53}$$

If unpolarized light goes through a perfect linear polarizer, the output light's Stokes vector is given by:

$$\overrightarrow{S} = \frac{S_0}{2}\begin{pmatrix} 1 & 1 & 0 & 0 \\ 1 & 1 & 0 & 0 \\ 0 & 0 & 0 & 0 \\ 0 & 0 & 0 & 0 \end{pmatrix}\begin{pmatrix} 1 \\ 0 \\ 0 \\ 0 \end{pmatrix} = \frac{S_0}{2}\begin{pmatrix} 1 \\ 1 \\ 0 \\ 0 \end{pmatrix} \tag{1.54}$$

We see that the output light is totally polarized. Moreover, the intensity of the output light is twice as low as the input light's.

Here, we presented the Mueller matrix of a linear polarizer with vertical and horizontal transmission axes. However, linear polarizers can be rotated. Rotation of a polarizing component, of Mueller matrix $\mathbf{M}$, by a physical angle θ is given by [74]:

$$\mathbf{M}(\theta) = \mathbf{M}_{Rot}(-\theta) \cdot \mathbf{M} \cdot \mathbf{M}_{Rot}(\theta) \tag{1.55}$$

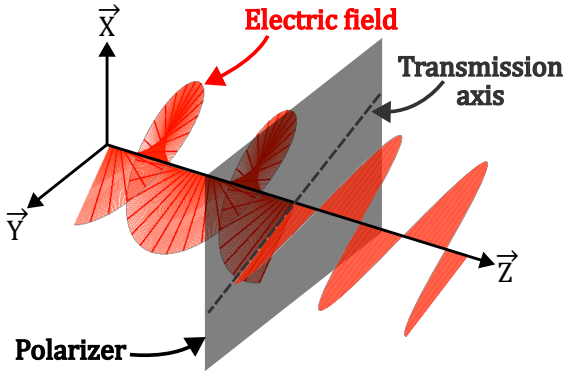

FIGURE 1.7. – Effect of a linear polarizer on a monochromatic elliptically polarized wave.

Where $\mathbf{M}_{\text{Rot}}$ is the Mueller matrix for a rotator:

$$\mathbf{M}_{Rot}(\theta) = \begin{pmatrix} 1 & 0 & 0 & 0 \\ 0 & \cos 2\theta & \sin 2\theta & 0 \\ 0 & -\sin 2\theta & \cos 2\theta & 0 \\ 0 & 0 & 0 & 1 \end{pmatrix} \tag{1.56}$$

Therefore, the Mueller matrix of linear polarizer rotated by an angle θ is given from Eq. 1.52 and Eq. 1.55 by:

$$\mathbf{M} = \frac{p^2}{2} \begin{pmatrix} 1 & \cos 2\iota \cos 2\theta & \cos 2\iota \sin 2\theta & 0 \\ \cos 2\iota \cos 2\theta & \cos^2 2\theta + \sin 2\iota \sin^2 2\theta & (1-\sin 2\iota)\sin 2\theta \cos 2\theta & 0 \\ \cos 2\iota \sin 2\theta & (1-\sin 2\iota)\sin 2\theta \cos 2\theta & \sin^2 2\theta + \sin 2\iota \cos^2 2\theta & 0 \\ 0 & 0 & 0 & \sin 2\iota \end{pmatrix} \tag{1.57}$$

A linear retarder creates a constant phase shift Φ between two components of a light beam, such as:

$$\begin{aligned} E_x^{out} &= e^{+i\Phi/2} \cdot E_x^{in} \\ E_y^{out} &= e^{-i\Phi/2} \cdot E_y^{in} \end{aligned} \tag{1.58}$$

Here, the $\overrightarrow{X}$ and $\overrightarrow{Y}$ axes of the retarder are referred to as the fast and slow axes respectively.
From Eq. 1.28 and Eq. 1.48, we can show that the linear retarder's Mueller matrix is given by:

$$\mathbf{M} = \begin{pmatrix} 1 & 0 & 0 & 0 \\ 0 & 1 & 0 & 0 \\ 0 & 0 & \cos\Phi & \sin\Phi \\ 0 & 0 & -\sin\Phi & \cos\Phi \end{pmatrix}, \quad 0 < \Phi < 2\pi \tag{1.59}$$

As for a linear polarizer, a waveplate can be rotated, its Mueller matrix being given by Eq. 1.55, such as:

$$\mathbf{M} = \begin{pmatrix} 1 & 0 & 0 & 0 \\ 0 & \cos^2 2\theta + \cos\phi \sin^2 2\theta & (1-\cos\phi)\sin 2\theta \cos 2\theta & -\sin\phi \sin 2\theta \\ 0 & (1-\cos\phi)\sin 2\theta \cos 2\theta & \sin^2 2\theta + \cos\phi \cos^2 2\theta & \sin\phi \cos 2\theta \\ 0 & \sin\phi \sin 2\theta & -\sin\phi \cos 2\theta & \cos\phi \end{pmatrix} \tag{1.60}$$

To express the output Stokes vector $\overrightarrow{S_{out}}$ of an input light, of Stokes vector $\overrightarrow{S_{in}}$, going through multiple polarizing components $(\mathbf{M}_1, ..., \mathbf{M}_n)$, $n > 1$, we can proceed step by step, by multiplying each Stokes vector of light coming out of the previous component by the following component's Mueller matrix, such as:

$$\overrightarrow{S_{out}} = \mathbf{M_n}\left(\mathbf{M_{n-1}}\left(...\left(\mathbf{M_2}\left(\mathbf{M_1}\overrightarrow{S_{in}}\right)\right)\right)\right) = \mathbf{M_n}\mathbf{M_{n-1}}...\mathbf{M_2}\mathbf{M_1}\overrightarrow{S_{in}} \tag{1.61}$$

1.3. Skylight polarization

In the previous section, we defined polarization and introduced the Stokes-Mueller formalism to describe polarized light and the effect of optical components on the state of polarization. In this section, we describe the scattering of light by particles and the resulting skylight polarization.

1.3.1. Rayleigh scattering

When interacting with particles, light is scattered. This scattered light has interesting polarization properties, essential to the understanding of skylight polarization.
In this section, we describe the scattering of an electron bounded to a nucleus. More specifically, we describe a specific case known as Rayleigh scattering [80].
We consider here an isotropic particle, meaning that, in response to an incident electromagnetic field, the bounded electron has no preferred direction of oscillation. We also suppose elastic scattering, which implies that the wavelength of the scattered light is the same as the wavelength of the incident light.
For an electron bounded to a nucleus and subject to an electric field, Newton's second law of motion can be given by [74]:

$$m\ddot{\overrightarrow{r}} + k\overrightarrow{r} = -e\overrightarrow{E} \tag{1.62}$$

Where $\overrightarrow{r}$, $\ddot{\overrightarrow{r}}$, e and m are the position, acceleration, charge and mass, respectively, of the electron, and $\overrightarrow{E}$ is the electric field. $k\overrightarrow{r}$ is the elastic restoring force linked to the bounding of the electron to the nucleus, k being a positive real number, and $-e\overrightarrow{E}$ is the Lorentz force induced by the electric field (the magnetic induced force being neglected in a non-relativistic regime).
By supposing that the electric field is transverse and propagating along the z direction,

we can show that the electron moves in the x, y plane, such as:

$$\begin{aligned}\ddot{x}(t) &= \frac{-e\omega^2}{m\left(\omega^2-\omega_0^2\right)}E_x(t)\\ \ddot{y}(t) &= \frac{-e\omega^2}{m\left(\omega^2-\omega_0^2\right)}E_y(t)\end{aligned} \tag{1.63}$$

where

$$\begin{aligned}E_x(t) &= E_{0x}\cdot e^{i\omega t+i\delta_x}\\ E_y(t) &= E_{0y}\cdot e^{i\omega t+i\delta_y}\end{aligned} \tag{1.64}$$

are the two components of the electric field along the $\overrightarrow{X}$ and $\overrightarrow{Y}$ directions respectively. ω is the frequency of the incident electric field, and $\omega_0 = \sqrt{\frac{k}{m}}$.
On the other side, we consider the wave equation of an electric field in an isotropic medium, we get from Eq. 1.4 (by assuming that $\overrightarrow{\text{grad}}\left(\frac{\rho}{\epsilon_0}\right) = \overrightarrow{0}$):

$$\triangle\overrightarrow{E} - \epsilon_0\mu_0\frac{\partial^2\overrightarrow{E}}{\partial t^2} = \mu_0\frac{\partial\overrightarrow{j}}{\partial t} \tag{1.65}$$

By using the relation:

$$\overrightarrow{j} = e\cdot\overrightarrow{v} \tag{1.66}$$

Where e is the charge, and $\overrightarrow{v}$ is the speed of the charge, we get:

$$\triangle\overrightarrow{E} - \epsilon_0\mu_0\frac{\partial^2\overrightarrow{E}}{\partial t^2} = \mu_0 e\frac{\partial\overrightarrow{v}}{\partial t} \tag{1.67}$$

Meaning that electric fields are generated by accelerating charges.
As a bounded charge radiates a spherical wave, the solution to this equation is given in spherical coordinates, such as [81]:

$$\begin{aligned}E_\theta &= \frac{e}{4\pi\varepsilon_0 c^2 R}\left(\ddot{x}\cos\theta - \ddot{z}\sin\theta\right)\\ E_\phi &= \frac{e}{4\pi\varepsilon_0 c^2 R}\ddot{y}\end{aligned} \tag{1.68}$$

Where $\ddot{x}$, $\ddot{y}$, $\ddot{z}$ are second derivatives with respect to time of the Cartesian coordinates x, y, z respectively of the moving charge. R is the distance to the charge from the observer, and θ is a coordinate associated with the spherical coordinate frame (cf. figure 1.8) such as:

$$\begin{aligned}\overrightarrow{u_r} &= \sin\theta\cos\phi\overrightarrow{X} + \sin\theta\sin\phi\overrightarrow{Y} + \cos\theta\overrightarrow{Z}\\ \overrightarrow{u_\theta} &= \cos\theta\cos\phi\overrightarrow{X} + \cos\theta\sin\phi\overrightarrow{Y} - \sin\theta\overrightarrow{Z}\\ \overrightarrow{u_\phi} &= -\sin\phi\overrightarrow{X} + \cos\phi\overrightarrow{Y}\end{aligned} \tag{1.69}$$

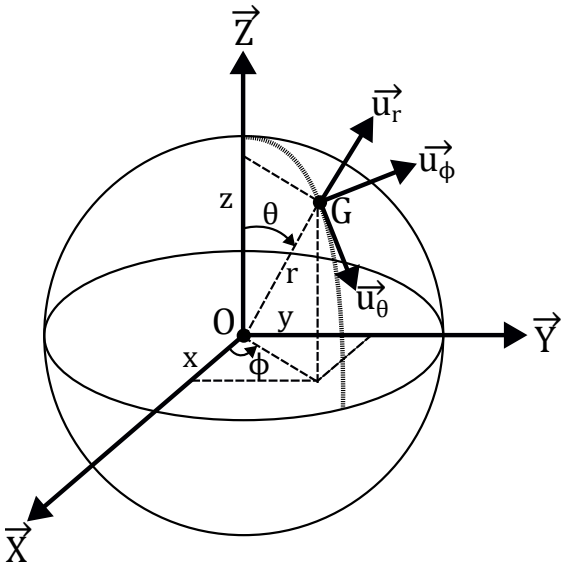

FIGURE 1.8. – Spherical and Cartesian coordinates of a point G.

E_θ and E_ϕ refer to the radiated electric field coordinates along $\overrightarrow{u_\theta}$ and $\overrightarrow{u_\phi}$ respectively. The radiated field is propagating along $\overrightarrow{u_r}$.
To obtain Eq. 1.68, we supposed that the observer is far from the bounded electron. This condition is known as the far field approximation, requiring two conditions:

$$\begin{aligned} l &\ll L \\ \frac{l^2}{\lambda} &\ll L \end{aligned} \tag{1.70}$$

Where l is the characteristic length of the source, L is the distance of the observer from the source, and λ is the wavelength of the radiated field. In our case, the bounded electron represents a particle in the sky observed from the surface of the Earth, which validates the first condition. Moreover, as discussed below, when considering Rayleigh scattering, we suppose that the particle is small compared to the wavelength. Therefore, we have $\frac{l^2}{\lambda} \ll L$. In our case, when considering Rayleigh scattering of atmospheric particles, we also have $\lambda \ll L$. Therefore, we can describe the bounded electron as an oscillating dipole. From the far field approximation, we can consider that the incident waves are plane waves.
In our case, the particle accelerates along the x and y axes only, therefore, we have:

$$\begin{aligned} E_\theta &= \frac{e}{4\pi\varepsilon_0 c^2 R}\ddot{x}\cos\theta \\ E_\phi &= \frac{e}{4\pi\varepsilon_0 c^2 R}\ddot{y} \end{aligned} \tag{1.71}$$

By combining Eq. 1.63 and Eq. 1.71, we get:

$$\begin{aligned} E_\theta &= \frac{-e^2\omega^2}{4\pi\varepsilon_0 mc^2 R\left(\omega^2-\omega_0^2\right)} E_x(t)\cos\theta \\ E_\phi &= \frac{-e^2\omega^2}{4\pi\varepsilon_0 mc^2 R\left(\omega^2-\omega_0^2\right)} E_y(t) \end{aligned} \tag{1.72}$$

When using spherical coordinates, we can define the Stokes parameters similarly than when considering Cartesian coordinates. Using complex notation of the electric field, we can show that the Stokes parameters using spherical coordinates are given in complex notation by [74]:

$$\begin{aligned} S_0 &= E_\phi E_\phi^* + E_\theta E_\theta^*, \\ S_1 &= E_\phi E_\phi^* - E_\theta E_\theta^* \\ S_2 &= E_\phi E_\theta^* - E_\theta E_\phi^* \\ S_3 &= i\left(E_\phi E_\theta^* - E_\theta E_\phi^*\right) \end{aligned} \tag{1.73}$$

Where $i = \sqrt{-1}$ and $*$ designate the conjugate of the complex number.
We can finally obtain the Stokes vector of scattered light from an electron bounded to a nucleus:

$$\overrightarrow{S} = \frac{1}{2}\left[\frac{-e^2}{4\pi\varepsilon_0 mc^2 R\left(\omega^2-\omega_0^2\right)}\right]^2 \omega^4 \begin{pmatrix} S_0\left(1+\cos^2\theta\right)+S_1\sin^2\theta \\ S_0\sin^2\theta + S_1\left(1+\cos^2\theta\right) \\ 2S_2\cos\theta \\ 2S_3\cos\theta \end{pmatrix} \tag{1.74}$$

Where S_0, S_1, S_2, and S_3 are the Stokes parameters of the incident light.
Moreover, we can also describe scattering by a bounded electron through a Mueller matrix, such as:

$$\mathbf{M} = \frac{1}{2}\left[\frac{-e^2}{4\pi\varepsilon_0 mc^2 R\left(\omega^2-\omega_0^2\right)}\right]^2 \omega^4 \begin{pmatrix} 1+\cos^2\theta & \sin^2\theta & 0 & 0 \\ \sin^2\theta & 1+\cos^2\theta & 0 & 0 \\ 0 & 0 & 2\cos\theta & 0 \\ 0 & 0 & 0 & 2\cos\theta \end{pmatrix} \tag{1.75}$$

We notice that the Mueller matrix for the scattering of a bounded electron corresponds to the Mueller matrix of a linear polarizer. Also, the polarization properties of the scattered field only depends on the angle θ called the scattering angle (cf. figure 1.9).

Rayleigh scattering is a particular case for which we consider that $\omega \ll \omega_0$. This condition is equivalent to assuming that the radius of the particle is much smaller than the wavelength. Assuming Rayleigh scattering, we remark that the intensity of the scattered light is proportional to the inverse of the fourth power of the incident's light wavelength (since $\omega = \frac{2\pi c}{\lambda}$, cf. 1.2.1). As discussed in the next section, Rayleigh scattering describes accurately skylight scattering. This dependence of Rayleigh scattering

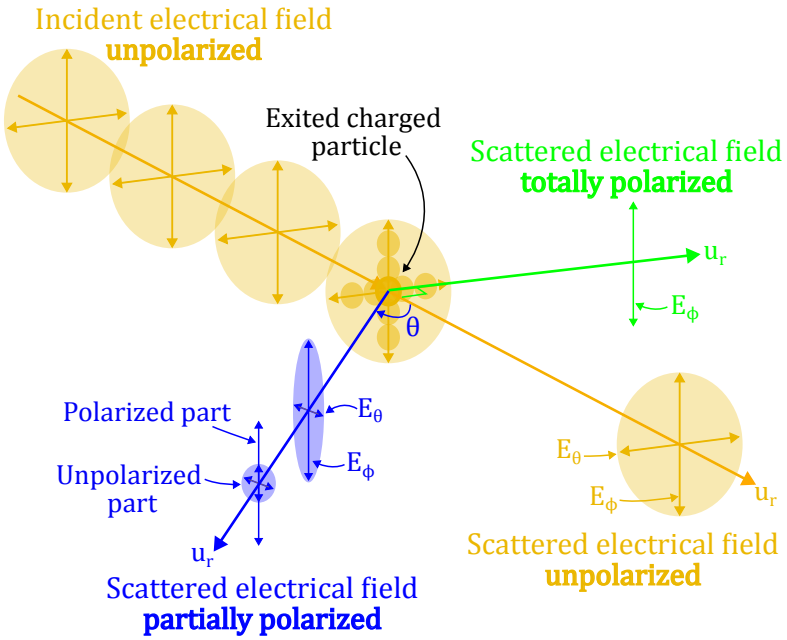

FIGURE 1.9. – Rayleigh scattering of a particle subject to an incident unpolarized light. The scattered electrical field is represented for three scattering angles θ, 0° (yellow), 90° (green) and $0° < \theta < 90°$ (blue). E_θ and E_ϕ refer to the radiated electric field coordinates along $\overrightarrow{u_\theta}$ and $\overrightarrow{u_\phi}$ respectively of the spherical frame. Figure adapted from [82].

on the wavelength explains why the sky is blue. Indeed, the intensity of scattered light increases when the wavelength decreases (ω being proportional to the inverse of the wavelength).

1.3.2. Scattering in the atmosphere

1.3.2.1. Rayleigh single scattering model

In the earth atmosphere, sun rays interact with particles which scatter light. The Earth atmosphere is composed of gases, ozone or aerosols such as dust, haze, or clouds composed of liquid droplets or frozen crystals. Aerosols are defined as fine solid particles or liquid droplets suspended in air.
Under a clear sky, with little aerosols, the atmosphere is mainly composed of nitrogen and oxygen which represent 78% and 21% respectively of the atmospheres's gases. When sun rays enter the atmosphere, they interact with those particles which scatter light. Due to their sizes, nitrogen and oxygen can be considered to scatter light as described through Rayleigh scattering is the previous section.
Sunlight can be modeled as a source of radiation emitted by randomly accelerating bounded charges. By using a similar method as in the previous section, but by removing the external electric field component from Eq. 1.62, we can demonstrate from this model that the sunlight is unpolarized [74]. Therefore, using the Stokes formalism,

we can consider the sunlight as a source described by the following Stokes vector:

$$\overrightarrow{S_{sun}} = S_0^{sun} \begin{pmatrix} 1 \\ 0 \\ 0 \\ 0 \end{pmatrix} \tag{1.76}$$

Where S_0^{sun} is the intensity of the sun ray.
Therefore, when a sun ray interacts with a gas particle of the atmosphere, the scattered light has, from Eq. 1.74, the following Stokes vector :

$$\overrightarrow{S_{scat}} \propto S_0^{sun} \begin{pmatrix} 1+\cos^2\theta \\ \sin^2\theta \\ 0 \\ 0 \end{pmatrix} \tag{1.77}$$

Where $\propto$ means "proportional to". By supposing only single scattering, meaning that light scattered from a particle is not scattered by another particle, the light measured from the Earth's surface is partially linearly polarized, with a degree of linear polarization (DoLP) P_l given by:

$$P_l = \frac{\sin^2(\theta)}{1+\cos^2(\theta)} \tag{1.78}$$

θ is referred to as the scattering angle, which is equivalent the angle between the direction of the Sun and the direction of the particle defined from the observer's position (cf. figure 1.10). We more often define this angle by using the letter γ.
Also, we can see from the Stokes vector of the scattered light that the light is polarized along the $\overrightarrow{u_\phi}$ direction. This means that the direction of polarization of the scattered light is orthogonal to the scattering plane (cf. figure 1.11), which is the plane containing the incident ray's wave vector (z direction in particle related Cartesian frame) and the scattered ray's wave vector (along $\overrightarrow{u_r}$ in observer's related spherical frame) (cf. figure 1.9).

We can see from Eq. 1.78, that when the scattering angle is equal to 90°, we have a circle of maximum degree of polarization, in this case, purely polarized light. The state of polarization of the scattered light from a particle as seen by an observer can be represented as a straight line named E-vector. The orientation of this line gives the direction of polarization of the scattered light, and its width gives the degree of polarization. Such representation is given in figure 1.12.

We can also represent the angle and degree of the skylight polarization by using false colors (cf. figure 1.13). The angle of polarization (AoP) being defined as the angle between the e-vector and an arbitrary fixed reference frame. As for the orientation of the ellipse of polarization (cf. Eq. 1.34), we can define the AoP ψ from the Stokes

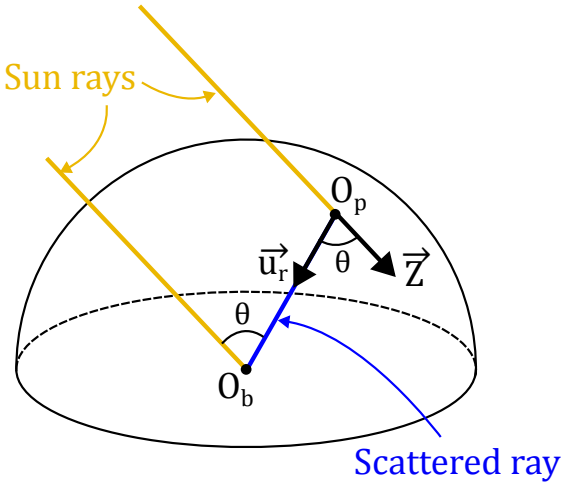

FIGURE 1.10. – Scattering angle θ. The sun rays are considered parallel. O_p is the position of the scattering particle in the atmosphere and O_b is the observer located on the surface of the Earth.

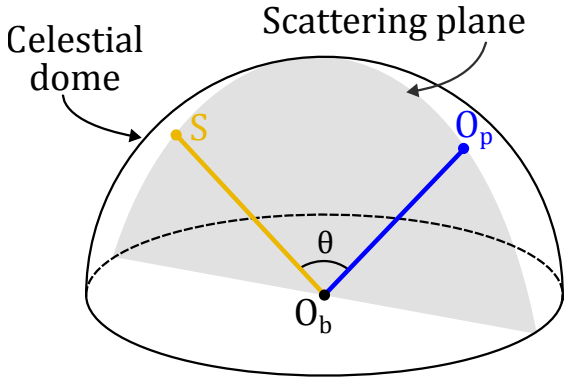

FIGURE 1.11. – Scattering plane containing the Sun S, the particle 0_p and the observer O_b. The Sun and the particle are represented as points on the celestial dome for which the distance of an observed source is not considered. θ is the scattering angle.

parameters, such as:

$$\tan 2\psi = \frac{S_2}{S_1} \tag{1.79}$$

The Rayleigh single scattering model can also be used to represent the scattering of light by a volume containing multiple particles. By considering randomly spaced particles, supposing that the scattering from a molecule is independent from neighboring particles and that there is no phase relationship between the scattered light from each particle, we can show that the scattering from a volume is equal to the sum of the scattering from each particle taken independently [73].
The presented model is referred to as the Rayleigh single scattering model [44]. As discussed in the following section, the real atmosphere can not be fully described

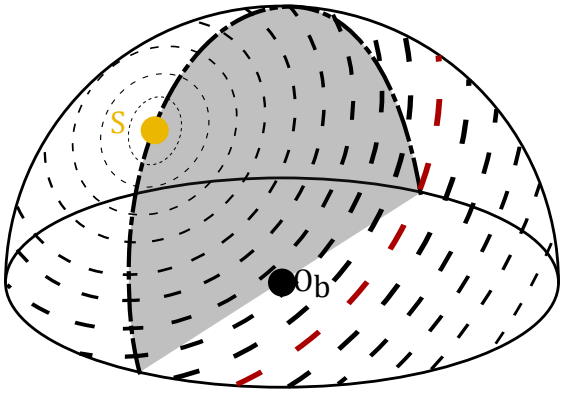

FIGURE 1.12. – Distribution of the E-vectors in the sky for a position S of the Sun and viewed by an observer O_b. Each line corresponds to the state of polarization of the scattered light from the corresponding particle, and in the direction of the observer O_b. We can notice that the direction of polarization is always orthogonal to the scattering plane (grey plane). The width of the E-vector lines increases with the DoLP, achieving maximum value at 90° from the Sun's position (red lines).

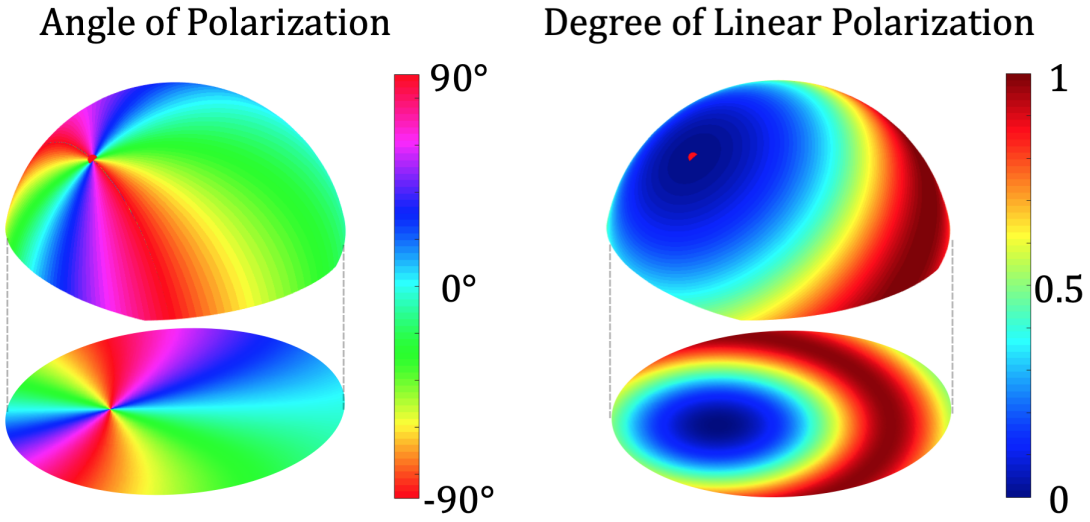

FIGURE 1.13. – False color patterns of angle and degree of the skylight's linear polarization simulated based on Rayleigh single scattering model [82]. The Sun's position is represented by a red dot. Top views are celestial dome representations of the angle and degree of linear polarization. Bottom views are projected views of the celestial dome, as seen with a fish-eye camera.

by Rayleigh scattering, leading to differences between the real skylight polarization pattern and the polarization pattern modeled through Rayleigh single scattering.

1.3.2.2. Real skylight polarization, and alternative skylight polarization models

In the previous section, we supposed that the atmosphere was mainly composed of nitrogen and oxygen gases, which scatter light as described by the Rayleigh scattering theory, and we considered only single scattering of light by particles. However, when observing the skylight polarization pattern, we do not exactly found what is predicted by the Rayleigh single scattering model [83]. For instance, in the sky, the maximum of polarization is lower than one, and its value changes depending on the date, the geographical location, and meteorological conditions (cf. figures 1.14 and 1.15). Also, when considering the Rayleigh single scattering model, two points are associated with unpolarized light, in the solar and anti solar directions. Those points are named neutral points. However, studies highlighted the presence of four neutral points in the atmosphere named Babinet, Brewster, Arago and the Fourth, the three first being named from scientist who discovered them. Those four neutral points are located above and below the solar and anti solar points, and have positions varying with the atmospheric conditions (cf. figures 1.14 and 1.16) [84]. They have been largely studied due to their link with the atmospheric turbidity.

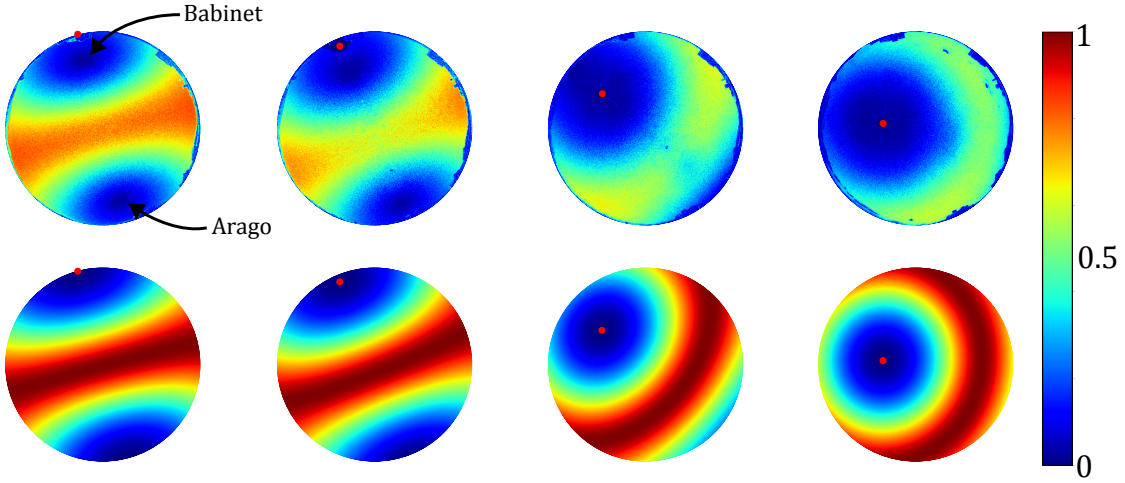

FIGURE 1.14. – Skylight DoLP variations under a clear sky. The red dots give the positions of the Sun on the images. On the first raw are displayed real skylight polarization images taken with a fish-eye polarimetric camera [85] (red channel), and on the second raw are displayed the corresponding simulated images based on Rayleigh single scattering model [82]. Images are obtained from an online database [86]. All images were taken the 11 of July 2022. Each column corresponds to a different moment, from left to right: 06:20am, 07:00am, 10:00am, 12:00am (local time). The corresponding Sun's elevations are, from left to right: 1°, 7.5°, 39.5°, 59.8°. On the first column, we clearly notice the presence of two neutral point: the Babinet and Arago points.

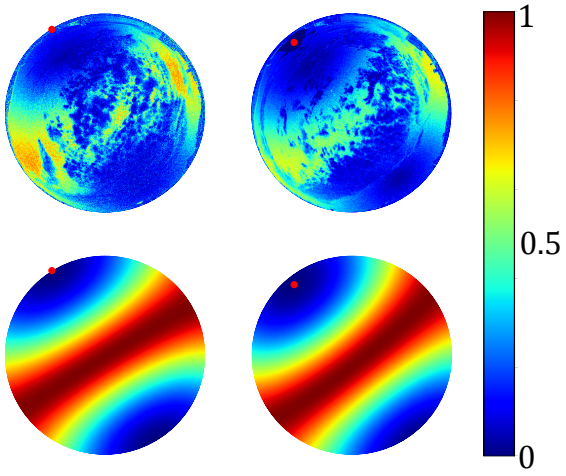

FIGURE 1.15. – Skylight DoLP under cloudy skies. The red dots give the positions of the Sun on the images. On the first raw are displayed real skylight polarization images taken with a fish-eye polarimetric camera [85] (red channel), and on the second raw are displayed the corresponding simulated images based on Rayleigh single scattering model [82]. Images are obtained from an online database [86]. Both images were taken the 26 of August 2022. Both columns correspond to a different moment, from left to right: 07:05am, 07:45am (local time). The corresponding Sun's elevations are left, 0.8°, and right, 8°.

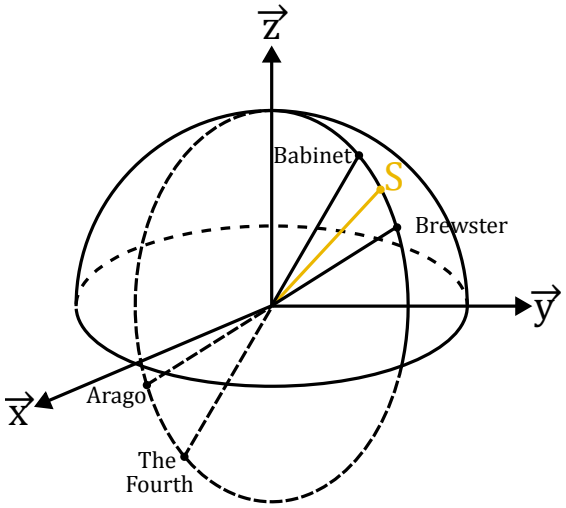

FIGURE 1.16. – The four neutral points in the celestial dome. S is the Sun.

In this section we discuss the Rayleigh single scattering assumptions based essentially on elements from the book "Polarization and Intensity of Light in the Atmosphere" by Coulson [73]. Interactions of light with particles from the atmosphere becomes very complex when considering other phenomena than Rayleigh single scattering. Therefore, this subject being out of the scope of this thesis, we will not give

theoretical explanations of the following elements.
Firstly, Rayleigh scattering supposes that particles have a radius which is much smaller than the wavelength of the incident light. It is generally assumed that Rayleigh scattering can model accurately particles having a radius lower than 0.03λ, where λ is the wavelength of the incident wave [73], which is the case for nitrogen and oxygen particles when considering ultraviolet or visible wavelengths. However, this assumption is not met anymore when considering aerosols in the atmosphere. Indeed, atmospheric aerosols such as dust, haze, pollution, pollen or spores have sizes ranging from $0.4\mu m$ to $10\mu m$. This wide range of sizes leads to varying effects of aerosols on light, adding complexity to the study of the skylight polarization in presence of aerosols. Moreover, the optical properties of aerosols vary with the air humidity, which modifies, for instance, the size and index of refraction of aerosols [87]. Also, the presence of aerosols, contrary to the atmospheric gases, varies greatly depending on the geographical location and the date. All these aspects on aerosols make the studies of their effect on skylight polarization a complex task [88]. Generally, aerosols induce multiple scattering in the atmosphere which depolarize light [89]. Multiple scattering occurs when scattered rays from a particle is scattered by another particle of the atmosphere.
Secondly, we supposed that the nitrogen and oxygen particles are isotropic. However, dinitrogen and dioxygen being diatomic particles, they are anisotropic. Anisotropy of particles induces depolarization of the scattered light, and a change in the distribution of the scattered intensity.
Thirdly, we supposed only single scattering, assuming that the distances between particles in the atmosphere are large enough so that the particles scatter light independently from each other. This hypothesis was shown, even though convenient, not to apply to the whole atmosphere. Indeed, multiple scattering depends on the optical depth of the atmosphere [87]. Depending on the position of the Sun and of the particle relative to the Sun, multiple scattering can occur in varying proportions. When the optical thickness of the atmosphere increases, light has more probabilities to be scattered multiple times than when the optical thickness is low. Also multiple scattering depends on the wavelength of light [90]. Indeed, as the scattered intensity is highly dependent on the wavelength, the scattered intensity being higher for lower wavelengths, multiple scattering affects more skylight polarization in lower wavelengths than in higher wavelengths under clear sky (cf. figure 1.17 first row). Multiple scattering generally implies a diminution of the degree of skylight polarization.

Fourthly, scattering can be altered due to reflections from the Earth's surface [91]. The Earth's surface is described by its albedo, giving the part of incident light being reflected towards the atmosphere. For instance, snow reflects more light than volcanic soils. Therefore, experiments where made to study skylight polarization in both environments, snow reflection was studied in Camp Century in North Greenland [92], and skylight polarization in low surface reflectance condition, from volcanic soils, was studied in Mauna Loa [93]. Both observations were made at high altitude, reducing the influence of aerosols on skylight polarization patterns. Those studies have shown the strong influence of surface reflectance on skylight polarization. High surface reflectance leads to multiple scattering, reducing the degree of polarization of

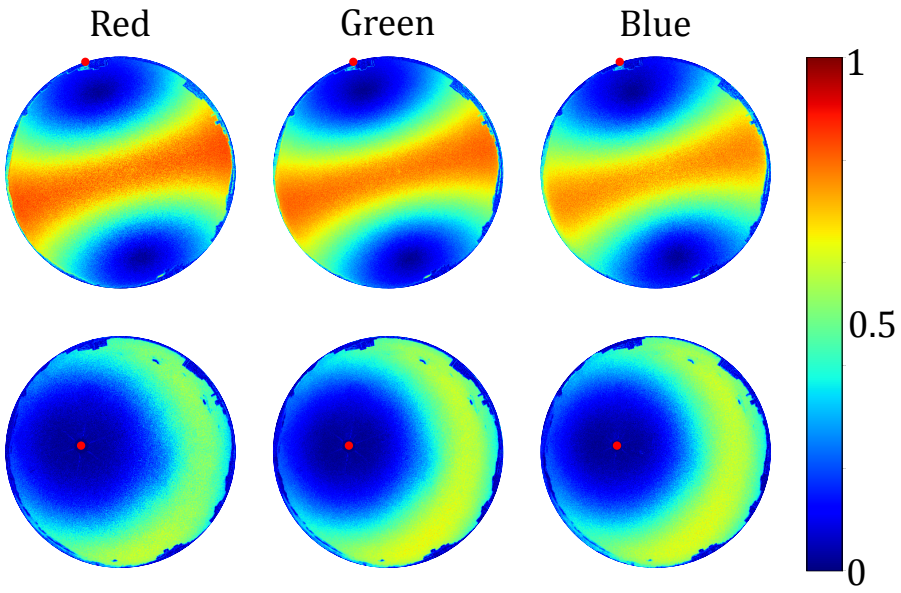

FIGURE 1.17. – Skylight DoLP under clear skies. The red dots give the positions of the Sun on the images. Images were taken with a fish-eye polarimetric camera [85]. Columns correspond to images taken with different color channel of the camera, from left to right: red, green and blue channels. Images are obtained from an online database [86]. First row images were taken the 11 of July 2022 at 06:20am, corresponding to a Sun elevation of 1°. Second row images where taken the 11 of July 2022 at 12:00pm, corresponding to a Sun elevation of 59.8°.

light. Therefore, snow reflections led to a maximum degree of skylight polarization of less than 50% [92] whereas, in presence of volcanic soils, the maximum degree of polarization went up to 85% [93]. Variations in the maximum degree of polarization during a day were also observed due to reflections varying when the Sun moves in the sky. In fact, when the Sun is higher in the sky, the surface reflection increases leading to a reduction of the maximum of polarization in the sky (cf. figure 1.14). The reflection from the Earth surface is also dependant on the wavelength. In figure 1.17, we see that when the Sun is high in the sky (second row), the maximum of DoLP increases when the wavelength decreases. This is probably due to the surface albedo increasing with the wavelength in urban areas [94].

In conclusion, the differences between the real skylight polarization and the Rayleigh single scattering model can be explained by multiple factors such as surface reflections, the presence of aerosols, liquids or other particles which do not meet the Rayleigh's assumptions, multiple scattering by atmospheric gases or anisotropy of gas particles in the atmosphere. The main factors explaining those differences being the presence of aerosols, clouds and surface reflections.

The skylight's pattern of angle of polarization was shown to be closer to that predicted by the Rayleigh single scattering model than the degree of polarization in presence of atmospheric perturbations, such as clouds [95, 96]. This explains why most studies

use the angle of polarization for skylight polarization based navigation (cf. section 3.1.2).
Other scattering models were proposed to describe more accurately the skylight polarization pattern. A skylight polarization model accounting for the existence of neutral points was proposed by Berry [84]. This model, even though relatively simple, provides more accurate simulations than the Rayleigh single scattering model, but requires knowledge about the neutral points' position. A clear explanation of this model is given in [82]. More complex models have also been proposed. Scattering by large spherical particles, as observed in clouds, fog, by water droplets or aerosols with condensed water, can be described by the more general Mie scattering theory [97, 98]. Moreover, Monte-Carlo simulation allows to take into account numerous parameters of the environment such as the surface reflectance and the optical thickness of the atmosphere by using probabilistic models, but are computationally expensive [99]. In this thesis, we only consider Rayleigh single scattering, for its simplicity.

1.3.3. Advantages of the UV light for skylight polarization based navigation

In the previous section, we discussed the Rayleigh single scattering model's assumptions in real sky conditions. We evoked the dependence of the skylight's pattern of polarization on the wavelength, and in particular, the fact that the degree of polarization is generally lower in clear sky condition for shorter wavelengths, due to multiple scattering having a stronger influence in the shorter wavelengths (cf. figure 1.17, first row).
Studies on the polarization vision of insects have demonstrated different wavelength sensitivity of insects to skylight polarization: ultraviolet (UV) for honey bees *Apis mellifera* [100] and *Cataglyphis* desert ants [101], blue for crickets *Gryllus* [102] or green for cockchafers *Melolontha* [103] (cf. [104] for review).
Interestingly, the UV sensitivity is common for insects using skylight polarization for navigation. This seems however paradoxical since the skylight's degree of polarization and intensity are usually lower in the UV than in blue or green wavelengths under clear skies [105]. This paradox is generally referred to as the "ultraviolet paradox of the perception of skylight polarization", or UV-pol-paradox [105]. In this section, we discuss this UV-pol-paradox.
As reviewed in [105], multiple assumptions were proposed to explain this paradox. A plausible explanation of this paradox was introduced in [106]. This hypothesis supposes that the UV sensitivity is advantageous in cloudy conditions, when the DoLP is lower in the sky, but presents no advantage under clear sky conditions. It is considered that skylight polarization is reliable for insect navigation when the DoLP is high enough in the sky ($> 5-10\%$ [107, 108]). Therefore, under clear skies, the DoLP is high enough in UV for navigation, even though lower than for blue and green. In [108], the proportion of the sky useful for navigation was measured in red (650nm), green (550nm) and blue (450nm) wavelengths. The measurements have shown that in cloudy skies, this proportion is higher for shorter wavelengths. In [105], a possible

explanation of this phenomenon was given. This study suggests that skylight polarization in cloudy skies is due to scattering of sun rays in the air layer between the clouds and the observer (cf. figure 1.18).

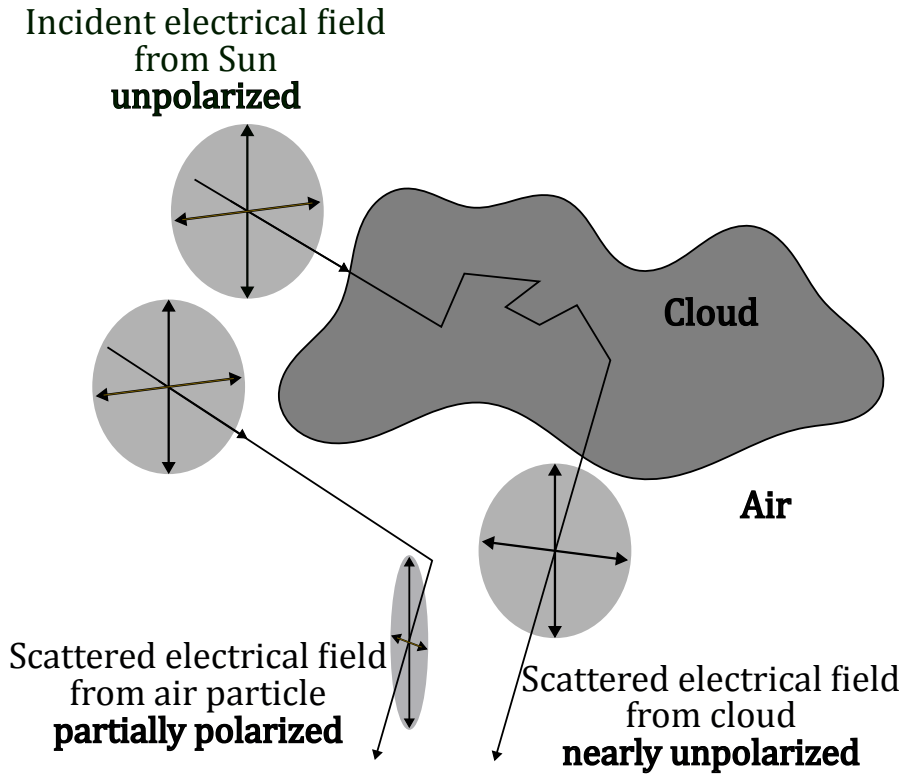

FIGURE 1.18. – Schematic representation of scattering in cloudy sky. Adapted from [105].

Indeed, clouds scatter nearly unpolarized light, due to multiple scattering in the clouds. Moreover cloud scattering can be described by Mie scattering (wavelengths with sizes comparable to the particles' sizes). Mie scattering for large particles is less dependent on the wavelength λ than Rayleigh scattering, explaining the white or grey color of clouds. Therefore, since Rayleigh scattering is stronger for shorter wavelengths, the ratio $r_I(\lambda) = I_{air}(\lambda)/I_{cloud}(\lambda)$ between the light intensity I_{air} scattered from the air layer between clouds and the observer, and the light intensity I_{cloud} scattered from clouds, is higher for shorter wavelengths. Since light scattered from clouds is considered unpolarized, the degree of polarization in the sky P_{sky} can be given as:

$$P_{sky} = \frac{I_{air}^{pol}}{I_{air} + I_{cloud}} = \frac{P_{air} \cdot I_{air}}{I_{air} + I_{cloud}} = \frac{P_{air} \cdot r_I}{1 + r_I} \tag{1.80}$$

Where I_{air}^{pol} is the polarized part of the scattered light from the air layer, and P_{air} is the degree of polarization of the scattered light from the air layer. Therefore, by assuming that P_{air} is independent from the wavelength, P_{sky} increases with r_I. Therefore, r_I increasing when the wavelength decreases, the degree of polarization in the sky is

higher for shorter wavelengths in presence of clouds (cf. figure 1.19). Measurements of the skylight polarization under cloudy skies in the UV and visible were performed in [109, 110].

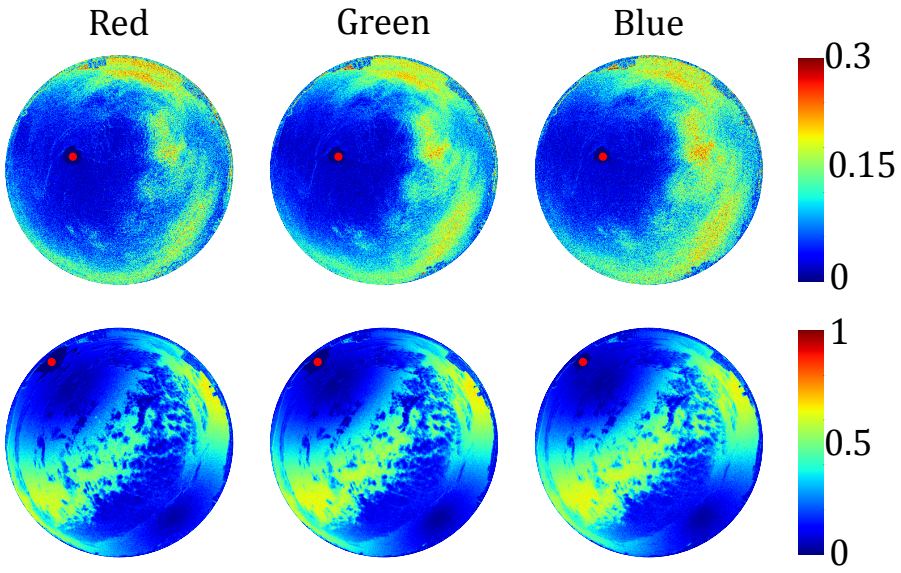

FIGURE 1.19. – Skylight DoLP under cloudy skies. The red dots give the positions of the Sun on the images. Images were taken with a fish-eye polarimetric camera [85]. Columns correspond to images taken with different color channel of the camera, from left to right: red, green and blue channels. Images are obtained from an online database [86]. First row images correspond to an overcast sky, and where taken the 23 of July 2022 at 11:22am, corresponding to a Sun elevation of 52°. Second row images corresponds to a partially cloudy sky, and where taken the 26 of August 2022 at 07:45am, corresponding to a Sun elevation of 8°.

Another interesting aspect of skylight polarization can be observed in figure 1.17 second row. We see that when the sun is high in the sky, the degree of polarization is higher under clear skies for blue wavelengths. This is probably due to reflections from the Earth being more intense for green and red wavelengths in urban environments [94]. Studies on the Earth reflectance showed that the albedo of sand or grass also increase with the wavelength [111]. Therefore, considering for instance the *Cataglyphis* desert ant, sensitive to UV polarized light, the DoLP may be higher in the UV than in other wavelengths when those ants are foraging (high Sun elevation) [112].

Very few studies on skylight polarization were performed in the UV due to the lack of polarimetric UV sensor. However, the UV-pol-paradox highlights the advantages of using UV sensors for skylight polarization navigation. There is, therefore, a need to develop such sensors for robust navigation using skylight polarization under both clear or cloudy conditions.

2. Polarimetric sensor: design and calibration

For skylight polarization navigation, different strategies can be adopted, depending on the sensor used. In this section, I review the existing polarimetric sensors. Only passive polarimetric devices will be considered, even though active polarimeters have been used to measure skylight polarization [74]. However, active polarimetric sensing is usually applied for the analysis of atmospheric composition, such as aerosols or clouds. To my knowledge, only passive polarized sensors have been used for navigation purposes.

2.1. Polarization sensors

Animals sense polarization thanks to intrinsic properties of their eyes. Some insects see polarization through the dorsal rim area (DRA) of their compound eyes, an area located in the upper part of their compound eyes, pointing toward the sky and sensitive to polarization. The DRA are made of a relatively small number of sensors (one or few hundreds per eye [15]), named ommatidium. An ommatidium contains stacked cylindrical photoreceptors, named microvilli, oriented perpendicular to the direction of propagation of the incident light and sensitive to polarization. Microvilli contain visual pigments, named rhodopsin, sensitive to photons. The sensitivity of insects to polarization is due to the presence of chromophore, a dichroic protein (absorbing light polarized along one direction preferentially), in the visual pigments, located in and along the cylindrical microvilli [15, 113]. The structure of the compound eye is represented in figure 2.1.

Contrary to insects' microvilli, most of the existing photodetectors are insensitive to polarization. However, by using polarizing filters, we can analyse the state of polarization of light as shown in section 1.2.3. Moreover, skylight polarization being mainly linearly polarized due to Rayleigh scattering (cf. section 1.3.2.1), we do not need to measure the circular part of polarization. Referring to Stokes parameters, we are interested in measuring only the three first Stokes parameters S_0, S_1, and S_2 of the input light. Using three orientations of a perfect polarizer, for instance 0°, 45° and 90°, we can then obtain those three Stokes parameters (cf. section 1.2.3, Eq 1.33). More generally, from n measurements ($n \geq 3$) with various orientations of a perfect polarizer ξ_i ($1 \leq i \leq n$), we can deduce the Stokes parameters by solving a set of n equations.

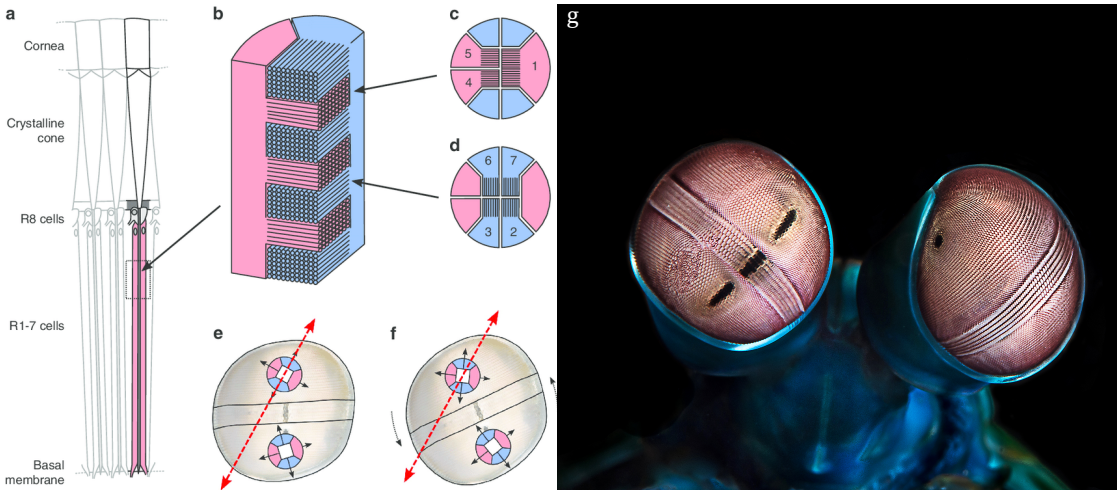

FIGURE 2.1. – Anatomy of a mantis shrimp polarization sensitive compound eye. (a) Longitudinal section through three neighbouring ommatidia. The pink region is called rhabdom. (b) Representation of a rhabdom containing stacked orthogonal cylindrical microvilli. (c-d) Orientation of microvilli in alternate layers of the main rhabdom. (e-f) orientations of rabdoms in each hemisphere of the compound eye, and after a rotation with respect to a fixed direction (red arrow). Credit: Martin How. Background image in e and f adapted from a photo by R Caldwell, CC BY-SA 4.0, via Wikimedia Commons. (g) Close-up on the eyes of a Odontodactylus scyllarus known as mantis shrimp, and sensitive to polarized light (original image cropped). Credit: Cédric Peneau CC BY-SA 4.0, via Wikimedia Commons.

From section 1.2.3, Eq. 1.29, we get:

$$\begin{cases} I(\xi_1) = \frac{1}{2}\left(S_0 + S_1\cos(2\xi_1) + S_2\sin(2\xi_1)\right) \\ I(\xi_2) = \frac{1}{2}\left(S_0 + S_1\cos(2\xi_2) + S_2\sin(2\xi_2)\right) \\ \vdots \\ I(\xi_n) = \frac{1}{2}\left(S_0 + S_1\cos(2\xi_n) + S_2\sin(2\xi_n)\right) \end{cases} \tag{2.1}$$

Where $I(\xi_1), ..., I(\xi_n)$ are the n measured intensities. We can rewrite this set of equations in a matrix form, such as:

$$\overrightarrow{I_{meas}} = \mathbf{D}\overrightarrow{S_{in}} \tag{2.2}$$

Where,

$$\mathbf{D} = \frac{1}{2}\begin{bmatrix} 1 & \cos(2\xi_1) & \sin(2\xi_1) \\ 1 & \cos(2\xi_1) & \sin(2\xi_1) \\ \vdots & \vdots & \vdots \\ 1 & \cos(2\xi_n) & \sin(2\xi_n) \end{bmatrix}, \overrightarrow{I_{meas}} = \begin{bmatrix} I(\xi_1) \\ I(\xi_2) \\ \vdots \\ I(\xi_n) \end{bmatrix}, \overrightarrow{S_{in}} = \begin{bmatrix} S_0 \\ S_1 \\ S_2 \end{bmatrix} \tag{2.3}$$

This equation can be solved by calculating the pseudo-inverse of the polarimetric measurement matrix $\mathbf{D}$, such as:

$$\overrightarrow{S_{in}} = \left(\mathbf{D}^T\mathbf{D}\right)^{-1}\mathbf{D}^T\overrightarrow{I_{meas}} \tag{2.4}$$

Where $\mathbf{D}^T$ designates the transpose matrix of $\mathbf{D}$, and $\left(\mathbf{D}^T\mathbf{D}\right)^{-1}$ is the inverse matrix of $\left(\mathbf{D}^T\mathbf{D}\right)$. This problem can be solved numerically by using the least squares method. We can then deduce the angle ψ and degree P_l of linear polarization from the three Stokes parameters, such as:

$$\begin{aligned} \tan 2\psi &= \frac{S2}{S1} \\ P_l &= \frac{\sqrt{S_1^2 + S_2^2}}{S_0} \end{aligned} \tag{2.5}$$

In the case of an imperfect polarizer having the following Mueller matrix (cf. section 1.2.4, Eq. 1.57):

$$\mathbf{M} = \frac{p^2}{2}\begin{pmatrix} 1 & \cos 2\iota\cos 2\theta & \cos 2\iota\sin 2\theta & 0 \\ \cos 2\iota\cos 2\theta & \cos^2 2\theta + \sin 2\iota\sin^2 2\theta & (1-\sin 2\iota)\sin 2\theta\cos 2\theta & 0 \\ \cos 2\iota\sin 2\theta & (1-\sin 2\iota)\sin 2\theta\cos 2\theta & \sin^2 2\theta + \sin 2\iota\cos^2 2\theta & 0 \\ 0 & 0 & 0 & \sin 2\iota \end{pmatrix} \tag{2.6}$$

The measured intensity is given by:

$$I(\xi) = \frac{p^2}{2}\left(S_0 + S_1\cos(2\iota)\cos(2\xi) + S_2\cos(2\iota)\sin(2\xi)\right) \tag{2.7}$$

In general, when analysing polarized light, the parameters of the polarization optics must be known. Those parameters can be obtained from the characterization of the polarizer.

To obtain measurements of the state of polarization of the incident light, several methods have been developed. Here, we present the state of the art polarimeters used to analyse the state of polarization of a partially and linearly polarized light beam, through time, space, or by splitting of the incident beam of light.

2.1.1. Division of time polarimeter

Division of time polarimeters consist in analyzing a light beam over time. By supposing that the state of polarization of the light beam is unchanged over the analysis time, we can proceed by rotating a linear diattenuator prior to a photodetector. When rotating the polarizer, the output light's intensity will vary according to the polarizer's orientation with respect to the incident light's direction of polarization (cf. section 1.2.3). By analyzing the light from at least three orientations of a polarizer, we can deduce the state of polarization of the input partially and linearly polarized light, as shown in Eq. 2.4 (cf. figure 2.2a). This method is simple to set up and can be very

cheap, depending on the rotation device used [26]. The two main drawbacks of this method are the measurement time, and the precision limit due to the rotation of the polarizer. The rotation of the polarizer can be achieved mechanically by using a rotation mount for instance. Another alternative is to place a wave plate or a rotator prior to the polarizer (cf. figure 2.2b). For instance, by using a half wave plate, creating a phase shift of 180°, and rotated by an angle θ, prior to an ideal linear polarizer, the output Stokes vector S_{out} will be given by (cf. section 1.2.4):

$$S_{out} = M_{LP} M_{HWP} S_{in} = \frac{1}{2} \begin{pmatrix} 1 & 1 & 0 & 0 \\ 1 & 1 & 0 & 0 \\ 0 & 0 & 0 & 0 \\ 0 & 0 & 0 & 0 \end{pmatrix} \begin{pmatrix} 1 & 0 & 0 & 0 \\ 0 & \cos 4\theta & \sin 4\theta & 0 \\ 0 & -\sin 4\theta & \cos 4\theta & 0 \\ 0 & 0 & 0 & 1 \end{pmatrix} \begin{pmatrix} S_0 \\ S_1 \\ S_2 \\ S_3 \end{pmatrix} \tag{2.8}$$

Where S_{in} is the incident light's Stokes vector, M_{LP} and M_{HWP} are the Mueller matrices of the linear polarizer and half wave plate respectively. The measured intensity I_{meas} will therefore be given by (first Stokes parameter of the output light S_0^{out}):

$$I_{meas} = S_0^{out} = \frac{1}{2} \left(S_0 + S_1 \cos 4\theta + S_2 \sin 4\theta \right) \tag{2.9}$$

This is equivalent to rotating a polarizer by an angle 2θ. The same result can be obtained by using a rotator, allowing for twice as more precision than when using a half wave plate (cf. section 1.2.4 and [74]).
Using a waveplate or a rotator instead of rotating a polarizer can be convenient since the mecanical rotation can be avoided by using a liquid crystal variable retarder (LCVR). LCVR are made of molecules that can be aligned when subject to an electric field, or to variations of the temperature. The retardance, fast and slow axes of the LCVR can be tuned depending on the electric field, allowing for high speed analysis of the state of polarization. Avoiding mechanical rotation also prevents moving parts from disturbing the alignment of the system [74]. However, using LCVR or regular waveplates can also cause measurement uncertainties. In fact, waveplates have a retardance depending on the wavelength of the incident light [114]. This issue can be dealt with by using achromatic waveplates. Moreover, LCVR are sensitive to external temperatures, and are not spatially homogeneous [115]. Other methods using rotating components are given in [74].

2.1.2. Instantaneous measurements

In the previous section, we presented time based measurements of the state of polarization assuming that the state of polarization was constant during the measurement time. However, this assumption may not always be met, for instance, when observing the skylight polarization using mobile robots such as drones. In this section, we present alternative methods based on instantaneous measurements of the input polarized beam of light.

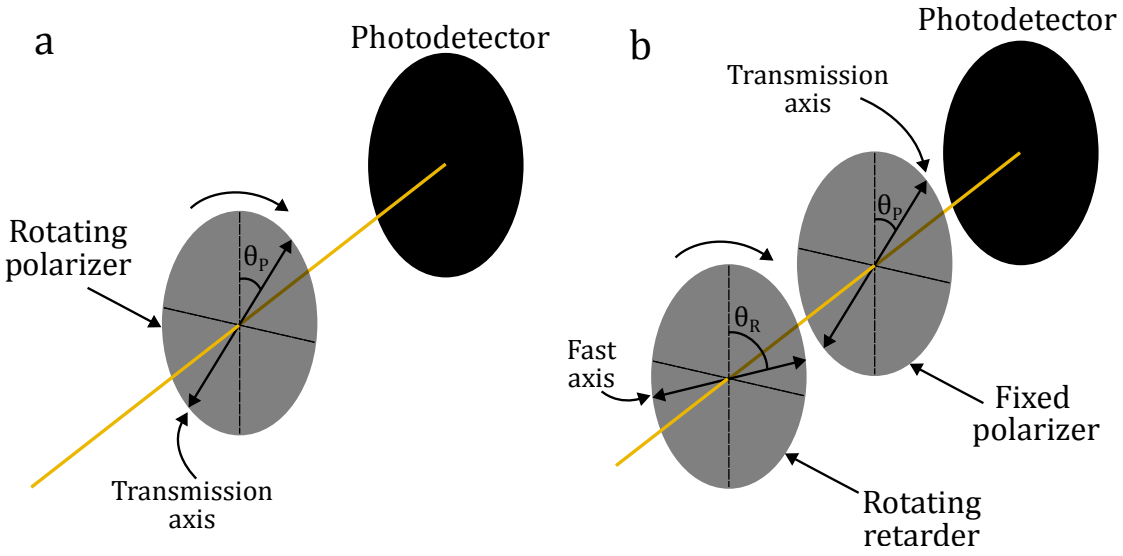

FIGURE 2.2. – Division of time polarimeter (a) by rotating a linear polarizer or (b) by rotating a retarder placed prior to a fixed polarizer.

2.1.2.1. Divison of amplitude polarimeter

Division of amplitude polarimeters analyse the state of polarization by dividing the amplitude of a light beam and analyzing each beam separately, for instance, by using polarizing beam splitters. A polarizing beam splitter usually splits a light beam in two orthogonally polarized beams with respective intensities depending on the state of polarization of the incident light beam. The reflected beam is polarized perpendicularly to the incidence plane (s-polarization, from the German word "senkrecht" meaning perpendicular), and the transmitted beam is polarized parallel to the incidence plane (p-polarization, from the German word "parallel") (cf. figure 2.3). The measurements of the split beams permit to compute the Stokes parameters (cf. Eq. 2.4). Such methods are generally expensive and bulky since they require multiple sensors and often multiple polarization optics. They allow, however, to sense polarization of a light beam without any assumption on time and space consistency of the input signal. A review of division of amplitude polarimeters is given in [74].

2.1.2.2. Division of wavefront polarimeter

Division of wavefront polarimeters consist in measuring independently the state of polarization of a light beam at different positions in a plane orthogonal to the direction of propagation of the beam. It supposes that the light beam has an homogeneous state of polarization on the space covered by all the measurement units. When measuring linear polarization, this type of polarimeter generally consists in four polarizers placed in front of four photodetectors, with orientations of 0°, 45°, 90° and 135° (cf. figure 2.4).

Therefore, to measure the state of polarization, we can obtain the Stokes parameters

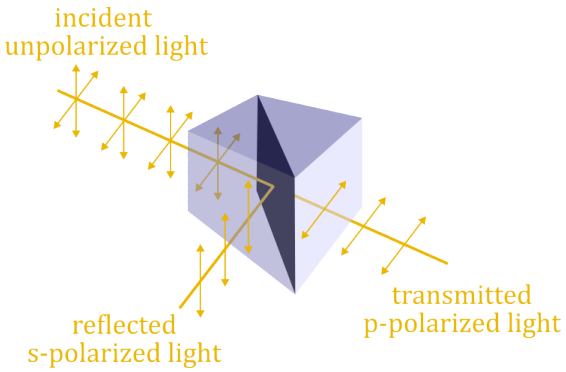

FIGURE 2.3. – Effect of a polarizing beam splitter on an incident unpolarized light.

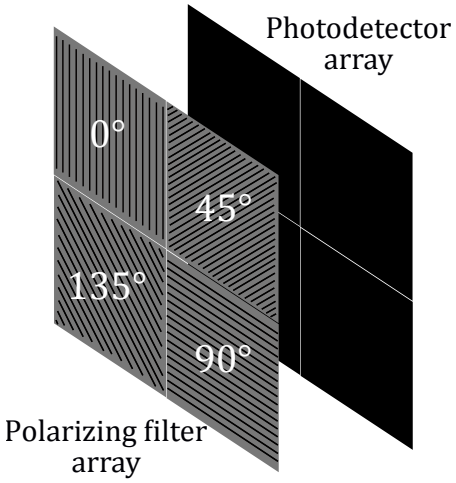

FIGURE 2.4. – Division of wavefront polarimeter consisting in four polarizers placed in front of four photodetectors, with orientations of 0°, 45°, 90° and 135°. The direction of the polarizers is given by the direction of the black stripes.

from the following (cf. section 1.2.3, Eq. 1.29):

$$\begin{aligned} I(0^\circ,0^\circ) &= \frac{1}{2}\left[S_0 + S_1\right], \\ I(45^\circ,0^\circ) &= \frac{1}{2}\left[S_0 + S_2\right], \\ I(90^\circ,0^\circ) &= \frac{1}{2}\left[S_0 - S_1\right] \\ I(135^\circ,0^\circ) &= \frac{1}{2}\left[S_0 - S_2\right] \end{aligned} \tag{2.10}$$

We finally obtain the Stokes parameters from the measured intensities, such as:

$$\begin{aligned} S_0 &= I\left(0°,0°\right) + I\left(90°,0°\right), \\ S_1 &= I\left(0°,0°\right) - I\left(90°,0°\right), \\ S_2 &= I\left(45°,0°\right) - I\left(135°,0°\right) \end{aligned} \tag{2.11}$$

This type of polarimeter is practical because of its simplicity, and its absence of moving parts. Moreover, the wavefront homogeneity constraint is troublesome mostly for scenes with high spatial variations, which is not the case for skylight polarization.

2.2. Skylight polarization sensors

In the previous sections, we presented different ways of measuring the state of polarization of a linearly polarized light beam. However, when sensing skylight polarization we may want to measure spatial polarization variations. In the animal kingdom, the two most common eye structures are compound eyes and camera eyes [113]. Compound eyes are made of a few thousands of independent sensors, named ommatidium, measuring light with a large angular field of view (cf. figure 2.1). Those sensors thus usually provide a low spatial resolution, but can allow for vision over a large field of view, covering almost 360° around the animal. On the other side, most vertebrates, such as birds or humans, sense light through camera eyes. Camera eyes are made of a lens projecting an image onto the retina of the eye, containing millions of photoreceptors (cf. figure 2.5). Those eyes allow for much higher spatial resolution than compound eyes. Homing pigeons, for instance, sense skylight polarization through their camera eyes. However, the mechanisms involving sensitivity of camera eyes to polarization remain poorly understood [15]. In this section, as for animals, we distinguish two types of sensors, namely non-imaging and imaging sensors, referring to compound and camera eyes, respectively.

2.2.1. Non-imaging sensors

Non-imaging sensors are generally made of one or more independant measurement units, each unit detecting the polarization of the sky in one direction. In the DRA of *Cataglyphis* desert ants, the ommatidia are composed of microvilli oriented in two orthogonal directions, comparable to two orthogonal polarizer's directions. As shown in [116], the difference of both signals, outputting from the orthogonal microvilli, is computed in the insect's brain. Since the two output signals have a logarithmic relation with the light intensity along the direction of the microvilli, this difference is equivalent to a logarithmic ratio between the intensity measured through a polarizer and the intensity measured through the orthogonal polarizer (cf. figure 2.6).

Using this method, the angle of polarization can easily be measured. In [117, 118, 119, 120], three pairs of orthogonal polarizers were used to sense skylight polarization in one direction. For each pair of polarizers, the logarithmic ratio of the measured

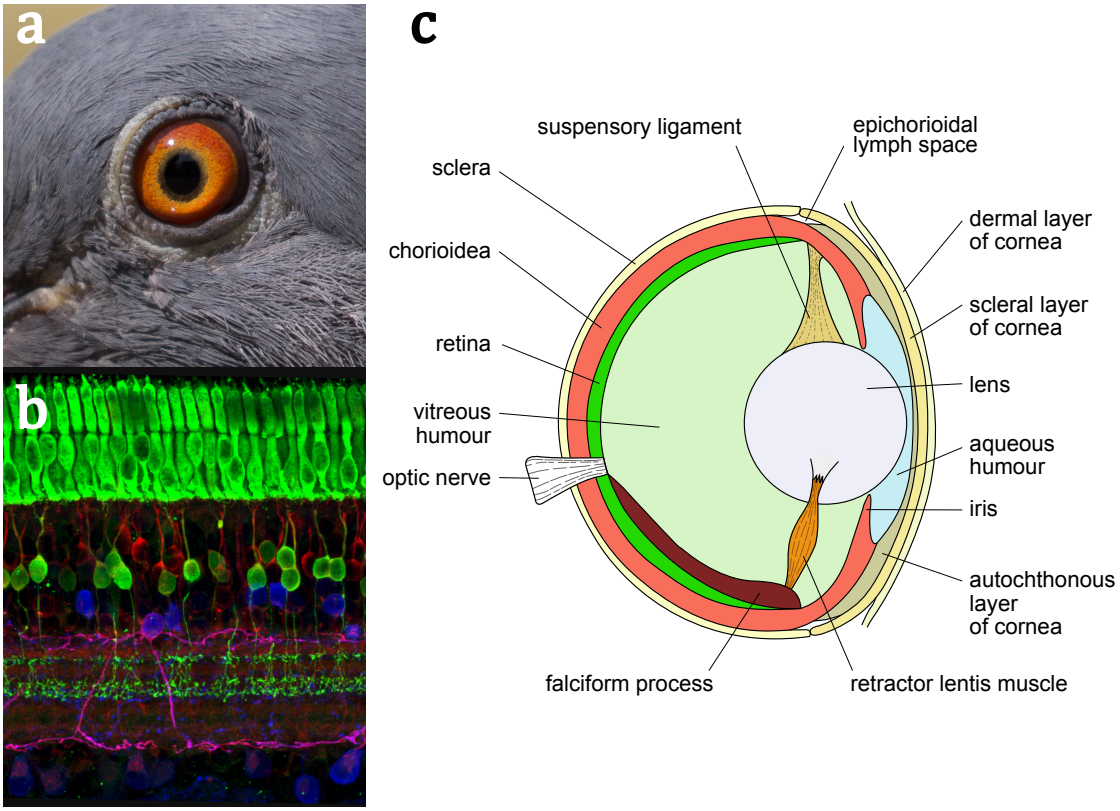

FIGURE 2.5. – Structure of the camera eye. (a) Camera eye of a rock dove (Columba livia). Credit: Carlos Delgado, CC BY-SA 4.0, via Wikimedia Commons. (b) Layers of nerve cells in the retina. The top layer (green) is made of photoreceptors of the retina. Credit: Wei Li, National Eye Institute, National Institutes of Health. (c) Diagrammatic vertical section of the eye of a bony fish. Credit: Gretarsson, CC BY-SA 4.0, via Wikimedia Commons.

intensity was calculated. Similarly, three polarizing beam splitters were used in [121] to sense skylight polarization in one direction. In [122], five pairs of the measurement units described in [118] were used to sense skylight polarization in 5 directions, and in [123] and [124], the polarization is measured simarly in 2 and 9 directions respectively. The robot AntBot, mimicking the navigation strategy of the *Cataglyphis* desert ant, used only two orthogonal rotating polarizers to analyze the skylight polarization in one direction, each polarizer being positioned above a UV photodetector [26]. In [125], a waveplate was rotated in front of a linear polarizer to analyse the skylight polarization in one direction. Then, the whole skylight was scanned by varying the orientation of the polarimeter. A schematic representation of non-imaging sensors is given in figure 2.7.

Unlike the polarimeters presented above, all units of skylight polarization sensors do not need to measure necessarily the three Stokes parameters allowing to describe linearly polarized light. Instead, two orientations of polarizers can be sufficient for

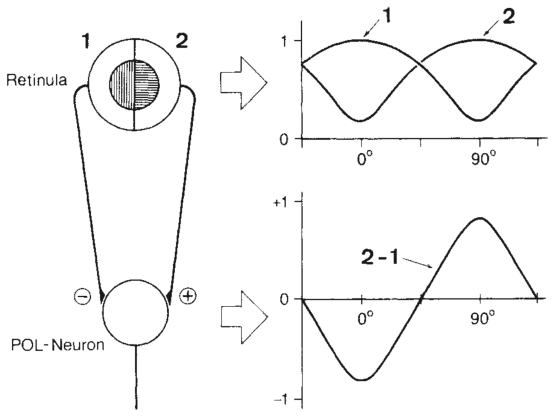

FIGURE 2.6. – Left is a schematic representation of polarization sensitive orthogonal photo-receptors in the crickets' DRA, and their link to a POL-neuron. 1 and 2 refer to the two orthogonal photo-receptors. Right upper graph is a representation of the output signals from the two photo-receptors as a function of the incident light's angle of polarization. Lower graph is the output signal from the POL-neuron, equal to the difference between the two input signals coming from the photo-receptors. Reproduced with permission from Springer Nature [116].

each measurement unit when sensing skylight polarization, because of the information redundancy in the pattern of polarization. Therefore, an ant-inspired sensor, consisting in 8 division of wavefront polarization measurement units, with only two orthogonal polarizer orientations for each unit, was implemented in [126].
Using non-imaging sensors is advantageous since those types of sensors are generally cheap, do not require a lot of memory footprint and are well suited for real-time applications because of the low amount of data to process. Moreover, contrary to imaging sensors, those systems do not suffer from glare due, for instance, to a direct view of the Sun, since the signal from photo-detectors are independent. However, such sensors are more sensitive to noise in the sky, such as clouds, than imaging sensors, even though they have been shown to enable robust Sun position estimation in presence of clouds [126].

2.2.2. Imaging sensors

Imaging sensors usually consist in one or multiple lens, a photo-detector array composed of pixels, and some polarization optics located either between the lens and the pixels, or prior to the lens.
The lens used for imaging sensors can be described by their focal length and mapping function. From those, a point in the sky can be associated to a point on the image plane. We can consider 5 standard mapping functions giving the distance r between the optical axis and the image point as a function of the focal length f and the angle θ

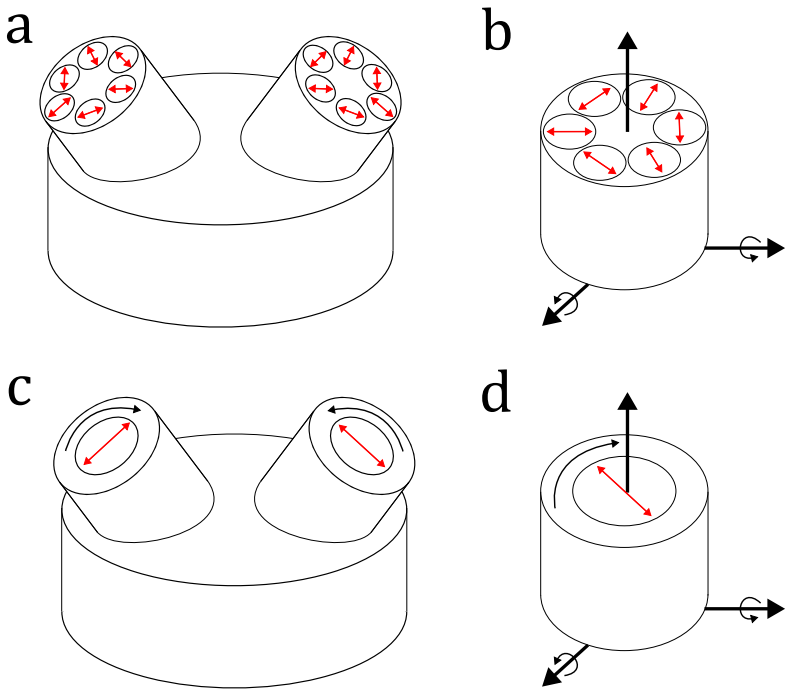

FIGURE 2.7. – Schematic representation of four types of non-imaging sensors. (a) Instantaneous polarization measurement in two fixed directions. (b) Division of time polarization measurement in two fixed directions. (c) Space scanning polarimeter with a single instantaneous polarization measurement unit. (d) Space scanning polarimeter with a single division of time polarization measurement unit. Red arrows give the orientation of the polarizer. Black curved arrows give the moving parts of the sensors.

of the input ray with respect to the optical axis of the lens (cf. figure 2.8), such as [127]:

$$\begin{aligned} r &= f\tan(\theta) \\ r &= 2f\tan(\theta/2) \\ r &= f\theta \\ r &= 2f\sin(\theta/2) \\ r &= f\sin(\theta) \end{aligned} \tag{2.12}$$

Those mapping functions correspond to a thin lens, and four fish-eye lens with stereographic, equidistant, equisolid angle and orthogonal projections respectively.

The polarization measurement can be, as described in the previous sections, of several types.
A division of time camera composed of two LCVR followed by a polarizer was implemented in [128] to analyse the four Stokes parameters of skylight polarization. In [129], a linear polarizer was rotated to measure the skylight's linear polarization, and in [130] and [131] a wheel containing multiple color and polarization filters with various orientations was used to measure optical properties of aerosols onboard satellites. An

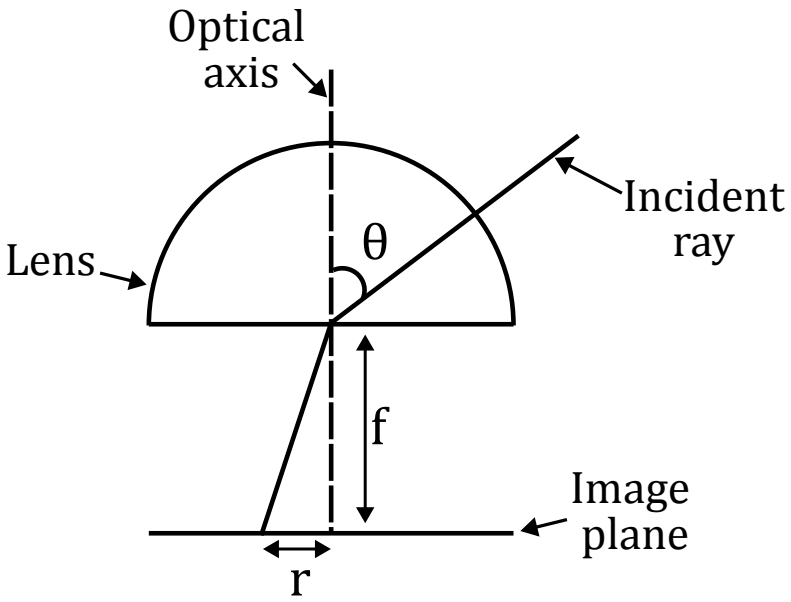

FIGURE 2.8. – Schematic representation of the projection of light ray by a lens, onto the image plane. f is the focal length, r the distance to the image center of a light ray with an incidence angle θ with respect to the optical axis of the lens.

imaging camera with a fixed polarizer pointing downwards to a sphere reflecting the skylight, and replacing a fish-eye lens was developed in [132] for UV sensing of the skylight polarization pattern. Instead of turning the polarizing filter, the whole device was rotated around its vertical axis.

A division of amplitude (DoAmp) camera composed of a beam splitter separating the input beam into three beams, and analyzed through fixed polarizers oriented at three different angles prior to three sensor arrays was presented in [133]. In [134], an hyperspectral DoAmp camera inspired from mantis shrimps was implemented, using stacked polarization-sensitive organic photovoltaics and polymer retarders.

Specific to imaging sensors, a division of aperture camera was introduced in [135]. Using a set of lens, four identical images were projected on the image plane. Each projected image came out of a polarizer oriented at 0°, 45°, 90° and 135°, allowing to compute the first three Stokes parameters.

Similarly, replication of aperture polarimetric devices consist in measuring polarization through multiple cameras with distinct polarizing filter orientations for each camera. A device consisting of 3 cameras with fixed polarizers oriented at 0°, 45° and 90° was implemented in [136]. Four cameras with fixed polarizers were used in [137].

Division of focal plane (DoFP) cameras consist in measuring polarization in each point of space through groups of neighboring pixels measuring light with varied polarizer orientations. Neighboring pixels analyzing the polarization in one direction form a division of wavefront polarimeter, generally referred to as a super pixel. A DoFP sensor, with polarizing filters oriented at 0°, 45°, 90° and 135°, was used in [138] for

astronomical measurements. A color DoFP sensor, inspired from the mantis shrimp's visual system, was developed in [139]. In [140], the image of a circular filter composed of three polarizers oriented at 0°, 60°, and 120° and placed side by side, was projected in different regions of the image plane, by using a microlens array. Similarly, multiple images of an S-waveplate followed by a polarizer was projected in the image plane in [141]. An S-waveplate, also called radial polarization converter, is a waveplate with spatially varying retardance. It transforms a spatially uniform linarly polarized light beam into a radially polarized light beam, meaning that at any point of the beam, the polarization vector points towards the center of the beam. In 2018, Sony developed the first commercial DoFP imaging polarimetric sensor, consisting in groups of 4 neighbouring pixels with polarizers oriented at 0°, 45°, 90° and 135°. Sony sensors are now widely used for polarization sensing applications, such as underwater geolocation [142], or polarization compass [143, 144, 145].
A schematic representation of imaging sensors is given in figure 2.9.

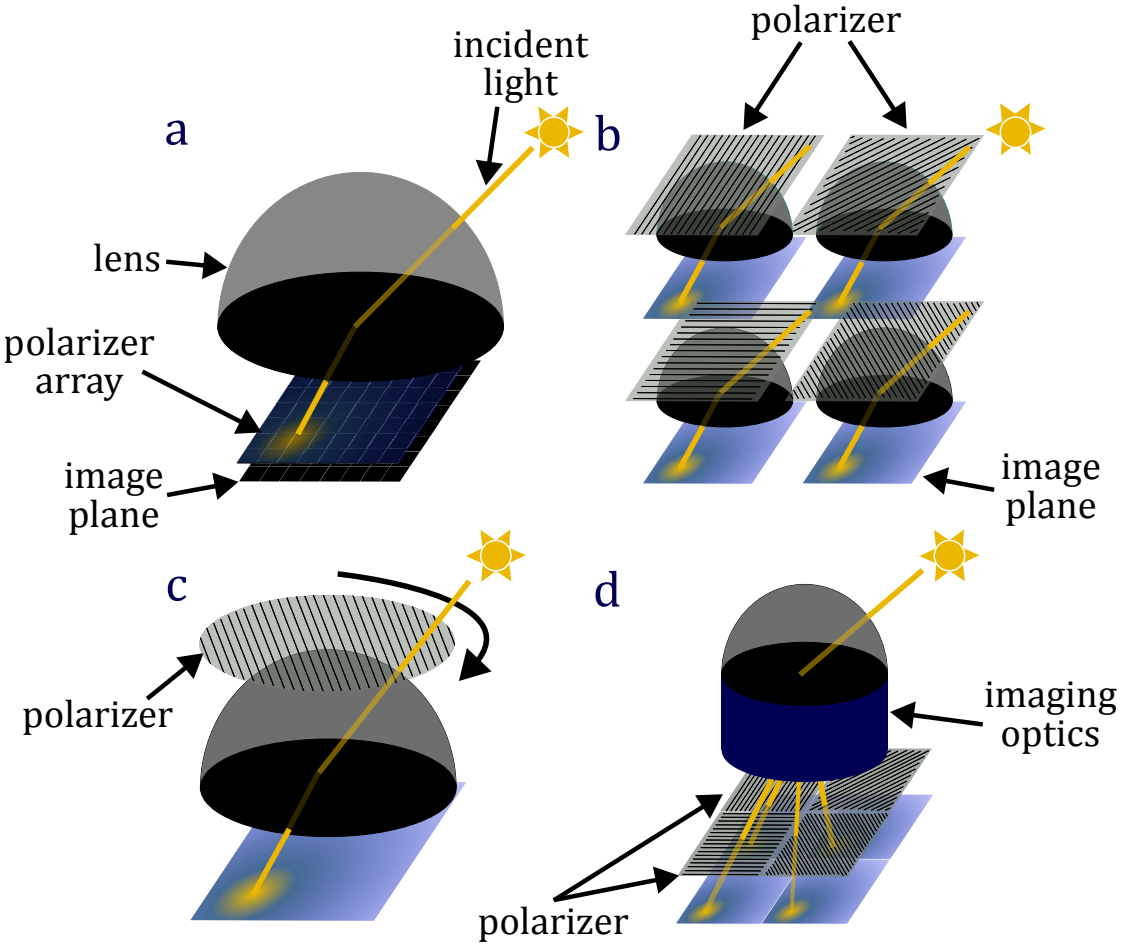

FIGURE 2.9. – Schematic representation of four types of imaging sensors. (a) Division of focal plane sensor. (b) Replication of aperture sensor. (c) Division of time sensor (curved arrow indicates the rotating polarizer). (d) Division of aperture sensor.

An alternative sensor, based on a fixed waveplate and a polarizer, taking advantage of the spatial properties of skylight polarization was presented in [146]. By noticing the waveplate's retardance variations according to the direction of the incident light, a pattern of iridescent colors could be observed, providing information on the skylight polarization pattern. In [147], a S-waveplate followed by a linear polarizer, both fixed, were placed prior to a camera, allowing to extract solar information without having to compute the angle or degree of polarization.
Imaging sensors are practical since they often rely on existing cameras and provide high spatial resolution compared to non imaging sensors. Division of time sensors are the most simple imaging sensors to implement, and allow for processing full resolution images. They, however, are not practical for all applications, as discussed earlier. Division of amplitude sensors require no assumption on the incident light field, but are generally bulky and expensive for robotic purposes. Replication of aperture and division of focal plane sensors require low spatial variations of the polarization. Replication of aperture are easy to implement but are expensive and bulky. Division of aperture and division of focal plane sensors induce a loss of spatial resolution. Interestingly, DoAmp sensors do not require a spatial uniformity assumption compared to DoFP. However, no DoAmp sensor is commercially available contrary to DoFP sensors. Compared to non-imaging sensors, camera sensors suffer from issues related to the structure of the sensor. When light rays go through a lens, the state of polarization is modified. The alteration of the polarization is low for rays propagating along the optical axis of the sensor. However, for high angles of incidence of a light beam, as obtained by using a fish-eye lens for instance, the state of polarization can be transformed dramatically. This phenomenon can be visualized by placing a lens between two crossed polarizers, leading to a pattern known as Maltese cross [77] (cf. figure 2.10). Moreover, the properties of polarizers vary depending on the angle of incidence of the incoming light [148]. Therefore, the measured state of polarization may not be correct, considering for instance peripheral pixels of a DoFP sensors using a fish-eye lens. Camera lens may also, in presence of an intense light source such a the Sun, generate parasite light known as flare or glare [149]. Those issues were dealt with in some experiments by hiding the Sun's direct rays [150], and glare effects can be reduced by shortening the sensor's integration time.

In this section, we reviewed the sensors developed for skylight polarization measurements. Several other reviews on polarization remote sensing were previously published [74, 24, 151]. For the sake of simplicity, we used a Sony DoFP sensor [85] to test the geolocation algorithms presented in section 3.3. This sensor being widely used, and easily available, its use allows for repeatability of the developed studies.

2.3. Calibration

In the previous section, we presented different types of sensors and how to measure the state of polarization from those devices. However, sensors may induce measurement errors due to their fabrication or to the electronics. To ensure accurate measure-

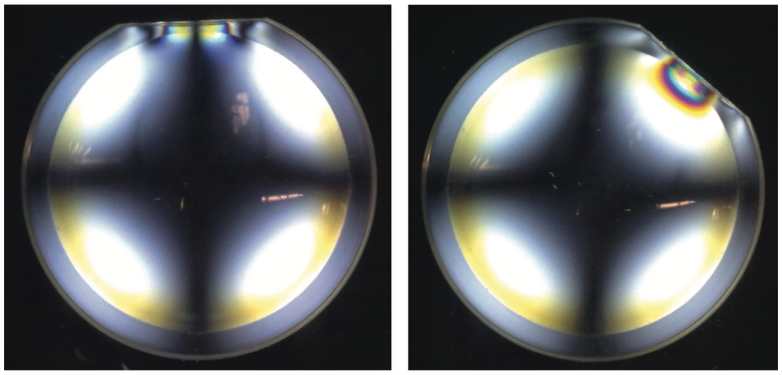

FIGURE 2.10. – An injection-molded lens with stress birefringence (left) between crossed polarizers (at the top) and (right) after rotating the lens by 45°. Reproduced with permission from CRC press [77].

ments, a calibratation should be processed. We present here three types of calibration, namely geometric calibration, radiometric calibration and polarimetric calibration. In this section, we will focus on the calibration of imaging sensors, the principles being similar for non-imaging sensors, except for lens related aspects.

2.3.1. Geometric calibration

Geometric calibration aims at mapping pixels' positions to directions of observation. When measuring skylight polarization, we must determine the direction of each measurement point in the sky with respect to each pixel of a measurement device. To achieve this, intrinsic and extrinsic geometric calibrations are processed. Intrinsic geometric calibration consists in determining the mapping function between the pixels of the sensor and the directions of observation in the camera frame. Extrinsic geometric calibration consists in establishing the orientation of the sensor with respect to a reference frame.

If the lens model is known, then, the intrinsic calibration of an imaging sensor can consist in determining two parameters describing the imager, namely the focal length of the lens and the optical center, also known as the principal point, which corresponds to the pixel located under the optical axis of the lens. Knowing the optical center of the image plane and the lens' focal length, the mapping function giving the direction of measurement for each pixel in the camera frame can be deduced from the lens model (cf. 2.2.2).
To obtain the intrinsic parameters of an imaging sensor, some points with a known position with respect to the camera can be used as a reference. From the image of those points by the camera, the sensor's parameters can be tuned to match the groundtruth position of the reference points to estimated position of those points based on the sensor's mapping function.
A standard way of obtaining those parameters is by acquiring multiple images with

varying orientations of a checkerboard having known properties [152]. A checkerboard is convenient since reference points can easily be detected between black and white squares. Also, the orientation of the checkerboard does not need to be given prior to the calibration. Indeed, because of geometric constraints of the checkerboard, and by detecting reference points on the checkerboard, the orientation of the checkerboard with respect to the sensor can be deduced during the calibration process. We do not further detail this method. In this thesis, to achieve the geometric calibration of intrinsic camera parameters, we used the checkerboard method and Matlab calibration toolbox (cf. figure 2.11).

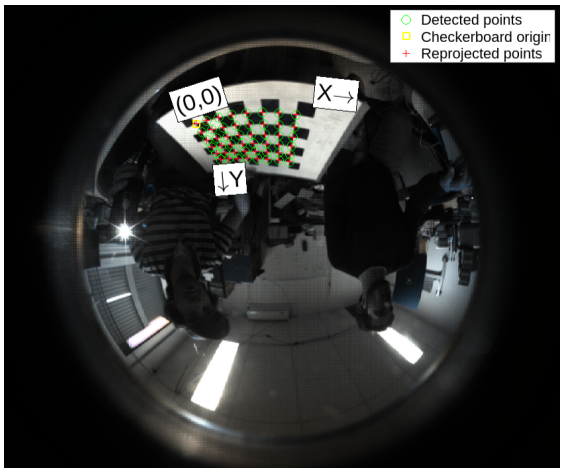

FIGURE 2.11. – Geometric calibration of a fish-eye camera with a checkerboard. Reference points on the checkerboard are detected through Matlab calibration toolbox [153].

To determine the orientation of a sensor with respect to an external frame, independent from the sensor, some reference points with known positions in the external frame should be measured by the sensor. By the measurements and the previous calibration of intrinsic geometrical parameters of the sensor, the position of the reference points with respect to the camera can be estimated. Then, the rotation between the camera frame and the external frame can be deduced to achieve the extrinsic geometric calibration.
A method to calibrate the orientation of a camera in the East, North, Up frame, based on the Sun's position, will be discussed in the following chapter (cf. section 3.3.1 and [85]).

2.3.2. Radiometric calibration

Radiometric calibration aims at determining the link between a sensor's output, given in digital number, and the incident light's irradiance. When considering polarimetric sensors, if only the AoP and DoLP need to be measured, the absolute value of the incident light's irradiance is not required. Thus, the calibration is aimed at

obtaining a uniform response of the pixels of a sensor to a uniform (unpolarized) source of light.
The pixels of a sensor are considered having a linear intensity response to light irradiance, except for low irradiances and at saturation, for high light irradiances (cf. figure 2.12). This linearity property can be ascertained by measuring, with the sensor, the variations of irradiance of a known light source. It can also be observed by modifying the integration time of a sensor illuminated by a constant light source (cf. figures 2.12 and 2.13). In the following, we will only consider the linear regime of a sensor for the radiometric calibration.

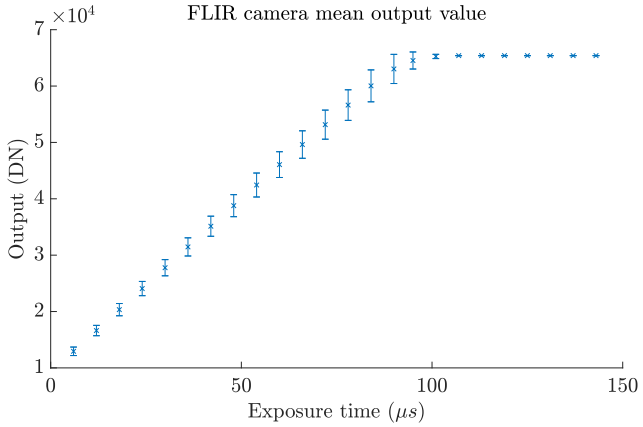

FIGURE 2.12. – Mean value of the pixels of a DoFP polarimetric sensor illuminated by visible light coming out of an integrating sphere for various exposure times of the camera. The intensity of light reaching the sensor is constant. Standard deviation of the pixels' mean value is displayed, showing the variation of the pixels' response. The experimental setup is pictured in figure 2.13.

The response of a sensor to a uniform light source will vary spatially (cf. figure 2.14) due to the fabrication process of the sensor and the lens, that can induce darkening in the corners of an image, known as vignetting. Response variations are also due to measurement noises. Read noise is generated by the sensor's electronics while measuring the charges of a photodiode, and is proportional to the number of photons reaching the sensor. This noise gives the maximum sensitivity of the sensor, describing the ability of the sensor to measure weak signals, and can not be removed. Other noises are independent from the measured light, such as dark current, also known as thermal noise, linked to the temperature, and measured when the sensor is in the dark. Contrary to read noise, dark noise can be removed.
To process the radiometric calibration of a sensor, we start by measuring the dark noise of the sensor. The dark noise D_{ij}, sometimes considered negligible [155, 156], can be modeled as a function of the integration time and temperature of the camera [157]. Once the dark noise is estimated, we tune, for each pixel, a multiplicative factor C_{ij}^{cal},

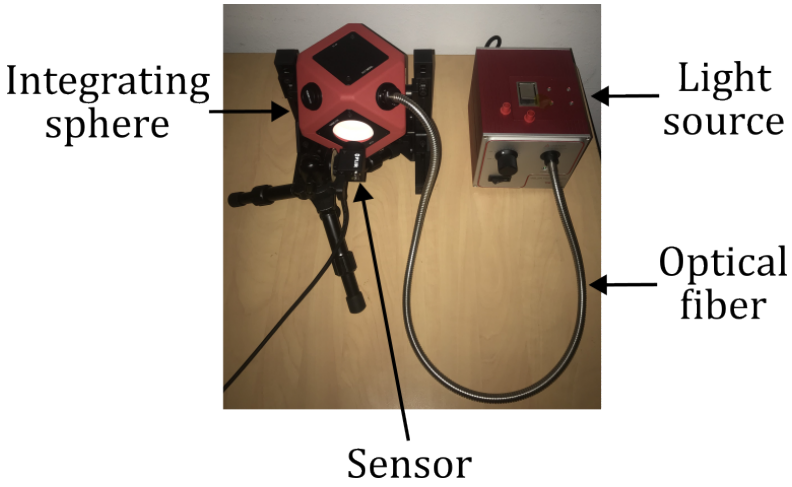

FIGURE 2.13. – Radiometric calibration setup of a polarized monochromatic camera (FLIR Blackfly S BFS-U3-51S5P). No lens is attached to the sensor. The integrating sphere (modular multi-port integrating sphere from Thorlabs) is illuminated by a fiber coupled 3200 K light source (Thorlabs OSL2). The sensor is placed near the integrating sphere to avoid non uniformity effects of the integrating sphere's output [154].

such as the response of the sensor to a homogeneous light is uniform. By supposing a linear response of the sensor to light irradiance, we can model the response R_{ij} of a pixel to an incident light of irradiance I as [158]:

$$R_{ij} = G_{ij} \cdot t \cdot C_{ij}^{cal} \cdot I + D_{ij} \tag{2.13}$$

Where G_{ij} is the gain of the pixel, and t is the integration time of the sensor. t is supposed to be equal for all pixels contrary to G_{ij}. Before calibration C_{ij}^{cal} is set to 1. An homogeneous response of the pixels can be obtained by setting $C_{ij}^{cal} = \frac{k}{G_{ij}}$ where k is an arbitrary number, equal for each pixel (cf. figure 2.14).

To determine the value of G_{ij}, the irradiance of an homogeneous incident light source, or the integration time of the sensor, should be varied. The value of G_{ij} can then be obtained by a linear regression, from equation 2.13. For relative radiometric calibration, the absolute value of the irradiance of the light source reaching the camera, does not need to be known. To generate a uniform light source, an integrating sphere can be used. Interestingly, integrating spheres generate a non polarized light, allowing for radiometric calibration independently from the polarization [160].

2.3.3. Polarimetric calibration

When considering a polarimetric camera, the response of the sensor also varies with respect to the state of polarization of the incident light. Pixels of a sensor are generally not sensitive to polarization, however, some photodetectors are intrinsically sensitive

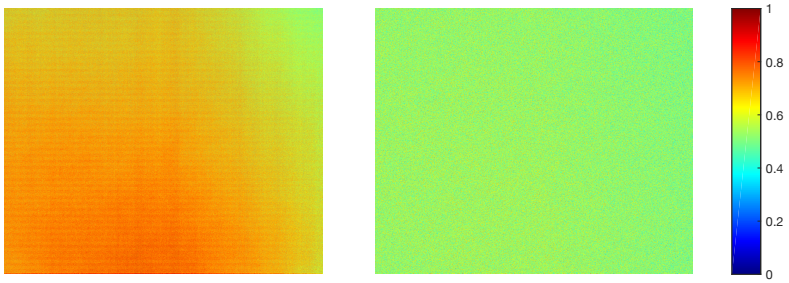

FIGURE 2.14. – Radiometric calibration of a polarized monochromatic DoFP sensor. Left: uncalibrated image of the sensor illuminated by a uniform light source. Right: calibrated image of the sensor illuminated by a uniform light source. The calibration setup is presented in figure 2.13. The calibration process is described in [159]. Since we used a DoFP sensor, the measured irradiance is also affected by the transmittance of the polarizers.

to polarized light [161, 162]. We only consider here photodetectors insensitive to polarized light, with polarizers placed above the photodetectors. The response of the pixels to polarized light depends on the Mueller matrix of the polarizing components and lens. Those polarizing components can induce measurement errors due to non uniform fabrication process of the polarizing components, imperfect alignment between the photodetectors and the filters (cf. figure 2.15), and polarizing effect of other optical components such as the lens [138, 163].

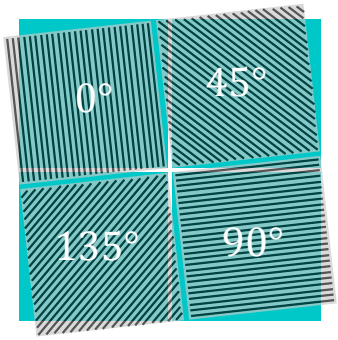

FIGURE 2.15. – Misalignment between the polarizing filters and the photodiodes of a DoFP sensor.

Non-uniform response of the pixels of a DoFP sensor, due to variations of the mean transmittance of polarizers prior to the pixels, is shown in figure 2.16. The mean transmittance of a polarizer describes the ratio between the transmitted and the incident light intensities averaged over all states of polarization (or between the transmitted and the unpolarized incident light intensities) [163].

In some DoFP sensors, a cross-talk effect was also observed, leading to measurements of light going through the polarizer placed prior to a pixel by neighbouring

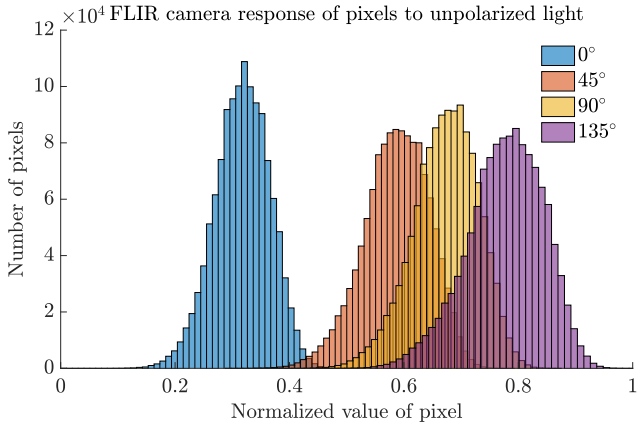

FIGURE 2.16. – Response variations of the pixels of a DoFP sensor, illuminated by a uniform unpolarized light source. Labels represent the orientation of the filters prior to the pixels. The experimental setup is presented in figure 2.13. The response variations between the different orientations of polarizing filters are due to variations of the mean transmittance of polarizers.

pixels (cf. figure 2.17). This effect was, however, reduced due to an improved design in the Sony DoFP sensors [164].

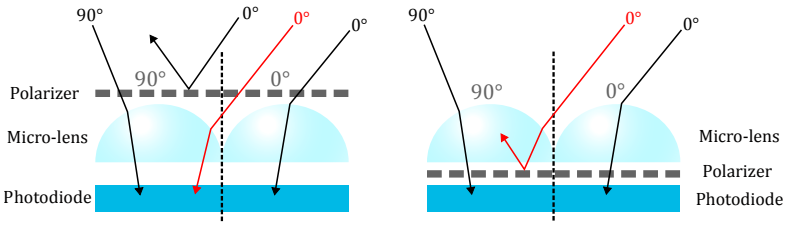

FIGURE 2.17. – Cross-talk effect of a DoFP sensor. Left: Cross talk effect allowing polarized beams with AoP of 0° to be detected by a neighbouring photodiode meant to measure polarized beams with 90° AoP. Right: Architecture developed by Sony, reducing the cross-talk effect. Micro-lens are meant to focus light on the photodiode, and are not to be confuse with the main lens attached to the sensor. Adapted from Lucid Vision Labs.

To calibrate a polarimetric camera, the Mueller matrix of each component or the equivalent Mueller matrix for the group of components prior to each pixel must be determined. Indeed, polarization properties of the optical components, such as lens, can vary in space, and the Mueller matrix of optical components will not be uniform over the sensor (cf. Maltese cross, figure 2.10). Moreover, properties of polarizers are generally given for an incident light normal to the polarizer, but vary depending on the tilt of the polarizer with respect to the incident beam, adding spatial variability

[148].
The Stokes vector $\overrightarrow{S_{out}}$ of light coming out of the optical components prior to a pixel can be expressed as (cf. section 1.2.4, equation 1.61):

$$\overrightarrow{S_{out}} = \mathbf{M_1 M_2} \dots \mathbf{M_n} \overrightarrow{S_{in}} = \mathbf{M} \overrightarrow{S_{in}} = \begin{pmatrix} m_{00} & m_{01} & m_{02} & m_{03} \\ . & . & . & . \\ . & . & . & . \\ . & . & . & . \end{pmatrix} \begin{pmatrix} S_0 \\ S_1 \\ S_2 \\ 0 \end{pmatrix} \tag{2.14}$$

Where $\overrightarrow{S_{in}}$ is the Stokes vector of the incident light. $\mathbf{M_1}, \mathbf{M_2}, \dots, \mathbf{M_n}$ are the Mueller matrices of the components prior to the pixel, their product being equal to $\mathbf{M}$. The intensity I measured by the pixel is considered being the first parameters of $\overrightarrow{S_{out}}$. Therefore, we have:

$$I = \mathbf{M}_0 \overrightarrow{S_{in}} = \begin{pmatrix} m_{00} & m_{01} & m_{02} & m_{03} \end{pmatrix} \begin{pmatrix} S_0 \\ S_1 \\ S_2 \\ 0 \end{pmatrix} \tag{2.15}$$

Where $\mathbf{M}_0$ is the first row of $\mathbf{M}$. Only the first row of $\mathbf{M}$ must thus be estimated during calibration. Moreover, as we consider only linearly polarized light (Stokes parameter $S_3 = 0$), only the three first parameters m_{00}, m_{01}, m_{02} of $\mathbf{M}_0$ must be measured. To determine the first row of the Mueller matrix $\mathbf{M}$, we can determine the Mueller matrix of each component prior to the pixels independently [165], but this method may not be convenient for an imaging sensor, since it would require to process this step for each pixel, due to the non uniform Mueller matrix of the optical components. Alternatively, we can measure the response of the sensor to a known uniform polarized light source with varying Stokes vectors. For each pixel of a sensor, if M different states of polarization of a source, with Stokes vectors $S_{in1}, S_{in2}, \dots, S_{inM}$, are generated, the M intensities $I_1, I_2, \dots, I_M$ of light reaching the sensor are given by :

$$\mathbf{I} = \mathbf{M}_0 \mathbf{S} \iff \begin{pmatrix} I_1 & I_2 & \dots & I_M \end{pmatrix} = \mathbf{M}_0 \begin{pmatrix} \overrightarrow{S_{in1}} & \overrightarrow{S_{in2}} & \dots & \overrightarrow{S_{inM}} \end{pmatrix} \tag{2.16}$$

We can deduce $\mathbf{M}_0$ by computing the pseudo-inverse of the known matrix $\mathbf{S}$. We therefore have:

$$\mathbf{M}_0 = \mathbf{I}\mathbf{S}^T \left(\mathbf{S}\mathbf{S}^T\right)^{-1} \tag{2.17}$$

Where $\mathbf{S}^T$ designates the transpose matrix of $\mathbf{S}$, and $\left(\mathbf{S}\mathbf{S}^T\right)^{-1}$ is the inverse matrix of $\left(\mathbf{S}\mathbf{S}^T\right)$. To obtain the intensity values $I_1, I_2, \dots, I_M$, from the sensor's outputs, a radiometric calibration of the pixels can be processed prior to the polarimetric calibration. However, when the polarizer can not be removed from the pixel, as for DoFP sensors, the gain of the pixel can not be computed independently from the Mueller matrix components. Indeed, the Mueller matrix $\mathbf{M}$ of an imperfect polarizer can be expressed

as (cf. section 1.2.4, equation 1.57):

$$\begin{aligned}\mathbf{M} &= \frac{p^2}{2}\begin{pmatrix} 1 & \cos 2\iota\cos 2\xi & \cos 2\iota\sin 2\xi & 0 \\ \cos 2\iota\cos 2\xi & \cos^2 2\xi + \sin 2\iota\sin^2 2\xi & (1-\sin 2\iota)\sin 2\xi\cos 2\xi & 0 \\ \cos 2\iota\sin 2\xi & (1-\sin 2\iota)\sin 2\xi\cos 2\xi & \sin^2 2\xi + \sin 2\iota\cos^2 2\xi & 0 \\ 0 & 0 & 0 & \sin 2\iota \end{pmatrix} \\ &= \frac{p^2}{2}\mathbf{M}'\end{aligned} \tag{2.18}$$

From equations 2.13, 2.15 and 2.18, the value returned by the pixel following the polarizer, without calibration, is given by:

$$R_{ij} = G_{ij}\cdot t\cdot\frac{p^2}{2}\cdot\mathbf{M}'_0\cdot\overrightarrow{S_{in}} + D_{ij} \tag{2.19}$$

Where $\mathbf{M}'_0$ is the first row of the Mueller matrix $\mathbf{M}'$. G_{ij} can therefore not be measured independently from p^2. For DoFP sensors, the pixel gain G_{ij} is computed as part of the Mueller matrix of the optical components prior to the pixels, requiring no radiometric calibration before the polarimetric calibration.
As reviewed in [166], other techniques, designed for DoFP sensors, were shown to improve the calibration results by taking into account neighbouring pixels, such as a whole super-pixel [167], during the calibration process, instead of processing pixels independently.
In practice, to create a calibration source with a varying Stokes vector, we can either modify the AoP ψ or the DoLP P_l of the source. Indeed, the Stokes vector $\overrightarrow{S}$ of a linearly polarized light source can be expressed as:

$$\overrightarrow{S} = S_0\begin{pmatrix} 1 \\ P_l\cos 2\psi \\ P_l\sin 2\psi \\ 0 \end{pmatrix} \tag{2.20}$$

Where S_0 is the intensity component of the Stokes vector. As the AoP can be tuned more easily than the DoLP, most studies calibrate their sensor by using an integrating sphere, generating unpolarized and uniform light, and a rotating polarizer to generate completely polarized light with varying AoP [138, 120, 142]. However, skylight polarization is generally partially polarized. It seems therefore appropriate to characterize the performances of a calibrated sensor based on a partially polarized light source. In the next section, we present a linearly polarized source, implemented in this thesis, for which the AoP and DoLP can be varied independently from each other.

2.3.4. Polarized light generation for DoLP measurement characterisation

In the previous section, we presented the usual process for polarimetric sensor calibration, based on purely polarized light. In chapter 3, we will describe a geolocation method based on skylight DoLP pattern variations. In this method, the measurement error of the DoLP pattern will directly affect the geolocation performances. Characterizing a sensor in terms of DoLP measurement accuracy and precision is therefore crucial. For this characterization, a light source allowing for precise control of the DoLP should be implemented. Several experiments were developed for this purpose. In this section we first review experiments aimed at controlling the DoLP of a light source, and, then, we present the source developed in this thesis.

2.3.4.1. Generation of partially polarized light

To generate a partially polarized light with adjustable AoP and DoLP, different strategies can be adopted.
Glass stacks were used to control the DoLP by refraction of an unpolarized light source [158, 168, 169, 170, 171]. Fresnel laws show that the light refracted or reflected from a material will have polarization properties varying with the angle of incidence of the incident light [74]. Therefore, by tilting glass stacks, the DoLP of a light source can be tuned, and a rotation of the glass stacks around the direction of propagation of the light source allows to tune the AoP. The AoP can also be tuned by using a rotator or half wave plate. The main advantage of this experiment is that it is easy to implement and requires few optical elements. However, this system does not allow to generate a large range of DoLP values. In [169], the DoLP could be set to values going up to 0.5. Moreover, the intensity of light transmitted through the glass stacks varies with respect to the glass stacks inclination, and is therefore not independent from the DoLP [74].
Similarly, through reflection of light, based on Fresnel laws, the DoLP and AoP can be tuned. Advantageously, using the reflection of light allows to obtain a full range of DoLP values, from 0 to 1 (at Brewster's angle) [172]. However, the reflected irradiance is often lower than the transmitted irradiance.
Another way of generating partially polarized light, is by combining two light beams with orthogonal polarization [173, 174], or by combining an unpolarized light beam with a purely polarized beam. The DoLP will therefore depend on the relative intensity between the two light beams. The AoP of such source can be modified, either before or after the combination of the light beams. To modify the AoP of a partially polarized light source without modifying the DoLP, a half-wave plate can be used. A similar experiment as the one implemented in [173] is described below, allowing to modify the intensity, AoP, and DoLP independently from each other.
The DoLP of a light source can also be tuned temporally. If a purely polarized light beam has a state of polarization alternating successively between two orthogonal polarization states, with a shorter time scale than the integration time of the sensor, the measured light can be considered partially polarized. The ratio between the duration

of each orthogonal state of polarization over the integration time of the sensor will determine the DoLP value measured. Indeed, as shown in equation 2.13 the measured intensity of a sensor is proportional to the integration time. This method is, therefore, equivalent to combining two orthogonal light beams with various relative intensities as discussed previously. Fast variations of the state of polarization can be achieved by using liquid crystal displays, as in [175]. This method is simple to implement, but the DoLP measured value depends on the integration time of the sensor.
Last, as for skylight polarization, scattering of light by particles can generate partially polarized light. To my knowledge, no method of this type has, however, been implemented for sensor characterization.

2.3.4.2. Experimental setup for controlling the AoP and DoLP of a light beam, independently

In the previous section, several ways of generating partially polarized light were introduced. We now present the principle and implementation of a partially polarized light source, based on the interference of two orthogonal linearly polarized light beams, inspired from the experiment developed in [173]. As we initially planed to sense skylight polarization in UV wavelengths, the source was developed for UV measurements, but can be adapted to visible wavelengths.

2.3.4.2.1. Conceptual explanation

To generate a light source with independently adjustable AoP and DoLP, a light beam is split in two orthogonal polarized beams. Then, the beams are summed, forming a partially polarized beam. The AoP of the source is finally modified by using a half-wave plate.
As shown in figure 2.18, the polarized light source consists in a collimated unpolarized beam of light, of Stokes vector $\overrightarrow{S}$, going through a linear polarizer, oriented at an angle θ_{LP}, and of Mueller matrix $\mathbf{M_{LP}}(\theta_{LP})$. The linearly polarized light is then split by using a polarizing beam splitter. The polarizing beam splitter can be modeled by a horizontal polarizer, of Mueller matrix $\mathbf{M_{PBS1}}(0)$, for transmission and a vertical polarizer, of Mueller matrix $\mathbf{M_{PBS1}}(\pi/2)$, for reflection [173]. Therefore, the ratio t between the transmitted light's irradiance I_t and the incident light's irradiance I_0 is given as a function of the incident light's AoP, such as (Malus law):

$$t = \frac{I_t}{I_0} = \frac{1+\cos(2\theta_{LP})}{2} \tag{2.21}$$

Where θ_{LP} is the angle of the polarizer preceding the beam splitter. Similarly, the ratio r between the reflected light's irradiance I_r and the incident light's irradiance I_0, is given by:

$$r = 1 - t = \frac{I_r}{I_0} = \frac{1-\cos(2\theta_{LP})}{2} \tag{2.22}$$

By considering that the reflected and transmitted beams are mutually incoherent, their Stokes vector can be added [74]. The resulting Stokes vector $\overrightarrow{S_+}$ is therefore given by (Mueller matrices are detailed in appendix B):

$$\begin{aligned}\overrightarrow{S_+} &= \mathbf{M_{PBS1}}(0)\cdot\mathbf{M_{LP}}(\theta_{LP})\cdot\overrightarrow{S} + \mathbf{M_{PBS1}}(\pi/2)\cdot\mathbf{M_{LP}}(\theta_{LP})\cdot\overrightarrow{S} \\ &= \frac{S_0}{2}\left(\frac{1+\cos(2\theta_{\mathrm{LP}})}{2}\right)\begin{pmatrix}1\\1\\0\\0\end{pmatrix} + \frac{S_0}{2}\left(\frac{1-\cos(2\theta_{\mathrm{LP}})}{2}\right)\begin{pmatrix}1\\-1\\0\\0\end{pmatrix} \\ &= \frac{S_0}{2}\begin{pmatrix}1\\\cos(2\theta_{\mathrm{LP}})\\0\\0\end{pmatrix}\end{aligned} \tag{2.23}$$

Which corresponds to light having a DoLP P_l given by:

$$P_l = |\cos(2\theta_{\mathrm{LP}})| \tag{2.24}$$

We notice that, when $t = r$, the light is unpolarized, when $t = 1$ the light is purely horizontally polarized, and when $r = 1$ the light is purely vertically polarized. More generally, the AoP of the source is the same as the beam having the maximum irradiance. If $t > r$, the light will be partially horizontally polarized, and if $t < r$, the light will be partially vertically polarized.
In practice, to combine the reflected and the transmitted beams, the reflected beam is reflected multiple times, by using mirrors and a second beam splitter. Using mirrors to reflect a polarized light beam can modify the state of polarization of the beam. However, in the given configuration, the reflected light is s-polarized, and therefore its polarization is not modified by reflection based on Fresnel's equations [74]. A second beam splitter is used to add the two light beams, and is modeled by an horizontal polarizer, of Mueller matrix $\mathbf{M_{PBS2}}(0)$, for transmission and a vertical polarizer, of Mueller matrix $\mathbf{M_{PBS2}}(\pi/2)$, for reflection. Finally, a half-wave plate, oriented at an angle α, and of Mueller matrix $\mathbf{M}_{\lambda/2}(\alpha)$, allows to modify the AoP without modifying the DoLP (Mueller matrices are detailed in appendix B).
To summarize, the Stokes vector of the transmitted beam $\overrightarrow{S_t}$ is given by:

$$\begin{aligned}\overrightarrow{S_t} &= \mathbf{M}_{\lambda/2}(\alpha)\mathbf{M_{PBS2}}(0)\mathbf{M_{PBS1}}(0)\mathbf{M_{LP}}(\theta_{LP})\overrightarrow{S} \\ &= \frac{S_0}{2}\left(\frac{1+\cos(2\theta_{\mathrm{LP}})}{2}\right)\begin{pmatrix}1\\\cos(4\alpha)\\\sin(4\alpha)\\0\end{pmatrix}\end{aligned} \tag{2.25}$$

And the Stokes vector of the reflected beam $\overrightarrow{S_r}$ is given by:

$$\begin{aligned}\overrightarrow{S_r} &= \mathbf{M_{\lambda/2}}(\alpha)\mathbf{M_{PBS2}}(\pi/2)\mathbf{M_{PBS1}}(\pi/2)\mathbf{M_{LP}}(\theta_{LP})\overrightarrow{S} \\ &= \frac{S_0}{2}\left(\frac{1-\cos(2\theta_{\mathrm{LP}})}{2}\right)\begin{pmatrix}1\\-\cos(4\alpha)\\-\sin(4\alpha)\\0\end{pmatrix}\end{aligned} \tag{2.26}$$

By adding those two Stokes vector, we obtain the output Stokes vector $\overrightarrow{S_{out}}$, such as:

$$\overrightarrow{S_{out}} = \frac{S_0}{2}\begin{pmatrix}1\\\cos(2\theta_{\mathrm{LP}})\cos(4\alpha)\\\cos(2\theta_{\mathrm{LP}})\sin(4\alpha)\\0\end{pmatrix} \tag{2.27}$$

Assuming $t > r$, and based on the Stokes vector $\overrightarrow{S_{out}}$, the source has a DoLP P_l and a AoP ψ given by (cf. section 1.2.3, equations 1.34 and 1.45):

$$\begin{aligned}P_l &= |\cos(2\theta_{\mathrm{LP}})| \\ \psi &= 2\alpha\end{aligned} \tag{2.28}$$

In this section, we presented theoretical materials describing a polarized light source based on the combination of two orthogonally polarized light beams. The two beams were supposed mutually incoherent. In practice, to achieve this, the optical path difference between the reflected and transmitted beams should be larger than the coherence length. The coherence length L_C can be approximated by [76]:

$$L_C = \frac{\lambda^2}{\Delta\lambda} \tag{2.29}$$

Where λ is the mean wavelength and $\Delta\lambda$ is the spectral range of the light beam. A $385nm$ light source, having a spectral range of about $10nm$, was used for this experiment. This corresponds to a coherence length of about $10^{-5}m$. As stated in [77], it is often considered that orthogonal polarization states do not interfere, however, they do interfere in polarization, without creating intensity fringes. Therefore, if analyzing the generated beam from this setup, using a polarizer (cf. figure 2.18), interference fringes can appear if the previously discussed condition is not met.

2.3.4.2.2. Implementation of the source

Having presented the principle of the partially polarized light source setup, we now present its implementation, pictured in figure 2.18.
The device was composed of a fiber coupled $385nm$ UV light source (Pyroistech COB-385), connected to a UV-enhanced aluminum reflective collimator (Thorlabs

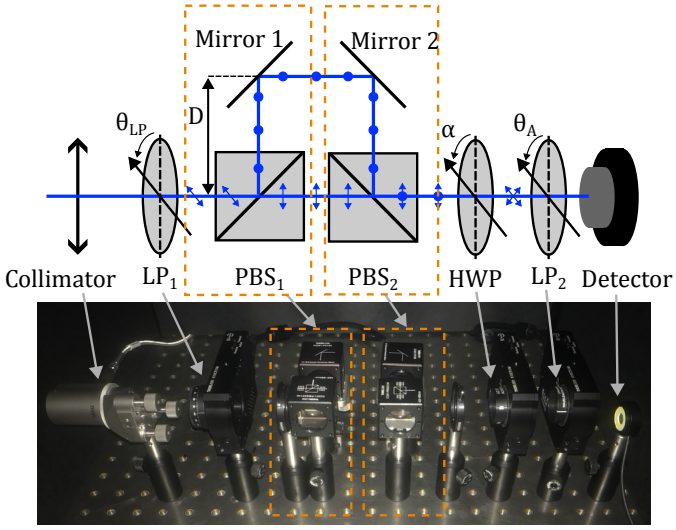

FIGURE 2.18. – Setup of the partially polarized light source. Up: Schematic representation of the setup. LP_1 is the first polarizer used to modify the DoLP. PBS_1 and PBS_2 are the two polarizing beam splitters used to split and combine the light beams. HWP is the half wave plate used to vary the AoP. Finally, LP_2 is the polarizer used to analyse the light beam. The distance D between the polarizing beam splitters and the mirrors should verify $D > \frac{L_C}{2}$ where L_C is the coherence length of the source. The blue arrows and dots describe the direction of polarization of the light. Adapted from [173] Down: picture of the setup.

RC12SMA-F01). The collimated source was considered unpolarized. Moreover, the source emitted visible light, enabling the alignment of the optical components from this source. Then, a $365-395nm$ UV linear polarizer (Thorlabs LPUV100), was placed prior to a polarizing beam splitter cube (Thorlabs CCM1-PBS251/M). Since no beam splitter was designed for UV light, we used a $420-680nm$ coating beam splitter, suitable for UV measurements. Two UV-enhanced aluminum mirror (Thorlabs CCM1-F01/M) were used to deviate the reflected beam, and a second polarizing beam splitter, identical to the first one, allowed to combine the reflected and transmitted beams from the first beam splitter. An achromatic $260-410nm$ half-wave plate (Thorlabs AHWP10M-340) was finally placed after the second polarizing beam splitter. The linear polarizer and the half wave plate were both mounted on a stepper motor rotation mount (Thorlabs K10CR1/M), allowing for unidirectional repeatability of $\pm 60\mu rad$.
To analyse the light beam, a UV linear polarizer (Thorlabs LPUV100), mounted on a stepper motor rotation mount (Thorlabs K10CR1/M), was placed prior to a $200-1100nm$ UV-extended Si photodiode power sensor (Thorlabs S120VC).
The state of polarization of the source was obtained from 18 measurements with orientations of the analyser varying from 0° to 180° by steps of 10°, and by using the least-squares method, as shown in section 2.1.
The reference angle of polarization was defined as the p-polarization transmitted

by the first polarizing beam splitter. The orientation of the analyser was obtained by measuring the AoP of the light comming out of the polarizing beam splitter, before placing the other components of the setup. Then, the polarizer placed prior to the the beam splitter was added to the setup, and its orientation with respect to the p-polarization was computed in a similar manner as for the analyser. For this, the analyser was fixed horizontally, in order to maximize the measured irradiance. It should be noticed here that rotating a polarizer preceding or following a fixed polarizer (polarizing beam splitter in transmission here) leads to the same results. Last, the half-wave plate was added to the setup, and its orientation determined. The orientation of the analyser is known by the previous calculus, and the orientation of the first polarizer is set to maximize the intensity transmitted by the polarizing beam splitter. By rotating the half-wave plate, the orientation of its (slow) axis, is obtained similarly to the polarizers. For each orientation α_j of the half-wave plate, given by the orientation of the motor, the measured irradiance I_j is given by:

$$I_j(\theta_A) = S_0 + S_1 \cos\left(2(\theta_A + 2\alpha_j)\right) + S_2 \sin\left(2(\theta_A + 2\alpha_j)\right) \tag{2.30}$$

Where θ_A is the orientation of the analyser, and S_0, S_1 and S_2 are the three first Stokes parameters of the light coming out of the beam splitter.
By setting:

$$\mathbf{D} = \begin{bmatrix} \cos(2(\theta_A + 2\alpha_1)) & \sin(2(\theta_A + 2\alpha_1)) & 1 \\ \cos(2(\theta_A + 2\alpha_2)) & \sin(2(\theta_A + 2\alpha_2)) & 1 \\ \vdots & \vdots & \vdots \\ \cos(2(\theta_A + 2\alpha_M)) & \sin(2(\theta_A + 2\alpha_M)) & 1 \end{bmatrix}, \overrightarrow{I_{meas}} = \begin{bmatrix} I_1 \\ I_2 \\ \vdots \\ I_M \end{bmatrix}, \overrightarrow{S_{in}} = \begin{bmatrix} S_0 \\ S_1 \\ S_2 \end{bmatrix} \tag{2.31}$$

Where M is the number of measurements. We obtain $\overrightarrow{S_{in}}$ from the following:

$$\overrightarrow{S_{in}} = \left(\mathbf{D}^T\mathbf{D}\right)^{-1}\mathbf{D}^T\overrightarrow{I_{meas}} \tag{2.32}$$

We can deduce the angle of polarization of the measured light by:

$$\psi = \frac{1}{2}\tan^{-1}\left(\frac{S_2}{S_1}\right) \tag{2.33}$$

This angle is given with respect to the axis of the half-wave plate. However, we know that the AoP is equal to zero with respect to the p-polarization coming out from the beam splitter. Therefore, this measured AoP gives the orientation of the axis of the half-wave plate with respect to horizontal reference. The three steps described here are represented in figure 2.19. The other components are finally added to the setup.

2.3.4.2.3. Results

The analysis of the source shows results similar to that predicted by the theory (cf. figure 2.20). However, differences occur in the experiments due to polarization

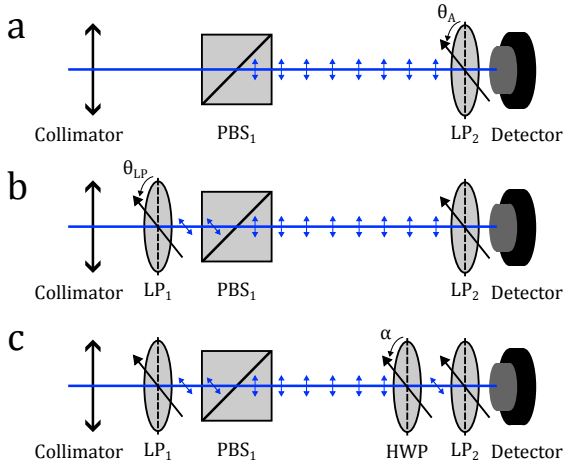

FIGURE 2.19. – Steps for determining the orientation of the rotating optical components of the setup. (a) First step: rotation of the analyser LP_2 to estimate its orientation θ_A. (b) Second step: rotation of the polarizer LP_1 to estimate its orientation θ_{LP}. (c) Third step: rotation of the half-wave plate HWP to estimate its orientation α.

optics being imperfect. Observed variations of the mean irradiance (cf. intersections of curves in figure 2.20a) are probably due to the collimated source being partially polarized (DoLP of about 2%), and to a variable loss of irradiance when the light beam is transmitted and refracted by the beam splitters, designed for visible wavelengths, and the mirrors. The maximum value of DoLP achieved is slightly lower than 1 due to the polarizing beam splitters being imperfect (cf. figures 2.20c and e). Indeed, the reflected and transmitted light, by the polarizing beam splitters, are never null. Moreover, variations of DoLP, up to 0.03, appear when rotating the half-wave plate (cf. figure 2.20e). A half-wave plate is not supposed to modify the DoLP. The half-wave plate used in this experiment may therefore present a polarizing effect. Similarly, the AoP varies, with up to 2.5° changes, when the linear polarizer is rotated (cf. figure 2.20d). As shown previously, the AoP should only be adjusted by the rotation of the half-wave plate. This can suggest a retardance effect of the polarizing beam splitters. A constant bias is observed between the theoretical and experimental DoLP in figure 2.20e. It is unclear why such difference occurs, but it may be due to a wrong estimation of the value of θ_{LP}. Further investigations should be conducted to understand this difference. The homogeneity of the source has not been studied yet, and should also be analyzed.

Due to those dissimilarities between the theory and experimental results, we decided to describe the state of polarization of the source, for different orientations of the polarizing components, through a lookup table giving the AoP and DoLP of the source for each angle of the polarizing components of the source, instead of describing the state of polarization through Mueller matrix calculus. Based on the unidirectional repeatability of the motor, we can approximate the AoP and DoLP repeatability based on the previous theoretical description of the source. By neglecting the effect of imper-

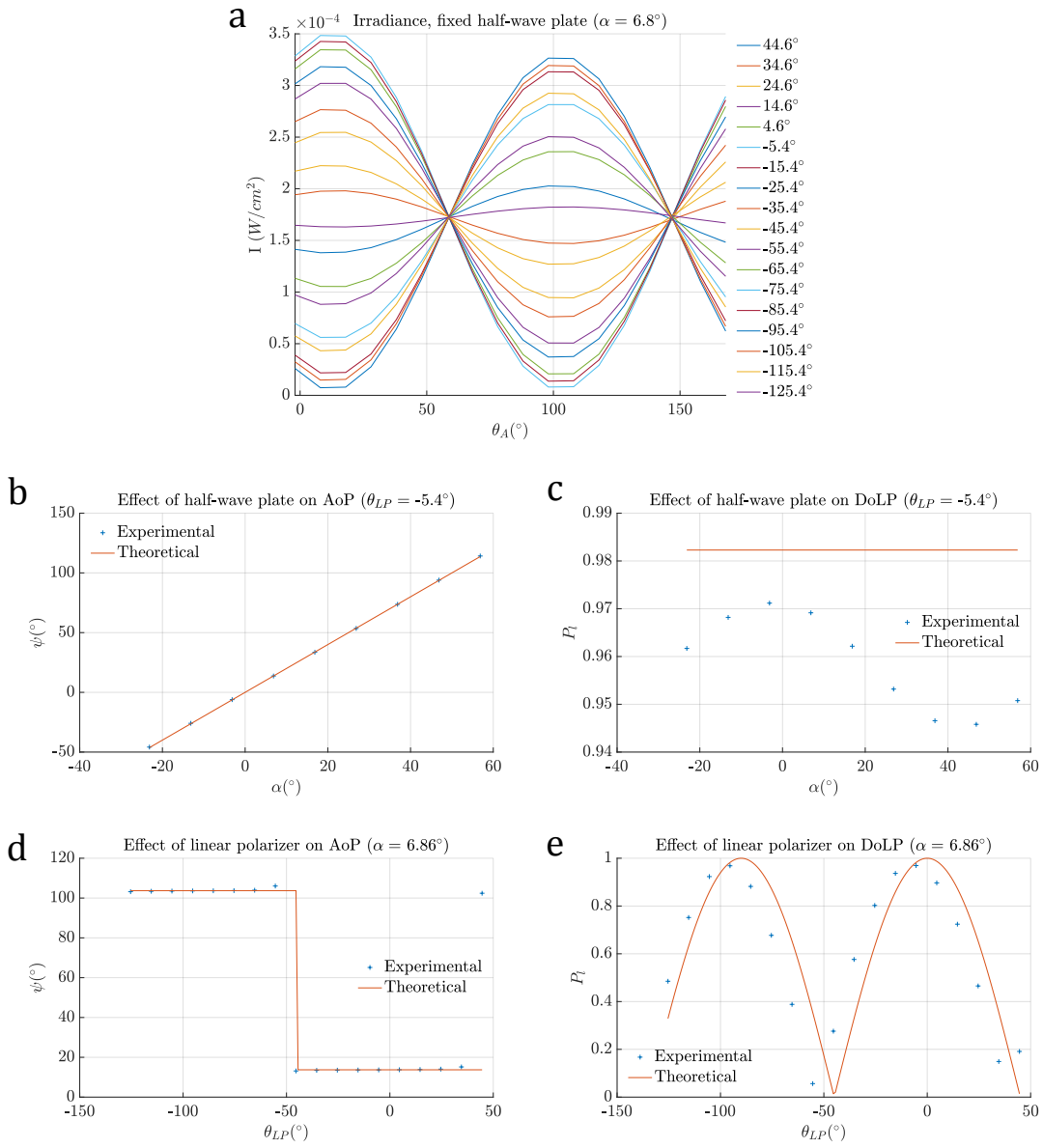

FIGURE 2.20. – Results obtained from the characterization setup. I is the irradiance measured by the photodetector. θ_{LP}, α and θ_A, represented in figure 2.18, are the angles of the first polarizer, the half-wave plate and the analyser, respectively. ψ and P_l are the AoP and DoLP, respectively. (a) Experimental data, legend give the value of θ_{LP}.

fect polarization components in the uncertainty calculus (low variations compared to the source's AoP and DoLP variations), the uncertainty of the state of polarization of the source due to the repeatability uncertainty of the motors can be computed from equation 2.28. The unidirectional repeatability $u_{\theta_{LP}}$ and u_α of the angles θ_{LP} and α, respectively, is given by the motors' unidirectional repeatability. From the propagation

of uncertainty, applied to equation 2.28, we have:

$$\begin{aligned} u_{P_l} &\approx \frac{dP_l}{d\theta_{LP}} \cdot u_{\theta_{LP}} \approx 2\sin(2\theta_{LP})\, u_{\theta_{LP}} < 2u_{\theta_{LP}} \\ u_\psi &\approx \frac{d\psi}{d\alpha} \cdot u_\alpha \approx 2u_\alpha \end{aligned} \tag{2.34}$$

Therefore, the AoP and DoLP repeatability u_ψ and u_{P_l}, respectively, can both be given as twice the motor unidirectional repeatability, that is $\pm 120 \mu rad$. The repeatability of AoP is therefore about $\pm 0.007°$ and for the DoLP, about ± 0.007. Twice lower repeatability of the AoP can be achieved by replacing the half-wave plate by a rotator. Indeed, a half-wave plate is equivalent to a rotator but a rotation of a half-wave plate doubles the amount of rotation of the polarization direction [74].

2.3.4.2.4. Discussion

In this section, we presented a source allowing to control independently the AoP and DoLP of light, and therefore to generate any linearly partially polarized light. This setup is well suited for characterization of polarization devices, allowing to describe their performances in situations corresponding to outdoor conditions. Its benefits for calibration are, however, unclear since, as discused in section 2.3.3, generating completely polarized light with varying angle of polarization is sufficient for calibration. The main issue with this source is the small radius of the emitted light beam, which do not allow to characterize all at once devices with large angular field of view. However, for sensors with fish-eye lens, most source are too small for this, and calibration or characterization of the device is achieved by a multi-step calibration, rotating the device with respect to the source [158, 176, 177].

2.4. Conclusion

In this chapter, we presented different types of sensor architectures for skylight polarization sensing, the measurement of the state of polarization of light based on those sensors, and their calibration process. Recent progress on fabrication of polarimetric sensors allow for cheaper devices, and therefore, more accessible commercial polarimetric applications. However, existing commercial sensors provide a large quantity of data (few megapixels), which, as observed through insects, is not necessary for navigation based on the skylight polarization. Future research on polarimetric sensors should therefore be aimed at reducing the quantity of data rather than increasing it, for performance and environmental considerations. For now, most developed sensors are composed of millions or a few dozen of photodiodes. Intermediate numbers of photodiodes could provide robust data without requiring much computing power. Another improvement, for skylight polarization navigation, would be to develop polarization devices sensitive to UV light. So far, no commercial UV polarimetric device was developed. The fabrication of such devices is currently studied in parallel to this

thesis, and their characterization is planed based on the implemented setup presented above. Last, the fabrication of photodiodes requires toxic materials, such as arsenic (AsGa). We started working, during this thesis, on photoresistive sensors based on zinc oxide (ZnO), which is non toxic and sensitive to UV light. This work was, however, only preliminary, and is not detailed in this manuscript.

3. Geolocation

In this chapter, we will describe navigation strategies based on skylight polarization developed either by animals or by humans skilled in the art. Then, we will present the methods developed as part of this thesis.

3.1. Skylight polarization navigation

In this section we will review the existing methods for navigation based on skylight polarization. We will start from insect-inspired navigation, and then we will present geolocation methods, based on classical navigation techniques.

3.1.1. Spherical astronomy definitions

Before presenting those navigation methods, we start by defining some useful astronomical variables.
For more details, we highly recommend the reading of Smart's textbook on spherical astronomy [10]. In particular, chapter II, "The Celestial Sphere" provides useful illustrated definitions.
Warning, Symbols used in this thesis might differ from those used in [10].

When considering the Earth or the sky, we often approximate both as spheres. For a sphere, we define a great circle as the intersection between the sphere and a plane containing the center of the sphere. Similarly, we define a small circle as the intersection between the sphere and a plane that does not contain the center of the sphere. The great circle distance between two points is the shortest distance between those two points (cf. figure 3.1).

The Earth equator is defined as the great circle located on a plane perpendicular to the axis of rotation of the Earth. We remind that the geographical north and south poles are defined as the intersection between the Earth's axis of rotation and the Earth surface, different from the magnetic poles. A meridian is defined as a semi great circle having its ends at the poles. Each point of the Earth meridian has the same longitude. On Earth, the longitude ℓ is defined as the angle between a meridian and the Greenwich meridian. The latitude ϕ is defined as the angle between a point on the equator and a point located on the same meridian, but on a small circle parallel to the equator. Each point of same latitude is said to be located on a parallel of latitude. The latitude varies between $-90°$ and $90°$, a point on the equator having $0°$ latitude.

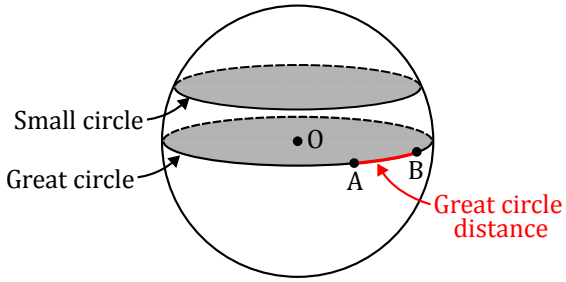

FIGURE 3.1. – Representation of a great circle and a small circle. The red arc is the great circle distance between the points A and B. O is the center of the sphere.

The colatitude is equal to 90° minus the latitude. Those Earth related definitions are represented in figure 3.2

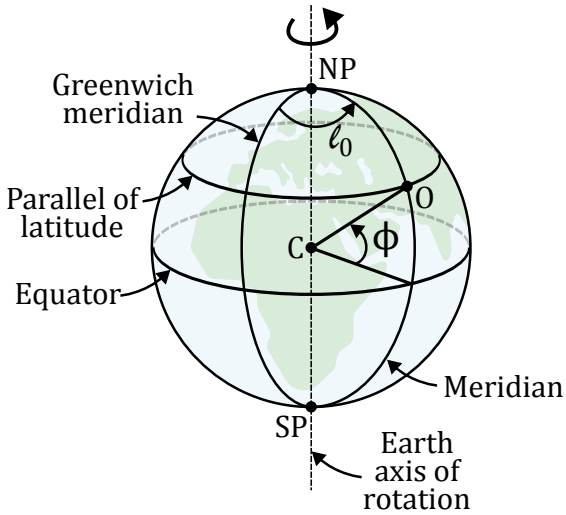

FIGURE 3.2. – Coordinates of an observer O located at the Earth surface. C is the center of the Earth, SP is the south pole and NP is the north pole. O has a latitude ϕ with respect to the Earth equator and a longitude ℓ_0 with respect to the Greenwich meridian.

When considering the sky, the distance of an object in the sky from Earth may not be accounted for. We, thus, consider that all celestial objects are located on a sphere with a large radius compared to the radius of Earth. This sphere is called the celestial sphere. Similarly to the Earth, we can define the north celestial pole (NCP) and south celestial pole (SCP) as the intersections of the Earth rotation axis with the celestial sphere. The celestial equator is defined as the intersection between the plane containing the Earth equator and the celestial sphere. To define coordinates of a celestial object, we can consider two coordinate frames centered either on the Earth or on an observer at the Earth surface, the equatorial coordinate system and the horizontal coordinate system, respectively. In the equatorial coordinate system, the coordinate of a star S is defined

by its declination and right ascension or hour angle. The declination δ is defined as the angular distance between the celestial equator and the circle describing the trajectory of the star, named a parallel of declination. The hour angle ω and right ascension both describe the position of the star on a parallel of declination (cf. figure 3.3).

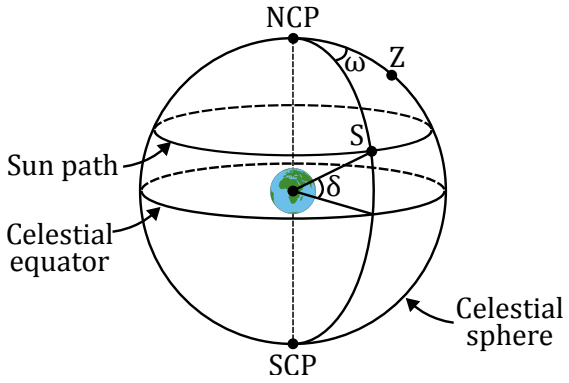

FIGURE 3.3. – Sun hour angle ω and declination δ represented on the celestial sphere. δ is expressed as the great circle distance between the Sun S and the intersection of the celestial equator and the meridian going through the Sun. ω is expressed as the angle between the meridian going through the zenith Z, and the meridian going through the Sun. Here the Sun's path for one day is defined by a plane parallel to the plane containing the celestial equator, by considering that the declination is constant during a day. NCP and SCP are the north and south celestial poles, respectively.

In the horizontal coordinate system, we consider that the observer can only see points above the horizon. The zenith of an observer is the point above the observer, defined as the intersection between the celestial sphere and the line going through the center of the Earth and the observer. The observer's meridian is defined in the equatorial coordinate system as the semi great circle having its ends at the south and north celestial poles and containing the zenith. In the horizontal coordinate system the observer's meridian is the semi-great circle having its ends at the north and south points of the horizon and containing the zenith. A vertical circle is a great circle containing the zenith (cf. figure 3.4).

The coordinates of a point in the horizontal coordinate system are the azimuth and altitude, also named elevation. The azimuth of a star is defined as the angle between the vertical circle containing the star and the observer's meridian. The zenith distance is defined as the angle between the star and the zenith on the vertical circle containing the star. The altitude is the complementary angle of the zenith distance, meaning that the altitude is equal to 90° minus the zenith distance (cf. figure 3.5).

The hour angle can also be defined as the angle between the observer's meridian and the meridian containing the star in the observer's related frame (cf. figure 3.6). Often, we use the East, North, Up (ENU) frame to describe the position of a point in the sky as seen by an observer on the surface of the Earth. Here, Up refers to the

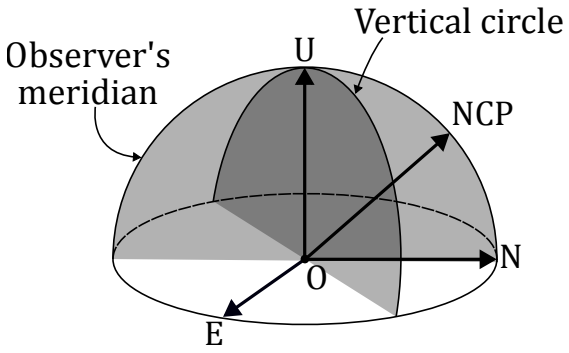

FIGURE 3.4. – Observer's meridian and a vertical circle in the horizontal East, North, Up (ENU) frame centered on the observer O is the observer. U is the zenith of the observer, and NCP the north celestial pole.

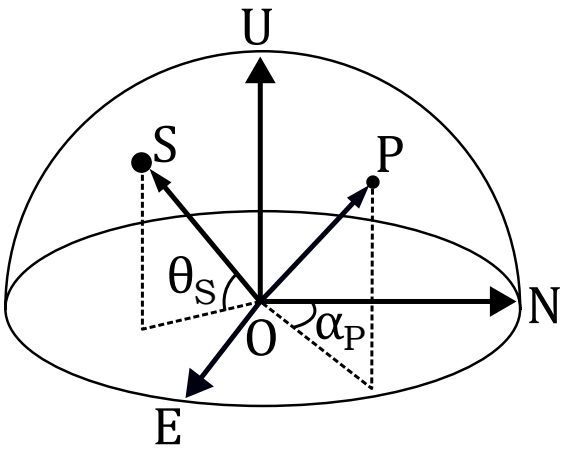

FIGURE 3.5. – Azimuth α_P of a point P and altitude θ_S of the Sun S in the horizontal coordinate system. Parameters are presented in the ENU frame, namely East, North, and Up frame, centered on the observer O.

observer's zenith direction.

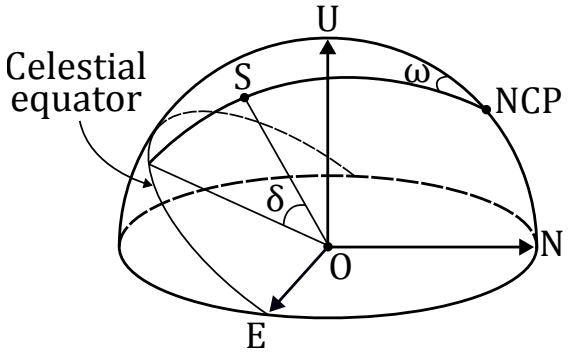

FIGURE 3.6. – Sun hour angle ω and declination δ of the Sun S represented in the ENU frame centered on the observer O.

3.1.2. Insect-inspired navigation

The use of skylight polarization by insects for navigation purposes was discovered in the begining of the 20th century. Behavioural studies and neuro-ethology have allowed for a deep understanding of the utilization and processing of skylight polarization information in insect localization. One of the simplest behaviour was discovered while observing ball-rolling dung beetles. Those insects roll dung into a ball, in order to feed and lay eggs. Once the ball formed, they move as fast as possible from the feces to avoid competition with other dung beetles. Their strategy consists in using the skylight polarization as a compass cue to leave in a straight line during day [15], and the Milky Way in a similar manner during night [14]. This strategy is known as the compass orientation strategy [12] (cf. figure 3.7b). Another strategy, adopted by the *Cataglyphis* desert ants, was intensely studied. *Cataglyphis* desert ants forage under extreme temperatures in the desert. To survive to such conditions, they must move rapidly, and stay as little as possible outside. Extreme temperatures do not allow desert ants to use pheromones to return to their nest. Instead, they use an inertial navigation strategy. Inertial navigation consists in determining its position with respect to an initial position by "keeping track of each leg of a journey" [12]. To achieve that, desert ants merge information from an odometer (distance estimation by steps counting), the ground optic flow (distance estimation from apparent visual motion) and a sky compass based on the skylight polarization. That information allows ants to compute distances and directions, providing enough cues to estimate their actual position with respect to their nest. They are finally able to go back to their nest in a straight line (cf. figure 3.7c).

This strategy was tested and proven succesfully onboard mobile robots, namely Sahabot, a wheeled robot [178, 179], and AntBot, a six-leg robot [26] (cf. figure 3.8).

Thanks to technological advances, the neural mechanisms underlying the insects' inertial navigation strategy became increasingly understood. A neural model for path integration in the bee brain was developed in [180]. In [181], a model of the skylight polarization compass of insects, based on neural studies was implemented and tested on simulated data. This study was, then, followed by the construction of a device aimed at processing skylight polarization in real conditions based on neural models [126]. As highlighted in section 2.2.1, few studies processed skylight polarization signal from orthogonal polarization sensors based on Labhart neural model [116]. In those studies, however, apart from the computation of orthogonal signals, the bearing is not computed from neural models. Instead, different strategies were adopted. In [26, 182, 183], the angle of polarization is measured at the zenith, giving a direct estimation of the Sun's azimuth. Indeed, as shown in section 1.3.2.1, considering the Rayleigh's single scattering model, the direction of polarization at the zenith is orthogonal to the vertical plane going through the Sun (cf. figure 3.9 left). Interestingly, a device known as the Pfund sky compass [184], providing navigation cues based on this simple method, was adopted for military flights near the magnetic poles where the magnetic field is unreliable, near the geographic poles were the gyro compass becomes unusable, and during twilight when the stars and the Sun are not visible. Another strategy consists

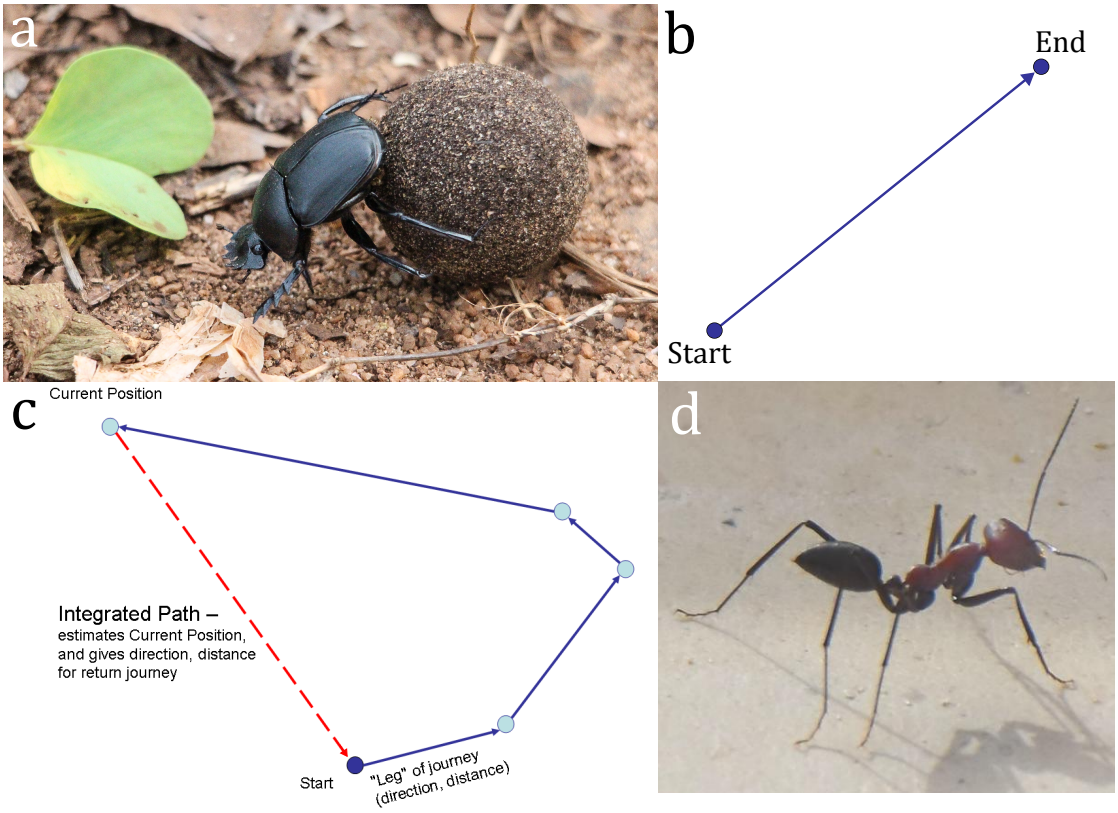

FIGURE 3.7. – Compass orientation and inertial navigation strategies. (a) Ball-rolling dung beetle. Credit: Peter van der Sluijs, CC BY-SA 3.0, via Wikimedia Commons. (b) Dung beetle's compass orientation strategy. (c) Path integration for inertial navigation. Chiswick Chap, CC BY-SA 3.0, via Wikimedia Commons (d) *Cataglyphis* desert ant. Credit: Jean-Claude Jamoulle, CC-BY-NC

in measuring the direction of polarization in multiple directions (at least two) in the sky to estimate the position of the Sun [185, 137] (cf. figure 3.9 right). From two e-vectors measurements in the sky, the Sun's position can be inferred by noticing that the e-vectors are perpendicular to the scattering plane, containing the observer, the Sun and the point of observation (cf. section 1.3.2.1). The direction of polarization $\overrightarrow{n}$ for a point P in the sky can thus be expressed as $\overrightarrow{n} = \overrightarrow{OS} \times \overrightarrow{OP}$, where O designates the observer and S the Sun, and $\times$ is the cross product. Therefore, by measuring the direction of polarization $\overrightarrow{n_1}$ and $\overrightarrow{n_2}$ for two points P_1 and P_2 respectively, we have:

$$\begin{aligned}
\overrightarrow{n_1} \times \overrightarrow{n_2} &= \left(\overrightarrow{OS} \times \overrightarrow{OP_1}\right) \times \left(\overrightarrow{OS} \times \overrightarrow{OP_2}\right) \\
&= \overrightarrow{OS}\left(\left(\overrightarrow{OS} \times \overrightarrow{OP_1}\right) \cdot \overrightarrow{OP_2}\right) - \overrightarrow{OP_2}\left(\left(\overrightarrow{OS} \times \overrightarrow{OP_1}\right) \cdot \overrightarrow{OS}\right) \\
&= \overrightarrow{OS}\left(\left(\overrightarrow{OP_1} \times \overrightarrow{OP_2}\right) \cdot \overrightarrow{OS}\right) \\
&= k\overrightarrow{OS}
\end{aligned} \tag{3.1}$$

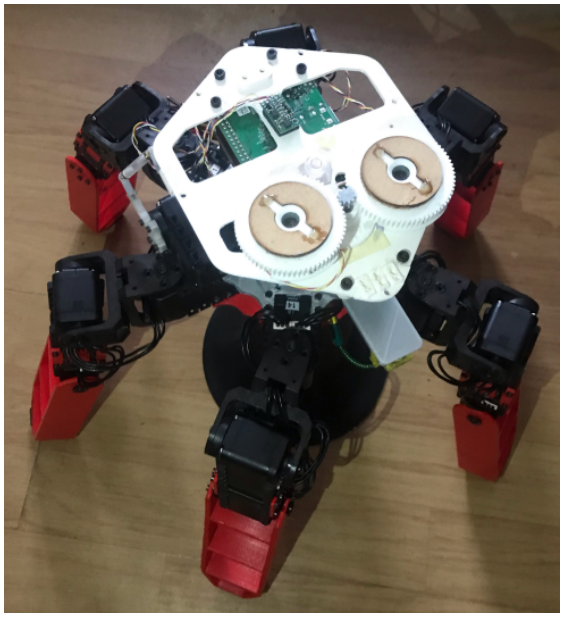

FIGURE 3.8. – Robot AntBot. The polarizers are located in the two eye-like wheels [26].

Where k is a real number. We can finally deduce:

$$\overrightarrow{OS} = \frac{(\overrightarrow{n_1} \times \overrightarrow{n_2})}{||\overrightarrow{n_1} \times \overrightarrow{n_2}||} \tag{3.2}$$

Where $||\cdot||$ is a vector norm.

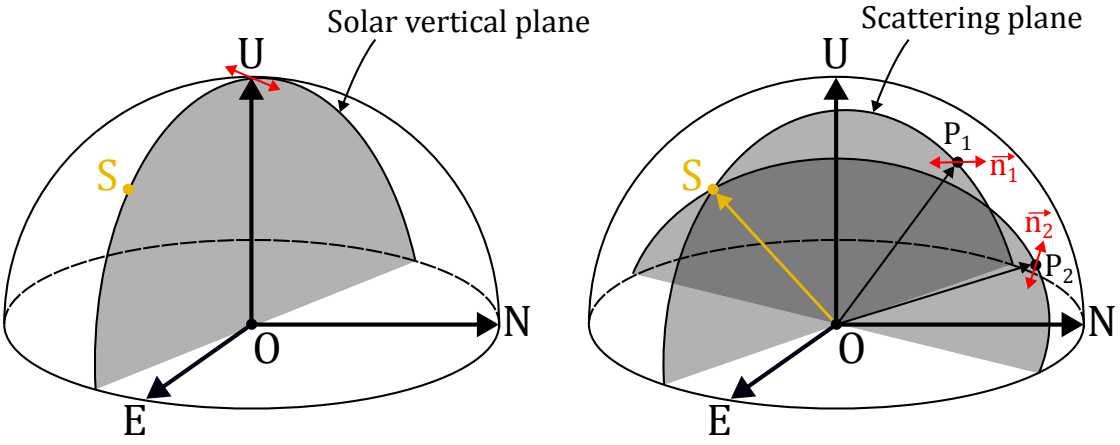

FIGURE 3.9. – Methods for measuring the Sun's position. Left: from the direction of polarization (red arrow) at the zenith. Right: from the directions of polarization $\overrightarrow{n_1}$ and $\overrightarrow{n_2}$ measured in two directions P_1 and P_2 respectively. S is the Sun represented in the ENU frame centered on the observer O.

Insects were shown to use the degree of polarization as information on the reliability of skylight polarization. If the maximum degree of polarization in the sky is lower

than a threshold value, the polarization is not used for navigation [15]. The Michelson contrast threshold in insects' visual system (defined as $\frac{L_{max}-L_{min}}{L_{max}+L_{min}}$, where L_{max} and L_{min} are the maximum and minimum luminance, respectively) is about 5%, and the only quantitative experiments on the detectability of DoLP was performed on crickets. The authors provided evidence that crickets exploited polarization down to an (average) polarization level of less than 7% [186]. We lack of neurophysiological results on other insects species. Some studies took advantage of the DoLP in a similar manner to obtain the position of the Sun, considering only measurements with DoLP higher than a threshold [187]. The DoLP was also used as a weighting factor to measure the Sun's position, measurements with higher DoLP having an increased influence on the solar estimation [188]. Other methods were developed essentially for imaging sensors. By knowing the maximum value of the DoLP in the sky, and measuring the DoLP at different positions, the scattering angle for each measurement point can be deduced, permitting the estimation of the Sun's position [189]. Contrary to the Rayleigh single scattering model discussed in section 1.3.2.1, the maximum of DoLP in the sky is lower than 1. The real DoLP P_l in the sky is often approximated by:

$$P_l(\gamma) = P_{l_{max}} P_{l_R}(\gamma) = P_{l_{max}} \cdot \frac{\sin^2(\gamma)}{1+\cos^2(\gamma)} \tag{3.3}$$

Where $P_{l_{max}}$ is the maximum of DoLP in the sky, P_{l_R} is the degree of polarization based on the Rayleigh single scattering model and γ is the scattering angle. We can then express the scattering angle as a function of the degree of polarization of a point in the sky and the maximum degree of polarization. However, the knowledge of the maximum of polarization may not be straightforward, especially in presence of clouds. A method to obtain the maximum degree of polarization is given in section 3.2.2.1.1. Another method, that does not require any knowledge of the maximum of polarization was developed in [189]. By measuring the gradient of DoLP at a point in the sky, a great circle going through the Sun and the point of observation can be obtained. Therefore, by repeating this process for different points in the sky, the position of the Sun is given as the intersection of the great circles going through each point of observation. In [190], the position of the Sun is obtained by matching the real skylight polarization with a skylight polarization pattern based on Rayleigh scattering model, with DoLP defined as in Eq. 3.3. An interesting approach, that has been widely used for estimating the solar azimuth, consists in representing the skylight's angle of polarization for each particle of the sky in the particle's frame. We therefore distinguish the global angle of polarization defined with respect to the sensor's frame, and the local angle of polarization defined locally for each particle (cf. figure 3.10). An explanation of this representation is given in [82].

This local angle of polarization forms an eight-shaped pattern in the sky, which allows for simple estimations of the vertical plane containing the Sun (cf. figure 3.11).

Using the local angle of skylight polarization, the solar vertical plane was obtained either from the symmetry of the pattern [191], by thresholding [144, 192], or by applying mathematical transforms on the polarization image [145, 133, 193, 194]. Each point

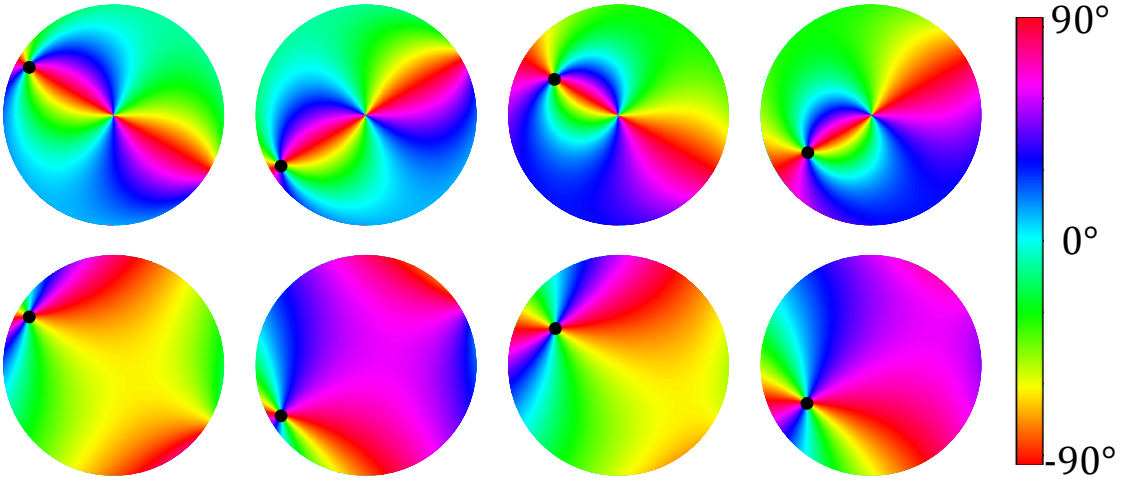

FIGURE 3.10. – Simulated angle of polarization in the local (first row) and global (second row) frame, as viewed by a polarimetric camera fitted with a fisheye lens. The two first columns correspond to a solar elevation of 10° and azimuth of 150° and 210°, respectively with respect to the camera frame. The two last columns correspond to a solar elevation of 30° and azimuth of 150° and 210°, respectively, with respect to the camera frame. Notice the similarity between the pattern of angle of polarization in the local frame. The Sun's position corresponds to the black dot.

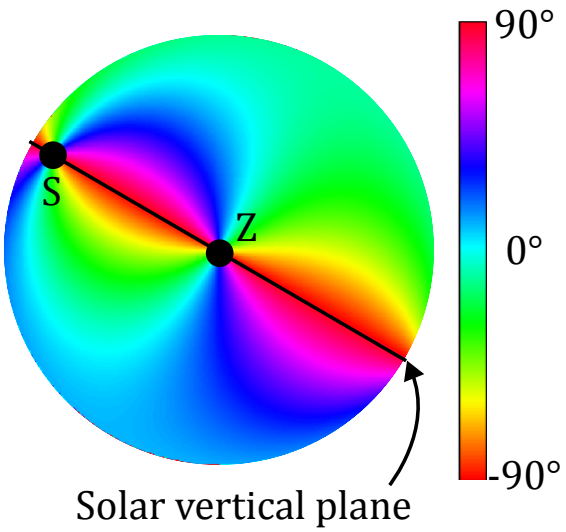

FIGURE 3.11. – Simulated local angle of polarization, as viewed by a polarimetric camera fitted with a fisheye lens. S is the position of the Sun and Z is the Zenith.

of the vertical plane having the same, or opposite, azimuth, the solar azimuth can be deduced from the estimation of this vertical plane. It should be noticed that when

measuring the Sun's position based on the Rayleigh single scattering model, there is an ambiguity between the solar and anti-solar positions because of the symmetries of patterns of polarization. Other information, such as the intensity gradient or color gradient can be used to remove this ambiguity [195]. Finally, with the recent advances of deep learning, several algorithms were implemented to obtain the Sun coordinates even in presence of obstacles such as clouds, buildings, or under the canopy [196, 197, 198, 199, 200, 201].
In this section, we presented some methods inspired by insects to find information on the position of the Sun. The Sun's coordinates can be used to estimate a relative heading with respect to Sun's azimuth or variations in heading or attitude of a system. Contrary to heading estimation, the use of the skylight polarization by insects for controlling their attitude still remains an open question [15]. The polarization related cues can be merged with information from other sensors such as inertial navigation sensors to add reliability to the navigation task. However, those methods only allow for estimating a position relative to an initial position, as do desert ants, for instance. Most insects are only able to measure a relative position with respect to landmarks or their nest. Some insects, such as the monarch butterfly, however, seem to rely on global cues to navigate. Those insects are thought to be using two compasses, a sky compass with a time compensation mechanism to compensate the Sun movement during time, and a magnetic compass [202, 203]. They are, however, considered being compass navigators, and therefore not able to geolocate. Recently, the magnetic field was also proven useful for *Cataglyphis* desert ants [204]. In the next section, we present existing methods to geolocate based on the skylight polarization pattern.

3.1.3. Geolocation using skylight polarization

After the discovery of the insect's polarization sensitivity, studies have shown that some vertebrates, such as homing pigeons, used skylight polarization to navigate. Homing pigeons are thought to be true navigators, meaning that they are able to know the location of a their goal on Earth, independently from landmarks. However, the mechanisms explaining this capability remain unclear [205]. Moreover, contrary to the insects' compound eyes, the polarization sensitivity of camera eyes is less understood (cf. section 2.2). For these reasons, most studies relying on skylight polarization for geolocation implement classical solar navigation methods, such as those developed for sextant based navigation. However, instead of observing the Sun directly, the pattern of polarization is used to infer the Sun's position by using methods presented in the previous section.
In the 1730s, the sextant, a navigation instrument, was created by John Hadley and Thomas Godfrey, enabling the precise localization of the Sun and other celestial bodies. A sextant requires a view of the horizon to calculate the celestial body's altitude, and is therefore intended mainly for marine navigation. Geolocation using a sextant during day is made possible by combining solar measurements with solar ephemeris, providing, for a given time, the Sun's geographic position, namely the position on Earth for which the Sun is at the zenith. From the solar zenith angle (or co-altitude), the

distance of the observer from the Sun can be simply obtained. Indeed, let us consider an observer O located at an angle ζ from the Sun's geographical position GP. As shown in figure 3.12, by considering that the Sun rays reaching the Earth are parallel, the Sun's zenith angle, as seen by the observer, will be equal to ζ. The sextant will provide the altitude θ of the Sun, related to the zenith angle by $\theta = \frac{\pi}{2} - \zeta$.

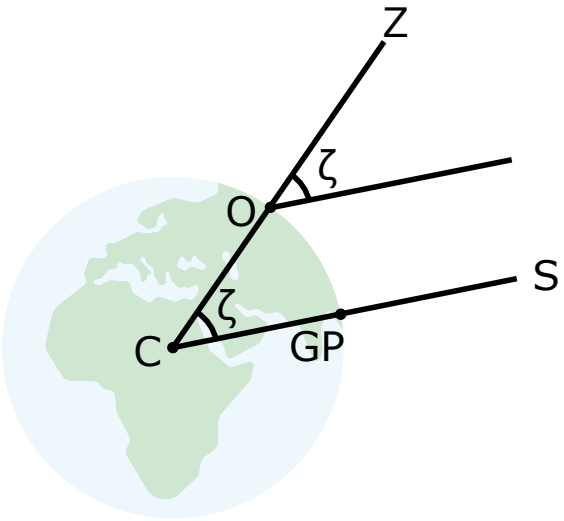

FIGURE 3.12. – Sun zenith angle for an observer O located at an angle ζ from the Sun's geographical position GP. S is the Sun, and C is the center of the Earth. We consider the Sun rays parallel.

From this property, if the geographic position of the Sun is known and the altitude of the Sun has been measured, we can conclude that the observer is located on a circle centered on the Sun's geographic position and of radius given by the co-altitude. This circle is known as the circle of position (cf. figure 3.13).

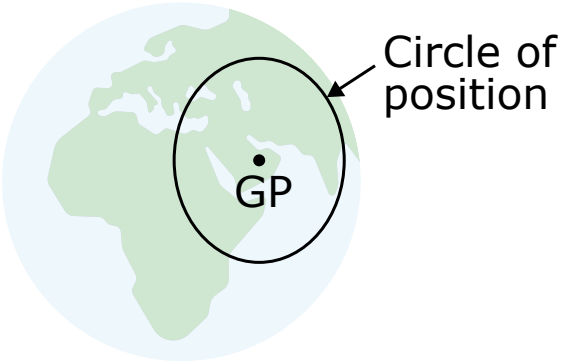

FIGURE 3.13. – Circle of position centered on the geographic position GP of the Sun.

To obtain our position on Earth different methods can be applied (cf. figure 3.14). If the observer's bearing is known with respect to the geographic north, for instance from a magnetic compass corrected from the magnetic declination, the Sun's azimuth

with respect to the observer allows the observer to find his position on the circle of position. If the bearing is not known, by observing simultaneously two celestial bodies, or the Sun at two distinct moments, two circles of position can be drawn. The observer will therefore be located at one of the two intersections of the circles of position. The observer's position can be given as the closest intersection from an estimated position, known as deduced reckoning position, which is generally based on inertial navigation.

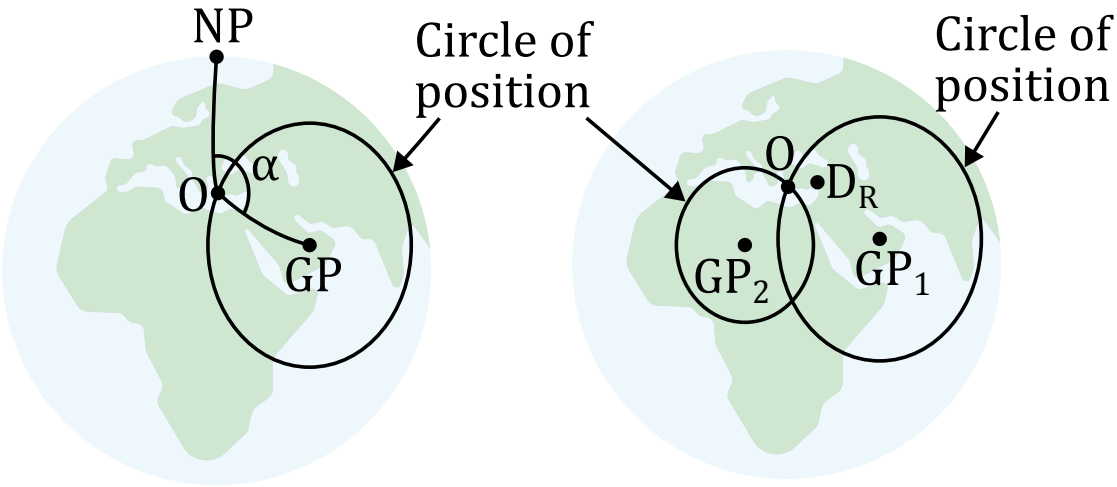

FIGURE 3.14. – Geopositioning methods using a sextant. Left: The observer's position O is obtained from the altitude of a celestial object of geographic position GP, and the azimuth α of the celestial object with respect to true north (NP is the north pole). Right: The observer's position is obtained from the intersection of two circles of position centered on GP_1 and GP_2, the geographic positions of two celestial objects or of one celestial object at two moments. The observer's position is the intersection closest to the deduced reckoning position D_R

In those methods, to obtain the geographic position of the Sun from ephemeris, the knowledge of the Greenwich mean time (GMT) is required. When observing the Sun, the measured hour angle gives the apparent solar time. However, as the Earth rotation speed varies during a year, a day is not always 24 hours long. To compensate for those variations, the equation of time was introduced (cf. figure 3.15), allowing the computation of a mean solar time from the apparent solar time. Considering the mean solar time, each day has the same duration. The GMT corresponds to the mean solar time at the Greenwich meridian. A precise knowledge of time is crucial when using a sextant for navigation. Indeed, as pointed in [206], since the Sun travels approximately 1° each 4 minutes, a 4 minutes error can produce a localization error up to 1 degree, which corresponds approximately to a localization error of 111 kilometers at the equator.

Going back to skylight polarization, the presented methods were implemented by replacing the sextant by polarimetric sensors, providing the Sun's position in the sky. The method consisting in measuring the Sun's position at one moment, and adding a

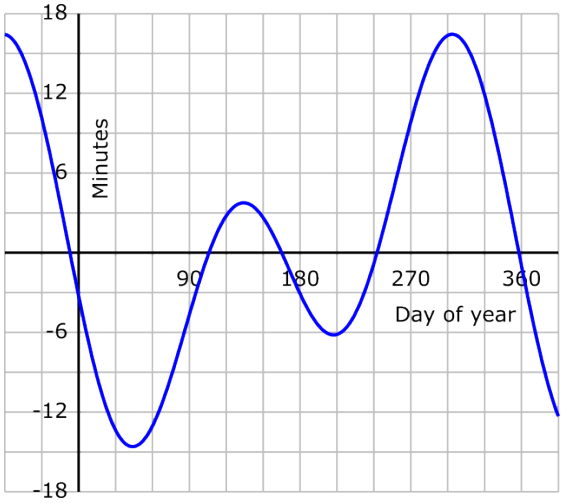

FIGURE 3.15. – Equation of time, showing the variations of a daylength during a year. Credit: Equation of time.png: User:Drini derivative work: Zazou, CC BY-SA 2.5, via Wikimedia Commons

bearing information with a magnetic compass was implemented in several studies [123, 136], and for underwater geolocation [142, 207, 208]. The skylight polarization can be observed underwater into a cone known as Snell's window [142]. The second method, consisting in estimating the position of a celestial body at two moments, was processed during day [209, 210, 207] and night [211]. During night, the skylight polarization is due to scattering of the moonlight in the atmosphere.
Alternatively, the bearing of an observer can be obtained from the known observer's position, and by measuring the azimuth of a celestial body. In fact, by considering the observer's position, the geographic position of the celestial object, and the north pole, we can draw a spherical triangle (cf. figure 3.16). From this spherical triangle, the azimuth α of the Sun with respect to the true north, which is the direction of the North Pole, at the observer's position can be calculated by the spherical law of cosines [10], such as:

$$\begin{aligned} \sin\theta &= \cos\omega\cos\phi\cos\delta + \sin\phi\sin\delta \\ \cos\alpha &= \frac{\sin\delta - \sin\phi\sin\theta}{\cos\phi\cos\theta} \end{aligned} \tag{3.4}$$

Where θ is the Sun's altitude, linked to the zenith angle ζ by $\theta = 90° - \zeta$. ω is the Sun's hour angle, δ the solar declination, and ϕ the observer's latitude. Finally, by combining the measured azimuth with respect to the observer's bearing and the calculated azimuth with respect to true north, we can deduce the bearing of the observer with respect to the true north.

This method was implemented using the skylight polarization to measure the Sun's azimuth in [119, 212].
Additionaly to the previous methods, some studies merge information from the sky-

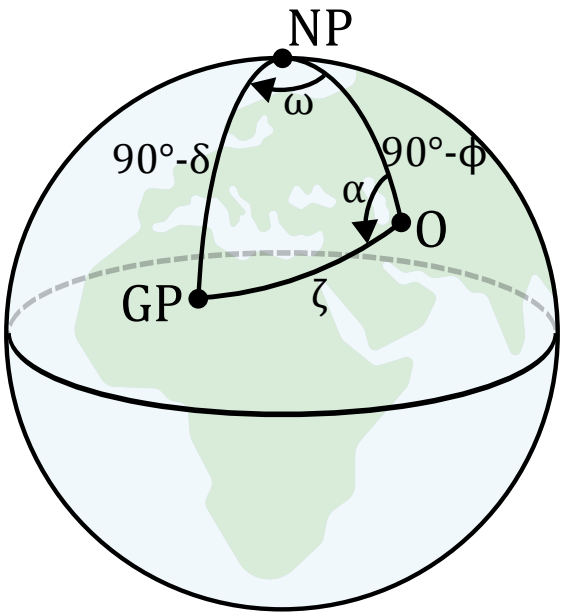

FIGURE 3.16. – Navigational triangle. O is the observer's position, GP is the geographic position of the celestial body, NP is the north pole. ζ, α, ω and δ are the Sun's zenith angle, azimuth, hour angle and declination respectively. ϕ is the observer's latitude. $90° - \delta$, $90° - \delta$, and ζ are the arc lengths of the navigational triangle.

light polarization with various sensors, such as inertial navigation sensors, or global navigation satellite systems in order to maintain robust and accurate geolocation [124, 213]

In this section, we presented the state of the art geolocation methods using skylight polarization. The main issues of these methods are the requirement of precise time information and the knowledge of the solar ephemeris. True navigators animals manage to find their position on Earth without relying on ephemeris. In the next section, we present a geolocation method inspired by migratory birds, that does not require solar ephemeris.

3.2. Migratory birds inspired navigation

As discussed earlier, true navigation is little understood in the animal world. To navigate, some migrating animals are thought to rely on a compass and a map. The understanding of the mental map of homing pigeons, one of the most studied migrating vertebrates, and of other long-distance migrants, is considered "the most challenging mystery" of animal navigation [12]. Henrik Mouritsen, a specialist in birds' magnetoreception, declared, regarding homing pigeons, that no matter what you publish, half the world will oppose you (cf. Sciences et Avenir), highlighting the intense

debates on this subject. On the other hand, although it still contains some mysteries, the mechanisms of birds' compass is becoming increasingly understood. In 1953, Gustav Kramer discovered that birds could use the Sun to navigate [214]. Following this discovery, Matthews suggested that pigeons may use the Sun to obtain true north, their latitude and longitude, based on the Sun's trajectory [215]. He supposed that birds manage to extrapolate the trajectory of the Sun based on a solar observation over a small time interval, in order to find the position at which the Sun is the highest. Finding this point would immediately provide true south. Moreover, he suggested that by comparing the highest elevation of the Sun at different positions on Earth, birds would be able to estimate their displacement in latitude. His hypothesis was however rejected by Pennycuick in 1960, who still did not discard the use of the Sun for bird navigation [216]. In the 1950s, birds were also proven to use the stars for orienting themselves during night [217]. In 1966, the use of the magnetic field by birds was discovered by Wiltschko and Merkel [218], leading to new assumptions on migratory bird's map and compass. It was only in 1982 that Able showed that the skylight polarization was used for navigation by homing pigeons [219]. In addition, studies highlighted connections between those different navigation cues, with a hierarchical relation between them, that may vary among species, and during the birds' life [220, 221]. Indeed, some migratory birds were shown to calibrate their magnetic compass during night [222, 223, 224] and day [225, 226, 227, 228], by using their stellar and polarization compass. Inversely, the magnetic field was shown to influence the stellar compass [229, 230] and the polarization compass of migratory birds [231]. In [232], Savannah Sparrows were also suggested to calibrate their stellar compass at sunset using the skylight polarization. Most mechanisms explaining those connections are however misunderstood. An interesting explanation has yet been proposed for the star compass. Savannah Sparrows [222], Garden Warblers [223], or Indigo Buntings [224] were shown to use the celestial rotation of stars in order to find true north. The celestial rotation refers to the apparent rotation of the sky for an observer located on the Earth's surface, due to the rotation of the Earth. When observing the celestial rotation during night, all the stars seem to rotate around a point (cf. figure 3.17). This point is the celestial pole.

An observer located on the Earth's north hemisphere will be able to see the north celestial pole, its azimuth providing true north. Inversely, the south celestial pole will be visible by an observer located on the south hemisphere, giving true south. The NCP has been widely used for human navigation, through the Polaris star, to locate true north. In fact, the Polaris star is located near the NCP. However, there is no equivalent star in the southern hemisphere, and the Polaris star's position with respect to the NCP varies in time due to the Earth's precession, nutation and polar motion, which are very slow Earth motions compared to the Earth rotation around its axis and around the Sun. Therefore, the Polaris star has not always been a convenient star to obtain the position of the NCP. Another interesting property of the celestial pole is that, by assuming that the Earth is spherical, the altitude of the NCP is equal to the latitude of the observer (cf . figure 3.18). Indeed, let us consider an observer located at a latitude ϕ. Since the Earth's radius is negligible in front of the celestial sphere's radius, we can



FIGURE 3.17. – Circumpolar startrails over the Atacama. Credit: ESO/B. Tafreshi (twanight.org).

consider that both lines going from the observer and from the north pole to the NCP are parallel. Therefore, we can see on the figure 3.18 that the NCP's zenith angle ζ as viewed from the observer is the same as the observer co-latitude. We therefore have $\zeta = \frac{\pi}{2} - \phi$.

Even though the celestial rotation could provide the latitude for migratory birds, it has not been proven yet if the elevation of the celestial pole was used for this purpose [233].

The use of the skylight polarization as a compass is less understood than the star compass. Savannah Sparrows were shown to use skylight polarization during sunrise and sunset to calibrate their magnetic compass [226], and by observing a sky region near the horizon [227]. The skylight polarization was even proven necessary to calibrate a magnetic compass during day, the Sun alone being insufficient [228]. However, the mechanisms of calibration using the skylight polarization is misunderstood. Interestingly, Brines, studying bees navigation, suggested that the celestial rotation of the skylight polarization could allow for obtaining the position of the celestial pole [234, 125]. Even though explanations about the variations of the skylight polarization around the celestial pole were given, no clear way of finding the celestial pole was yielded. No other study suggested a way of using skylight polarization to locate the celestial pole.

From the reviewed studies on bird migration and the preliminary description of the celestial rotation of skylight polarization by Brines, a method to find the celestial pole based on skylight polarization was developed in this thesis [235, 236]. Following this study, we show how skylight polarization can be used to obtain the solar declination, and time. In the following sections, we describe the relation between the skylight polarization, the NCP and the solar declination. Subsequently, algorithms are presented to locate the NCP.

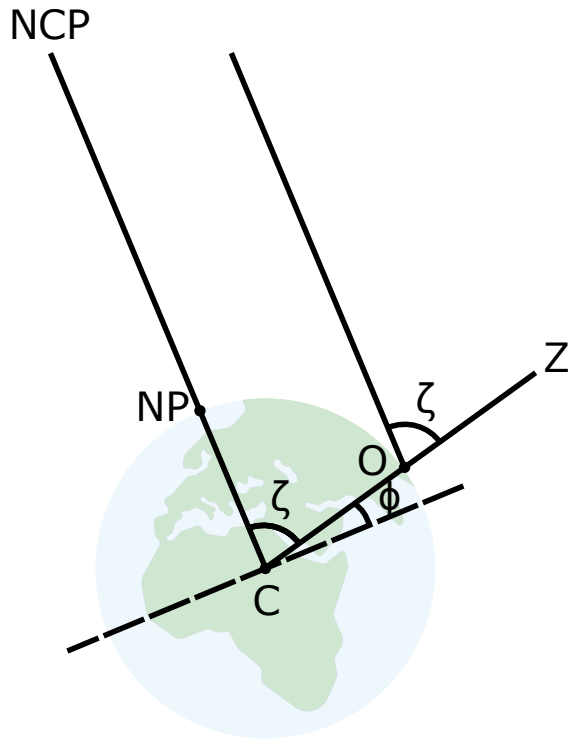

FIGURE 3.18. – Zenith angle ζ of the NCP, as seen by an observer O, at a latitude ϕ. C is the center of the Earth, NP the north pole, and Z the observer's Zenith.

3.2.1. Skypole: locating the celestial pole from temporal variations of the skylight polarization pattern

During day, as the Earth rotates around itself, the apparent Sun, seen by an observer on the Earth surface, moves in a circular trajectory around the celestial pole (cf. figure 3.19).

Interestingly, due to symmetries of the skylight's DoLP pattern, when comparing the DoLP at two moments of a day, the DoLP remains unchanged on two circles, named radial and plane invariances. By noticing that the celestial pole is located on one of those circles, and is the only point in the sky having a constant DoLP during a whole day, we can deduce its position by observing the variations of DoLP over time, and more specifically of the DoLP invariances.

In this section, we detail those invariances of the skylight's DoLP pattern. We focus here on the NCP for simplicity, by considering an observer located on the north hemisphere, but the calculus are similar for the SCP. We first express the trajectory of the Sun in the ENU frame, centered on the observer, as a function of equatorial coordinates. Next, we give the condition for a point in the sky to have an invariant DoLP between two times, and express this condition in terms of the Sun's coordinates. We deduce, from this condition, that the NCP has a constant DoLP during a day, assuming that the solar declination is constant, and we provide the sets of points having a constant DoLP between two times. We finally show that the NCP is the only point in the sky having a

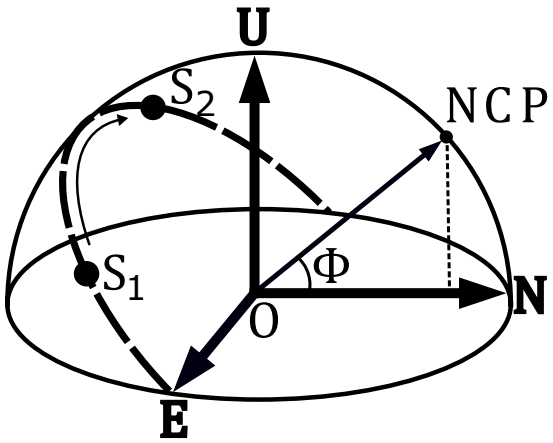

FIGURE 3.19. – The trajectory of the sun in the ENU frame, centered on an observer O located at latitude ϕ. NCP is the north celestial pole. The Sun moves on a plane perpendicular to the observer-NCP vector.

constant DoLP during a whole day.

3.2.1.1. Sun trajectory

The Sun turns in the sky around the celestial pole due to the Earth rotation. This trajectory is, however, not exactly circular since the Earth also spins around the Sun, leading to variations in the solar declination. By considering that the Earth rotation is much faster around itself than around the Sun, we can neglect the variations of solar declination during a one day observation. Similarly, we neglect the movements of nutation and precession of the Earth.
If we consider the origin O of the ENU frame, and a point P on the celestial sphere, the vector going from O to P is noted $\vec{P}$ in the following sections. We consider $\vec{P}$ as a unit vector.
The Sun vector $\vec{S}$ with respect to the latitude ϕ of the observer, the declination δ and the hour angle ω in the ENU frame (the Up direction is noted $\vec{Z}$ for zenith) is defined as follows (cf. [237], and figure 3.6):

$$\vec{S} = -\cos\delta\sin\omega\,\vec{E} + (\sin\delta\cos\phi - \cos\delta\sin\phi\cos\omega)\,\vec{N} + (\cos\delta\cos\phi\cos\omega + \sin\delta\sin\phi)\,\vec{Z} \tag{3.5}$$

Where $\phi \in [-\frac{\pi}{2}, \frac{\pi}{2}]$ in radians, $\delta \in [-0.41, 0.41]$ in radians, and $\omega = (hour - 12)15°$, with $hour$ the local apparent solar time (0-24h), such as in radians, $\omega \in [-\pi, \pi]$. For the sake of simplicity, we will suppose $\phi \in]-\frac{\pi}{2}, \frac{\pi}{2}[$

3.2.1.2. DoLP variations at the celestial pole

Interestingly, due to the Sun's motion, the scattering angle at the celestial pole remains constant, leading to a constant value of DoLP at the celestial pole.

3.2.1.2.1. DoLP invariance condition

To demonstrate this assumption, let us consider a point P, whose scattering angle is given by the time dependant function γ_P. From Rayleigh single scattering model (cf. equation 1.78), the DoLP P_l at the point P is invariant between two times t_1 and t_2 if and only if :

$$\begin{aligned} P_l(\gamma_P(t_1)) = P_l(\gamma_P(t_2)) &\iff \frac{1-\cos^2\left(\gamma_P(t_1)\right)}{1+\cos^2\left(\gamma_P(t_1)\right)} = \frac{1-\cos^2\left(\gamma_P(t_2)\right)}{1+\cos^2\left(\gamma_P(t_2)\right)} \\ &\iff \cos^2\left(\gamma_P(t_1)\right) = \cos^2\left(\gamma_P(t_2)\right) \\ &\iff \cos\left(\gamma_P(t_1)\right) = \pm\cos\left(\gamma_P(t_2)\right) \\ &\iff \overrightarrow{S_1}\cdot\overrightarrow{P} = \pm\overrightarrow{S_2}\cdot\overrightarrow{P} \end{aligned} \tag{3.6}$$

Where S_1 and S_2 denote the Sun at time t_1 and t_2 respectively, and $\cdot$ is the scalar product.

Moreover, if we consider a given point on the celestial sphere $\overrightarrow{P}(x_p, y_p, z_p)$, at a given time t, we have from equation 3.5:

$$\begin{aligned} \overrightarrow{S}\cdot\overrightarrow{P} = &- x_p\cos\delta\sin\omega + y_p(\sin\delta\cos\phi - \cos\delta\sin\phi\cos\omega) \\ &+ z_p(\cos\delta\cos\phi\cos\omega + \sin\delta\sin\phi) \end{aligned} \tag{3.7}$$

3.2.1.2.2. DoLP invariance at the celestial pole

Having determined the condition for the DoLP to be invariant, we will now show that the DoLP is time invariant at the NCP.

At the NCP, we have $x_p = 0$ (North bearing in ENU frame), $y_p = \cos\phi$ and $z_p = \sin\phi$ (altitude of NCP is equal to the latitude ϕ of the observer). Thus, equation 3.7 becomes:

$$\begin{aligned} \overrightarrow{S}\cdot\overrightarrow{P_{NCP}} &= \cos\phi(\sin\delta\cos\phi - \cos\delta\sin\phi\cos\omega) + \sin\phi(\cos\delta\cos\phi\cos\omega + \sin\delta\sin\phi) \\ &= \cos^2\phi\sin\delta + \sin^2\phi\sin\delta = \sin\delta \end{aligned} \tag{3.8}$$

We notice here that the DoLP is only dependant on the Sun's declination. However, we assumed earlier that the rotation of the Earth around the Sun was negligible, meaning that the solar declination is constant. Therefore, we can reasonably assume that the DoLP is constant at the NCP during a one day observation.

3.2.1.3. DoLP invariances in the celestial dome

More generally, due to the plane and radial symmetries of the skylight's DoLP (cf figure 3.20), when comparing the DoLP at two moments in a day, we can observe two circles for which the value of DoLP is invariant. Those circles can be obtained easily by computing the absolute difference between the DoLP at both times. We refer to those

invariances as plane and radial invariances, linked to the plane and radial symmetries of the DoLP respectively. The radial symmetry of the DoLP is due to the dependence of the DoLP on the scattering angle only, meaning that all points on a same small circle centered on the Sun will have equal DoLP. The plane symmetry is due to the relation $P_l(\gamma) = P_l(\pi - \gamma)$ where P_l is the DoLP and γ is the scattering angle.

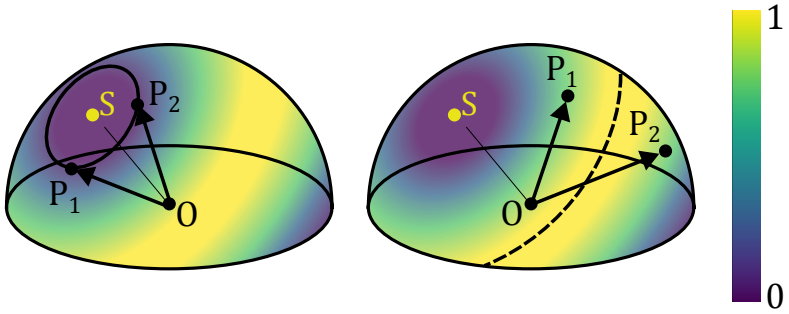

FIGURE 3.20. – Symmetries of skylight DoLP pattern. Left: radial symmetry about the solar vector $\overrightarrow{S}$. The DoLP is the same for all points of the small circle containing P_1 and P_2. Right: plane symmetry about the plane perpendicular to the solar vector, including the observer O. P_1 is symmetric to P_2 with respect to the plane perpendicular to the solar vector (dotted line), and therefore have the same DoLP.

Those invariances can be obtained mathematically by seeking for all the points with DoLP invariant between two successive instants t_1 and t_2. To find all the solutions, we should solve, from equation 3.6, the equations $\overrightarrow{S_1} \cdot \overrightarrow{P} = \overrightarrow{S_2} \cdot \overrightarrow{P}$ and $\overrightarrow{S_1} \cdot \overrightarrow{P} = -\overrightarrow{S_2} \cdot \overrightarrow{P}$.

3.2.1.3.1. First Set, radial invariance

Let us consider the first equation $\overrightarrow{S_1} \cdot \overrightarrow{P} = \overrightarrow{S_2} \cdot \overrightarrow{P}$
From equation 3.7, we have:

$$\begin{aligned}\overrightarrow{S_1} \cdot \overrightarrow{P} - \overrightarrow{S_2} \cdot \overrightarrow{P} =& -x_p \cos\delta\,[\sin\omega_1 - \sin\omega_2] - y_p \cos\delta \sin\phi\,[\cos\omega_1 - \cos\omega_2] \\ &+ z_p \cos\delta \cos\phi\,[\cos\omega_1 - \cos\omega_2] \\ =& \cos\delta\left(-x_p\,[\sin\omega_1 - \sin\omega_2] + \left(-y_p \sin\phi + z_p \cos\phi\right)[\cos\omega_1 - \cos\omega_2]\right) \\ =& 0\end{aligned} \tag{3.9}$$

Where ω_1 and ω_2 are the hour angles related to S_1 and S_2 respectively.

Moreover, the point P can be expressed in hemispherical coordinates by two coordinates only, the azimuth α and the altitude θ (α is null for a point in the north direction and positive when turning from North to East, and θ is null for a point on the horizon and 90° at the zenith), which reduces the equation to two independent unknowns. We therefore consider $\overrightarrow{P}(\cos\theta\sin\alpha, \cos\theta\cos\alpha, \sin\theta)$. Equation 3.9 then becomes:

$$\begin{aligned}\overrightarrow{S_1}\cdot\overrightarrow{P}-\overrightarrow{S_2}\cdot\overrightarrow{P} &= \cos\delta(-\cos\theta\sin\alpha\,[\sin\omega_1-\sin\omega_2]\\ &\quad+\left(-\cos\theta\cos\alpha\sin\phi+\sin\theta\cos\phi\right)[\cos\omega_1-\cos\omega_2])=0\\ \iff \tan\theta &= \frac{\cos\alpha\sin\phi\tan\left(\frac{\omega_1+\omega_2}{2}\right)-\sin\alpha}{\cos\phi\tan\left(\frac{\omega_1+\omega_2}{2}\right)}\end{aligned} \tag{3.10}$$

Therefore, the set of solutions (α,θ) of the equation $\overrightarrow{S_1}\cdot\overrightarrow{P}=\overrightarrow{S_2}\cdot\overrightarrow{P}$ is:

$$\boldsymbol{Set_1}=\left\{\left(\alpha,\tan^{-1}\left[\frac{\cos\alpha\sin\phi\tan\left(\frac{\omega_1+\omega_2}{2}\right)-\sin\alpha}{\cos\phi\tan\left(\frac{\omega_1+\omega_2}{2}\right)}\right]\right),\alpha\in[-\pi,\pi[\right\} \tag{3.11}$$

This set fully describes the radial invariance.
We can shown that the NCP is located on the radial invariance. Indeed, for the NCP, $\alpha=0$, and $\theta=\phi$, which verifies the condition given in equation 3.11.

3.2.1.3.2. Second Set, plane invariance

Let us now consider the second equation $\overrightarrow{S_1}\cdot\overrightarrow{P}=-\overrightarrow{S_2}\cdot\overrightarrow{P}$
We have from equation 3.7:

$$\begin{aligned}\overrightarrow{S_1}\cdot\overrightarrow{P}+\overrightarrow{S_2}\cdot\overrightarrow{P} &= -x_p\cos\delta\,[\sin\omega_1+\sin\omega_2]+y_p(2\sin\delta\cos\phi-\cos\delta\sin\phi\,[\cos\omega_1+\cos\omega_2])\\ &\quad+z_p(\cos\delta\cos\phi\,[\cos\omega_1+\cos\omega_2]+2\sin\delta\sin\phi)=0\end{aligned} \tag{3.12}$$

As before, we replace the cartesian coordinates of the point by hemispherical coordinates. We thus obtain:

$$\begin{aligned}\overrightarrow{S_1}\cdot\overrightarrow{P}+\overrightarrow{S_2}\cdot\overrightarrow{P} &= -\cos\theta\sin\alpha\cos\delta\,[\sin\omega_1+\sin\omega_2]\\ &\quad+\cos\theta\cos\alpha(2\sin\delta\cos\phi-\cos\delta\sin\phi\,[\cos\omega_1+\cos\omega_2])\\ &\quad+\sin\theta(\cos\delta\cos\phi\,[\cos\omega_1+\cos\omega_2]+2\sin\delta\sin\phi)=0\\ \iff \tan\theta &= \frac{\sin\alpha\cos\delta\,[\sin\omega_1+\sin\omega_2]}{\cos\delta\cos\phi\,[\cos\omega_1+\cos\omega_2]+2\sin\delta\sin\phi}\\ &\quad+\frac{\cos\alpha\left(-2\sin\delta\cos\phi+\cos\delta\sin\phi\,[\cos\omega_1+\cos\omega_2]\right)}{\cos\delta\cos\phi\,[\cos\omega_1+\cos\omega_2]+2\sin\delta\sin\phi}\end{aligned} \tag{3.13}$$

Finally, the set of solutions (α,θ) of the equation $\overrightarrow{S_1}\cdot\overrightarrow{P}=-\overrightarrow{S_2}\cdot\overrightarrow{P}$ is:

$$\begin{aligned}\boldsymbol{Set_2}=\Bigg\{\Bigg(\alpha,\tan^{-1}\Bigg[&\frac{\sin\alpha\cos\delta\,[\sin\omega_1+\sin\omega_2]}{\cos\delta\cos\phi\,[\cos\omega_1+\cos\omega_2]+2\sin\delta\sin\phi}\\ &+\frac{\cos\alpha\left(-2\sin\delta\cos\phi+\cos\delta\sin\phi\,[\cos\omega_1+\cos\omega_2]\right)}{\cos\delta\cos\phi\,[\cos\omega_1+\cos\omega_2]+2\sin\delta\sin\phi}\Bigg]\Bigg),\alpha\in[-\pi,\pi]\Bigg\}\end{aligned} \tag{3.14}$$

This set fully describes the plane invariance.
Remark : for an observer located on Earth, the only visible solutions are those with $\theta \geq 0$ (without considering Earth curvature effects).
A visual explanation of the plane and radial invariances is given in figure 3.21.
The invariance pattern is displayed in figure 3.22.

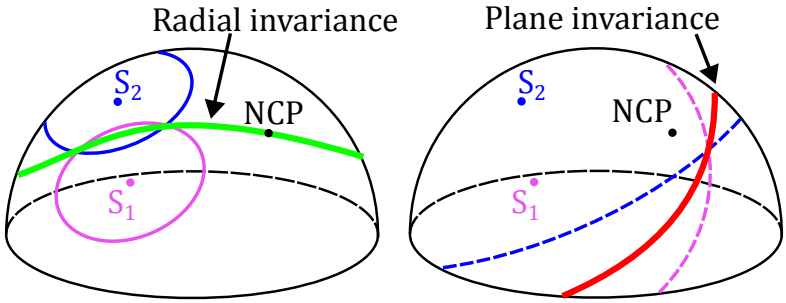

FIGURE 3.21. – Invariance circles on the celestial sphere, corresponding to points with equal DoLP at time t_1 and t_2. Left: The green circular arc is the radial invariance, linked to the radial symmetry of the DoLP pattern (cf. Eq. 3.11). S_1 and S_2 are the Sun at time t_1 and t_2 respectively. The two colored circles centered on S_1 and S_2 correspond to circles with the same constant scattering angle with respect to S_1 and S_2, respectively. Right: The red circular arc is the plane invariance linked to the plane symmetry of the DoLP pattern (cf. Eq. 3.14). S_1 and S_2 are the Sun at time t_1 and t_2, respectively. The two colored dotted circular arcs define a circle centered on S_1 and S_2 and correspond to the maximum value of polarization in the sky. They are at the intersection between the celestial sphere and the plane of symmetry of the DoLP patterns for S_1 and S_2, respectively (cf. figure 3.20).

3.2.1.4. Variations of the DoLP invariances during a whole day

Now, we show that the NCP is the only point in the sky having a constant DoLP during a whole day. We proceed in two times, first by proving that the NCP is the only point included in the radial invariance at any time, and then, by showing that, in general, there is no point located on the plane invariance anytime during a whole day.

3.2.1.4.1. The NCP is the only point included in the radial invariance set at any time

This section aims at showing that if a point is on the radial invariance for different times, then this point is necessarily the NCP.
Let $(\omega_1, \omega_2) \in [-\pi, \pi[^2$, and $\boldsymbol{Set}_{\mathbf{1}(\omega_1,\omega_2)}$ the set of $(\alpha, \theta) \in [-\pi, \pi[^2$ solution of:

$$\overrightarrow{S_{\omega_1}} \cdot \overrightarrow{P(\alpha,\theta)} = \overrightarrow{S_{\omega_2}} \cdot \overrightarrow{P(\alpha,\theta)} \tag{3.15}$$

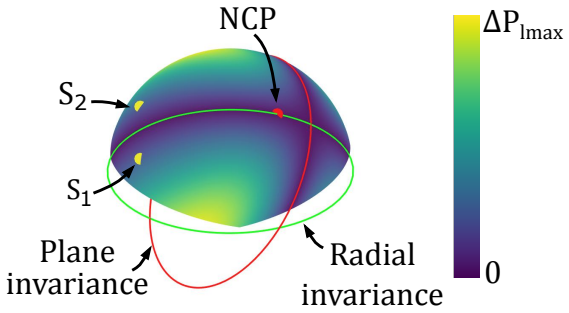

FIGURE 3.22. – Invariance circles on the celestial sphere. Comparison between simulated and analytical sets of solutions. The green circle is the radial invariance circle, the red circle is the plane invariance circle computed from analytical calculations (cf. Eq. 3.11 and Eq. 3.14). The colored half sphere is the simulated absolute difference between two DoLP patterns associated with the Sun's positions S_1 and S_2 at two different times. The red dot is the NCP, and ΔP_{lmax} is the maximum value of the absolute difference of DoLP.

Where $\overrightarrow{S_{\omega_1}}$ and $\overrightarrow{S_{\omega_2}}$ are the sun vectors at time ω_1 and ω_2 respectively.
Let us show the assertion :

$$\forall(\omega_1,\omega_2)\in[-\pi,\pi[^2,(\alpha,\theta)\in \boldsymbol{Set_1}_{(\omega_1,\omega_2)} \iff (\alpha,\theta)=(0,\phi) \tag{3.16}$$

Demonstration: We already know that $(0,\phi)$ is always in $\boldsymbol{Set_1}_{(\omega_1,\omega_2)}$ (cf. section 3.2.1.3.1). Let us show that this solution is unique. Let $(\omega_1,\omega_2,\omega_3)\in[-\pi,\pi[^3$, and $(\alpha,\theta)\in \boldsymbol{Set_1}_{(\omega_1,\omega_2)}\cap \boldsymbol{Set_1}_{(\omega_1,\omega_3)}$.

Since $(\alpha,\theta)\in \boldsymbol{Set_1}_{(\omega_1,\omega_2)}$, we have:

$$\tan\theta=\frac{\cos\alpha\sin\phi\tan\left(\frac{\omega_1+\omega_2}{2}\right)-\sin\alpha}{\cos\phi\tan\left(\frac{\omega_1+\omega_2}{2}\right)} \tag{3.17}$$

We also have $(\alpha,\theta)\in \boldsymbol{Set_1}_{(\omega_1,\omega_3)}$, so :

$$\tan\theta=\frac{\cos\alpha\sin\phi\tan\left(\frac{\omega_1+\omega_3}{2}\right)-\sin\alpha}{\cos\phi\tan\left(\frac{\omega_1+\omega_3}{2}\right)} \tag{3.18}$$

Without loss of generality, we set $t_1=\frac{\omega_1+\omega_2}{2}$ and $t_2=\frac{\omega_1+\omega_3}{2}$. Then, from equation 3.17 and 3.18, and since $\theta\in[-\pi,\pi[$, we have

$$\frac{\cos\alpha\sin\phi\tan t_1-\sin\alpha}{\cos\phi\tan t_1}=\frac{\cos\alpha\sin\phi\tan t_2-\sin\alpha}{\cos\phi\tan t_2} \tag{3.19}$$

By assuming $t_1, t_2 \neq 0$ and $\phi \neq \pm\frac{\pi}{2}$, we have from equation 3.19:

$$\sin\alpha\cos\phi\tan t_2 = \sin\alpha\cos\phi\tan t_1 \tag{3.20}$$

Therefore, since $\phi \neq \pm\frac{\pi}{2}$ and assuming $t_1 \neq t_2$, we must have $\sin\alpha = 0$. Thus $\alpha \in \{0, -\pi\}$. If $\alpha = 0$, then $\theta = \phi$, and if $\alpha = -\pi$, then $\theta = -\phi$. Yet, for an observer located on the Earth surface only positive altitudes are considered, so $(\alpha,\theta) = (0,\phi)$ (observer on North hemisphere), which is by definition the NCP position.

3.2.1.4.2. There is no point included in the plane invariance set at any time

In this section, we will show that there is no point such as the NCP in the plane invariance set.
Let us consider $(\omega_1,\omega_2) \in [-\pi,\pi[^2$, and $\boldsymbol{Set_2}_{(\omega_1,\omega_2)}$ the set of $(\alpha,\theta) \in [-\pi,\pi[^2$ solution of:

$$\overrightarrow{S_{\omega_1}} \cdot \overrightarrow{P(\alpha,\theta)} = -\overrightarrow{S_{\omega_2}} \cdot \overrightarrow{P(\alpha,\theta)} \tag{3.21}$$

Let us show the assertion :

$$\begin{aligned}\exists(\phi,\delta) \in [-\frac{\pi}{2},\frac{\pi}{2}] \times [-0.41, 0.41], \forall(\alpha,\theta) \in [-\pi,\pi[^2, \exists(\omega_1,\omega_2) \in [-\pi,\pi[^2,\\ (\alpha,\theta) \notin \boldsymbol{Set_2}_{(\omega_1,\omega_2)}\end{aligned} \tag{3.22}$$

Demonstration: We know from equation 3.14 that for a given $(\omega_1,\omega_2,\omega_3) \in [-\pi,\pi[^3$,

$$\begin{aligned}(\alpha,\theta) \in \boldsymbol{Set_2}_{(\omega_1,\omega_2)} \iff \tan\theta = &\frac{\sin\alpha\cos\delta\,[\sin\omega_1 + \sin\omega_2]}{\cos\delta\cos\phi\,[\cos\omega_1 + \cos\omega_2] + 2\sin\delta\sin\phi}\\ &+\frac{\cos\alpha\left(-2\sin\delta\cos\phi + \cos\delta\sin\phi\,[\cos\omega_1 + \cos\omega_2]\right)}{\cos\delta\cos\phi\,[\cos\omega_1 + \cos\omega_2] + 2\sin\delta\sin\phi}\end{aligned} \tag{3.23}$$

and

$$\begin{aligned}(\alpha,\theta) \in \boldsymbol{Set_2}_{(\omega_1,\omega_3)} \iff \tan\theta = &\frac{\sin\alpha\cos\delta\,[\sin\omega_1 + \sin\omega_3]}{\cos\delta\cos\phi\,[\cos\omega_1 + \cos\omega_3] + 2\sin\delta\sin\phi}\\ &+\frac{\cos\alpha\left(-2\sin\delta\cos\phi + \cos\delta\sin\phi\,[\cos\omega_1 + \cos\omega_3]\right)}{\cos\delta\cos\phi\,[\cos\omega_1 + \cos\omega_3] + 2\sin\delta\sin\phi}\end{aligned} \tag{3.24}$$

Therefore, from equation 3.23 and 3.24, and since $\theta \in [-\pi,\pi[$,

$$
\begin{aligned}
&(\alpha,\theta) \in \boldsymbol{Set_2}_{(\omega_1,\omega_2)} \cap \boldsymbol{Set_2}_{(\omega_1,\omega_3)} \\
\iff &\frac{\sin\alpha\cos\delta\,[\sin\omega_1+\sin\omega_2]+\cos\alpha\left(-2\sin\delta\cos\phi+\cos\delta\sin\phi\,[\cos\omega_1+\cos\omega_2]\right)}{\cos\delta\cos\phi\,[\cos\omega_1+\cos\omega_2]+2\sin\delta\sin\phi} \\
&-\frac{\sin\alpha\cos\delta\,[\sin\omega_1+\sin\omega_3]+\cos\alpha\left(-2\sin\delta\cos\phi+\cos\delta\sin\phi\,[\cos\omega_1+\cos\omega_3]\right)}{\cos\delta\cos\phi\,[\cos\omega_1+\cos\omega_3]+2\sin\delta\sin\phi} \\
&=0
\end{aligned}
\tag{3.25}
$$

Let us consider $f:[-\pi,\pi[\to\mathbb{R}$ such that

$$
\begin{aligned}
f(\alpha) = &\frac{\sin\alpha\cos\delta\,[\sin\omega_1+\sin\omega_2]+\cos\alpha\left(-2\sin\delta\cos\phi+\cos\delta\sin\phi\,[\cos\omega_1+\cos\omega_2]\right)}{\cos\delta\cos\phi\,[\cos\omega_1+\cos\omega_2]+2\sin\delta\sin\phi} \\
&-\frac{\sin\alpha\cos\delta\,[\sin\omega_1+\sin\omega_3]+\cos\alpha\left(-2\sin\delta\cos\phi+\cos\delta\sin\phi\,[\cos\omega_1+\cos\omega_3]\right)}{\cos\delta\cos\phi\,[\cos\omega_1+\cos\omega_3]+2\sin\delta\sin\phi}
\end{aligned}
\tag{3.26}
$$

Let us consider some fixed parameters, for example $\delta=0.2$, $\phi=\frac{\pi}{4}$, $\omega_1=0$, $\omega_2=\frac{\pi}{5}$. By plotting this function for $\alpha\in[-\pi,\pi[$, and $\omega_3\in\left\{\frac{2\pi}{5};\frac{3\pi}{5}\right\}$, we see in figure 3.23 that when $\omega_3=\frac{2\pi}{5}$, α solutions of $f(\alpha)=0$ are not solution of $f(\alpha)=0$ when $\omega_3=\frac{3\pi}{5}$. Therefore there is no $(\alpha,\theta)\in[-\pi,\pi[^2$ such that $(\alpha,\theta)\in\boldsymbol{Set_2}_{(0,\frac{\pi}{5})}\cap\boldsymbol{Set_2}_{(0,\frac{2\pi}{5})}\cap\boldsymbol{Set_2}_{(0,\frac{3\pi}{5})}$.

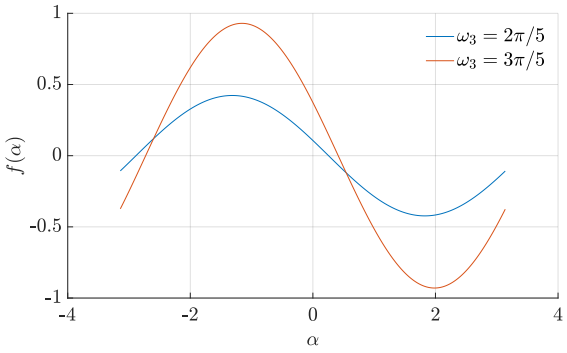

FIGURE 3.23. – Plot of equation 3.26 for $\omega_3=\frac{2\pi}{5}$ and $\omega_3=\frac{3\pi}{5}$

3.2.2. Polendar: Measuring the solar declination from skylight polarization patterns

In the previous section, we presented the time invariances of the skylight DoLP pattern, and their relation to the NCP. In this section, we go deeper in the study of those invariances, and show how they are related to the solar declination. More precisely, we

will demonstrate that the intersection of the plane and radial invariances is located at a distance from the celestial pole approximately equal to that of the solar declination δ, when the time interval between two skylight polarization observations is small (cf. figure 3.24). To demonstrate this, two properties of the invariances will be introduced before. We will first show that the intersection of the plane and radial invariances is located at 90° from the positions of Sun linked to the invariances, meaning that this point has a maximum of DoLP in the sky. Then, we will show that the two invariances are great circles.

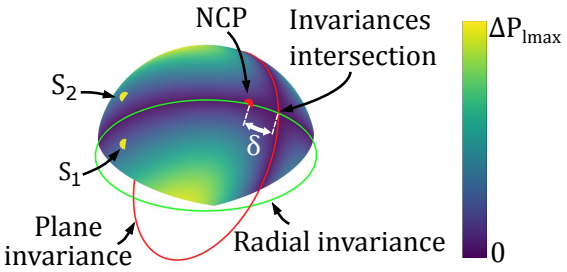

FIGURE 3.24. – Invariance circles on the celestial sphere, and the solar declination δ equal to the distance between the NCP and the intersection of the plane and radial invariances. Comparison between simulated and analytical sets of solutions. The green circle is the radial invariance circle, the red circle is the plane invariance circle computed from analytical calculations (cf. Eq. 3.11 and Eq. 3.14). The colored half sphere is the simulated absolute difference between two DoLP patterns associated with the Sun's positions S_1 and S_2 at two different times. The red dot is the NCP, and ΔP_{lmax} is the maximum value of the absolute difference of DoLP.

3.2.2.1. Lemmas

3.2.2.1.1. Intersection of the plane and radial invariances is located at 90° from the positions of Sun

The radial invariance is defined with respect to the equation $\vec{S_1} \cdot \vec{P} = \vec{S_2} \cdot \vec{P}$, and the plane invariance by the equation $\vec{S_1} \cdot \vec{P} = -\vec{S_2} \cdot \vec{P}$. Therefore, a point is at the intersection of the radial and plane invariances if and only if $\vec{S_1} \cdot \vec{P} = \vec{S_2} \cdot \vec{P} = 0$, meaning that $\vec{S_1} \perp \vec{P}$ and $\vec{S_2} \perp \vec{P}$. From Rayleigh single scattering model, we can conclude that the point at the intersection of the radial and plane invariances has the maximum value of DoLP at time t_1 and t_2. As we are working with unit vectors, we can also conclude that $\vec{P} = \pm \vec{S_1} \times \vec{S_2}$, where $\times$ is the cross product. A visualization of the radial and plane invariances' intersection is given in figure 3.25.

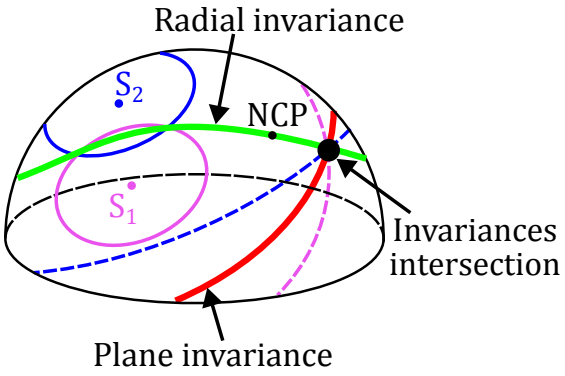

FIGURE 3.25. – Intersection of the plane and radial invariance circles on the celestial sphere. The green circular arc is the radial invariance, linked to the radial symmetry of the DoLP pattern (cf. Eq. 3.11). S_1 and S_2 are the Sun at time t_1 and t_2, respectively. The two colored circles centered on S_1 and S_2 correspond to circles with the same constant scattering angle with respect to S_1 and S_2, respectively. The red circular arc is the plane invariance linked to the plane symmetry of the DoLP pattern (cf. Eq. 3.14). The two colored dotted circular arc centered on S_1 and S_2 correspond to the maximum value of polarization in the sky, and are at the intersection between the celestial sphere and the plane of symmetry of the DoLP patterns for S_1 and S_2, respectively (cf. figure 3.20).

3.2.2.1.2. Plane and radial invariances are great circles

A point P is on the radial invariance if and only if $\overrightarrow{S_1}\cdot\overrightarrow{P} = \overrightarrow{S_2}\cdot\overrightarrow{P}$. Therefore, $\left(\overrightarrow{S_1}-\overrightarrow{S_2}\right)\cdot\overrightarrow{P} = 0$, meaning that $\left(\overrightarrow{S_1}-\overrightarrow{S_2}\right)\perp\overrightarrow{P}$. The set of point P defining the radial invariance can be expressed as $\left\{P\in S(O,1);\left(\overrightarrow{S_1}-\overrightarrow{S_2}\right)\perp\overrightarrow{P}\right\}$, where $S(O,1)$ is the sphere of center O and radius 1, called celestial sphere. Moreover, $\left\{P\in S(O,1);\left(\overrightarrow{S_1}-\overrightarrow{S_2}\right)\perp\overrightarrow{P}\right\}\subset\left\{P\in\mathbb{R}^3;\left(\overrightarrow{S_1}-\overrightarrow{S_2}\right)\perp\overrightarrow{P}\right\}$, which defines a plane including the point O ($\overrightarrow{O}=\overrightarrow{0}$) and with $\overrightarrow{S_1}-\overrightarrow{S_2}$ being a normal vector to this plane. We also have $\left\{P\in S(O,1);\left(\overrightarrow{S_1}-\overrightarrow{S_2}\right)\perp\overrightarrow{P}\right\} = \left\{P\in\mathbb{R}^3;\left(\overrightarrow{S_1}-\overrightarrow{S_2}\right)\perp\overrightarrow{P}\right\}\cap S(O,1)$. Thus, the radial invariance, given as the set of solutions of the equation $\overrightarrow{S_1}\cdot\overrightarrow{P} = \overrightarrow{S_2}\cdot\overrightarrow{P}$ is the intersection of a plane containing O and a sphere of center O, so this set defines a great circle.

In the same way, we can demonstrate that the plane invariance is a great circle. Indeed,

we have:

$$\begin{aligned} \overrightarrow{S_1} \cdot \overrightarrow{P} &= -\overrightarrow{S_2} \cdot \overrightarrow{P} \\ \iff \left(\overrightarrow{S_1} + \overrightarrow{S_2}\right) \cdot \overrightarrow{P} &= 0 \\ \iff P \in \left\{P \in S(O,1); \left(\overrightarrow{S_1} + \overrightarrow{S_2}\right) \perp \overrightarrow{P}\right\} & \\ = \left\{P \in \mathbb{R}^3; \left(\overrightarrow{S_1} + \overrightarrow{S_2}\right) \perp \overrightarrow{P}\right\} \cap S(O,1) & \end{aligned} \tag{3.27}$$

3.2.2.2. Relation between the solar declination and the intersection of the radial and plane invariances

Having introduced two properties of the skylight's DoLP invariance pattern, we will now demonstrate that the distance between the NCP and the intersection of the plane and radial invariances approaches the solar declination when the time interval between two measurements approaches zero.

In this section, we will refer to Fig. 3.26 representing the celestial sphere from different points of view.
In those figures, O refers to the the center of the celestial sphere, which is also the center of the Earth. P_N and P_S are the north celestial pole and the south celestial pole respectively (**warning:** this notation may be confusing but was adopted instead of NCP and SCP for readability). S_1 and S_2 are the Sun at two different times of the same day. E is the point at the intersection between the celestial equator and the great circle containing points S_1, P_N and P_S (represented as a blue circle). The great circle distance between E and S_1 is equal to the solar declination δ. The point I is at the intersection between the radial invariance (green great circle), and the plane invariance (red great circle) linked to Sun S_1 and S_2. Finally, D is the point on the radial invariance of which the great circle distance to the north celestial pole P_N is equal to the solar declination δ. D is located on the same meridian (great circle) as C, at 90 degrees from C, C being the point between S_1 and S_2.

3.2.2.2.1. Demonstration

Now, let us show that when S_1 and S_2 are near to each other, I is approximately the same as D. Let us first consider our reference frame, represented in the three figures. The center O of the frame is the center of the celestial sphere. $\overrightarrow{Z}$ is defined as $\overrightarrow{Z} = \overrightarrow{P_N}$. We consider the radial plane as the plane containing the radial invariance. The $\overrightarrow{Y}$ axis of our frame is the normal vector to the radial plane. Finally, $\overrightarrow{X}$ is defined such as the XYZ basis is an orthonormal basis. This frame can be considered as the equatorial coordinate system rotated around the Z axis.

It was shown before that I, being the intersection of the invariances, is located on the

plane perpendicular to $\overrightarrow{S_1}$ and containing O. We consider $\overrightarrow{S_1}\begin{pmatrix}\sin(\theta)\cos(\alpha)\\ \sin(\theta)\sin(\alpha)\\ \cos(\theta)\end{pmatrix}$, where θ is the angle of $\overrightarrow{S_1}$ with respect to the Z axis, being also the complementary angle to the solar declination, and α is the angle of $\overrightarrow{S_1}$ with respect to the X axis. α is equal to $\frac{\omega_1-\omega_2}{2}$, where ω_1 is the hour angle of S_1 and ω_2 is the hour angle of S_2.
We have $\overrightarrow{Y}\begin{pmatrix}0\\1\\0\end{pmatrix}$, being normal to the radial plane. I is by definition located on the radial plane, therefore on the plane normal to $\overrightarrow{Y}$, and on the plane normal to $\overrightarrow{S_1}$. We thus have $\overrightarrow{I} = \pm\overrightarrow{Y}\times\overrightarrow{S_1} = \pm\begin{pmatrix}\cos(\theta)\\ 0\\ -\sin(\theta)cos(\alpha)\end{pmatrix}$. In our frame, we have $\overrightarrow{I} = \begin{pmatrix}-\cos(\theta)\\ 0\\ \sin(\theta)\cos(\alpha)\end{pmatrix}$.
Moreover, the point D being at 90 degrees from the point C whose coordinates are $\overrightarrow{C} = \begin{pmatrix}\sin(\theta)\\ 0\\ \cos(\theta)\end{pmatrix}$, we have $\overrightarrow{D} = \begin{pmatrix}-\cos(\theta)\\ 0\\ \sin(\theta)\end{pmatrix}$.
We finally see that when $\alpha \ll 1$, $\cos(\alpha) \approx 1$. Therefore I is approximately the same as D and the great circle distance (on the radial invariance) between I and P_N is approximately equal to the solar declination.

3.2.2.2.2. Difference between the solar declination and the great circle distance between I and P_N

In the previous section, we demonstrated that the solar declination could be approximated by the distance between the NCP and the intersection of the plane and radial invariances, when $\alpha \ll 1$. We now study this approximation as a function of the time interval between two DoLP measurements.
The great circle distance $\Delta\sigma$ between points I and D can be given by the following formula:

$$\Delta\sigma = 2\arcsin\left(\frac{\sqrt{(\sin\theta\,(1-\cos\alpha))^2}}{2}\right) \tag{3.28}$$

Since $\sin\theta < 1$ and $\cos\alpha \geq 1-\frac{\alpha^2}{2}$, we have $\Delta\sigma \leq 2\arcsin\left(\frac{\alpha^2}{4}\right)$. Since the Earth spins at about 15° per hour, we can approximate $\alpha \approx \frac{15\pi t}{2\cdot 180}$, in radian, where t is the time between the two measurements. Therefore,

$$\Delta\sigma \leq 2\arcsin\left(\frac{\alpha^2}{4}\right) \approx 2\arcsin\left(\frac{\left(\frac{15\pi t}{2\cdot 180}\right)^2}{4}\right) \tag{3.29}$$

The result are plotted on Fig. 3.27. We computed the approximation error with simulated data using Rayleigh single scattering model and the same camera as the one used for experimentation (cf. section 3.3.1), but with 4 times higher resolution in DoLP

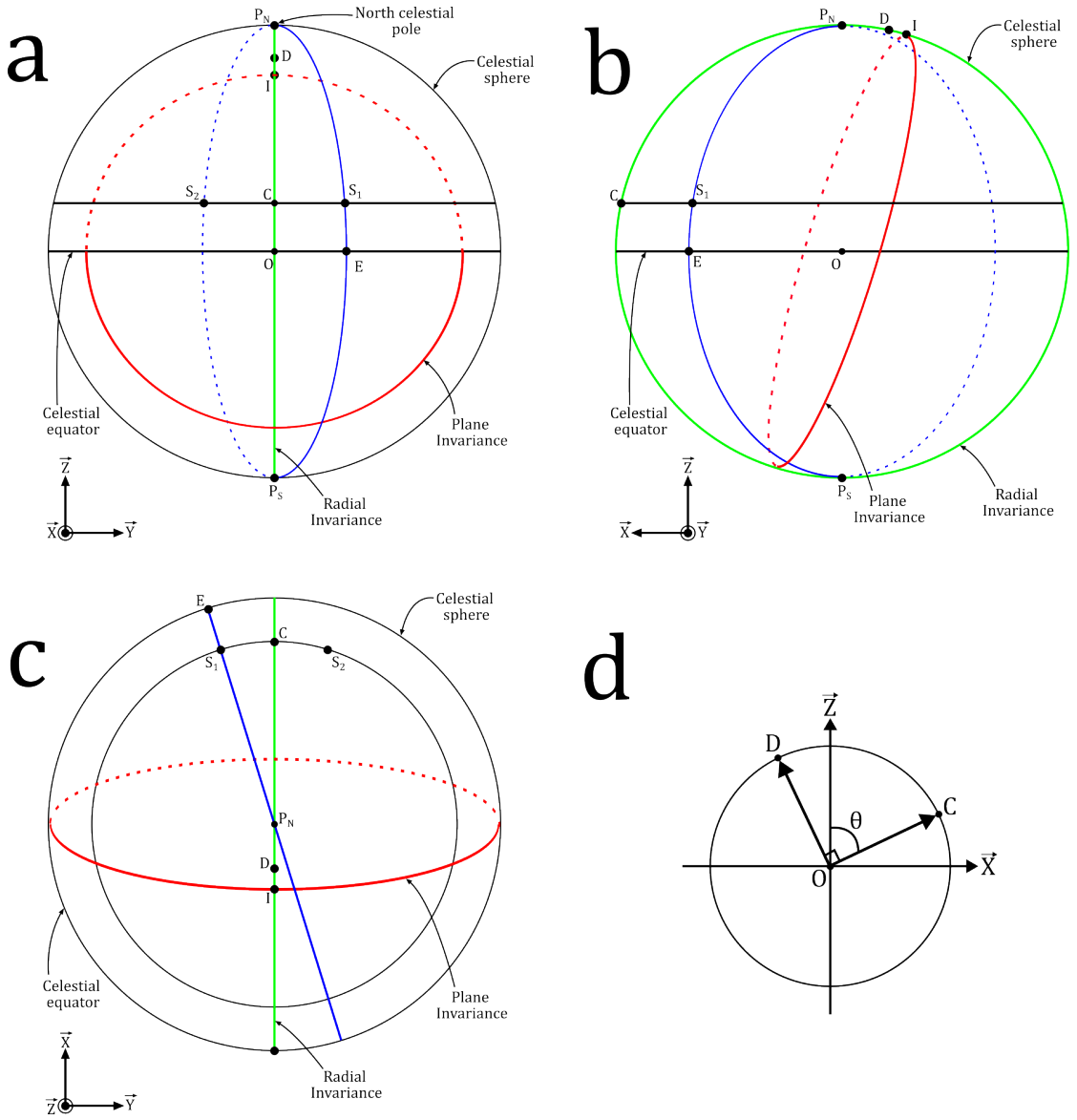

FIGURE 3.26. – (a-c) Three different points of view of the celestial sphere (d) Explanation of the coordinates of point D.

(2048x2448 pixels). Data was simulated with random dates between the 1st January 2015 and the 1st January 2018. For each date, a second date was randomly selected in a range varying between 0.15 and 2h from the first date. For each set of two dates, a random latitude and longitude on Earth was given (also on the south hemisphere, NCP replaced by SCP). For each date, latitude and longitude, the Sun's position was obtained from solar ephemeris, using Python libraries suncalc and PyAstronomy [238]. Then, Rayleigh single scattering model is simulated using the OpenSky simulator [82]. We computed the great circle distance between the NCP and the intersection of the radial and plane invariances using Vincenty's formula for an ellipsoid with equal minor and major axes. The algorithm to obtain the intersection of the radial

and plane invariances is presented below (cf. section 3.3.4.1). For small time intervals, values are higher than the upper bound. This is due to the algorithm and the maximum resolution of the camera. When using a lower resolution camera, those low time interval values become even higher. Some outlier data, removed in Fig. 3.27, were due to an ambiguity appearing when the intersection of the plane and radial invariances is under the horizon. The detected point is then the opposite intersection of the invariances.

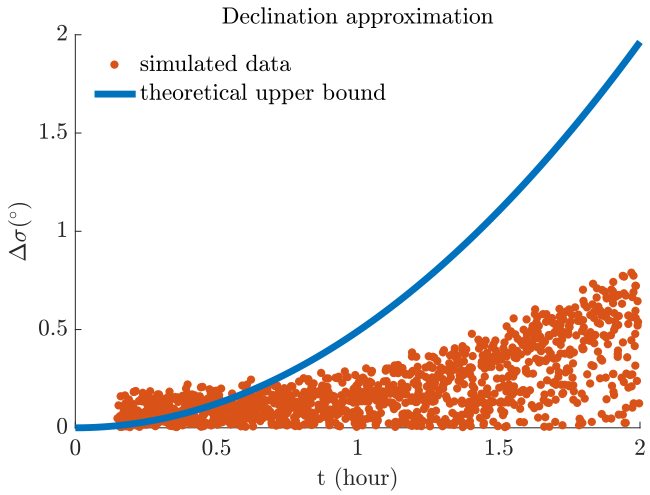

FIGURE 3.27. – Approximation error induced by the hypothesis $\alpha \ll 1$. The theoretical upper bound is given in equation 3.29.

3.2.3. Measuring time from skylight polarization patterns, the Wheatstone polar clock and the polar chronometer

In the previous section, we indicated how the polarization invariances were linked to the solar declination, equivalent to the date. In this section, we show how the skylight polarization can be used to obtain the apparent solar time, and how the time invariances can be used to measure time intervals.
First, the direction of polarization at the NCP can be measured, providing the apparent solar time. Indeed, the hour angle is defined as the angle between the observer's meridian (containing the zenith and the NCP), and the plane containing the NCP, the Sun and the observer, which is the scattering plane for the NCP. As discussed in section 1.3.2.1, e-vectors are always perpendicular to the scattering plane. Therefore, by measuring the direction of polarization at the NCP, we obtain a vector orthogonal to the scattering plane that allows the measurement of the hour angle (cf. figure 3.28). A device, known as the Wheatstone polar clock was developed in 1848 by Charles Wheatstone, to measure the apparent solar time based on the skylight polarization at the NCP [68]. By first estimating the position of the NCP from the skylight DoLP

invariances, we can then measure the hour angle from the angle of polarization at the NCP.

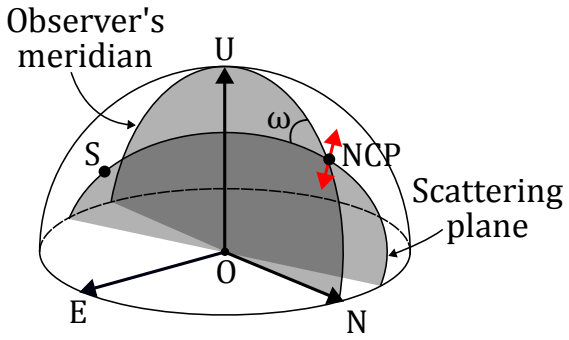

FIGURE 3.28. – Sun hour angle from the direction of polarization at the NCP, represented in the ENU frame, centered on an observer O. ω is the hour angle, defined as the angle between the observer's meridian and the scattering plane for the NCP. Red arrow is the direction of polarization at the NCP, orthogonal to the scattering plane, and S is the Sun.

In a similar manner, we can consider the radial invariance as the intersection between the scattering plane containing the NCP and the Sun's mean position between the two measurements, and the celestial sphere. We can therefore measure the angle between the radial invariance and the observer's meridian, giving the hour angle of the mean Sun. Then, if knowing the time interval between the two skylight measurements, we can deduce the actual solar time. Compared to the Wheatstone polar clock, we can not obtain an instantaneous measurement of the hour angle. However, using this method, only the DoLP should be measured, and we do not only rely on a single point, leading to more robust time measurements. The Wheatstone polar clock could be improved by processing measurements from the whole sky to estimate the angle of polarization at the NCP, using Rayleigh single scattering model, for instance.

Using only the skylight DoLP invariances, a polar chronometer can also be implemented. We can show that each point located between the Sun and the NCP on the radial invariance, obtained from two DoLP measurements at time t_1 and t_2 with Sun's hour angle ω_1 and ω_2, respectively, have an hour angle $\omega_{C12} = \frac{\omega_2+\omega_1}{2}$ (cf. point C, figure 3.26). Similarly, each point located between the Sun and the NCP on the radial invariance obtained from measurements between time t_1 and t_3 have an hour angle $\omega_{C13} = \frac{\omega_3+\omega_1}{2}$. The elapsed time between t_2 and t_3 can be estimated by measuring the angle between the radial invariances obtained from measurements at time t_1 and t_2, and t_1 and t_3. Indeed, the angle $\Delta\omega_{23}$ between those radial invariances will be given as

$$\Delta\omega_{23} = \omega_3 - \omega_2 = 2\left(\frac{\omega_3+\omega_1}{2} - \frac{\omega_2+\omega_1}{2}\right) = 2\left(\omega_{C13} - \omega_{C12}\right) \tag{3.30}$$

A schematic explanation is given in figure 3.29.

None of those methods for time measurements were implemented in this thesis.

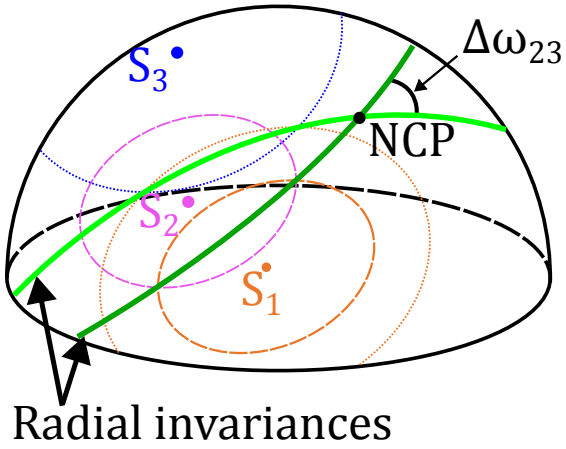

FIGURE 3.29. – Principle of the polar chronometer. S_1, S_2 and S_3 are the Sun at time t_1, t_2 and t_3, respectively. $\Delta\omega_{23}$ is the elapsed time between t_2 and t_3. The radial invariances are obtained from the symmetries of the DoLP, represented by the small circles, as shown in figure 3.22. Dark green and light green circular arcs are the radial invariances obtained from measurements at time t_1 and t_2, and t_1 and t_3, respectively.

They are, however, mentioned since the solar time, as discussed later, is useful to determine the longitude. The polar chronometer can also be useful to calibrate a clock for instance.

3.3. Methodological approach to skylight navigation using the time invariances of the skylight polarization patterns

From the description of the DoLP time invariances, algorithms were developed to obtain the position of the NCP. All those algorithms were tested with simulated data and experimental data. Simulated data were generated from the OpenSky simulator [82], and with camera parameters corresponding to those of the camera used to acquire the experimental data. We start by presenting the measurement device and its orientation calibration. Then, we present three algorithms to compute the position of the NCP.

3.3.1. Measurement device

Experimental data were obtained with a 5 megapixels division of focal plane color-polarimetric camera (PHX050S-QC from Lucid Vision Labs, sensor ref. Sony IMX250MYR) (cf. figure 3.30) topped with a 185° fisheye lens (Fujinon FE185C57HA-1) [85] (cf. figure 3.31). The camera was installed on the roof of the INT Lab at La Timone, Marseille,

France (43.286990365824785°N, 5.403361407820939°E), and was roughly pointing towards the zenith. Data were acquired with a camera aperture of $f/2.8$ [156].

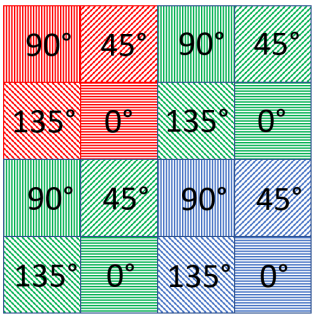

FIGURE 3.30. – Four neighboring color-polarization super pixels of the DoFP measurement device. The color of the pixels represent their color sensitivity, and the numbers are the orientations of the polarizing filters. Credit: Léo Poughon [85].

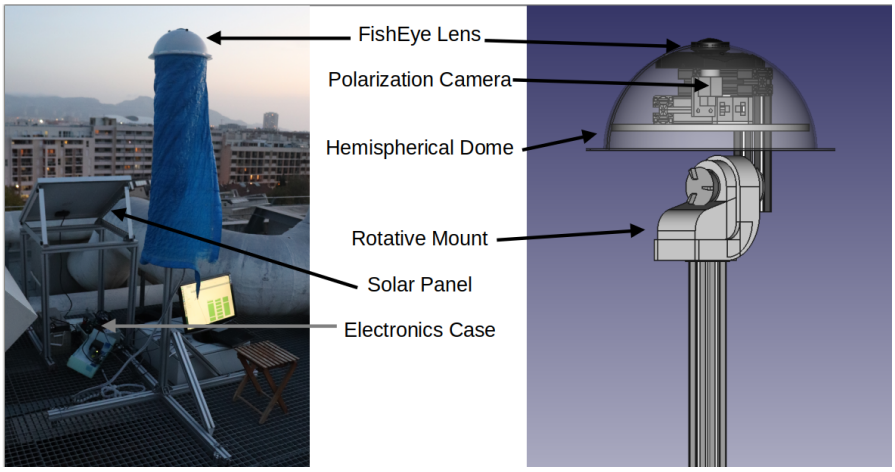

FIGURE 3.31. – Global view and mechanical layout of the measurement device. Credit: Léo Poughon [85].

As the device was left several days unmoved on the roof, an orientation calibration was performed. In order to make the Sun appear as a spot on the sensor, several clear sky pictures were taken with minimal time of exposure ($34\mu s$). Then, the successive positions of the Sun were computed each time as the centroïd of the spot on the sensor plane. Next, with the distortion model provided by the manufacturer, the 2D centroïds coordinates were transformed to 3D hemispherical coordinates in the camera frame. The Matlab calibration camera toolbox was also used to estimate the intrinsic parameters (focal length and center of distorsion in pixels) of the camera with a fisheye lens. Simultaneously, the groundtruth positions of the Sun in the ENU frame centered on the camera were computed by using ephemeris estimated with the AstroPy python library [239]. Two sets of solar vectors were obtained, a set of

groundtruth solar vectors expressed in the ENU frame and a set of measured solar vectors expressed in the camera frame. The optimal rotation between the two sets of vectors derived in the least-squares [240] way allowed us to deduce the rotation matrix between the two frames and finally the absolute camera orientation. The device's assembly, its calibration and the data acquisition were performed by Léo Poughon. The processed data are available online [86, 241].

3.3.2. The SkyPole method

Having introduced the theory of the skylight's DoLP invariances, and the measurement device used in this thesis, we here present a practical method to find the position of the NCP using patterns of skylight DoLP. We start by presenting the algorithm based on simulations of the Rayleigh single scattering model, using the OpenSky simulator [82]. We then present the experimental approach, and the results obtained.

3.3.2.1. Algorithm

To get the invariances between two skylight polarization images, we can simply process the difference between each pixel of the images, and search for the points for which the difference of DoLP is equal to 0. A simple way of doing this is by computing the absolute difference between the images, and then applying a threshold to isolate values near 0. For instance, the threshold function f_t can be defined as:

$$\begin{aligned} f_t &: \mathbb{R} \to \mathbb{R} \\ x &\mapsto \begin{cases} 1 & \text{if } x \leq t \\ 0 & \text{else} \end{cases} \end{aligned} \tag{3.31}$$

Where t is the threshold value.
Having a set of at least three DoLP images, we can implement this threshold step on each pair of images. Then, by superimposing the threshold images, for instance by adding them, the NCP will be located at the intersection of the radial invariances. Using this threshold method does not, however, allow distinguishing between the plane and radial invariances. Therefore, multiple intersections of invariances may appear, including intersections between the radial and plane invariances. However, as demonstrated, the NCP being the only point in the sky having a constant DoLP during a day, by taking at least four skylight polarization images with a sufficiently long time range will lead to only one intersection of all invariances, corresponding to the NCP. The method is represented in figure 3.32.

In this method, if three images are used, two invariance patterns will intersect. Therefore, the NCP will be located at the intersection of two radial invariances, but the two plane invariances may also intersect, either each other, or with the radial invariances, adding ambiguity (cf. figure 3.33). The only situation for which no ambiguity would be noticed is when the NCP is located at the intersection of the plane and radial invariances.

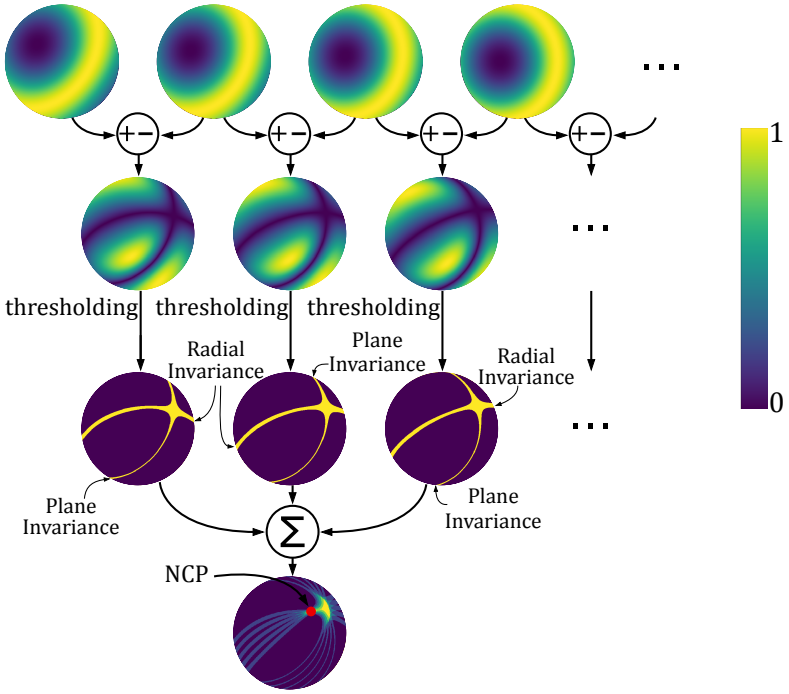

FIGURE 3.32. – Method for finding the NCP based on the skylight's DoLP pattern. In the first row are the DoLP patterns taken at 4 different times. Absolute differences between DoLP patterns were then computed, giving the second row. A thresholding step was then applied to those images and the results are presented in the third row. Lastly, binary images were summed, and the NCP was then located at the intersection between the radial invariances [235].

3.3.2.2. Experimentation

This method was tested with experimental data obtained with the DoFP polarimetric camera presented in section 3.3.1. The methodology is first explained, then, the results are presented.

3.3.2.2.1. Methodology

The DoLP was calculated by selecting only the blue channel of the sensor, and by making the assumption that the four micro-polarizers of a pixel cluster [242] were roughly viewing the same spot in the sky. After the DoLP was computed, a circular averaging filter was applied to the DoLP data. Next, we implemented the absolute difference in DoLP between several moments of time (with time intervals ranging from 30 to 60 minutes) in order to display the radial and plane invariance axes. A threshold was then applied to those absolute differences to segment the invariances, and the resulting segmented images were added. The NCP was located by searching for the maximum valued point, namely the intersection between all the radial invariance axes

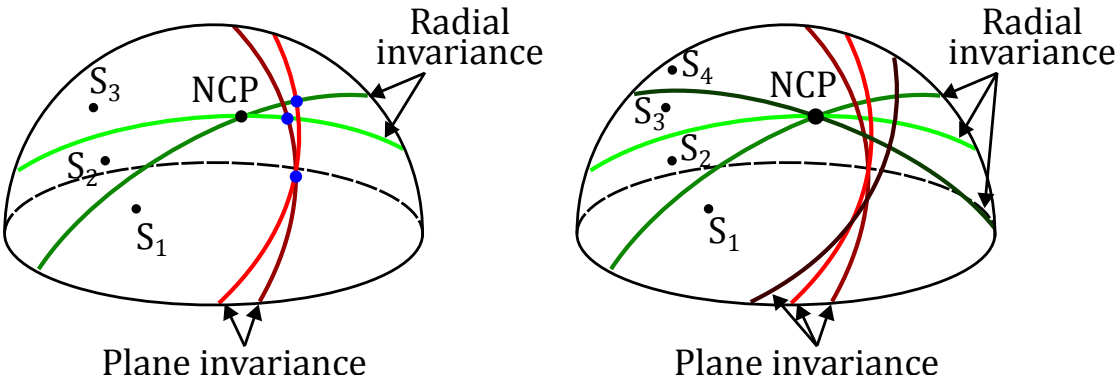

FIGURE 3.33. – Multiple intersections of invariances. Left: two patterns of invariances obtained from three sky measurements at time t_1, t_2 and t_3, with positions of the Sun S_1, S_2 and S_3, respectively. The blue dots are ambiguous points, at the intersection of two invariances, similarly to the NCP. Right: three patterns of invariances obtained from four sky measurements at time t_1, t_2, t_3 and t_4, with positions of the Sun S_1, S_2, S_3 and S_4. The only point at the intersection of three invariances is the NCP.

(cf. figure 3.32). Lastly, the coordinates of the point were transformed to true north and latitude coordinate and compared with the ground truth values.

3.3.2.2.2. Results

Data were acquired on 23 September 2022. As shown in figure 3.34, the results obtained by applying the SkyPole method to experimental data were consistent with the simulated results presented in figure 3.32.

We also estimated the NCP's position with an azimuth of the camera ranging from 0 to 170° in steps of 10° (cf. figure 3.35). A mean absolute azimuth error of 2.6° and a mean absolute latitude error of 3.8° were obtained [235].

3.3.3. The SkyPole method with machine learning

In the previous section, we presented a method requiring only simple processing steps. However, as discussed previously, this method may provide ambiguous results, due to multiple intersections of invariances. To avoid this issue, the radial invariance can be separated from the plane invariance. Here, we suggest a method for segmenting the radial invariance using a neural network. We first present the algorithm, and then the simulated and experimental results obtained.

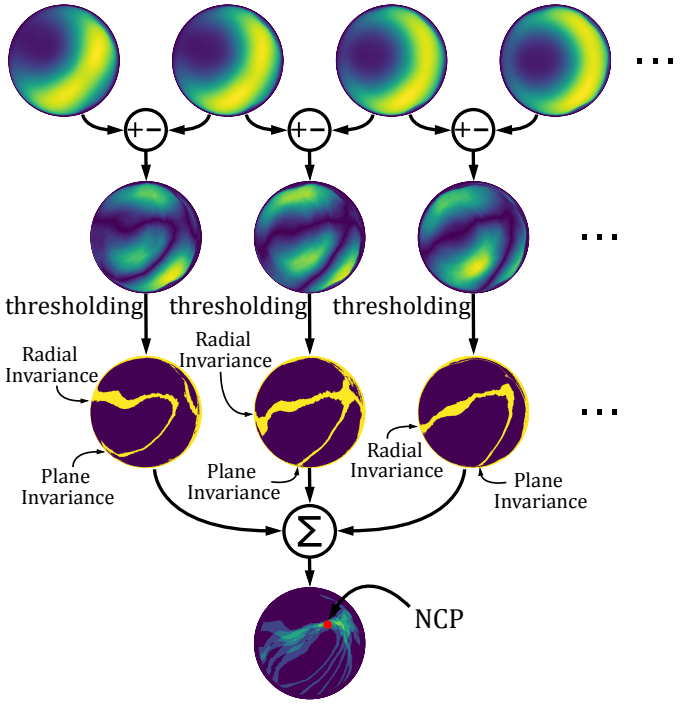

FIGURE 3.34. – SkyPole algorithm applied to experimental data for finding the NCP. Preprocessing of the first row of DoLP images consisted in filtering the images obtained using a circular averaging filter. Details of the following steps are presented in figure 3.32

3.3.3.1. Deep learning models for polarization image processing

Image processing can be complex even for tasks that seem easy for humans. For instance, classifying hand-written numbers through imperative programming requires to define precise, step-by-step instructions to handle the vast variability and nuances in human handwriting. In this thesis, a complex task can be to remove unwanted polarization sources, such as windows reflections, or to process skylight polarization in presence of clouds. Data-driven models, on the other hand, allow for dealing with complex issues, without needing prior physical knowledge about the data. The difficulty for such a model is gathering unbiased data that allows for completely describing a task and learning from that data. Neural networks, for instance, are based on this principle. Those networks are composed of connected units inspired from human neurons. A single unit is known as a perceptron, or neuron (cf. figure 3.36). Its output o is obtained from a linear combination of the input values $(i_k)_{1\leq k\leq n} \in \mathbb{R}^n$, where $n \in \mathbb{N}$, to which we apply a non linear function f, known as activation function, such as:

$$o = f\left(\sum_{k=1}^{n} w_k \cdot i_k\right) \tag{3.32}$$

Where $(w_k)_{1\leq k\leq n} \in \mathbb{R}^n$, are weighting factors.

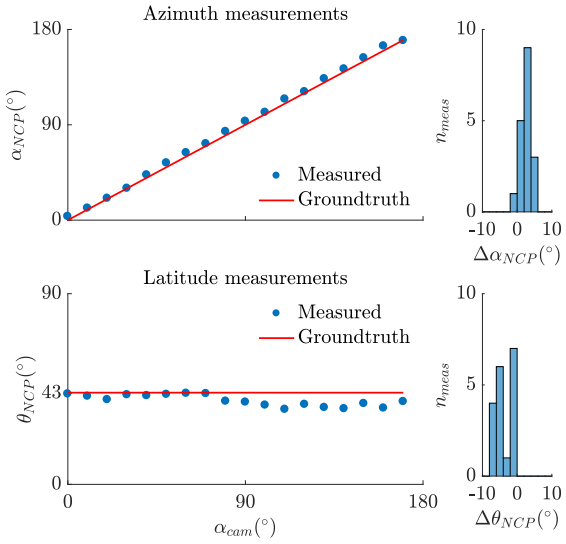

FIGURE 3.35. – NCP coordinates computed with the SkyPole algorithm (Fig. 3.34) from experimental data versus ground truth NCP coordinates. α_{cam} is the azimuth of the camera with respect to the North. α_{NCP} is the azimuth of the NCP with respect to the azimuth of the camera. θ_{NCP} is the altitude of the NCP, which is also equal to the camera's latitude. $\Delta\alpha_{NCP}$ and $\Delta\theta_{NCP}$ are the azimuth and altitude error, respectively, of the NCP measured with respect to the ground truth values. n_{meas} is the number of measurements for each error interval [235].

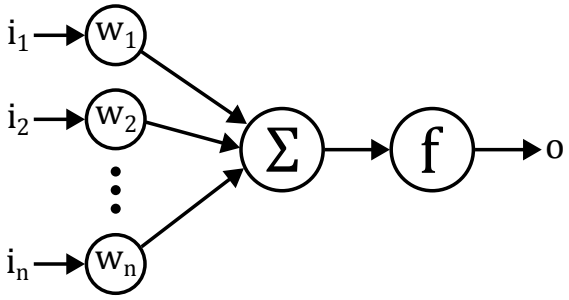

FIGURE 3.36. – Schematic representation of a perceptron. $(i_k)_{1\leq k\leq n}$, where $n \in \mathbb{N}$, are the inputs, $(w_k)_{1\leq k\leq n}$ are the weights, Σ is the sum symbol, f is the activation function and o is the output of the perceptron.

More generally, a neural network may be composed of multiple layers with each layer consisting in multiple perceptrons (or neurons) (cf. figure 3.37). The output of a layer is therefore computed from a linear combination of the previous layer's outputs, such as:

$$o_{l,j+1} = f_{l,j+1}\left(\sum_{k=1}^{n_j} w_{k,j} \cdot o_{k,j}\right) \tag{3.33}$$

Where $o_{l,j+1}$ and $f_{l,j+1}$ are the output value and the activation function of the layer $j+1$, and row l, respectively. n_j is the number of neurons in the layer j, and $w_{k,j}$ is the weighting factor associated with the output $o_{k,j}$ of the layer j, column k. l, j, and $n_j \in \mathbb{N}$.

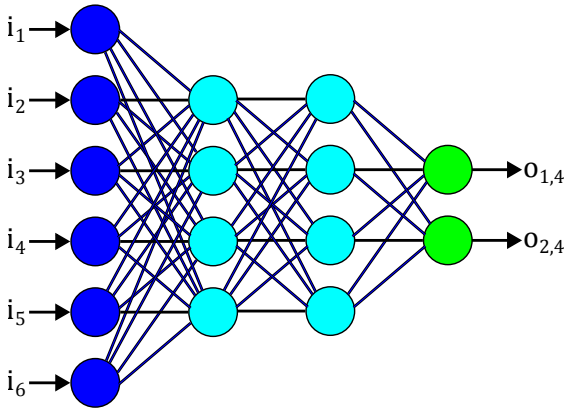

FIGURE 3.37. – Schematic representation of a multi-layer perceptron (or neuron). Each colored circle is a perceptron. Outputs of a layer become inputs of the following layer. Dark blue circles form the input layer, light blue circles form the hidden layers and green circles form the output layer. $(i_k)_{1\leq k\leq 6}$ are the inputs, and $o_{1,4}$, $o_{2,4}$ are the outputs of the neural network.

The output of a neural network is computed forward, starting by the outputs of the first layer of neurons, known as input layer, and then calculating the outputs of the following layers, the outputs of a layer being the inputs of the following layer. The last layer is known as output layer, and all the other layers are known as hidden layers.
Training a neural network consists in tuning the weights of the neural network to minimize an error. For skylight polarization images, the output error of the neural network can be given as a mathematical distance between the outputs of the neural network and the labels of the images given as input. A label can be for instance the solar azimuth, or elevation. Each weight of the neural network can be tuned by computing the derivative of the error with respect to the weight.
The tuning of each weight of a neural network can be achieved by the gradient descent method. A local minimum of the error function corresponds to a null gradient of the error function. Therefore, the error being a function of the weighting factors, a local minimum of the error function can be obtained by minimizing the gradient of the error with respect to each weight. Considering the gradient descent method, the weights can be tuned in the following way:

$$w_{k,j}^{t+1} = w_{k,j}^{t} + l_r \frac{\partial e}{\partial w_{k,j}^{t}} \tag{3.34}$$

Where $w_{k,j}^{t+1}$ and $w_{k,j}^{t}$ are the weight of row k, layer j, after and before the tuning step,

respectively. l_r is a real number known as the learning rate, and $\frac{\partial e}{\partial w_{k,j}^t}$ is the partial derivative of the error e with respect to the weight $w_{k,j}^t$.
The partial derivative of the error with respect to the weights can be computed by starting with the output layer and then proceeding derivatives backward, layer by layer, ending with the weights of the input layer. Doing so, the derivatives of the error with respect to the weights can be calculated as functions of previously computed parameters. This process is known as backpropagation, simplifying the computation of the derivatives. This process is not detailed in this thesis. Detailed explanations on deep learning can be found in [243].
To process data, various neural networks architectures have been proposed. Here, we present some widely used neural networks.
Multi-layer perceptrons (MLP) consist in multiple layers with each neuron of a layer being connected to all neurons of the previous layer (fully connected layer). Those networks are conceptually simple, but can be hard to train due to the large number of weights associated with each connection between neurons. To overcome this issue, convolutional neural networks (CNN) were created, allowing for quick and efficient learning, especially in image processing. Those networks are not fully connected contrary to MLP, instead, a fixed size kernel, that can consist in only 9 parameters (3x3 kernel), scans an input image for instance, and outputs a new image, as a classical convolution (cf. figure 3.38). Therefore, the number of parameters to be learned is given by the sizes of the kernels for each layer of the CNN, independently from the size of the inputs. Therefore, much less parameters must be learned when training CNN compared to MLP. CNN's output layers are generally fully connected layers, but with few parameters, the sizes of the input images being reduced by pooling techniques throughout the network. Another type of neural network is the recurrent neural network (RNN). Such networks were created to learn temporal data. Those networks possess bi-directional connections contrary to previously discussed networks, meaning that the output of a layer can affect previous layers.

For skylight polarization image processing, several neural networks architecture were implemented. MLP were used in [196, 197] to estimate the solar azimuth. In [197], the solar azimuth errors obtained from a MLP model consisting in 4 layers of neurons is compared to those obtained with two complex CNN models (AlexNet model, and ResNet-50 model), showing better results for the MLP. CNN models were implemented to restore noisy skylight polarization images in order to detect the solar vertical plane [201, 200], showing impressive image restoration results. Those studies are based on convolutional autoencoder structures, consisting in compressing the input information in a latent space through an encoding step and then reconstructing the image through a decoding step. In [201], a U-Net neural network is trained for image reconstruction. A general review on deep learning for polarimetric imaging was produced in [244].

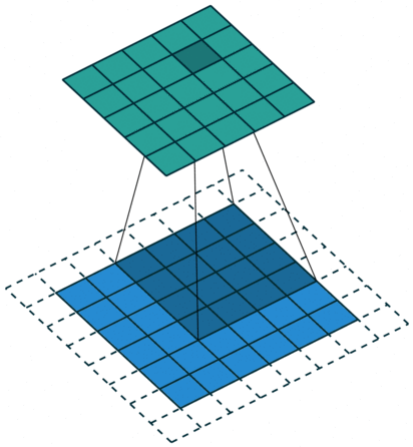

FIGURE 3.38. – Schematic representation of a convolution layer, with a 4x4 kernel. Blue image is the input image, green image is the output image. Credit: Vincent Dumoulin, Francesco Visin, MIT

3.3.3.2. Algorithm

To isolate the radial invariance, and based on the previously published methods, we chose to use a U-Net neural network [245]. U-Net is a CNN first developed for image segmentation, that has the advantage of returning accurate segmentation outputs. The U-Net model was trained from [246] on PyTorch, by using a database of simulated polarized images. The database consisted of pairs of DoLP images simulated by means of the OpenSky simulator [82]. For each pair of images, a binary image representing the radial invariance projected in our camera image plane was simulated and used as our ground-truth label. To simulate the radial invariance, we projected a subset of the radial invariance set (cf. equation 3.11) into the camera image plane.
Often, simulation requires the position of the Sun to be given in azimuth and elevation. A simple change of Sun coordinates can provide the set in equation 3.11 as a function of the azimuth α_{S_1} and α_{S_2}, and elevation θ_{S_1} and θ_{S_2} of the Sun's two positions:

$$\boldsymbol{Set_1} = \{(\alpha,\ \tan^{-1}\left[\frac{\sin\alpha\left(\cos\theta_{S_1}\sin\alpha_{S_1}-\cos\theta_{S_2}\sin\alpha_{S_2}\right)}{\sin\left(\theta_{S_2}\right)-sin(\theta_{S_1})}\right. \\ \left.+\frac{\cos\alpha\left(\cos\theta_{S_1}\cos\alpha_{S_1}-\cos\theta_{S_2}\cos\alpha_{S_2}\right)}{\sin\left(\theta_{S_2}\right)-sin(\theta_{S_1})}\right]\Big),\ \alpha\in[-\pi,\pi[\} \quad (3.35)$$

The dataset consisted of 1892 sets of labeled images, each set being composed of two input DoLP images and the corresponding radial invariance label. This dataset was augmented by applying random rotations and random crops to the images. The two input images and the label image had to be rotated and cropped in the same way. The dataset was composed of images of 512×612 pixels before crop, and 416×416 after. We also augmented the dataset by applying a random erasing of various sizes

to the DoLP input images. Random erasing occurred with a probability of 30%, and the erasing area was a zero valued rectangle representing a proportion of the image ranging from 2% to 13%. Data augmentation is applied to a dataset in order to reduce the learning bias induced by the data. For instance, a dataset consisting in skylight polarization images taken with a fixed camera is highly biased, since the Sun does only cover a small region of the sky. Therefore, adding azimutal rotations of the images can partially prevent from this bias. We trained a U-Net model with two input channels, one output channel and 32 features in the first layer, with no pre-training. The U-Net was trained by using a mean squared error loss function and Adam optimizer, batch size of 8, learning rate of 0.01, and the selected trained model corresponding to the 45th epoch. The training set was shuffled using a fixed seed for reproducibility. 80% of the database was used for training, and 20% for testing.
After being trained, the U-Net was given as input two DoLP simulation images, and returned the radial invariance in the image plane of the camera. The output image was not binary so we applied a threshold to change all values over 0.5 to one. By repeating this step for each set of two DoLP images, the NCP was finally located at the intersection of the radial invariances. For experimental data, the same neural network was used, but simulated images were matched to the real images before applying the previously described steps. For this step, we estimated, using the least square method (lmfit library python [240]), the simulation parameters that minimized the absolute difference between the DoLP simulation images and the real DoLP images obtained from the polarimetric camera. The DoLP of simulated images was based on equation 3.3. Initial azimuth, elevation and maximum of DoLP where set at 5°, 5° and 0.5, respectively. The Sun's azimuth could vary between -180° and +180°, elevation between 0° and 90° and maximum DoLP between 0 and 1. Since this step is only made to match a simulated image to a real image, the Sun's azimuth and elevation used for the camera simulation can be expressed in any random camera frame and may not correspond to those of the real images (details in appendix A). The algorithm is represented in figure 3.39.

3.3.3.3. Simulation results

We tested our algorithm on data simulated using Rayleigh single scattering model and the camera model equivalent to the one used for experimentation. Data was simulated with random dates between the 1st January 2015 and the 1st January 2018. For each date, a second and a third date were randomly selected in a range varying between 0.5 and 2h from the first and second date, respectively. For each set of three dates, a random latitude and longitude on Earth was generated (also on the south hemisphere, but by estimating the position of the south celestial pole). For each date, latitude and longitude, the Sun's position was obtained from solar ephemeris, using Python libraries suncalc and PyAstronomy[238]. Then, Rayleigh single scattering model was simulated using the OpenSky simulator [82]. For each set of three images, we computed the position of the celestial pole using the proposed algorithm, without the least square step, which was skipped. We observe that some errors occurs near the

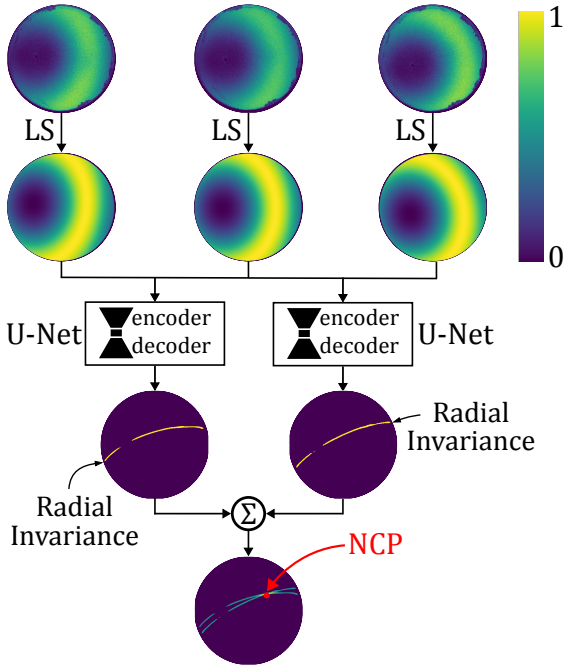

FIGURE 3.39. – Method for finding the NCP based on the skylight's DoLP pattern. In the first row are the DoLP patterns taken at 3 different times (more images will improve the results). Least square method was applied to match simulated images to the real images, giving the second row. The radial invariances were then segmented by using a U-Net neural network, the results being presented in the third row. Lastly, the radial invariances images were summed, and the NCP was then located at the intersection between the radial invariances, which has the highest value in terms of pixel intensity.

poles or the equator. Near the poles, the celestial pole is close to the zenith. Since our simulated camera is placed horizontally, we obtain high errors due to the singularity in azimuth of the camera near the zenith. Near the equator, since the celestial pole is at the horizon, we may sometimes detect the opposite intersection of radial invariances leading to 180° errors in azimuth. We therefore decided to quantitatively present our results before and after removing outliers with Matlab function rmoutliers (default parameters). We obtained 1879 measurements after removing outliers from a total of 2078 measurements. We analysed our results with and without outliers using Matlab rmoutliers function. We finally obtained a mean absolute error (MAE) of 1.0273 degrees in azimuth (3.5528 degrees with outliers), and 0.6752 degrees in azimuth (1.0173 degrees with outliers). Results are plotted in figure 3.40.

3.3.3.4. Experimental results

We tested our method on data recorded with the camera presented in section 3.3.1. Processed data was acquired during the whole month of August 2022, each day from

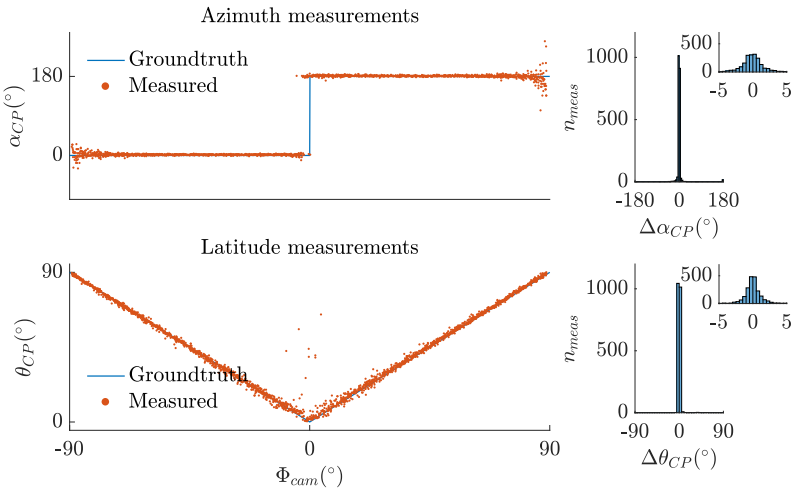

FIGURE 3.40. – Celestial Pole (CP) coordinates estimation error (north celestial pole for positive latitudes, and south celestial pole for negative latitudes). CP coordinates were computed from simulated data with the proposed algorithm (Fig. 3.39), by skipping the least square step. Φ_{cam} is the camera latitude. α_{CP} and θ_{CP} are the azimuth and altitude, respectively, in degrees, of the measured and groundtruth CP. $\Delta\alpha_{CP}$ and $\Delta\theta_{CP}$ are the azimuth and altitude errors, respectively, in degrees, of the CP measured with respect to the ground truth values. n_{meas} is the number of measurements for each error interval of the histogram. The zoomed in histograms corresponds to CP coordinates values with absolute error lower than 5 degrees. It represents 1926 measurements out of 2078 in azimuth, and 2058 measurements out of 2078 in elevation.

8:00am to 6:00pm [86]. Only data with a $DoLP_{max}$ higher than 0.2 was processed. Since we were located on the Earth north hemisphere, we detected the position of the NCP. Each estimation of the NCP was made using four images taken with time intervals of 100 minutes. Once the celestial pole's position was estimated, we computed the True North and the camera's latitude from the coordinates of the celestial pole. We obtained a mean absolute error of 2.6194 degrees in True North and of 1.8059 degrees in latitude of the camera. Results are displayed in figure 3.41.

3.3.4. The Polendar method

The two previous algorithms consisted in searching for the intersection of radial invariances, requiring at least three skylight observations. In this section, the link between the solar declination and the polarization invariances (cf. figure 3.42), described in section 3.2.2, is used to find the position of the NCP from only two skylight polarization measurements. This method consists in computing the polarization invariances, then finding the intersection between the plane and radial invariances, and

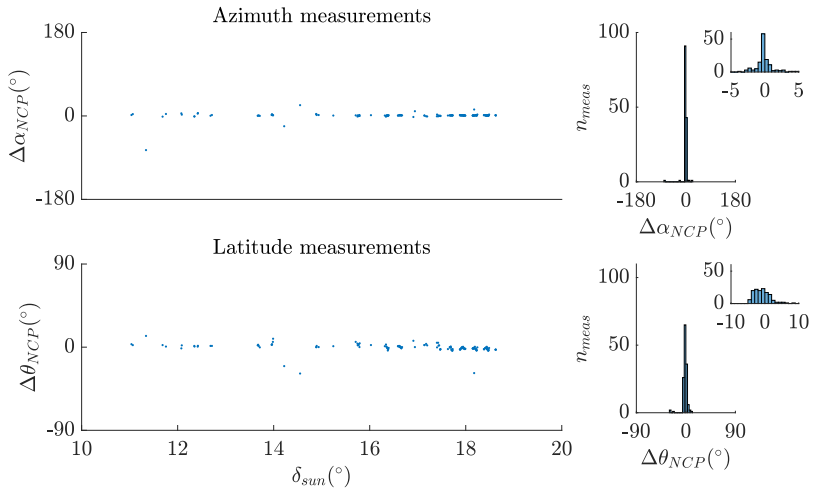

FIGURE 3.41. – North Celestial Pole (NCP) coordinates estimation error. NCP coordinates were computed from experimental data with the proposed algorithm (Fig. 3.39). δ_{sun} is the solar declination in degrees. $\Delta\alpha_{NCP}$ and $\Delta\theta_{NCP}$ are the azimuth and altitude errors, respectively, in degrees, of the NCP measured with respect to the ground truth values. n_{meas} is the number of measurements for each error interval of the histogram. The zoomed in histogram corresponds to NCP coordinates values with absolute error lower than 5 and 10 degrees for azimuth and latitude, respectively. It represents 162 measurements out of 226 in azimuth, and 217 measurements out of 226 in elevation. For each estimation, we computed our algorithm using four images taken with time intervals of 100 minutes.

finally deducing the position of the NCP on the radial invariance, at a distance from the intersection of the plane and radial invariances equal to the solar declination, considered known.

3.3.4.1. Algorithm

The algorithm for computing the polarization data is as follows: first, we use the least square method to match a skylight polarization simulation based on the Rayleigh single scattering model with the acquired skylight polarization image (cf. figure 3.43, step LS). Then, we estimate the intersection of the two invariances by using a convolutional filter, and isolate the radial invariance with a U-Net neural network (cf. Fig. 3.43, step U-Net). Finally, we deduce the position of the NCP, which is located on the radial invariance, at an angular distance equal to the solar declination from the intersection of the invariances (cf. Fig. 3.43). The least square step and U-Net step, were detailed in section 3.3.3.
The estimation of the position of the radial and plane invariances intersection is done

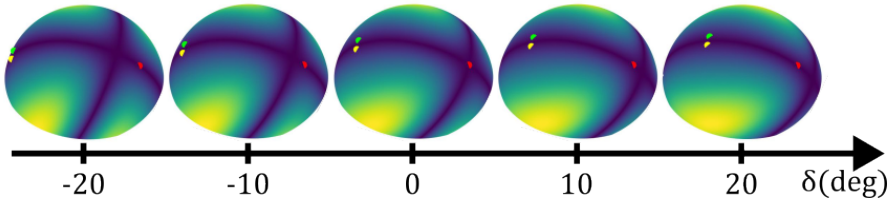

FIGURE 3.42. – Variation of the relative position between the NCP and the intersection of the radial and plane invariances as a function of the declination δ. Images were computed from pairs of polarization images simulated using the Rayleigh single scattering model. The red dot is the NCP, the yellow and green dot are the Sun's positions corresponding to the two polarization images used to compute the invariances. The declination δ is the only variable, hour angles and latitude being constant for those images.

by taking two polarization simulation images obtained in the first step from experimental data measured with a relatively small time interval (20 minutes here). Then, we compute their absolute difference. To isolate the intersection of the polarization invariances, we convolute the absolute difference image with a kernel having all values equal to one, and binarize the image. This is based on the fact that when we apply the previous convolution, values near the intersection of the two invariances have the lowest values. We simultaneously apply another threshold to the absolute difference image. Then, we apply a logical AND operator to the first binary invariance image and also to the second binary invariance intersection image for more precision. These two last steps are optional. The intersection of the invariances is finally given as the mean value of the selected intersection points.
The intersection of the plane and radial invariance could have been obtained by training a U-Net to segment the plane invariance. The plane and radial invariances would then have been segmented, and their intersection trivially obtained.
Once the intersection of invariances is estimated and the radial invariance isolated, the NCP is obtained by searching the points on the radial invariance of which the distance to the invariances intersection is equal to the solar declination. As shown in figure 3.42, the NCP generally has a higher elevation than the intersection of the invariances when the declination is positive. This condition may sometimes lead to false results in some specific conditions (cf. section 3.3.4.2). The method is presented in figure 3.43.

3.3.4.2. Simulation results

We implemented the proposed method on simulated data (cf. section 3.3.3.3). For each set of two images, we computed the position of the celestial pole using our method. We distinguished two cases to compute the celestial pole's position. First, if the latitude and the solar declination had opposite sign, then, we considered that the intersection of the invariances had a higher elevation compared to the celestial

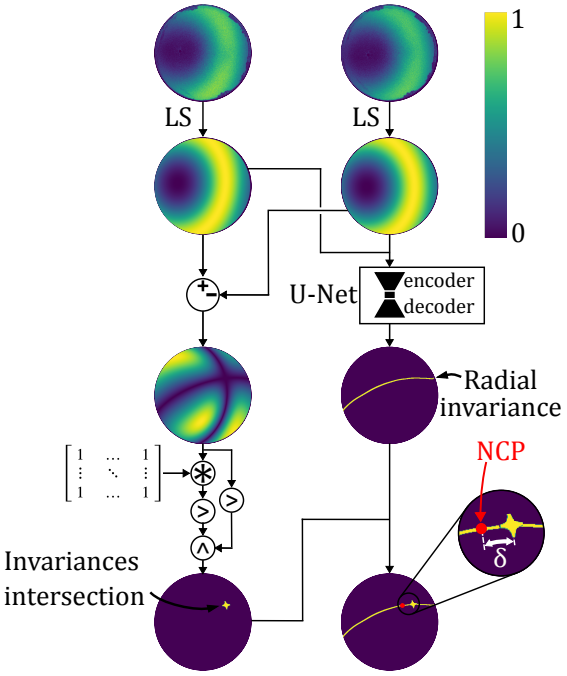

FIGURE 3.43. – Method for finding the NCP based on the skylight's DoLP pattern and the solar declination δ. In the first row is a pair of DoLP patterns obtained with a DoFP polarimetric camera equipped with a fisheye lens. Those images are then matched with a Rayleigh based simulation using the least square method. The absolute differences between the simulated DoLP patterns is then computed. Next, the intersection of the invariances is obtained by binarizing the images with a threshold represented by the $>$ symbol, a convolution, represented with the $*$ symbol and a logical AND operator represented by the $\wedge$ symbol. Simultaneously, the radial invariance is isolated by using a U-Net neural network. Finally, the NCP position is estimated by combining the radial invariance, the intersection of the polarization invariances and the solar declination δ.

pole's elevation. Second, if the latitude and the solar declination had the same sign, then, we considered that the intersection of the invariances had a lower elevation compared to the celestial pole's elevation. By analysing the results, we can see that those two conditions are true for a majority of cases. However, we observe that in some conditions the results differ a lot from what was expected. Most errors occur near the poles or the equator. Near the poles, the celestial pole is close to the zenith. Therefore, the intersection of the invariances will most often have a lower elevation than the celestial pole, which is not a case covered by our algorithm. Near the equator, we will often observe the opposite intersection of invariances, which explains the near 180° errors in azimuth around 0° latitudes. For those reasons, we analysed our results with and without outliers using Matlab rmoutliers function. We finally obtained a

mean absolute error (MAE) of 0.7111 degrees in azimuth (10.4908 with outliers), and 0.4639 degrees in azimuth (1.6776 degrees with outliers). Results are plotted on Fig. 3.44

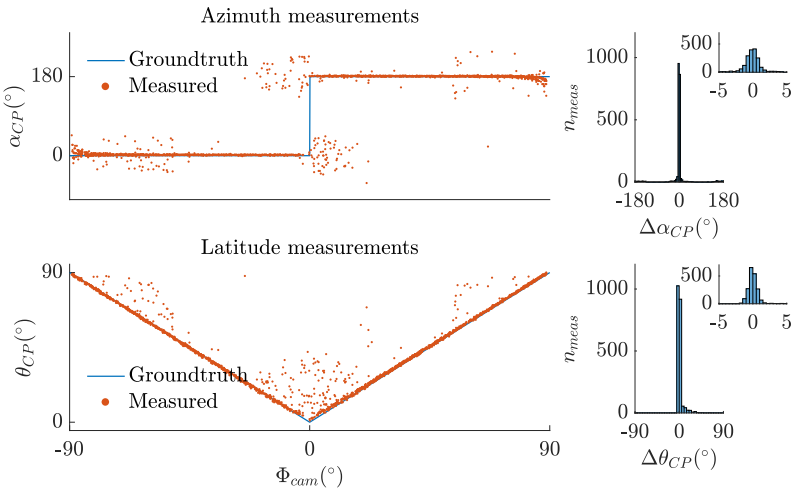

FIGURE 3.44. – Celestial pole coordinates computed from simulated data with the proposed algorithm (cf. figure 3.43). α_{CP} is the azimuth of the celestial pole with respect to the camera frame (north has 180° azimuth). θ_{CP} is the altitude of the celestial pole, which is also equal to the camera's latitude Φ_{cam}. $\Delta\alpha_{CP}$ and $\Delta\theta_{CP}$ are the azimuth and altitude error, respectively, in degrees, of the celestial pole measured with respect to the ground truth values. n_{meas} is the number of measurements for each error interval of the histogram. The zoomed in histogram corresponds to NCP coordinates values with absolute error lower than 5 degrees. It represents 1926 measurements out of 2078 in azimuth, and 2058 measurements out of 2078 in elevation.

3.3.4.3. Experimental results

We tested our method over the period from the 29 July 2022 to the 29 August 2022. This period corresponds to a solar declination ranging from 18.7 degrees to 9.35 degrees, respectively. We used sets of two DoLP images taken at 20 minute intervals, between sunrise and sunset. Our data comprises various weather conditions, from clear to overcast sky. The dataset used for this experiment can be accessed on an open archive [86]. The data processing used to obtain our results prevents outliers results by processing only images with maximum DoLP, detected from the least square step, higher than 0.2. Since buildings appeared in the field of view, we only applied the least squares to central pixels, corresponding approximately to points in the sky with elevations higher than 10 degrees with respect to the camera frame. Moreover, the algorithm sometimes could not yield a usable result when the neural network

failed to correctly isolate the radial invariance. However, outlier values could still appear due to the least square step and the deep learning step. We therefore decided to quantitatively present our results before and after removing outliers with Matlab function rmoutliers (default parameters). We finally obtained 671 measurements after removing outliers from a total of 791 measurements. After removing outliers with rmoutliers, we obtained a mean absolute error (MAE) of 1.6244 degrees in azimuth (9.0040 degrees with outliers), and 1.8303 degrees in latitude (4.3273 degrees with outliers). Results, with outliers, are presented in Fig. 3.45.

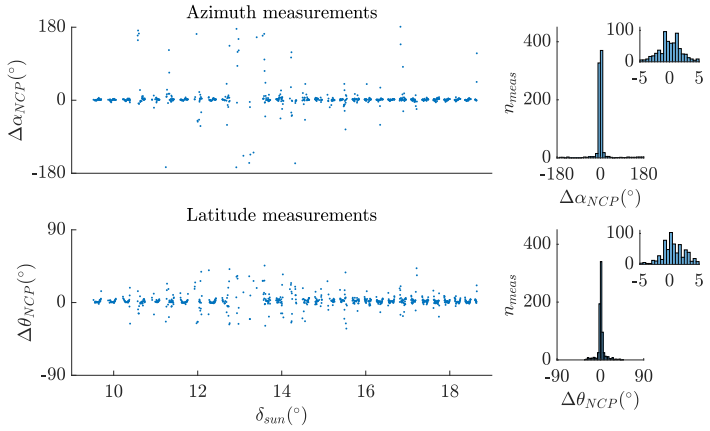

FIGURE 3.45. – NCP coordinates estimation error. NCP coordinates were computed from experimental data with the proposed algorithm (cf. Fig. 3.43). δ_{sun} is the solar declination in degrees. $\Delta\alpha_{NCP}$ and $\Delta\theta_{NCP}$ are the azimuth and altitude error, respectively, in degrees, of the NCP measured with respect to the ground truth values. n_{meas} is the number of measurements for each error interval of the histogram. The zoomed in histogram corresponds to NCP coordinate values with an absolute error lower than 5 degrees. It represents 645 measurements out of 791 in azimuth, and 627 measurements out of 791 in elevation.

3.4. Discussion

3.4.1. Navigation algorithms

In this chapter, we described the time variations of the skylight DoLP based on the Rayleigh single scattering model, and suggested three algorithms to detect the NCP. The efficiency of our methods have been proved in simulations and under experimental conditions, thus confirming the validity of the theoretical models.
The first algorithm, named SkyPole (cf. section 3.3.2), requires only visual observations of the skylight polarization patterns to detect the NCP. No knowledge of time, date, or ephemeris, and no estimates of the actual or initial position are required for this

purpose. The image processing steps do not rely on large computational resources, and have been kept as simple as possible. The main difficulty of this algorithm is the choice of the threshold value, that may be tuned depending on the time interval between two measurements. The presented algorithm requires at least four skylight polarization measurements, with time intervals between each measurements of 30 to 60 minutes, leading to long acquisition times.
The acquisition time was drastically reduced through the second algorithm (cf. section 3.3.3), which allows the removal of a potential ambiguity due to multiple intersections between the plane and radial DoLP time invariances. In this algorithm, the skylight polarization images are processed with a neural network, in order to segment the radial invariance. Using this algorithm, three images are necessary to obtain the position of the NCP. Moreover, by using a neural network, the threshold used for the segmentation of the radial invariance is tuned automatically, meaning the algorithm's parameters should not be modified manually by its user. This algorithm, however, is more complex than the previous one, since it requires the training of a neural network, and the matching of the experimental images with simulated images based on the least squares method, which is computationally expensive. The neural network used to isolate the radial invariance, could be replaced by directly simulating the radial invariance from the Sun's positions and the equation 3.35. Indeed, as shown in section 3.1.2, a large amount of methods were developed in order to locate the Sun from polarization patterns. However, the purpose of using a neural network was to show the feasibility of isolating the radial invariance directly from DoLP patterns. Ideally, a neural network should return the radial invariance image straight from real DoLP images, meaning that the least squares step would be optional. Using a neural network approach, rather than least squares, can prevent prediction errors linked to noise, such as buildings or clouds, which are difficult to avoid automatically. Indeed, in our experiments, even though the conditions where ideal, taking into account the whole image to compute the least square method led to biased results, due to buildings reflecting polarized light in the camera field of view. We therefore processed images without considering pixels near the horizon.
When training a neural network to isolate the radial invariance, particular attention should be given to the following elements. First, distinguishing the plane and radial invariances can be ambiguous when the Sun is under the horizon. Indeed, because of the symmetry of the DoLP pattern, only using this information does not tell whether the Sun is over or under the horizon. We thus chose to train our neural network using only positive Sun elevations. Next, the database used for training the network can be biased. Indeed, if a dataset is acquired using one camera in a fixed orientation, as in [86], the Sun will only move within a small region of the sky with respect to the camera. Therefore, applying data augmentation techniques to the dataset, such as random rotations, is crucial to obtain unbiased results.
The last algorithm (cf. section 3.3.4) also allows for reducing the acquisition time, by adding information, namely the solar declination. By using this information, the NCP can be located from two DoLP measurements. Solar declination is a convenient parameter since it varies slowly over time and can be easily obtained. To get a good

estimation of the solar declination, it is important to know the time. However, knowing only the date can be sufficient. Over the course of a day, solar declination can vary up to about 0.5 degree [247], therefore, if no approximation of the hour is given, by considering the declination at 12:00am, the declination error will have an upper bound of 0.25 degree. This bound is actually an overestimation since no measurements are considered when there is no sunlight. Moreover, this method supposes that the time interval between two observations is small. But how small should that time interval be? Through the approximation made in the section 3.2.2.2.2, we see that observations of under 30 minutes will induce less than 0.2 degree of error. Lower time intervals will yield lower errors. However, a trade-off should be made between reducing the time interval to minimize the approximation induced error, and increasing the invariances segmentation error when the time interval is decreased.
In the Polendar algorithm, we first used the least squares method to match a simulation image to a real image. Using a simulation to compute our algorithm is advantageous since our theoretical materials are based on Rayleigh's single scattering model, which differs from the real skylight polarization. A critical aspect of our method is the possibility for the maximum DoLP to change between two measurements (cf. section 1.3.2.2). Indeed, when the maximum DoLP changes, the intersection of the radial and plane invariances disappears (cf. figure 3.46).

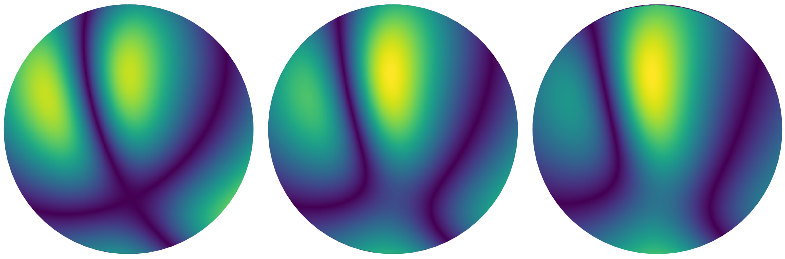

FIGURE 3.46. – DoLP invariance patterns for varying maximum of DoLP. Each figure was obtained by computing the absolute difference between two DoLP patterns simulated with Sun elevations 15° and 25°, and Sun azimuths 15° and 25°, respectively. The maximum DoLP for the DoLP pattern corresponding to Sun azimuth and elevation both equal to 15° was set to 0.7. The second image's maximum of DoLP was set, from left to right, to 0.7, 0.75 and 0.8.

In [96], clouds were shown to have a critical influence on the sky's DoLP. To avoid issues related to the variation of maximum DoLP, our method should be applied using short time intervals. When reducing the time interval between two images, the variations in the whole image decrease, and the invariances become less easily detected from the rest of the image. In our case, we fixed this issue by matching real images with simulated images having the same maximum DoLP value.
The last step of the Polendar algorithm, which consists in detecting the NCP from the intersection of the radial and plane invariances, and the solar declination, should also be discussed. In this step, the main difficulty is to find the position of the NCP given

two options, namely below or over the intersection of the radial and plane invariances. To remove the ambiguity, one can use the Sun's positions or a rough estimate of it, and the sign of the declination. However, the Sun position may not be known. Therefore, studying the DoLP near the intersection of invariances can give a cue whereas the NCP is above the intersection of invariances or not. Unfortunately, we do not have a universal condition yet for this issue. To select the NCP, we used the following condition for our data, for positive declination, the NCP was considered having a higher elevation than the intersection of the invariances. This condition works for most of the cases, but fails for some conditions, for instance, when the celestial pole is near the zenith or near the horizon, the intersection of the invariances will frequently have lower or higher elevation respectively (cf. section 3.3.4.2). Also, an ambiguity can be related to the intersection of the invariances itself. In fact, for some conditions, the intersection of invariances will be located under the horizon. However, in this case, we will detect the opposite intersection of invariances, which, if not spotted, will induce an error in the estimation of the NCP. An alternative would be to combine the Polendar method with the SkyPole method. In fact, combining those two methods would remove the ambiguity of the Polendar method. However, at least three measurements would be required for the SkyPole method.

The accuracy of the three algorithms is too low for some geolocation applications. Indeed, one degree error in latitude represents more than 100km error. One degree error in true north has a lower impact (cf figure 3.47).

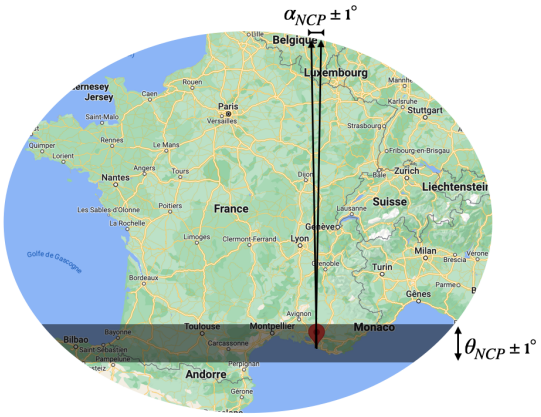

FIGURE 3.47. – Representation of 1° error in latitude and true north on a map, for the camera's position. α_{NCP} is the azimuth of the NCP and θ_{NCP} is the elevation of the NCP.

It is worth noting, however, that the first algorithm has been kept as simple as possible, and all three algorithms were meant to process DoLP images in a visual manner, and were not optimized. Also, the NCP position is rounded to the closest pixel. The best result, we can achieve, is therefore half a pixel on the processed image. Moreover, we processed only the blue channel of our polarization sensor, reducing the resolution

by a factor of two, and the computation of the DoLP from a super pixel also reduced the resolution by a factor two. Therefore, the best pixel precision achievable by our algorithm is only two pixels of the camera sensor. In addition, the use of a fisheye lens, practical for visualizing the whole sky is not the best suited for precise measurements. Indeed, since the total field of view is large, the angular precision of each pixel is lower than when using a lens providing a smaller field of view. In order to improve the algorithms results, the four color channels should be computed, and a fisheye lens may not be used. Instead, a rectilinear lens could be used. A rectilinear lens may not allow a view of the whole sky dome. However, as the sky polarization gives redundant information on the position of the Sun, the whole skylight pattern can be interpolated from a small region in the sky. An interesting aspect about rectilinear lens is that they perform gnomonic projection. Such projections transform a great circle into a straight line. Therefore, by using a rectilinear lens, the invariances would be straight lines, and a linear regression of the invariances could thus be implemented to find the NCP even if it is not in the camera's field of view.
In the presented algorithms, the largest source of error originates from skylight noise due to multiple scattering or non-Rayleigh scattering in the atmosphere, such as Mie scattering, for instance. In this thesis, in order to reduce the influence of this kind of noise, we used data with low noise levels, corresponding to a clear blue sky or an only slightly overcast sky. In order to cope with noisy skies, in cloudy situations for instance, denoising techniques can be applied prior to the proposed algorithms. Alternatively, since the theory of the invariances was descibed, the processing of the sky invariances can be done indirectly, by computing the Sun's position. As shown in section 3.1.2, the Sun's position can be obtained from DoLP and AoP patterns. Therefore, the accuracy of the NCP localization would be linked to the accuracy of the Sun localization. Furthermore, as the DoLP is more sensitive to clouds and aerosols than the AoP [108], adding information of the AoP in our algorithms would increase the robustness of the NCP localization. However, the advantage of the invariances is that they represent sparse data. Therefore, they may require lower amounts of data to process than when computing the position of the Sun based on the whole pattern of polarization, or may be less expensive to compute. Apart from considering new techniques of data processing, which offer promising results [201, 200], the influence of clouds on our results could have been reduced by using ultraviolet (UV) wavelength [109]. Many animals are sensitive to UV light and use this for navigation, the skylight pattern of polarization being robust to clouds in the UV [105, 110] (cf. section 1.3.3). Last, it is worth noting that, since our algorithm is time based, as we increase the number of skylight DoLP measurements, we may improve the precision of the NCP localization.

In this section, we discussed about the algorithms developed in this thesis. Even though those algorithms suffer from a low precision, they provide encouraging results. The theory developed simultaneously offers a great understanding of the time variations of the skylight polarization, and allows for solving the skylight polarization based navigation problem through an innovative bird's-eye view.

3.4.2. Animals navigation

In the previous section, we presented technical aspects about the developed algorithms. Yet, since the presented navigation methods are inspired from migrating animals, it seems relevant to discuss those from an animal perspective. Here, we discuss the suitability of those methods for animal navigation.
The SkyPole algorithm presented in section 3.3.2 was made voluntarily as simple as possible, consisting only in tasks that can be achieved by animals, such as memorizing [12], subtracting or adding images [248], and finding the intersection of lines. This suggests that locating the celestial pole from skylight polarization invariances would be conceivable for animal navigation. Interestingly, studies on the visual magnetoreception of migratory birds introduced patterns similar to the polarization invariances to describe the perception of the magnetic field by migratory birds to find True North [249]. However, the DoLP is generally thought as an indicator of the reliability of polarization information for navigation [250]. The use of the celestial pole's elevation to obtain a latitude estimation is actually discussed [233].
The Polendar method suggests that using short time intervals when observing the time variations of skylight polarization could be advantageous. Moreover, studies suggest that pigeons can perceive very slow movements, even as slow as the rotation of the sky [251]. Real time calibration of their magnetic compass is therefore conceivable using skylight polarization. Additionally, the two solar equinoxes are of particular interest when considering solar declination. During the equinoxes, around the 20 March and the 23 September, solar declination is null. This simplifies the Polendar method considerably since the NCP coincides more or less with the intersection of the invariances. As a consequence, no calculations are needed, only the intersection of the invariances has to be detected, and interestingly, many birds migrate around the equinoxes [252].
Apart from navigating, skylight polarization can be considered as a convenient source for animals to synchronize their circannual clock. Two types of migratory birds can be distinguished, namely facultative and obligate migrants. The first do not necessarily migrate, and do so depending on local conditions such as food and weather. The second migrate at a precise timing during the year, independently from variable conditions. Obligate migrants are thought to rely on a circannual clock to determine the moment at which they migrate. Going back to the polarization invariances, if the position of the NCP is known without knowledge of the solar declination, we can deduce the solar declination from the distance between the NCP and the intersection of the invariances, and thus calibrate a circannual clock. For instance, at dawn and dusk, when polarized sunlight and stars are both visible, stars can be used to detect the celestial pole and combined with the polarization invariances to compute the solar declination (cf figure 3.48).

As evoked in section 3.2.3, the longitude, not measured in the presented algorithms, can be deduced from a double clock mechanism. Indeed, if a first clock is synchronized on the solar time of an initial position, and compared to the solar time measured at a second position, then, the difference of longitude between the two positions

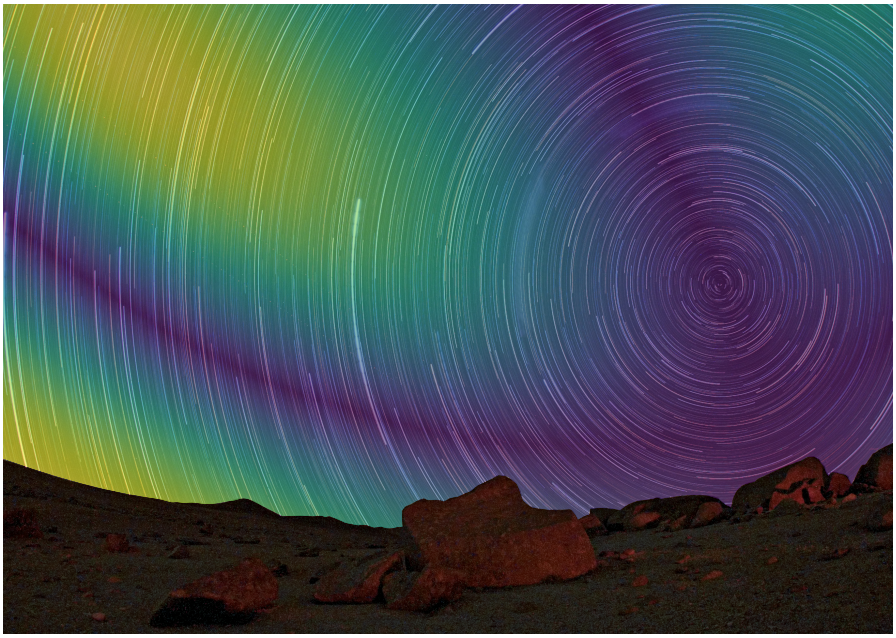

FIGURE 3.48. – Artistic view of the celestial rotation of stars during night and of skylight polarization during day. Adapted from ESO/B. Tafreshi (twanight.org) (cf. figure 3.17).

can be obtained from the difference of time between the two clocks. Migratory birds' internal clock was shown to be set, and to remain, at the time of their starting location during migration [253]. However, the double clock hypothesis for birds migration was contested by showing that a dark-light regime had no influence on the longitude estimation [254]. Yet, this study did not take skylight polarization into account. More generally, since migratory birds are thought to locate with a 2 kilometers precision, the use of the Sun to measure the longitude was considered unlikely, requiring an extremely precise clock [255]. Instead, a popular hypothesis suggests that birds can locate by means of a bi-coordinate map, different from latitude and longitude, based on magnetic fields [255]. The magnetoreception of birds is still misunderstood [256, 257] and controversial [22]. The rejection of the Sun hypothesis for longitude estimation based on the localization precision of migratory birds seems questionable. Indeed, birds may rely on multiple cues for navigation. Some, as skylight polarization, could provide a coarse positioning, which may be adjusted by using other cues, such as odors [258]. Moreover, in some studies, instead of the celestial pole, the Sun's azimuth was considered as a compass cue, requiring a clock. Based on this assumption, clock shifting experiments were implemented and led to the conclusion that birds do not use the Sun for estimating their longitude [259, 260]. Those studies, however, did not lead to the orientation changes expected if the Sun and a clock were involved in the birds' compass.

To conclude this discussion, the mechanisms involved in the true navigation of migratory birds remain uncertain. Studies on skylight polarization are difficult to implement.

Using linear polarizers to vary the observed angle of polarization in the sky removes all variations in AoP and DoLP. Therefore, using a half-wave plate should be preferred, since it allows modifying the angle of polarization without changing the DoLP. However, wave plates and other polarizing components have properties depending on the tilt of the component with respect to the incident ray [261, 146], which may cause non-uniform modifications of the skylight polarization for animal studies. In addition, to study the celestial rotation during day, using a fixed polarizing component, such as a half-wave plate, may not allow for detecting behavioural changes since this phenomenon may be only related to variations of the polarization. Also, rotating a half-wave plate will not change the DoLP, but only the AoP, which may not have any influence on the celestial compass if based on DoLP invariances. To study the celestial rotation during night, artificial skies were displayed in a planetarium. Doing so with skylight polarization is much harder, in particular because of skylight being partially polarized. Those technical challenges must be met to improve our understanding of skylight polarization based navigation. The rotation of skylight polarization seems to be a convenient cue for animal navigation, and was proven necessary even for insects such as *Cataglyphis* desert ants [262].

Conclusion

In this manuscript, the skylight polarization was studied as a navigation cue. As discussed in the introduction, the aim of this thesis was to study the acquisition and processing of skylight polarization in noisy situations, namely cloudy skies or in presence of obstacles in the field of view, and to design a geolocation method based on skylight polarization. The optimization of skylight polarization acquisition was addressed through UV sensing, which was shown to provide reliable polarization information in presence of clouds. A setup was implemented to characterize the performances of a UV sensor illuminated under partially polarized light, with controllable DoLP and AoP. This setup allows to describe a sensor's characteristics in conditions similar to those observed outdoor. However, no sensor was yet characterized using this setup, and the use of UV sensors for skylight polarization measurements was not further investigated. On the other side the geolocation task was more deeply studied. An innovative geolocation method, inspired from migratory birds, was developed, requiring only skylight DoLP measurements over time. This method allows to estimate the position of the celestial pole, and therefore estimate the measurement device's latitude and True North. The solar declination and local solar time could also be measured, allowing to estimate variations of longitude. This step was, however, not processed in this thesis.

Even though this thesis provided new insights on the use of skylight polarization for geolocation, unresolved questions still remain concerning optimal ways of sensing and processing skylight polarization, and on geolocation based on skylight polarization. As this subject is inspired from animals, these questions are, in addition to technical aspects, linked to animal navigation. We discuss next some perpectives concerning the presented work.
Existing sensors offer good performances for sensing skylight polarization. Yet, few UV polarimetric sensors where developed and available. As indicated in chapter 2, UV sensors are being designed in parallel to this thesis. In addition to UV sensing, sensors could be optimized, by taking inspiration from animals. As for insects, the number of photoreceptors of devices could be kept low to optimize the quantity of data to analyse. Also, insects possess only two orthogonal orientations of their « polarizing filters » per photodetector, which does not allow them to measure the AoP and DoLP in each point of the sky. Therefore, polarimetric sensors could be optimized by considering spatial redundancy of the skylight polarization pattern. The spectral properties of skylight polarization are not often considered, but could help processing polarization images. Most insects sense polarization in a single color, but some animals, such as the mantis shrimp sense polarization in multiple colors. Moreover, migratory birds sense magnetic fields through vision, which could have an influence on the perception

of skylight polarization. However, birds vision remains misunderstood, and, to my knowledge, no sensor was developed for light-based measurements of magnetic fields. Regarding navigation methods, the performances of the proposed algorithms can be improved by image processing methods. However, an analysis of factors influencing the algorithms' performances should be done. This analysis must indicate what precision can be expected, as a function of the measurement time. As a first approximation, in clear sky conditions, the precision obtained by using a sextant (a few hundred meters) should be achievable by using a polarimetric device. However, to obtain precise measurements, some hypotheses should be reconsidered. For instance, when using a sextant, the Earth curvature is not neglected. This hypothesis may not have a strong influence on skylight polarization measurements, since most devices are pointing towards the zenith, but its effects should be studied. The proposed algorithms could also be studied for underwater geolocation or during night, by using the polarization pattern induced by moonlight, which is similar to that induced by sunlight, during day. As discussed in section 3.4.1, small errors in the detection of celestial cues can induce high localization error. It is not clear yet if skylight polarization is used by animals for positioning or only for finding true north. If skylight polarization was used for geolocation, however, it could provide a coarse position. A precise localization could then be obtained by using local information such as landscapes and odors. Sensor fusion appears to be crucial for robust navigation. The proposed navigation algorithms lead to ambiguous results near the equator. Combining skylight polarization with magnetic fields can remove this ambiguity. Migratory birds were also shown to extract compass information from different cues, such as the magnetic field, skylight polarization and stars. Finally, the presented navigation methods may question some conclusions of animals studies. Indeed, it is often considered that migratory birds' polarization compass are time-based. However, these methods show that a polarization compass may not necessarily be time-dependent. It could be interesting to analyse results obtained through clock-shifting experiments by also considering that a polarization compass could be independent from time.

Bibliographie

[1] B RENFRO, Miquela STEIN, E REED et al. « An Analysis of Global Positioning System (GPS) Standard Positioning Service Performance for 2019 ». In : *The University of Texas at Austin* (2020), p. 1-111. URL : https://www.gps.gov/systems/gps/performance/2019-GPS-SPS-performance-analysis.pdf (cf. p. 19).

[2] Tomislav KOS, Ivan MARKEZIC et Josip POKRAJCIC. « Effects of multipath reception on GPS positioning performance ». In : *Proceedings ELMAR-2010*. 2010, p. 399-402. URL : https://ieeexplore.ieee.org/document/5606130 (cf. p. 19).

[3] Abdulghani MOHAMED, Reece CLOTHIER, Simon WATKINS et al. « Fixed-Wing MAV Attitude Stability in Atmospheric Turbulence PART 1 : Suitability of Conventional Sensors ». In : *Progress in Aerospace Sciences* 70 (oct. 2014), p. 69-82. DOI : 10.1016/j.paerosci.2014.06.001 (cf. p. 19).

[4] Tegg WESTBROOK. « Will GPS Jammers Proliferate in the smart city ? » In : *Salus Journal* 7.2 (2019), p. 45-67. URL : https://journals.csu.domains/index.php/salusjournal/article/view/102 (cf. p. 19).

[5] Jonathan A. LARCOM et Hong LIU. « Modeling and characterization of GPS spoofing ». In : *2013 IEEE International Conference on Technologies for Homeland Security (HST)*. 2013, p. 729-734. DOI : 10.1109/THS.2013.6699094 (cf. p. 19).

[6] Todd HUMPHREYS, B. LEDVINA, Mark PSIAKI et al. « Assessing the Spoofing Threat : Development of a Portable GPS Civilian Spoofer ». In : *Proceedings of the 21st International Technical Meeting of the Satellite Division of The Institute of Navigation (ION GNSS 2008)*. Jan. 2008, p. 2314-2325. URL : https://gps.mae.cornell.edu/humphreys_etal_iongnss2008.pdf (cf. p. 19).

[7] Moshe KAM, Xiaoxun ZHU et Paul KALATA. « Sensor fusion for mobile robot navigation ». In : *Proceedings of the IEEE* 85.1 (1997), p. 108-119. DOI : 10.1109/JPROC.1997.554212 (cf. p. 19).

[8] David M BEVLY. « Global positioning system (GPS) : A low-cost velocity sensor for correcting inertial sensor errors on ground vehicles ». In : *J. Dyn. Sys., Meas., Control* 126.2 (2004), p. 255-264. DOI : 10.1115/1.1766027 (cf. p. 19).

[9] Arnaud CHULLIAT, Gauthier HULOT, Lawrence NEWITT et al. « What Caused Recent Acceleration of the North Magnetic Pole Drift ? » In : *EOS Transactions* 91 (déc. 2010). DOI : 10.1029/2010EO510001 (cf. p. 19).

[10] W. M. SMART. *Textbook on Spherical Astronomy*. 6e éd. Cambridge University Press, 1977. DOI : 10.1017/CBO9781139167574 (cf. p. 19, 86, 98).

[11] INTERNATIONAL MARITIME ORGANIZATION. *International Convention for the Safety of Life at Sea (SOLAS)*. Amended and updated through subsequent sessions. 1974. URL : https://www.imo.org/en/About/Conventions/Pages/International-Convention-for-the-Safety-of-Life-at-Sea-(SOLAS),-1974.aspx (cf. p. 19).

[12] James GOULD et Carol GOULD. *Nature's Compass : The Mystery of Animal Navigation*. Princeton University Press, déc. 2012. ISBN : 9781400841660. DOI : 10.1515/9781400841660 (cf. p. 19, 20, 90, 99, 140).

[13] Blair E WITHERINGTON et Karen A BJORNDAL. « Influences of wavelength and intensity on hatchling sea turtle phototaxis : implications for sea-finding behavior ». In : *Copeia* (1991), p. 1060-1069. DOI : 10.2307/1446101 (cf. p. 20).

[14] Marie DACKE, Emily BAIRD, Marcus BYRNE et al. « Dung beetles use the Milky Way for orientation ». In : *Current biology* 23.4 (2013), p. 298-300. DOI : 10.1016/j.cub.2012.12.034 (cf. p. 20, 90).

[15] Gábor HORVÁTH, Amit LERNER et Nadav SHASHAR. *Polarized light and polarization vision in animal sciences*. T. 2. Springer, 2014. URL : https://link.springer.com/book/10.1007/978-3-642-54718-8 (cf. p. 20, 24, 30, 55, 61, 90, 93, 95).

[16] VP BINGMAN et K CHENG. « Mechanisms of animal global navigation : comparative perspectives and enduring challenges ». In : *Ethology Ecology & Evolution* 17.4 (2005), p. 295-318. DOI : 10.1080/08927014.2005.9522584 (cf. p. 20).

[17] Albert C PERDECK. « Two types of orientation in migrating starlings, Sturnus vulgaris L., and chaffinches, Fringilla coelebs L., as revealed by displacement experiments ». In : *Ardea* 46 (1958), p. 1-37. DOI : 10.5253/arde.v1i2.p1. URL : https://doi.org/10.5253/arde.v1i2.p1 (cf. p. 20).

[18] Kasper THORUP et Jørgen RABØL. « Compensatory behaviour after displacement in migratory birds : a meta-analysis of cage experiments ». In : *Behavioral Ecology and Sociobiology* 61 (2007), p. 825-841. DOI : 10.1007/s00265-006-0306-x (cf. p. 20).

[19] Rüdiger WEHNER et Martin MÜLLER. « Piloting in desert ants : Pinpointing the goal by discrete landmarks ». In : *The Journal of experimental biology* 213 (déc. 2010), p. 4174-9. DOI : 10.1242/jeb.050674 (cf. p. 20).

[20] DM VOWLES. « Sensitivity of ants to polarized light ». In : *Nature* 165.4190 (1950), p. 282-283. DOI : 10.1038/165282a0 (cf. p. 20, 23).

[21] Martin MÜLLER et Rüdiger WEHNER. « Path integration in desert ants, Cataglyphis fortis ». In : *Proceedings of the National Academy of Sciences* 85.14 (1988), p. 5287-5290. DOI : 10.1073/pnas.85.14.5287. URL : https://www.pnas.org/doi/abs/10.1073/pnas.85.14.5287 (cf. p. 20).

[22] Jonathan T HAGSTRUM. « Avian navigation : the geomagnetic field provides compass cues but not a bicoordinate "map" plus a brief discussion of the alternative infrasound direction-finding hypothesis ». In : *Journal of Comparative Physiology A* 210.2 (2024), p. 295-313. DOI : 10.1007/s00359-023-01627-9 (cf. p. 20, 141).

[23] Larry BOLES et Kenneth LOHMANN. « True Navigation and Magnetic Maps in Spiny Lobsters ». In : *Nature* 421 (fév. 2003), p. 60-3. DOI : 10.1038/nature01226 (cf. p. 20).

[24] Julien R. SERRES, Pierre-Jean LAPRAY, Stéphane VIOLLET et al. « Passive Polarized Vision for Autonomous Vehicles : A Review ». In : *Sensors* 24.11 (2024). ISSN : 1424-8220. DOI : 10.3390/s24113312. URL : https://www.mdpi.com/1424-8220/24/11/3312 (cf. p. 20, 67).

[25] Karl von FRISCH. « Die Polarisation des Himmelslichtes als orientierender Faktor bei den Tänzen der Bienen ». In : *Experientia* 5 (1949), p. 142-148. URL : https://api.semanticscholar.org/CorpusID:37498871 (cf. p. 20, 23).

[26] Julien DUPEYROUX, Julien SERRES et Stéphane VIOLLET. « AntBot : A six-legged walking robot able to home like desert ants in outdoor environments ». In : *Science Robotics* 4 (fév. 2019), eaau0307. DOI : 10.1126/scirobotics.aau0307 (cf. p. 20, 58, 62, 90, 92).

[27] Julien DUPEYROUX, Stephane VIOLLET et Julien R SERRES. « An ant-inspired celestial compass applied to autonomous outdoor robot navigation ». In : *Robotics and Autonomous Systems* 117 (2019), p. 40-56. DOI : https://doi.org/10.1016/j.robot.2019.04.007 (cf. p. 21).

[28] R. BARTHOLIN. *Experimenta Crystalli Islandici disdiaclastici, quibus mira et insolita refractio detegitur*. 1669. URL : https://books.google.fr/books?id=F7RAAAAAcAAJ (cf. p. 22).

[29] C. HUYGENS. *Traite de la lumiere : Où sont expliquées les causes de ce qui luy arrive dans la reflexion, & dans la refraction. Et particulierement dans l'etrange refraction du cristal d'Islande*. Chez Pierre vander Aa, 1690. URL : https://books.google.fr/books?id=X9PKaZlChggC (cf. p. 22).

[30] I. NEWTON. *Optique*. Optique vol. 2. Ph. D. Pierres, chez Leroy, 1787. URL : https://books.google.fr/books?id=Cc51wtmvzvIC (cf. p. 22).

[31] Thomas YOUNG. « I. The Bakerian Lecture. Experiments and calculations relative to physical optics ». In : *Philosophical Transactions of the Royal Society of London* (1804), p. 1-16. DOI : 10.1098/rstl.1804.0001 (cf. p. 22).

[32] EL MALUS. « Sur une propriété de la lumière réfléchie ». In : *Mém. Phys. Chim. Soc. d'Arcueil* 2 (1809), p. 143-158. URL : https://fr.wikisource.org/wiki/Sur_une_propri%C3%A9t%C3%A9_de_la_lumi%C3%A8re_r%C3%A9fl%C3%A9chie (cf. p. 22).

[33] F. ARAGO et J.A. BARRAL. *Oeuvres complètes de François Arago : secrétaire perpétuel de l'Académie des sciences*. Gide et J. Baudry, 1854. URL : https://books.google.fr/books?id=r8Yo0AEACAAJ (cf. p. 22).

[34] J BABINET. « Sur un nouveau point neutre dans l'atmosphere ». In : *CR Acad. Sci. Paris* 11 (1840), p. 618-620 (cf. p. 22).

[35] D BREWSTER. « On the existence of a new neutral point and two secondary neutral points ». In : *Rep. Brit. Assoc. Adv. Sci* 2 (1842), p. 13-25 (cf. p. 23).

[36] Gábor HORVÁTH, Balázs BERNÁTH, Bence SUHAI et al. « First observation of the fourth neutral polarization point in the atmosphere ». In : *J. Opt. Soc. Am. A* 19.10 (oct. 2002), p. 2085-2099. DOI : 10.1364/JOSAA.19.002085. URL : https://opg.optica.org/josaa/abstract.cfm?URI=josaa-19-10-2085 (cf. p. 23).

[37] David BREWSTER. « IX. On the laws which regulate the polarisation of light by reflexion from transparent bodies. By David Brewster, LL. DFRS Edin. and FSA Edin. In a letter addressed to Right Hon. Sir Joseph Banks, Bart. KBPR S ». In : *Philosophical Transactions of the Royal Society of London* (1815), p. 125-159. DOI : 10.1098/rstl.1815.0010 (cf. p. 23).

[38] Augustin FRESNEL. *Oeuvres complètes d'Augustin Fresnel*. T. 3. Imprimerie impériale, 1870. URL : https://archive.org/details/bub_gb_3QgAAAAAMAAJ (cf. p. 23).

[39] Wilhelm HAIDINGER. « Ueber das directe Erkennen des polarisirten Lichts und der Lage der Polarisationsebene ». In : *Annalen der Physik* 139.9 (1844), p. 29-39. DOI : https://doi.org/10.1002/andp.18441390903. eprint : https://onlinelibrary.wiley.com/doi/pdf/10.1002/andp.18441390903. URL : https://onlinelibrary.wiley.com/doi/abs/10.1002/andp.18441390903 (cf. p. 23).

[40] George Gabriel STOKES. « On the composition and resolution of streams of polarized light from different sources ». In : *Transactions of the Cambridge Philosophical Society* 9 (1851), p. 399. URL : https://www.cambridge.org/core/books/abs/mathematical-and-physical-papers/on-the-composition-and-resolution-of-streams-of-polarized-light-from-different-sources/A021426E1F3E9BD366E8E1F967FBE3CE (cf. p. 23).

[41] H POINCARÉ. « Théorie mathématique de la lumière Vol. II Ch ». In : *XII (Gauthier-Villars, Paris, 1892)* (1892). URL : https://fr.wikisource.org/wiki/Livre:Henri_Poincar%C3%A9_-_Th%C3%A9orie_math%C3%A9matique_de_la_lumi%C3%A8re,_Tome_2,_1892.djvu (cf. p. 23).

[42] James Clerk MAXWELL. « VIII. A dynamical theory of the electromagnetic field ». In : *Philosophical transactions of the Royal Society of London* (1865), p. 459-512. DOI : 10.1098/rstl.1865.0008 (cf. p. 23).

[43] John TYNDALL. « IV. On the blue colour of the sky, the polarization of skylight, and on the polarization of light by cloudy matter generally ». In : *Proceedings of the Royal Society of London* (1869), p. 223-233. DOI : 10.1098/rspl.1868.0033 (cf. p. 23).

[44] J.W. STRUTT. « XV. On the light from the sky, its polarization and colour ». In : *The London, Edinburgh, and Dublin Philosophical Magazine and Journal of Science* 41.271 (1871), p. 107-120. DOI : 10.1080/14786447108640452. eprint : https://doi.org/10.1080/14786447108640452. URL : https://doi.org/10.1080/14786447108640452 (cf. p. 23, 46).

[45] Edwin H LAND. « Some aspects of the development of sheet polarizers ». In : *JOSA* 41.12 (1951), p. 957-963. DOI : 10.1364/JOSA.41.000957 (cf. p. 23).

[46] R Clark JONES. « A new calculus for the treatment of optical systemsi. description and discussion of the calculus ». In : *Josa* 31.7 (1941), p. 488-493. DOI : 10.1364/JOSA.31.000488 (cf. p. 23).

[47] Nathan Grieb PARKE III. « Optical algebra ». In : *Journal of Mathematics and Physics* 28.1-4 (1949), p. 131-139. DOI : 10.1002/sapm1949281131 (cf. p. 23).

[48] Subrahmanyan CHANDRASEKHAR. *Radiative transfer*. Courier Corporation, 1960. URL : https://archive.org/details/radiativetransfe0000chan/page/n7/mode/1up (cf. p. 23, 31).

[49] Felix SANTSCHI. « L'orientation sidérale des fourmis, et quelques considérations sur leurs différentes possibilités d'orientation ». In : *Mém. Soc. Vaudoise Sci. Nat.* 4 (1923), p. 137-175. URL : https://www.e-periodica.ch/digbib/view?pid=msv-001%5C%3A1922%5C%3A1%5C%3A%5C%3A207#207 (cf. p. 23).

[50] WG WELLINGTON. « Motor responses evoked by the dorsal ocelli of Sarcophaga aldrichi Parker, and the orientation of the fly to plane polarized light ». In : *Nature* 172.4391 (1953), p. 1177-1179. DOI : 10.1038/1721177b0 (cf. p. 23).

[51] F PAPI. « Orientamento astronomico in alcuni Carabidi ». In : *Atti. Soc. Toscana Sci. Nat. Mem., B* 62 (1955), p. 83-97 (cf. p. 23).

[52] F PAPI. « Ricerche sull'orientamento astronomico di Arctosa perita (Latr.)(Araneae, Lycosidae) ». In : *Pubbl. Staz. Zool. Napoli* 27 (1955), p. 76-103 (cf. p. 23).

[53] Humberto FERNÁNDEZ-MORAN. « Fine structure of the insect retinula as revealed by electron microscopy ». In : *Nature* 177.4512 (1956), p. 742-743. DOI : 10.1038/177742a0 (cf. p. 23).

[54] John B PHILLIPS et Jerry A WALDVOGEL. « Celestial polarized light patterns as a calibration reference for sun compass of homing pigeons ». In : *Journal of Theoretical Biology* 131.1 (1988), p. 55-67. DOI : https://doi.org/10.1016/S0022-5193(88)80120-6 (cf. p. 23).

[55] Kuno KIRSCHFELD, M LINDAUER et H MARTIN. « Problems of menotactic orientation according to the polarized light of the sky ». In : *Zeitschrift für Naturforschung C* 30.1-2 (1975), p. 88-90. DOI : 10.1515/znc-1975-1-219 (cf. p. 23).

[56] Michael Leo BRINES. *Skylight polarization patterns as cues for honey bee orientation; physical measurements and behavioral experiments*. The Rockefeller University, 1978. URL : https://digitalcommons.rockefeller.edu/student_theses_and_dissertations/611/ (cf. p. 23).

[57] Hilbert Willem VAN DER GLAS. « Polarization Induced Colour Patterns : a Model of the Perception of the Polarized Skylight By Insects ». In : *Netherlands Journal of Zoology* 25.4 (1974), p. 476-505. DOI : 10.1163/002829675X00074 (cf. p. 23).

[58] Paul L. HERRLING. *Topographische Untersuchungen zur funktionellen Anatomie der Retina von Cataglyphis bicolor Fabr. (Formicidae, Hymenoptera) /*. Zürich : Juris Druck Verl., 1975 (cf. p. 24).

[59] Samuel ROSSEL et Rüdiger WEHNER. « How bees analyse the polarization patterns in the sky : experiments and model ». In : *Journal of Comparative Physiology A* 154 (1984), p. 607-615. DOI : 10.1007/BF01350213 (cf. p. 24).

[60] Thorkild RAMSKOU. *Solstenen : primitiv navigation i norden før kompasset*. Rhodos., 1969 (cf. p. 24).

[61] Curt ROSLUND et Claes BECKMAN. « Disputing Viking navigation by polarized skylight ». In : *Applied optics* 33 (juill. 1994), p. 4754-5. DOI : 10.1364/AO.33.004754 (cf. p. 24).

[62] Ramn HEGEDS, Susanne AKESSON, Rüdiger WEHNER et al. « Could Vikings have navigated under foggy and cloudy conditions by skylight polarization? On the atmospheric optical prerequisites of polarimetric Viking navigation under foggy and cloudy skies ». In : *Proceedings of The Royal Society A Mathematical Physical and Engineering Sciences* 463 (fév. 2007). DOI : 10.1098/rspa.2007.1811 (cf. p. 24).

[63] Guy ROPARS, Gabriel GORRE, Albert FLOCH et al. « A depolarizer as a possible precise sunstone for Viking navigation by polarized skylight ». In : *Royal Society of London Proceedings Series A* 468 (nov. 2011), p. 671-684. DOI : 10.1098/rspa.2011.0369 (cf. p. 24).

[64] Balázs BERNÁTH, Miklós BLAHÓ, Adam EGRI et al. « Orientation with a Viking sun-compass, a shadow-stick, and two calcite sunstones under various weather conditions ». In : *Applied optics* 52 (sept. 2013), p. 6185-6194. DOI : 10.1364/AO.52.006185 (cf. p. 24).

[65] András BARTA, Gabor HORVATH et Victor MEYER-ROCHOW. « Psychophysical study of the visual sun location in pictures of cloudy and twilight skies inspired by Viking navigation ». In : *Journal of the Optical Society of America. A, Optics, image science, and vision* 22 (juill. 2005), p. 1023-34. DOI : 10.1364/JOSAA.22.001023 (cf. p. 24).

[66] Alexandra FARKAS, Denes SZAZ, Adam EGRI et al. « Accuracy of sun localization in the second step of sky-polarimetric Viking navigation for north determination : A planetarium experiment ». In : *Journal of the Optical Society of America A* 31 (juin 2014), p. 1645. DOI : 10.1364/JOSAA.31.001645 (cf. p. 24).

[67] Gabor HORVATH, András BARTA, István POMOZI et al. « On the trail of Vikings with polarized skylight : Experimental study of the atmospheric optical prerequisites allowing polarimetric navigation by Viking seafarers ». In : *Philosophical transactions of the Royal Society of London. Series B, Biological sciences* 366 (mars 2011), p. 772-82. DOI : 10.1098/rstb.2010.0194 (cf. p. 24).

[68] Charles WHEATSTONE. « On a means of determining the apparent Solar Time by the Diurnal Changes of the Plane of Polarization at the North Pole of the Sky ». In : *The Scientific Papers of Sir Charles Wheatstone*. Cambridge Library Collection - Technology. Cambridge University Press, 1879, p. 285-289. DOI : 10.1017/CBO9781139057950.028 (cf. p. 24, 116).

[69] P DRUDE. « Ueber oberflächenschichten. II. theil ». In : *Annalen der Physik* 272.4 (1889), p. 865-897. DOI : 10.1002/andp.18892720409 (cf. p. 24).

[70] AH PFUND. « A Polaroid Half-Shade Analyzer ». In : *JOSA* 26.12 (1936), p. 453-453. DOI : 10.1364/JOSA.26.000453 (cf. p. 24).

[71] Pierre-Yves DESCHAMPS, Maurice HERMAN, A. PODAIRE et al. « POLDER instrument : mission objectives ». In : *Polarization and Remote Sensing*. Sous la dir. de Walter G. EGAN. T. 1747. International Society for Optics et Photonics. SPIE, 1992, p. 72-91. DOI : 10.1117/12.138835. URL : https://doi.org/10.1117/12.138835 (cf. p. 24).

[72] Todd AYCOCK, Art LOMPADO, Troy WOLZ et al. « Passive optical sensing of atmospheric polarization for GPS denied operations ». In : *Sensors and Systems for Space Applications IX*. T. 9838. SPIE. 2016, p. 266-279. DOI : 10.1117/12.2227140 (cf. p. 24).

[73] K.L. COULSON. *Polarization and Intensity of Light in the Atmosphere*. Studies in geophysical optics and remote sensing. A. Deepak Pub., 1988. ISBN : 9780937194126. URL : https://books.google.fr/books?id=1y5RAAAAMAAJ (cf. p. 24, 46, 49, 50).

[74] D.H. GOLDSTEIN. *Polarized Light*. CRC Press, 2017. ISBN : 9781439830413. URL : https://books.google.fr/books?id=w6PMBQAAQBAJ (cf. p. 24, 26-28, 30, 34, 36-38, 40, 43, 44, 55, 58, 59, 67, 76, 78, 84).

[75] Damian P. HAMPSHIRE. « A derivation of Maxwell's equations using the Heaviside notation ». In : *Philosophical Transactions of the Royal Society A : Mathematical, Physical and Engineering Sciences* 376.2134 (oct. 2018), p. 20170447. ISSN : 1471-2962. DOI : 10.1098/rsta.2017.0447. URL : http://dx.doi.org/10.1098/rsta.2017.0447 (cf. p. 25).

[76] Max BORN et Emil WOLF. *Principles of optics : electromagnetic theory of propagation, interference and diffraction of light*. Elsevier, 2013. DOI : 10.1017/CBO9781139644181 (cf. p. 25, 26, 31, 79).

[77] Russell CHIPMAN, Wai Sze Tiffany LAM et Garam YOUNG. *Polarized light and optical systems*. CRC press, 2018. DOI : 10.1201/9781351129121 (cf. p. 29, 32, 67, 68, 79).

[78] Benjamin LE TEURNIER. « Imagerie polarimétrique basée sur un capteur à micro-grilles : caractérisation et détection des erreurs dues aux fluctuations spatiales ». Theses. Université Paris-Saclay, déc. 2022. URL : https://pastel.hal.science/tel-04031838 (cf. p. 31).

[79] Richard BARAKAT. « Statistics of the Stokes parameters ». In : *JOSA A* 4.7 (1987), p. 1256-1263. DOI : 10.1364/JOSAA.4.001256 (cf. p. 32).

[80] Hon. R. J. STRUTT. « LVIII. On the scattering of light by small particles ». In : *Philosophical Magazine Series 1* 41 (1871), p. 447-454. URL : https://api.semanticscholar.org/CorpusID:124116052 (cf. p. 40).

[81] John David JACKSON. *Classical electrodynamics*. 3rd ed. New York, NY : Wiley, 1999. ISBN : 9780471309321. URL : http://www.fisica.ugto.mx/~ggutj/CV/Classical_Electrodynamics_Jackson_1a_Edicion.pdf (cf. p. 41).

[82] Antoine MOUTENET, Léo POUGHON, Bruno TOULON et al. « OpenSky : a modular and open-source simulator of sky polarization measurements ». In : *IEEE Transactions on Instrumentation and Measurement* (2024), p. 1-1. DOI : 10.1109/TIM.2024.3374965 (cf. p. 44, 47-49, 52, 93, 115, 118, 120, 127, 128).

[83] Bence SUHAI et Gábor HORVÁTH. « How well does the Rayleigh model describe the E-vector distribution of skylight in clear and cloudy conditions? A full-sky polarimetric study ». In : *JOSA A* 21.9 (2004), p. 1669-1676. DOI : 10.1364/JOSAA.21.001669 (cf. p. 48).

[84] MV BERRY, MR DENNIS et RL LEE. « Polarization singularities in the clear sky ». In : *New Journal of Physics* 6.1 (2004), p. 162. DOI : 10.1088/1367-2630/6/1/162 (cf. p. 48, 52).

[85] Léo POUGHON, Vincent AUBRY, Jocelyn MONNOYER et al. « A stand-alone polarimetric acquisition system for producing a long-term skylight dataset ». In : *2023 IEEE SENSORS*. IEEE. 2023, p. 1-4. DOI : 10.1109/SENSORS56945.2023.10325176 (cf. p. 48, 49, 51, 54, 67, 69, 118, 119).

[86] Leo POUGHON, Vincent AUBRY, Jocelyn MONNOYER et al. *A 2 month-long annotated skylight polarization images database*. Version V1. 2024. DOI : 10.57745/9L2YUB. URL : https://doi.org/10.57745/9L2YUB (cf. p. 48, 49, 51, 54, 120, 130, 134, 136).

[87] Laura M ESHELMAN et Joseph A SHAW. « The VIS–SWIR spectrum of skylight polarization ». In : *Applied Optics* 57.27 (2018), p. 7974-7986. DOI : 10.1364/AO.57.007974 (cf. p. 50).

[88] Shuai LI, Rui WANG, Congming DAI et al. « Impact of aerosols on the polarization patterns of full-sky background radiation ». In : *Optics Express* 31.12 (2023), p. 19918-19930. DOI : 10.1364/OE.492041 (cf. p. 50).

[89] Alexander KOKHANOVSKY. « Optical properties of terrestrial clouds ». In : *Earth-Science Reviews* 64.3-4 (2004), p. 189-241. DOI : https://doi.org/10.1016/S0012-8252(03)00042-4 (cf. p. 50).

[90] Nathan J PUST et Joseph A SHAW. « Wavelength dependence of the degree of polarization in cloud-free skies : simulations of real environments ». In : *Optics Express* 20.14 (2012), p. 15559-15568. DOI : 10.1364/OE.20.015559 (cf. p. 50).

[91] Yan CUI, Muhammad Mubashir NAVEED, Zhou YE et al. « Investigation of Skylight Polarization Mode at Different Surface Albedo ». In : *North American Academic Research* (oct. 2022). DOI : 10.5281/zenodo.7234810. URL : https://doi.org/10.5281/zenodo.7234810 (cf. p. 50).

[92] Kurt BULLRICH, Reiner EIDEN et Wolfram NOWAK. « Sky Radiation, polarization and twilight radiation in Greenland ». In : *pure and applied geophysics* 64 (1966), p. 220-242. DOI : 10.1007/BF00875549 (cf. p. 50, 51).

[93] Andrew R DAHLBERG, Nathan J PUST et Joseph A SHAW. « Effects of surface reflectance on skylight polarization measurements at the Mauna Loa Observatory ». In : *Optics Express* 19.17 (2011), p. 16008-16021. DOI : 10.1364/OE.19.016008 (cf. p. 50, 51).

[94] Xi XU, Takashi ASAWA et Hideki KOBAYASHI. « Narrow-to-Broadband Conversion for Albedo Estimation on Urban Surfaces by UAV-Based Multispectral Camera ». In : *Remote Sensing* 12 (juill. 2020), p. 2214. DOI : 10.3390/rs12142214 (cf. p. 51, 54).

[95] Ramón HEGEDÜS, Susanne AKESSON et Gabor HORVATH. « Polarization patterns of thick clouds : Overcast skies have distribution of the angle of polarization similar to that of clear skies ». In : *Journal of the Optical Society of America. A, Optics, image science, and vision* 24 (sept. 2007), p. 2347-56. DOI : 10.1364/JOSAA.24.002347 (cf. p. 51).

[96] Nathan J PUST et Joseph A SHAW. « Digital all-sky polarization imaging of partly cloudy skies ». In : *Applied optics* 47.34 (2008), H190-H198. DOI : 10.1364/AO.47.00H190 (cf. p. 51, 137).

[97] Gustav MIE. « Beiträge zur Optik trüber Medien, speziell kolloidaler Metallösungen ». In : *Annalen der physik* 330.3 (1908), p. 377-445. DOI : 10.1002/andp.19083300302 (cf. p. 52).

[98] Julius Adams STRATTON. *Electromagnetic theory*. T. 33. John Wiley & Sons, 2007. DOI : 10.1002/9781119134640 (cf. p. 52).

[99] George W KATTAWAR, Gilbert N PLASS et John A GUINN JR. « Monte Carlo calculations of the polarization of radiation in the earth's atmosphere-ocean system ». In : *Journal of Physical Oceanography* 3.4 (1973), p. 353-372. DOI : https://doi.org/10.1175/1520-0485(1973)003<0353:MCCOTP>2.0.CO;2 (cf. p. 52).

[100] Otto von HELVERSEN et Wolfgang EDRICH. « The spectral sensitivity of polarized light orientation in the honeybee ». In : *Journal of comparative physiology* 94 (1974), p. 33-47. DOI : 10.1007/bf00610156 (cf. p. 52).

[101] Michael I MOTE et Rüdiger WEHNER. « Functional characteristics of photoreceptors in the compound eye and ocellus of the desert ant, Cataglyphis bicolor ». In : *Journal of comparative physiology* 137 (1980), p. 63-71. DOI : 10.1007/BF00656918 (cf. p. 52).

[102] Dieter HERZMANN et Thomas LABHART. « Spectral sensitivity and absolute threshold of polarization vision in crickets : a behavioral study ». In : *Journal of Comparative Physiology A* 165 (1989), p. 315-319. DOI : 10.1007/BF00619350 (cf. p. 52).

[103] Thomas LABHART, Eric P MEYER et Leslie SCHENKER. « Specialized ommatidia for polarization vision in the compound eye of cockchafers, Melolontha melolontha (Coleoptera, Scarabaeidae) ». In : *Cell and tissue research* 268 (1992), p. 419-429. DOI : 10.1007/BF00319148 (cf. p. 52).

[104] Thomas LABHART et Eric P MEYER. « Detectors for polarized skylight in insects : a survey of ommatidial specializations in the dorsal rim area of the compound eye ». In : *Microscopy research and technique* 47.6 (1999), p. 368-379. DOI : https://doi.org/10.1002/(SICI)1097-0029(19991215)47:6<368::AID-JEMT2>3.0.CO;2-Q (cf. p. 52).

[105] András BARTA et Gábor HORVÁTH. « Why is it advantageous for animals to detect celestial polarization in the ultraviolet? Skylight polarization under clouds and canopies is strongest in the UV ». In : *Journal of theoretical biology* 226.4 (2004), p. 429-437. DOI : https://doi.org/10.1016/j.jtbi.2003.09.017 (cf. p. 52, 53, 139).

[106] Michael L BRINES et James L GOULD. « Skylight polarization patterns and animal orientation ». In : *Journal of Experimental Biology* 96.1 (1982), p. 69-91. DOI : 10.1242/jeb.96.1.69 (cf. p. 52).

[107] R WEHNER. « Visuelle Navigation : Kleinstgehirn-Strategien ». In : *Verh Dtsch Zool Ges* 84 (1991), p. 89-104 (cf. p. 52).

[108] István POMOZI, Gábor HORVÁTH et Rüdiger WEHNER. « How the clear-sky angle of polarization pattern continues underneath clouds : full-sky measurements and implications for animal orientation ». In : *Journal of Experimental Biology* 204.17 (2001), p. 2933-2942. DOI : 10.1242/jeb.204.17.2933 (cf. p. 52, 139).

[109] Antoine MOUTENET, Julien R SERRES et Stéphane VIOLLET. « Ultraviolet vs. Visible Skylight Polarization Measurements ». In : *2023 IEEE SENSORS*. IEEE. 2023, p. 01-04. DOI : 10.1109/SENSORS56945.2023.10325144 (cf. p. 54, 139).

[110] Xin WANG, Jun GAO et Zhiguo FAN. « Empirical corroboration of an earlier theoretical resolution to the UV paradox of insect polarized skylight orientation ». In : *Naturwissenschaften* 101 (2014), p. 95-103. DOI : 10.1007/s00114-013-1134-2 (cf. p. 54, 139).

[111] Uwe FEISTER et Rolf GREWE. « Spectral albedo measurements in the UV and visible region over different types of surfaces ». In : *Photochemistry and Photobiology* 62.4 (1995), p. 736-744. DOI : 10.1111/j.1751-1097.1995.tb08723.x (cf. p. 54).

[112] Alain LENOIR, Serge ARON, Xim CERDÁ et al. « Cataglyphis desert ants : a good model for evolutionary biology in Darwin's anniversary year - A review ». In : *Israel Journal of Entomology* vol. 39 (jan. 2009), pages 1-32. URL : https://hal.science/hal-00550993/ (cf. p. 54).

[113] Thomas W CRONIN, Sönke JOHNSEN, N Justin MARSHALL et al. *Visual ecology*. Princeton University Press, 2014. URL : https://press.princeton.edu/books/hardcover/9780691151847/visual-ecology?srsltid=AfmBOoos8ulA08ppdh7-CcvV-vj4dTZc2PWEqrcwMnyiYJpHCGOjljtA (cf. p. 55, 61).

[114] S DE NICOLA, P FERRARO, A FINIZIO et al. « Wavelength dependence of the phase retardation of a quarter-wave plate ». In : *Applied Physics B* 60.4 (1995), p. 405-407. DOI : 10.1007/BF01082277 (cf. p. 58).

[115] Javier VARGAS, Néstor URIBE-PATARROYO, Juan Antonio QUIROGA et al. « Optical inspection of liquid crystal variable retarder inhomogeneities ». In : *Appl. Opt.* 49.4 (fév. 2010), p. 568-574. DOI : 10.1364/AO.49.000568. URL : https://opg.optica.org/ao/abstract.cfm?URI=ao-49-4-568 (cf. p. 58).

[116] Thomas LABHART. « Polarization-opponent interneurons in the insect visual system ». In : *Nature* 331.6155 (1988), p. 435-437. DOI : 10.1038/331435a0 (cf. p. 61, 63, 90).

[117] Zhiwen XIAN, Xiaoping HU, Junxiang LIAN et al. « A Novel Angle Computation and Calibration Algorithm of Bio-Inspired Sky-Light Polarization Navigation Sensor ». In : *Sensors (Basel, Switzerland)* 14 (sept. 2014), p. 17068-17088. DOI : 10.3390/s140917068 (cf. p. 61).

[118] Jinkui CHU, Kaichun ZHAO, Qiang ZHANG et al. « Construction and performance test of a novel polarization sensor for navigation ». In : *Sensors and Actuators A : Physical* 148.1 (2008), p. 75-82. ISSN : 0924-4247. DOI : https://doi.org/10.1016/j.sna.2008.07.016. URL : https://www.sciencedirect.com/science/article/pii/S0924424708004081 (cf. p. 61, 62).

[119] Guixia GUAN, Jingbo GU et Minhua WU. « The Novel Method of North-finding Based on the Skylight Polarization ». In : *Journal of Engineering Science and Technology Review* 6 (juill. 2013), p. 107-110. DOI : 10.25103/jestr.061.21 (cf. p. 61, 98).

[120] Tao DU, Xiong LI, Yuehai WANG et al. « Multiple Disturbance Analysis and Calibration of an Inspired Polarization Sensor ». In : *IEEE Access* PP (mai 2019), p. 1-1. DOI : 10.1109/ACCESS.2019.2914565 (cf. p. 61, 75).

[121] Jian YANG, Ben NIU, C. LI et al. « A Bionic Polarization Navigation Sensor Based on Polarizing Beam Splitter ». In : *IEEE Access* PP (jan. 2018), p. 1-1. DOI : 10.1109/ACCESS.2018.2794524 (cf. p. 62).

[122] Yinlong WANG, Jinkui CHU, Ran ZHANG et al. « Orthogonal vector algorithm to obtain the solar vector using the single-scattering Rayleigh model ». In : *Appl. Opt.* 57.4 (fév. 2018), p. 594-601. DOI : 10.1364/AO.57.000594. URL : https://opg.optica.org/ao/abstract.cfm?URI=ao-57-4-594 (cf. p. 62).

[123] Wang YINLONG, Jinkui CHU, Ran ZHANG et al. « A novel autonomous real-time position method based on polarized light and geomagnetic field ». In : *Scientific reports* 5 (avr. 2015), p. 9725. DOI : 10.1038/srep09725 (cf. p. 62, 98).

[124] Qingyun ZHANG, Jian YANG, Panpan HUANG et al. « Bionic Integrated Positioning Mechanism Based on Bioinspired Polarization Compass and Inertial Navigation System ». In : *Sensors* 21 (fév. 2021), p. 1055. DOI : 10.3390/s21041055 (cf. p. 62, 99).

[125] ML. BRINES. « Skylight polarization patterns as cues for honey bee orientation, physical measurements and behavioural experiments ». In : *Dissertation Abstracts International B Sciences and Engineering,* 411 (1980), p. 29 (cf. p. 62, 101).

[126] Evripidis GKANIAS, Robert MITCHELL, Jan STANKIEWICZ et al. « Celestial compass sensor mimics the insect eye for navigation under cloudy and occluded skies ». In : *Communications Engineering* 2 (nov. 2023). DOI : 10.1038/s44172-023-00132-w (cf. p. 63, 90).

[127] Wenguang HOU, Mingyue DING, Nannan QIN et al. « Digital deformation model for fisheye image rectification ». In : *Opt. Express* 20.20 (sept. 2012), p. 22252-22261. DOI : 10.1364/OE.20.022252. URL : https://opg.optica.org/oe/abstract.cfm?URI=oe-20-20-22252 (cf. p. 64).

[128] Nathan PUST et Joseph SHAW. « Dual-field imaging polarimeter using liquid crystal variable retarders ». In : *Applied optics* 45 (sept. 2006), p. 5470-8. DOI : 10.1364/AO.45.005470 (cf. p. 64).

[129] Yujie WANG, Xiaoping HU, Jun-xiang LIAN et al. « Design of a Device for Sky Light Polarization Measurements ». In : *Sensors (Basel, Switzerland)* 14 (2014), p. 14916-14931. DOI : 10.3390/s140814916 (cf. p. 64).

[130] Yves ANDRE, Jean-Marc LAHERRERE, Thierry BRET-DIBAT et al. « Instrumental concept and performances of the POLDER instrument ». In : *Remote Sensing and Reconstruction for Three-Dimensional Objects and Scenes*. Sous la dir. de Toni F. SCHENK. T. 2572. International Society for Optics et Photonics. SPIE, 1995, p. 79-90. DOI : 10.1117/12.216932. URL : https://doi.org/10.1117/12.216932 (cf. p. 64).

[131] Zhengqiang LI, Weizhen HOU, Jin HONG et al. « Directional Polarimetric Camera (DPC) : Monitoring aerosol spectral optical properties over land from satellite observation ». In : *Journal of Quantitative Spectroscopy and Radiative Transfer* 218 (2018), p. 21-37. ISSN : 0022-4073. DOI : https://doi.org/10.1016/j.jqsrt.2018.07.003. URL : https://www.sciencedirect.com/science/article/pii/S002240731830253X (cf. p. 64).

[132] Nicole CAREY et Wolfgang STÜRZL. « An insect-inspired omnidirectional vision system including UV-sensitivity and polarisation ». In : *2011 IEEE International Conference on Computer Vision Workshops (ICCV Workshops)*. 2011, p. 312-319. DOI : 10.1109/ICCVW.2011.6130258 (cf. p. 65).

[133] Haihong JIN, Xianqiu WANG, Zhiguo FAN et al. « Linear Solution Method of Solar Position for Polarized Light Navigation ». In : *IEEE Sensors Journal* PP (avr. 2021), p. 1-1. DOI : 10.1109/JSEN.2021.3074416 (cf. p. 65, 93).

[134] Ali ALTAQUI, Pratik SEN, Harry SCHRICKX et al. « Mantis shrimp–inspired organic photodetector for simultaneous hyperspectral and polarimetric imaging ». In : *Science Advances* 7.10 (2021), eabe3196. DOI : 10.1126/sciadv.abe3196 (cf. p. 65).

[135] J. Larry PEZZANITI et David B. CHENAULT. « A division of aperture MWIR imaging polarimeter ». In : *Polarization Science and Remote Sensing II*. Sous la dir. de Joseph A. SHAW et J. Scott TYO. T. 5888. International Society for Optics et Photonics. SPIE, 2005, p. 58880V. DOI : 10.1117/12.623543. URL : https://doi.org/10.1117/12.623543 (cf. p. 65).

[136] Jun LIU, Jiangtao YANG, Yubo WANG et al. « Global positioning method based on polarized light compass system ». In : *Review of Scientific Instruments* 89 (mai 2018), p. 054503. DOI : 10.1063/1.5026870 (cf. p. 65, 98).

[137] Wolfgang STÜRZL et Nicole CAREY. « A Fisheye Camera System for Polarisation Detection on UAVs ». In : *Computer Vision – ECCV 2012. Workshops and Demonstrations*. Sous la dir. d'Andrea FUSIELLO, Vittorio MURINO et Rita CUCCHIARA. Berlin, Heidelberg : Springer Berlin Heidelberg, 2012, p. 431-440. ISBN : 978-3-642-33868-7. DOI : 10.1007/978-3-642-33868-7_43 (cf. p. 65, 91).

[138] Dmitry VOROBIEV, Zoran NINKOV et Neal BROCK. « Astronomical Polarimetry with the RIT Polarization Imaging Camera ». In : *Publications of the Astronomical Society of the Pacific* 130 (mai 2018), p. 064501. DOI : 10.1088/1538-3873/aab99b (cf. p. 65, 72, 75).

[139] Missael GARCÍA, Christopher EDMISTON, Radoslav MARINOV et al. « Bio-inspired color-polarization imager for real-time in situ imaging ». In : *Optica* 4 (oct. 2017), p. 1263. DOI : 10.1364/OPTICA.4.001263 (cf. p. 66).

[140] Zhang JING, Yu CAO, Xuanzhe ZHANG et al. « Sky light polarization detection with linear polarizer triplet in light field camera inspired by insect vision ». In : *Applied Optics* 54 (oct. 2015), p. 8962. DOI : 10.1364/AO.54.008962 (cf. p. 66).

[141] Wenjing ZHANG, Xuanzhe ZHANG, Yu CAO et al. « Robust sky light polarization detection with an S-wave plate in a light field camera ». In : *Appl. Opt.* 55.13 (mai 2016), p. 3518-3525. DOI : 10.1364/AO.55.003518. URL : https://opg.optica.org/ao/abstract.cfm?URI=ao-55-13-3518 (cf. p. 66).

[142] Samuel POWELL, Roman GARNETT, Justin MARSHALL et al. « Bioinspired polarization vision enables underwater geolocalization ». In : *Science Advances* 4 (avr. 2018), eaao6841. DOI : 10.1126/sciadv.aao6841 (cf. p. 66, 75, 98).

[143] Wang JUE, Hu PENGWEI, Qian JIANQIANG et al. « Confocal Ellipse Hough Transform for Polarization Compass in the Nonideal Atmosphere ». In : *IEEE Transactions on Instrumentation and Measurement* PP (jan. 2023), p. 1-1. DOI : 10.1109/TIM.2023.3256476 (cf. p. 66).

[144] Guillaume COURTIER, Pierre-Jean LAPRAY, Ronan ADAM et al. « Ground Vehicle Navigation Based on the Skylight Polarization ». In : *2023 IEEE/ION Position, Location and Navigation Symposium (PLANS)*. 2023, p. 1373-1379. DOI : 10.1109/PLANS53410.2023.10140044 (cf. p. 66, 93).

[145] Qianhui LI, Yao HU, Qun HAO et al. « Skylight polarization patterns under urban obscurations and a navigation method adapted to urban environments ». In : *Optics Express* 29 (nov. 2021). DOI : 10.1364/OE.443321 (cf. p. 66, 93).

[146] Léo POUGHON, Vincent AUBRY, Jocelyn MONNOYER et al. « Skylight polarization heading sensor using waveplate retardance shift with incidence ». In : *Journée des Jeunes Chercheurs en Robotique 2023 (JJCR'23)*. HAL, oct. 2023. URL : https://hal.science/hal-04521170 (cf. p. 67, 142).

[147] Yuanyi FAN, Ran ZHANG, Liu ZE et al. « A Skylight Orientation Sensor Based on S-Waveplate and Linear Polarizer for Autonomous Navigation ». In : *IEEE Sensors Journal* PP (août 2021), p. 1-1. DOI : 10.1109/JSEN.2021.3106951 (cf. p. 67).

[148] Jan KORGER, Tobias KOLB, Peter BANZER et al. « The polarization properties of a tilted polarizer ». In : *Opt. Express* 21.22 (nov. 2013), p. 27032-27042. DOI : 10.1364/OE.21.027032. URL : https://opg.optica.org/oe/abstract.cfm?URI=oe-21-22-27032 (cf. p. 67, 74).

[149] Dikpal REDDY et Ashok VEERARAGHAVAN. « Lens Flare and Lens Glare ». In : *Computer Vision : A Reference Guide*. Cham : Springer International Publishing, 2021, p. 741-744. ISBN : 978-3-030-63416-2. DOI : 10.1007/978-3-030-63416-2_481. URL : https://doi.org/10.1007/978-3-030-63416-2_481 (cf. p. 67).

[150] Laura ESHELMAN et Joseph SHAW. « Visualization of all-sky polarization images referenced in the instrument, scattering, and solar principal planes ». In : *Optical Engineering* 58 (mai 2019), p. 1. DOI : 10.1117/1.OE.58.8.082418 (cf. p. 67).

[151] J. Scott TYO, Dennis L. GOLDSTEIN, David B. CHENAULT et al. « Review of passive imaging polarimetry for remote sensing applications ». In : *Appl. Opt.* 45.22 (août 2006), p. 5453-5469. DOI : 10.1364/AO.45.005453. URL : https://opg.optica.org/ao/abstract.cfm?URI=ao-45-22-5453 (cf. p. 67).

[152] Zhengyou ZHANG. « A flexible new technique for camera calibration ». In : *IEEE Transactions on pattern analysis and machine intelligence* 22.11 (2000), p. 1330-1334. DOI : 10.1109/34.888718 (cf. p. 69).

[153] Davide SCARAMUZZA, Agostino MARTINELLI et Roland SIEGWART. « A toolbox for easily calibrating omnidirectional cameras ». In : *2006 IEEE/RSJ International Conference on Intelligent Robots and Systems*. IEEE. 2006, p. 5695-5701. DOI : 10.1109/IROS.2006.282372 (cf. p. 69).

[154] *Integrating Sphere Theory and Applications*. Labsphere, Inc. 2017. URL : https://www.labsphere.com/wp-content/uploads/2021/09/Integrating-Sphere-Theory-and-Applications.pdf (cf. p. 71).

[155] Joaquin RODRIGUEZ, Lew LEW-YAN-VOON, Renato MARTINS et al. « A practical calibration method for RGB micro-grid polarimetric cameras ». In : *IEEE Robotics and Automation Letters* 7.4 (2022), p. 9921-9928. DOI : 10.1109/LRA.2022.3192655 (cf. p. 70).

[156] Connor LANE, David RODE et Thomas RÖSGEN. « Calibration of a polarization image sensor and investigation of influencing factors ». In : *Applied Optics* 61.6 (2022), p. C37-C45. DOI : 10.1364/AO.437391 (cf. p. 70, 119).

[157] Manchun LEI, Christophe MEYNARD, Jean-Michael MULLER et al. « Calibration radiométrique et géométrique d'une caméra fish-eye pour la mesure de l'hémisphère de luminance incidente ». Thèse de doct. Institut national de l'information géographique et forestière, 2022. URL : https://hal.science/hal-03665394v1/file/lei22_rep_camera_calibration_upload_202205.pdf (cf. p. 70).

[158] Chan HUANG, Guangfeng XIANG, Yuyang CHANG et al. « Pre-flight calibration of a multi-angle polarimetric satellite sensor directional polarimetric camera ». In : *Optics Express* 28.9 (2020), p. 13187-13215. DOI : 10.1364/OE.391078 (cf. p. 71, 76, 84).

[159] Musaddeque Anwar Al Abedin SYED. *Characterization of a division-of-focal-plane polarization imager*. Master's thesis. Example City, CA, avr. 2020. URL : https://scholarworks.montana.edu/items/0d7ea4d6-25b9-45a1-a41d-fffbe945df28 (cf. p. 72).

[160] David A HANER, Brendan T MCGUCKIN et Carol J BRUEGGE. « Polarization characteristics of Spectralon illuminated by coherent light ». In : *Applied optics* 38.30 (1999), p. 6350-6356. DOI : 10.1364/AO.38.006350 (cf. p. 71).

[161] Chaoyang LIU, Tao ZHENG, Kaixiang SHU et al. « Polarization-Sensitive Self-Powered Schottky Photodetector with High Photovoltaic Performance Induced by Geometry-Asymmetric Contacts ». In : *ACS Applied Materials & Interfaces* 16.11 (2024), p. 13914-13926. DOI : 10.1021/acsami.3c16047 (cf. p. 72).

[162] Zecheng CHEN, Jianming HUANG, Mengmeng YANG et al. « Bi2O2Se Nanowire/MoSe2 Mixed-Dimensional Polarization-Sensitive Photodiode with a Nanoscale Ultrafast-Response Channel ». In : *ACS Applied Materials & Interfaces* 15.25 (2023), p. 30504-30516. DOI : 10.1021/acsami.3c05283 (cf. p. 72).

[163] Yilbert Cristóbal GIMÉNEZ-HENRÍQUEZ. « Caractérisation et étalonnage des systèmes d'imagerie de stokes à matrice de filtres polariseurs ». Thèse de doct. Mulhouse, 2022 (cf. p. 72).

[164] A DELIWALA et V GRUEV. « Optical crosstalk in division of focal plane imagers ». In : *Polarization : Measurement, Analysis, and Remote Sensing XIV*. T. 11412. SPIE. 2020, p. 84-90. DOI : 10.1117/12.2560211 (cf. p. 73).

[165] Brian G HOOVER, David A RUGELY, Christopher M FRANCIS et al. « Bistatic laser polarimeter calibrated to 1% at visible-SWIR wavelengths ». In : *Optics Express* 24.17 (2016), p. 19881-19894. DOI : 10.1364/OE.24.019881 (cf. p. 74).

[166] Yilbert GIMÉNEZ, Pierre-Jean LAPRAY, Alban FOULONNEAU et al. « Calibration algorithms for polarization filter array camera : survey and evaluation ». In : *Journal of Electronic Imaging* 29.4 (2020), p. 041011-041011. DOI : https://hal.science/hal-02546953/document (cf. p. 75).

[167] S Bear POWELL et Viktor GRUEV. « Calibration methods for division-of-focal-plane polarimeters ». In : *Optics express* 21.18 (2013), p. 21039-21055. DOI : 10.1364/OE.21.021039 (cf. p. 75).

[168] Chan HUANG, Yuyang CHANG, Guangfeng XIANG et al. « Polarization measurement accuracy analysis and improvement methods for the directional polarimetric camera ». In : *Optics Express* 28.26 (2020), p. 38638-38666. DOI : 10.1364/OE.405834 (cf. p. 76).

[169] Thierry BRET-DIBAT, Yves ANDRE et Jean-Marc LAHERRERE. « Preflight calibration of the POLDER instrument ». In : *Infrared Spaceborne Remote Sensing III*. T. 2553. SPIE. 1995, p. 218-231. DOI : 10.1117/12.221357 (cf. p. 76).

[170] Anna-Britt MAHLER et Russell A CHIPMAN. « Polarization state generator : a polarimeter calibration standard ». In : *Applied Optics* 50.12 (2011), p. 1726-1734. DOI : 10.1364/AO.50.001726 (cf. p. 76).

[171] Bengt NORDEN et Stefan SETH. « Critical aspects of measurement of circular and linear dichroism : a device for absolute calibration ». In : *Applied spectroscopy* 39.4 (1985), p. 647-655. DOI : https://doi.org/10.1366/0003702854250356 (cf. p. 76).

[172] Zhengqiang LI, Luc BLAREL, Thierry PODVIN et al. « Calibration of the degree of linear polarization measurement of polarized radiometer using solar light ». In : *Applied optics* 49.8 (2010), p. 1249-1256. DOI : 10.1364/AO.49.001249 (cf. p. 76).

[173] Angel LIZANA, Irene ESTÉVEZ, Fabián A TORRES-RUIZ et al. « Arbitrary state of polarization with customized degree of polarization generator ». In : *Optics Letters* 40.16 (2015), p. 3790-3793. DOI : 10.1364/OL.40.003790 (cf. p. 76, 77, 80).

[174] Xiaobo LI, Haofeng HU, Tiegen LIU et al. « Optimal distribution of integration time for intensity measurements in degree of linear polarization polarimetry ». In : *Optics Express* 24.7 (2016), p. 7191-7200. DOI : 10.1364/OE.24.007191 (cf. p. 76).

[175] Alba PEINADO, Angel LIZANA et Juan CAMPOS. « Use of ferroelectric liquid crystal panels to control state and degree of polarization in light beams ». In : *Optics Letters* 39.3 (2014), p. 659-662. DOI : 10.1364/OL.39.000659 (cf. p. 77).

[176] Olivier MOREL, Ralph SEULIN et David FOFI. « Handy method to calibrate division-of-amplitude polarimeters for the first three Stokes parameters ». In : *Optics express* 24.12 (2016), p. 13634-13646. DOI : 10.1364/OE.24.013634 (cf. p. 84).

[177] Xiaoyang BAI, Zhongmin ZHU, Alexander SCHWING et al. « Angle of polarization calibration for omnidirectional polarization cameras ». In : *Optics Express* 31.4 (2023), p. 6759-6769. DOI : 10.1364/OE.483337 (cf. p. 84).

[178] Dimitrios LAMBRINOS, Hiroshi KOBAYASHI, Rolf PFEIFER et al. « An Autonomous Agent Navigating with a Polarized Light Compass ». In : *Adaptive Behavior* 6.1 (1997), p. 131-161. DOI : 10.1177/105971239700600104. eprint : https://doi.org/10.1177/105971239700600104. URL : https://doi.org/10.1177/105971239700600104 (cf. p. 90).

[179] Dimitrios LAMBRINOS, Ralf MÖLLER, Thomas LABHART et al. « A mobile robot employing insect strategies for navigation ». In : *Robotics and Autonomous Systems* 30.1 (2000), p. 39-64. ISSN : 0921-8890. DOI : https://doi.org/10.1016/S0921-8890(99)00064-0. URL : https://www.sciencedirect.com/science/article/pii/S0921889099000640 (cf. p. 90).

[180] Thomas STONE, Barbara WEBB, Andrea ADDEN et al. « An Anatomically Constrained Model for Path Integration in the Bee Brain ». In : *Current Biology* 27.20 (2017), 3069-3085.e11. ISSN : 0960-9822. DOI : https://doi.org/10.1016/j.cub.2017.08.052. URL : https://www.sciencedirect.com/science/article/pii/S0960982217310904 (cf. p. 90).

[181] Evripidis GKANIAS, Benjamin RISSE, Michael MANGAN et al. « From skylight input to behavioural output : A computational model of the insect polarised light compass ». In : *PLOS Computational Biology* 15.7 (juill. 2019), p. 1-30. DOI : 10.1371/journal.pcbi.1007123. URL : https://doi.org/10.1371/journal.pcbi.1007123 (cf. p. 90).

[182] Jinshan LI, Jinkui CHU, Ran ZHANG et al. « Brain-Inspired Navigation Model Based on the Distribution of Polarized Sky-Light ». In : *Machines* 10.11 (2022). ISSN : 2075-1702. DOI : 10.3390/machines10111028. URL : https://www.mdpi.com/2075-1702/10/11/1028 (cf. p. 90).

[183] Tao DU, Yun ZENG, Jian YANG et al. « Multi-sensor fusion SLAM approach for the mobile robot with a bio-inspired polarised skylight sensor ». In : *IET Radar, Sonar and Navigation* 14 (oct. 2020), p. 1950-1957. DOI : 10.1049/iet-rsn.2020.0260 (cf. p. 90).

[184] Lieutenant Commander Alton B MOODY. « The pfund sky compass ». In : *NAVIGATION : Journal of the Institute of Navigation* 2.7 (1950), p. 234-239. DOI : 10.1002/j.2161-4296.1950.tb00567.x (cf. p. 90).

[185] Guangmin LI, Ya ZHANG, Shiwei FAN et al. « Attitude and heading measurement based on adaptive complementary Kalman filter for PS/MIMU integrated system ». In : *Optics Express* 32 (fév. 2024). DOI : 10.1364/OE.519417 (cf. p. 91).

[186] Miriam J. HENZE et Thomas LABHART. « Haze, clouds and limited sky visibility : polarotactic orientation of crickets under difficult stimulus conditions ». In : *Journal of Experimental Biology* 210.18 (sept. 2007), p. 3266-3276. ISSN : 0022-0949. DOI : 10.1242/jeb.007831. eprint : https://journals.biologists.com/jeb/article-pdf/210/18/3266/1258788/3266.pdf. URL : https://doi.org/10.1242/jeb.007831 (cf. p. 93).

[187] Qingyun ZHANG, Jian YANG, Xin LIU et al. « A Bio-Inspired Navigation Strategy Fused Polarized Skylight and Starlight for Unmanned Aerial Vehicles ». In : *IEEE Access* PP (avr. 2020), p. 1-1. DOI : 10.1109/ACCESS.2020.2988529 (cf. p. 93).

[188] Qingfeng DOU, Tao DU, Yan WANG et al. « Optimal vector matching fusion method for bionic compound eye polarization compass and inertial sensor integration ». In : *ISA transactions* 141 (2023), p. 496-506. DOI : 10.1016/j.isatra.2023.07.006 (cf. p. 93).

[189] Moshe HAMAOUI. « Polarized skylight navigation ». In : *Applied Optics* 56 (jan. 2017), B37. DOI : 10.1364/AO.56.000B37 (cf. p. 93).

[190] Jiangtao YANG, Situo LIU, Mingkai WANG et al. « Solar position detection method by bionic polarized light compass ». In : *Opt. Express* 32.3 (jan. 2024), p. 3751-3763. DOI : 10.1364/OE.512069. URL : https://opg.optica.org/oe/abstract.cfm?URI=oe-32-3-3751 (cf. p. 93).

[191] Huijie ZHAO, Wujian XU, Ying ZHANG et al. « Polarization patterns under different sky conditions and a navigation method based on the symmetry of the AOP map of skylight ». In : *Optics express* 26.22 (2018), p. 28589-28603. DOI : 10.1364/OE.26.028589 (cf. p. 93).

[192] Hao-yuan CHENG, Shi-min YU, Hao YU et al. « Bioinspired underwater navigation using polarization patterns within Snell's window ». In : *China Ocean Engineering* 37.4 (2023), p. 628-636. DOI : 10.1007/s13344-023-0053-z (cf. p. 93).

[193] Zhihe CHEN, Lianwei TENG, Wenzhou ZHOU et al. « Bio-inspired Sky Polarized Orientation based on the atmospheric polarization symmetry mode and Inertial Sensors ». In : *Journal of Physics : Conference Series*. T. 2640. IOP Publishing. 2023, p. 012018. DOI : 10.1088/1742-6596/2640/1/012018 (cf. p. 93).

[194] Hao LU, Kaichun ZHAO, Zheng YOU et al. « Angle algorithm based on Hough transform for imaging polarization navigation sensor ». In : *Optics express* 23.6 (2015), p. 7248-7262. DOI : 10.1364/OE.23.007248 (cf. p. 93).

[195] Myriam FRANZKE. « Keep on track : The use of visual cues for orientation in monarch butterflies ». Thèse de doct. Universität Würzburg, 2023. URL : https://opus.bibliothek.uni-wuerzburg.de/opus4-wuerzburg/frontdoor/deliver/index/docId/28470/file/Franzke_Myriam_monarch_butterflies.pdf (cf. p. 95).

[196] Huaju LIANG, Hongyang BAI, Ke HU et al. « Bioinspired polarized skylight orientation determination artificial neural network ». In : *Journal of Bionic Engineering* 20.3 (2023), p. 1141-1152. DOI : 10.1007/s42235-022-00310-0 (cf. p. 95, 126).

[197] Xin WANG, Jun GAO et Nicholas William ROBERTS. « Bio-inspired orientation using the polarization pattern in the sky based on artificial neural networks ». In : *Optics Express* 27.10 (2019), p. 13681-13693. DOI : 10.1364/OE.27.013681 (cf. p. 95, 126).

[198] Huaju LIANG, Hongyang BAI, Zhengmao LI et al. « Polarized light sun position determination artificial neural network ». In : *Applied Optics* 61.6 (2022), p. 1456-1463. DOI : 10.1364/AO.453177 (cf. p. 95).

[199] Donghua ZHAO, Yueze LIU, Xindong WU et al. « Attitude-Induced error modeling and compensation with GRU networks for the polarization compass during UAV orientation ». In : *Measurement* 190 (2022), p. 110734. DOI : 10.1016/j.measurement.2022.110734 (cf. p. 95).

[200] Xiankun PU, Xin WANG, Xinjian GAO et al. « Sky Polarization Pattern Reconstruction and Neutral Line Detection Based on Adversarial Learning ». In : *IEEE Transactions on Instrumentation and Measurement* (2023). DOI : 10.1109/TIM.2023.3318720 (cf. p. 95, 126, 139).

[201] Tian YANG, Hongbo BO, Xinyu YANG et al. « Conditional LS-GAN Based Skylight Polarization Image Restoration and Application in Meridian Localization ». In : *ICASSP 2023-2023 IEEE International Conference on Acoustics, Speech and Signal Processing (ICASSP)*. IEEE. 2023, p. 1-5. DOI : 10.1109/ICASSP49357.2023.10096855 (cf. p. 95, 126, 139).

[202] Steven REPPERT et Jacobus ROODE. « Demystifying Monarch Butterfly Migration ». In : *Current Biology* 28 (sept. 2018), R1009-R1022. DOI : 10.1016/j.cub.2018.02.067 (cf. p. 95).

[203] Eli SHLIZERMAN, James PHILLIPS-PORTILLO, Daniel B FORGER et al. « Neural Integration Underlying a Time-Compensated Sun Compass in the Migratory Monarch Butterfly ». In : *Cell Reports* 15 (avr. 2016). DOI : 10.1016/j.celrep.2016.03.057 (cf. p. 95).

[204] Pauline Nikola FLEISCHMANN, Robin GROB, Valentin Leander MÜLLER et al. « The geomagnetic field is a compass cue in Cataglyphis ant navigation ». In : *Current Biology* 28.9 (2018), p. 1440-1444. DOI : https://doi.org/10.1016/j.cub.2018.03.043 (cf. p. 95).

[205] Roswitha WILTSCHKO et Wolfgang WILTSCHKO. « Animal navigation : how animals use environmental factors to find their way ». In : *The European Physical Journal Special Topics* 232.2 (2023), p. 237-252. DOI : 10.1140/epjs/s11734-022-00610-w (cf. p. 95).

[206] Ron DAVIDSON. *Celestial Navigation Practical Theory and Application of Principles*. Nov. 2021. URL : https://seatracker.ru/viewtopic.php?t=49868 (cf. p. 97).

[207] Pengwei HU, Jian YANG, Xiang YU et al. « Underwater Autonomous Geolocalization Using Time Differential Polarization Field Against Measurement Deviations ». In : *IEEE Transactions on Aerospace and Electronic Systems* (2023). DOI : 10.1109/TAES.2023.3323418 (cf. p. 98).

[208] Xiaoyang BAI, Zuodong LIANG, Zhongmin ZHU et al. « Polarization-based underwater geolocalization with deep learning ». In : *eLight* 3.1 (2023), p. 15. DOI : 10.1186/s43593-023-00050-6 (cf. p. 98).

[209] Zhen CHENG, Tao MEI et Huawei LIANG. « Positioning algorithm based on skylight polarization navigation ». In : *IFAC Proceedings Volumes* 46.10 (2013), p. 97-101. DOI : https://doi.org/10.3182/20130626-3-AU-2035.00040 (cf. p. 98).

[210] Jian YANG, Xin LIU, Qingyun ZHANG et al. « Global autonomous positioning in GNSS-challenged environments : A bioinspired strategy by polarization pattern ». In : *IEEE Transactions on Industrial Electronics* 68.7 (2020), p. 6308-6317. DOI : 10.1109/TIE.2020.2994883 (cf. p. 98).

[211] Taihang CHEN, Xiao ZHANG, Xueqian CHI et al. « An Autonomous Positioning Method Utilizing Feature Extraction from Polarized Moonlight ». In : *IEEE Sensors Journal* (2023). DOI : 10.1109/JSEN.2023.3344728 (cf. p. 98).

[212] Guangmin LI, Ya ZHANG, Shiwei FAN et al. « Underwater biomimetic orientation method using imaging polarization sensor based on direct sunlight compensation ». In : *Optics Express* 32.10 (2024), p. 17893-17910. DOI : 10.1364/OE.520710 (cf. p. 98).

[213] Qingfeng DOU, Tao DU, Shanpeng WANG et al. « A novel polarized skylight navigation model for bionic navigation with marginalized unscented Kalman filter ». In : *IEEE Sensors Journal* 22.5 (2021), p. 4472-4483. DOI : 10.1109/JSEN.2021.3139353 (cf. p. 99).

[214] Gustav KRAMER. « Wird die Sonnenhöhe bei der Heimfindeorientierung verwertet? » In : *Journal für Ornithologie* 94.3 (1953), p. 201-219 (cf. p. 100).

[215] G. MATTHEWS. « Sun navigation in homing pigeons ». In : *J. exp. Biol.* 30 (jan. 1953). DOI : 10.1242/jeb.30.2.243 (cf. p. 100).

[216] C PENNYCUICK. « The physical basis of astro-navigation in birds : Theoretical considerations ». In : *J. Exp. Biol.* 37 (jan. 1960). DOI : 10.1242/jeb.37.3.573 (cf. p. 100).

[217] EG Franz SAUER et Eleonore M SAUER. « Star Navigation of Nocturnal Migrating Birds The 1958 Planetarium Experiments ». In : *Cold Spring Harbor Symposia on Quantitative Biology*. T. 25. Cold Spring Harbor Laboratory Press. 1960, p. 463-473. DOI : 10.1101/sqb.1960.025.01.048 (cf. p. 100).

[218] Wolfgang WILTSCHKO et Friedrich W MERKEL. « Orientierung zugunruhiger Rotkehlchen im statischen Magnetfeld ». In : *Verh. Dtsch. Zool. Ges* 59 (1966), p. 362-367 (cf. p. 100).

[219] Kenneth P ABLE. « Skylight polarization patterns at dusk influence migratory orientation in birds ». In : *Nature* 299.5883 (1982), p. 550-551. DOI : 10.1038/299550a0 (cf. p. 100).

[220] Kenneth ABLE. « Orientation cues used by migratory birds : A review of cue-conflict experiments ». In : *Trends in ecology & evolution* 8 (oct. 1993), p. 367-71. DOI : 10.1016/0169-5347(93)90221-A (cf. p. 100).

[221] Wolfgang WILTSCHKO et Roswitha WILTSCHKO. « Magnetic versus celestial orientation in migrating birds ». In : *Trends in ecology & evolution* 3 (jan. 1988), p. 13-5. DOI : 10.1016/0169-5347(88)90076-6 (cf. p. 100).

[222] Kenneth ABLE et Mary ABLE. « Calibration of the magnetic compass of a migratory bird by celestial rotation ». In : *Nature* 347 (sept. 1990), p. 378-380. DOI : 10.1038/347378a0 (cf. p. 100).

[223] WOLFGANG WILTSCHKO, PETRA DAUM, Angelika FERGENBAUER-KIMMEL et al. « The Development of the Star Compass in Garden Warblers, Sylvia borin ». In : *Ethology* 74 (jan. 2010), p. 285-292. DOI : 10.1111/j.1439-0310.1987.tb00939.x (cf. p. 100).

[224] Stephen T. EMLEN. « Celestial Rotation : Its Importance in the Development of Migratory Orientation ». In : *Science (New York, N.Y.)* 170 (jan. 1971), p. 1198-201. DOI : 10.1126/science.170.3963.1198 (cf. p. 100).

[225] Kenneth ABLE et Mary ABLE. « Interactions in the flexible orientation system of a migratory bird ». In : *Nature* 375 (mai 1995), p. 230-232. DOI : 10.1038/375230a0 (cf. p. 100).

[226] Kenneth ABLE et M. ABLE. « Manipulations of polarized skylight calibrate magnetic orientation in a migratory bird ». In : *Journal of Comparative Physiology A* 177 (jan. 1995), p. 351-356. DOI : 10.1007/BF00192423 (cf. p. 100, 101).

[227] Rachel MUHEIM, John PHILLIPS et Susanne AKESSON. « Polarized Light Cues Underlie Compass Calibration in Migratory Songbirds ». In : *Science (New York, N.Y.)* 313 (sept. 2006), p. 837-9. DOI : 10.1126/science.1129709 (cf. p. 100, 101).

[228] Kenneth ABLE et Mary ABLE. « Daytime calibration of magnetic orientation in a migratory bird requires a view of skylight polarization ». In : *Nature* 364 (août 1993), p. 523-525. DOI : 10.1038/364523a0 (cf. p. 100, 101).

[229] Wolfgang WILTSCHKO et Roswitha WILTSCHKO. « The interaction of stars and magnetic field in the orientation system of night migrating birds. I. Autumn experiments with European Warblers (Gen. Sylvia). » In : *Zeitschrift fur Tierpsychologie* 37.4 (1975), p. 337-355. DOI : 10.1111/j.1439-0310.1975.tb00885.x (cf. p. 100).

[230] Wolfgang WILTSCHKO et Roswitha WILTSCHKO. « The interaction of stars and magnetic field in the orientation system of night migrating birds : II. Spring experiments with European Robins (Erithacus rubecula) ». In : *Zeitschrift für Tierpsychologie* 39.1-5 (1975), p. 265-282. DOI : 10.1111/j.1439-0310.1975.tb00912.x (cf. p. 100).

[231] Verner P BINGMAN. « Importance of earth's magnetism for the sunset orientation of migratory naive savannah sparrows ». In : *Monitore Zoologico Italiano-Italian Journal of Zoology* 17.4 (1983), p. 395-400. DOI : 10.1080/00269786.1983.10736438 (cf. p. 100).

[232] Frank R. MOORE. « Integration of environmental stimuli in the migratory orientation of the savannah sparrow (Passerculus sandwichensis) ». In : *Animal Behaviour* 33.2 (1985), p. 657-663. ISSN : 0003-3472. DOI : https://doi.org/10.1016/S0003-3472(85)80089-0. URL : https://www.sciencedirect.com/science/article/pii/S0003347285800890 (cf. p. 100).

[233] James FOSTER, Jochen SMOLKA, Dan NILSSON et al. « How animals follow the stars ». In : *Proceedings of the Royal Society B : Biological Sciences* 285 (jan. 2018), p. 20172322. DOI : 10.1098/rspb.2017.2322 (cf. p. 101, 140).

[234] Michael BRINES. « Dynamic patterns of skylight polarization as clock and compass ». In : *Journal of theoretical biology* 86 (nov. 1980), p. 507-12. DOI : 10.1016/0022-5193(80)90349-5 (cf. p. 101).

[235] Thomas KRONLAND-MARTINET, Leo POUGHON, Marcel PASQUINELLI et al. « SkyPole-A method for locating the north celestial pole from skylight polarization patterns ». In : *Proceedings of the National Academy of Sciences of the United States of America* 120 (juill. 2023), e2304847120. DOI : 10.1073/pnas.2304847120 (cf. p. 101, 121, 122, 124).

[236] Thomas KRONLAND-MARTINET, Léo POUGHON, Marcel PASQUINELLI et al. « SkyPole : a geolocation algorithm based on polarized vision without using astronomical ephemerides ». In : *Polarization : Measurement, Analysis, and Remote Sensing XVI*. T. 13050. SPIE. 2024, p. 74-79. DOI : 10.1117/12.3013560 (cf. p. 101).

[237] Alistair SPROUL. « Derivation of the solar geometric relationships using vector analysis ». In : *Renewable Energy* 32 (juin 2007), p. 1187-1205. DOI : 10.1016/j.renene.2006.05.001 (cf. p. 103).

[238] Stefan CZESLA, Sebastian SCHRÖTER, Christian P. SCHNEIDER et al. *PyA : Python astronomy-related packages*. Juin 2019. ascl : 1906.010 (cf. p. 115, 128).

[239] ASTROPY COLLABORATION, Adrian M. PRICE-WHELAN, Pey Lian LIM et al. « The Astropy Project : Sustaining and Growing a Community-oriented Open-source Project and the Latest Major Release (v5.0) of the Core Package ». In : *apj* 935.2, 167 (août 2022), p. 167. DOI : 10.3847/1538-4357/ac7c74. arXiv : 2206.14220 [astro-ph.IM] (cf. p. 119).

[240] Matthew NEWVILLE, Till STENSITZKI, Daniel B. ALLEN et al. *LMFIT : Non-Linear Least-Square Minimization and Curve-Fitting for Python*. Version 0.8.0. Sept. 2014. DOI : 10.5281/zenodo.11813. URL : https://doi.org/10.5281/zenodo.11813 (cf. p. 120, 128).

[241] Stephane VIOLLET et Thomas KRONLAND-MARTINET. *SkyPole*. Juin 2023. URL : osf.io/fcsgk (cf. p. 120).

[242] Francelino FREITAS CARVALHO, Carlos AUGUSTO DE MORAES CRUZ, Greicy COSTA MARQUES et al. « Angular Light, Polarization and Stokes Parameters Information in a Hybrid Image Sensor with Division of Focal Plane ». In : *Sensors* 20.12 (2020). ISSN : 1424-8220. DOI : 10.3390/s20123391. URL : https://www.mdpi.com/1424-8220/20/12/3391 (cf. p. 121).

[243] Ian GOODFELLOW, Yoshua BENGIO et Aaron COURVILLE. *Deep Learning*. http://www.deeplearningbook.org. MIT Press, 2016 (cf. p. 126).

[244] Xiaobo LI, Lei YAN, Pengfei QI et al. « Polarimetric imaging via deep learning : A review ». In : *Remote Sensing* 15.6 (2023), p. 1540. DOI : 10.3390/rs15061540 (cf. p. 126).

[245] Olaf RONNEBERGER, Philipp FISCHER et Thomas BROX. « U-Net : Convolutional Networks for Biomedical Image Segmentation ». In : *Medical Image Computing and Computer-Assisted Intervention – MICCAI 2015*. Sous la dir. de Nassir NAVAB, Joachim HORNEGGER, William M. WELLS et al. Cham : Springer International Publishing, 2015, p. 234-241. ISBN : 978-3-319-24574-4. DOI : https://doi.org/10.48550/arXiv.1505.04597 (cf. p. 127).

[246] Mateusz BUDA, Ashirbani SAHA et Maciej A MAZUROWSKI. « Association of genomic subtypes of lower-grade gliomas with shape features automatically extracted by a deep learning algorithm ». In : *Computers in Biology and Medicine* 109 (2019). DOI : 10.1016/j.compbiomed.2019.05.002 (cf. p. 127).

[247] Victor GRIGORIEV, Kypros MILIDONIS, Manuel BLANCO et al. « Polyharmonic splines for interpolation over sun path ». In : *Solar Energy* 235 (mars 2022), p. 209-218. DOI : 10.1016/j.solener.2022.02.025 (cf. p. 137).

[248] Wolfgang STÜRZL et Jochen ZEIL. « Depth, contrast and view-based homing in outdoor scenes ». In : *Biological cybernetics* 96.5 (2007), p. 519-531. DOI : 10.1007/s00422-007-0147-3 (cf. p. 140).

[249] Susannah BOURNE-WORSTER, Henrik MOURITSEN et P HORE. « A light-dependent magnetoreception mechanism insensitive to light intensity and polarization ». In : *Journal of The Royal Society Interface* 14 (sept. 2017), p. 20170405. DOI : 10.1098/rsif.2017.0405 (cf. p. 140).

[250] Glenn S SMITH. « The polarization of skylight : An example from nature ». In : *American Journal of Physics* 75.1 (2007), p. 25-35. DOI : 10.1119/1.2360991 (cf. p. 140).

[251] A. WHITEN. « Operant studies of pigeon orientation and navigation ». In : *Animal Behaviour* 26 (1978), p. 571-610. ISSN : 0003-3472. DOI : https://doi.org/10.1016/0003-3472(78)90072-6. URL : https://www.sciencedirect.com/science/article/pii/0003347278900726 (cf. p. 140).

[252] Rachel MUHEIM, John PHILLIPS et Mark DEUTSCHLANDER. « White-throated Sparrows calibrate their magnetic compass by polarized light cues during both autumn and spring migration ». In : *The Journal of experimental biology* 212 (nov. 2009), p. 3466-72. DOI : 10.1242/jeb.032771 (cf. p. 140).

[253] Thomas ALERSTAM, Gudmundur A. GUDMUNDSSON, Martin GREEN et al. « Migration Along Orthodromic Sun Compass Routes by Arctic Birds ». In : *Science* 291.5502 (2001), p. 300-303. DOI : 10.1126/science.291.5502.300. eprint : https://www.science.org/doi/pdf/10.1126/science.291.5502.300. URL : https://www.science.org/doi/abs/10.1126/science.291.5502.300 (cf. p. 141).

[254] Dmitry KISHKINEV, Nikita CHERNETSOV et Henrik MOURITSEN. « A Double-Clock or Jetlag Mechanism is Unlikely to be Involved in Detection of East—West Displacements in a Long-Distance Avian Migrant ». In : *The Auk* 127.4 (2010), p. 773-780. DOI : 10.1525/auk.2010.10032 (cf. p. 141).

[255] James L GOULD. « Animal navigation : the longitude problem ». In : *Current Biology* 18.5 (2008), R214-R216. DOI : https://doi.org/10.1016/j.cub.2008.01.011 (cf. p. 141).

[256] Kenneth J LOHMANN, Kayla M GOFORTH, Alayna G MACKIEWICZ et al. « Magnetic maps in animal navigation ». In : *Journal of Comparative Physiology A* (2022), p. 1-27. DOI : 10.1007/s00359-021-01529-8 (cf. p. 141).

[257] Will T SCHNEIDER, Richard A HOLLAND et Oliver LINDECKE. « Over 50 years of behavioural evidence on the magnetic sense in animals : what has been learnt and how? » In : *The European Physical Journal Special Topics* 232.2 (2023), p. 269-278. DOI : 10.1140/epjs/s11734-022-00755-8 (cf. p. 141).

[258] F PAPI, L FIORE, V FIASCHI et al. « The influence of olfactory nerve section on the homing capacity of carrier pigeons ». In : *Monitore Zoologico Italiano-Italian Journal of Zoology* 5.4 (1971), p. 265-267. DOI : 10.1080/00269786.1971.10736180 (cf. p. 141).

[259] Hans WALLRAFF. « Navigation by homing pigeons ». In : *Ethology Ecology & Evolution* 2 (mai 1990), p. 81-115. DOI : 10.1080/08927014.1990.9525495 (cf. p. 141).

[260] Hans WALLRAFF. « Navigation by homing pigeons : Updated perspective ». In : *Ethology Ecology & Evolution - ETHOL ECOL EVOL* 13 (mars 2001). DOI : 10.1080/08927014.2001.9522786 (cf. p. 141).

[261] Léo POUGHON, Stefano MAFRICA, Jocelyn MONNOYER et al. *Procédé et système pour déterminer des données caractérisant un cap suivi par un véhicule automobile à un instant courant*. Patent. Oct. 2021. URL : https://data.inpi.fr/brevets/FR3128528?q=FR3128528#FR3128528 (cf. p. 142).

[262] Robin GROB, Oliver CUNZ, Kornelia GRÜBEL et al. « Rotation of skylight polarization during learning walks is necessary to trigger neuronal plasticity in Cataglyphis ants ». In : *Proceedings of The Royal Society of London* 289 (jan. 2022), p. 20212499. DOI : 10.1098/rspb.2021.2499 (cf. p. 142).

APPENDIX

A. Matching of a simulated image to a real image

In this appendix, we detail the least squares step applied to match a simulated image to a real image.
For each pixel of coordinates (i, j) pointing towards a point $P_{i,j}$, the simulated DoLP $P^{simu}_{l,(i,j)}$ is defined, through Rayleigh scattering, as:

$$P^{simu}_{l,(i,j)}\left(\overrightarrow{S}, P_{l_{max}}\right) = P_{l_{max}} \cdot \frac{1 - \left(\overrightarrow{S} \cdot \overrightarrow{P_{i,j}}\right)^2}{1 + \left(\overrightarrow{S} \cdot \overrightarrow{P_{i,j}}\right)^2} \tag{A.1}$$

Where S is the position of the Sun, and $P_{l_{max}}$ is the maximum of polarization in the sky. As $\overrightarrow{S}$ can be expressed through the Sun's azimuth α and elevation θ, the simulated DoLP can be expressed as:

$$P^{simu}_{l,(i,j)}\left(\alpha, \theta, P_{l_{max}}\right) = P_{l_{max}} \cdot \frac{1 - \left(\overrightarrow{S}\,(\alpha,\theta) \cdot \overrightarrow{P_{i,j}}\right)^2}{1 + \left(\overrightarrow{S}\,(\alpha,\theta) \cdot \overrightarrow{P_{i,j}}\right)^2} \tag{A.2}$$

To match a simulated image to a real image, the following function can be minimized for each pixel:

$$f_{i,j}\left(\alpha, \theta, P_{l_{max}}\right) = \left(P^{exp}_{l,(i,j)} - P^{simu}_{l,(i,j)}\left(\alpha, \theta, P_{l_{max}}\right)\right)^2 \tag{A.3}$$

Where $P^{exp}_{l,(i,j)}$ is the DoLP measured at a pixel of coordinated (i, j). Therefore, for a whole image, the following matrix function should be minimized:

$$f\left(\alpha, \theta, P_{l_{max}}\right) = \begin{pmatrix} f_{1,1}\left(\alpha, \theta, P_{l_{max}}\right) & f_{1,2}\left(\alpha, \theta, P_{l_{max}}\right) & \dots & f_{1,m}\left(\alpha, \theta, P_{l_{max}}\right) \\ f_{2,m}\left(\alpha, \theta, P_{l_{max}}\right) & f_{2,2}\left(\alpha, \theta, P_{l_{max}}\right) & \dots & f_{2,m}\left(\alpha, \theta, P_{l_{max}}\right) \\ \vdots & \vdots & \vdots & \vdots \\ f_{n,1}\left(\alpha, \theta, P_{l_{max}}\right) & f_{n,2}\left(\alpha, \theta, P_{l_{max}}\right) & \dots & f_{n,m}\left(\alpha, \theta, P_{l_{max}}\right) \end{pmatrix} \tag{A.4}$$

The minimizer fonction from the lmfit library, in Python, was used to minimize this matrix, and deduce the three parameters α, θ, and $P_{l_{max}}$.

B. Mueller matrices of the characterization setup's components

In this appendix, we detail the Mueller matrices of the optical components of the characterization setup presented in section 2.3.4.2 of this manuscript.

— Linear polarizer rotated at an angle θ_{LP}:

$$\mathbf{M_{LP}}(\theta_{LP}) = \frac{1}{2}\begin{pmatrix} 1 & \cos(2\theta_{LP}) & \sin(2\theta_{LP}) & 0 \\ \cos(2\theta_{LP}) & \cos^2(2\theta_{LP}) & \cos(2\theta_{LP})\sin(2\theta_{LP}) & 0 \\ \sin(2\theta_{LP}) & \cos(2\theta_{LP})\sin(2\theta_{LP}) & \sin^2(2\theta_{LP}) & 0 \\ 0 & 0 & 0 & 0 \end{pmatrix} \tag{B.1}$$

— Polarizing beam splitter in transmission:

$$\mathbf{M_{PBS1}}(0) = \mathbf{M_{PBS2}}(0) = \frac{1}{2}\begin{pmatrix} 1 & 1 & 0 & 0 \\ 1 & 1 & 0 & 0 \\ 0 & 0 & 0 & 0 \\ 0 & 0 & 0 & 0 \end{pmatrix} \tag{B.2}$$

— Polarizing beam splitter in reflection:

$$\mathbf{M_{PBS1}}(\pi/2) = \mathbf{M_{PBS2}}(\pi/2) = \frac{1}{2}\begin{pmatrix} 1 & -1 & 0 & 0 \\ -1 & 1 & 0 & 0 \\ 0 & 0 & 0 & 0 \\ 0 & 0 & 0 & 0 \end{pmatrix} \tag{B.3}$$

— Half-wave plate rotated at an angle α:

$$\mathbf{M}_{\lambda/2}(\alpha) = \begin{pmatrix} 1 & 0 & 0 & 0 \\ 0 & \cos^2(2\alpha) - \sin^2(2\alpha) & 2\cos(2\alpha)\sin(2\alpha) & 0 \\ 0 & 2\cos(2\alpha)\sin(2\alpha) & \sin^2(2\alpha) - \cos^2(2\alpha) & 0 \\ 0 & 0 & 0 & -1 \end{pmatrix} \tag{B.4}$$

The Stokes vector of the incident unpolarized light is:

$$\overrightarrow{S} = S_0 \begin{pmatrix} 1 \\ 0 \\ 0 \\ 0 \end{pmatrix} \tag{B.5}$$

C. Descriptif détaillé de la thèse

Les systèmes mondiaux de navigation par satellites (GNSS pour Global Navigation Satellite Systems) sont très répandus du fait de leur précision. Cependant, ces systèmes sont sensibles au brouillage et à l'usurpation d'identité. Pour renforcer leur fiabilité, l'information issue des systèmes de navigation satellitaires peut être fusionnée avec des informations provenant de capteurs complémentaires tels que des centrales inertielles, des caméras, des radars ou des lidars. Les centrales inertielles permettent d'obtenir une position relativement à une position initiale à partir de données d'accélération et d'orientation, de manière robuste. Cependant, ces systèmes sont soumis à une dérive de leur signal dans le temps, et nécessitent donc d'être régulièrement calibrés. Les caméras, radars et lidars offrent des résultats remarquables, en milieu urbain notamment, mais nécessitent une connaissance a priori de l'environnement dans lequel ils évoluent. Une alternative à de tels systèmes peut être trouvée dans le monde animal. Certains animaux, tels que les oiseaux migrateurs, parcourent des distances conséquentes, et sont considérés être en mesure de déterminer leur position sur Terre. Les mécanismes qui sous-tendent ces capacités de navigation sont encore méconnus. Les recherches menées sur ces animaux montrent l'utilisation de sources d'information variées, telles que le champ magnétique terrestre, les étoiles ou encore le motif de polarisation du ciel. Les deux premiers sont bien connus car largement utilisés pour la navigation, avant l'avènement du GPS, système de navigation satellitaire américain. L'utilisation du dernier pour la navigation, en revanche, a été découvert plus récemment, en 1947, par un entomologiste du nom de Karl von Frisch, alors qu'il étudiait le vol des abeilles. Le motif de polarisation du ciel est un motif invisible à l'œil humain, dont les propriétés varient en fonction de la position du soleil dans le ciel. Il permet ainsi de naviguer en utilisant le soleil de manière indirecte. Contrairement aux systèmes de navigation basés sur le soleil, tel que le sextant, l'utilisation du motif de polarisation du ciel pour la navigation ne nécessite pas une vue directe du soleil, et peut donc être utilisée en environnement urbain, lorsque le soleil est caché par un obstacle par exemple. À la suite de cette découverte, des systèmes de navigation sans GPS, basés sur le motif de polarisation du ciel ont été développés. Des compas solaires utilisant le motif de polarisation du ciel ont montré des résultats prometteurs. En particulier, au sein de l'Institut des Sciences du Mouvement, à Aix-Marseille Université, un robot nommé AntBot, et navigant à la manière de la fourmi du désert Cataglyphis, une fourmi dont les capacités de navigation reposent en grande partie sur le motif de polarisation du ciel, a été développé. À la manière de la fourmi du désert, ce robot permet d'obtenir sa position relativement à une position initiale. Les résultats encourageants obtenus au cours de cette étude ont mené à la présente thèse, dont le but est d'étudier la géolocalisation, à partir du motif de polarisation du ciel.

La géolocalisation basée sur le motif de polarisation est envisageable car le motif de polarisation du ciel permet d'obtenir la position du soleil, et ainsi d'estimer sa position sur Terre, de manière similaire à la navigation à l'aide d'un sextant. La principale limite liée à l'utilisation du motif de polarisation du ciel est sa sensibilité aux perturbations atmosphériques, tels que les nuages. Cependant, comme étudié dans le cadre du projet AntBot, le motif de polarisation du ciel est plus robuste à la présence de nuages, dans les faibles longueurs d'onde, notamment l'ultraviolet (UV). L'utilisation d'un capteur sensible à l'UV est donc étudiée dans cette thèse, à travers la mise en place d'une source de caractérisation permettant de contrôler l'état de polarisation, et ainsi de décrire les performances d'un capteur polarimétrique sensible à l'UV.
Dans ce manuscrit de thèse, la définition de la polarisation est d'abord introduite, suivi d'une description du motif de polarisation du ciel. L'intérêt de l'UV pour la navigation basée sur le motif de polarisation du ciel est ensuite expliqué. La deuxième partie de ce manuscrit présente les différents types de capteurs de polarisation ainsi que des méthodes de calibration et caractérisation d'un capteur polarimétrique. La théorie et l'implémentation d'une source UV dont l'état de polarisation peut être contrôlé sont introduites. Enfin, la troisième partie de ce manuscrit présente une méthode de géolocalisation sans GPS, basée sur le motif de polarisation du ciel, et inspirée d'oiseaux migrateurs calibrant leur compas magnétique par la rotation céleste des étoiles. Ces parties sont résumées ci-dessous.

Polarisation et diffusion de la lumière

La polarisation est une propriété de la lumière décrivant l'évolution du champ électrique de la lumière dans le temps. Pour une onde monochromatique, le vecteur champ électrique, observé à travers un plan perpendiculaire à la direction de propagation de l'onde, décrit une ellipse, nommée ellipse de polarisation. L'onde est dite, dans le cas général, polarisée elliptiquement. Une telle ellipse est définie par son ellipticité et son orientation. L'ellipticité indique si la trajectoire du vecteur champ électrique est plus proche d'un cercle ou d'une droite. Deux cas particuliers peuvent alors être considérés, le cas d'une onde polarisée circulairement et d'une onde polarisée linéairement. Ce dernier cas sera particulièrement important ici car la lumière diffusée dans le ciel est polarisée linéairement. En pratique, la lumière est polychromatique. Les différentes ondes composant la lumière ne se propagent pas nécessairement de la même manière. Le vecteur champ électrique de la lumière peut alors décrire une trajectoire totalement aléatoire. On dit alors que la lumière est non polarisée. La lumière issue du soleil est, par exemple, considérée comme non polarisée. Lorsque toutes les ondes composant la lumière sont polarisées de la même manière, le vecteur champ électrique de la lumière décrira une ellipse. La lumière est dite purement polarisée. Enfin, dans le cas général, la lumière possède une partie polarisée et une partie non polarisée. Il s'agit du cas le plus fréquent dans la nature, la lumière est alors dite partiellement polarisée. La lumière diffusée dans le ciel est, par exemple, partiellement polarisée linéairement. Ainsi, en plus de l'ellipticité et

de l'orientation, ou angle de polarisation, l'état de polarisation de la lumière peut être décrit par le degré de polarisation, correspondant au ratio d'intensité lumineuse polarisée sur l'irradiance totale. Une lumière purement polarisée aura un degré de polarisation de 1, et une lumière non polarisée aura un degré de polarisation de 0. Pour une lumière partiellement polarisée linéairement, le degré de polarisation linéaire (DoLP) peut également être introduit.
En pratique, l'ellipse de polarisation n'est pas mesurable car les variations du champ électrique de la lumière sont trop rapides pour la majorité des capteurs, ainsi que pour l'œil humain. Afin d'étudier la polarisation de la lumière, une grandeur mesurable, l'intensité lumineuse (ou irradiance), correspondant à une moyenne temporelle d'une fonction de l'amplitude du champ électrique de la lumière, est privilégiée. Le formalisme de Stokes permet de décrire l'état de polarisation de la lumière à partir de grandeurs mesurables (irradiance), stockées dans un vecteur, nommé vecteur de Stokes. Les capteurs ne sont en général pas sensibles à la polarisation de la lumière. Afin de mesurer l'état de polarisation de la lumière, l'intensité lumineuse est mesurée à travers des filtres polarisant. L'effet d'un filtre sur l'état de polarisation de la lumière peut être décrit par une matrice, nommée matrice de Mueller, dont la multiplication avec le vecteur de Stokes d'une lumière incidente, donne le vecteur de Stokes de la lumière après interaction avec le filtre, et permet donc d'obtenir son état de polarisation. Pour décrire l'état de polarisation d'une lumière polarisée linéairement, au moins trois mesures, à l'aide d'un ou plusieurs polariseurs linéaires orientés différemment, doivent être réalisées. Un polariseur linéaire est un filtre bloquant la lumière polarisée linéairement dans une direction et laissant passer la lumière polarisée linéairement dans la direction orthogonale. La rotation d'un tel filtre par rapport à une lumière incidente polarisée linéairement, va induire une variation de l'intensité lumineuse, dont la mesure permet de décrire l'état de polarisation.
Dans le ciel, la polarisation de la lumière est due à l'interaction de la lumière non polarisée du soleil, avec les particules composant l'atmosphère. Lorsque la lumière interagit avec ces particules, ces dernières diffusent la lumière dans toutes les directions. La lumière diffusée a un état de polarisation dépendant de la position relative de la particule par rapport au soleil et variant selon la direction de diffusion. Ce phénomène peut être décrit par le modèle de diffusion de Rayleigh, supposant que les particules dans l'atmosphère sont petites devant la longueur d'onde de l'onde incidente. À partir de ce modèle, la polarisation en chaque point du ciel peut être décrite, en fonction de la position du soleil et de la position d'un observateur relativement au soleil et au point du ciel observé. Cela permet de simuler un motif de polarisation dans le ciel, semblable à celui observé expérimentalement. Cependant, certaines différences ont pu être observées entre le motif de polarisation basé sur le modèle de Rayleigh et le motif de polarisation réel. Cela est dû aux hypothèses formulées. Tout d'abord, la taille des particules est effectivement petite devant la longueur d'onde associée aux rayons du soleil, si l'on considère les particules d'azote et d'oxygène, qui composent en grande partie les gaz présents dans l'atmosphère. Cependant, si l'on considère également les aérosols et nuages, cette hypothèse n'est plus valable et la lumière diffusée à des propriétés différentes de celles formulées à travers le modèle de diffusion de

Rayleigh. Une deuxième hypothèse est celle de la diffusion simple. Dans le modèle considéré, la lumière diffusée est supposée diffusée par une seule particule, sans interaction avec d'autres particules dans l'atmosphère. En pratique, cependant, la lumière peut être diffusée de multiples fois, ce qui a pour effet de dépolariser la lumière de l'atmosphère. Ainsi, le motif de polarisation du ciel présente une valeur maximale de DoLP théorique égale à 1, ce qui n'est pas le cas en pratique, le DoLP maximal étant inférieur à 1, et cette valeur peut varier selon les conditions atmosphériques et les propriétés géographique, liées notamment à la réflexion de la lumière par le sol. Le modèle de diffusion simple de Rayleigh reste néanmoins simple et assez proche de l'atmosphère réelle, notamment sous un ciel clair, sans nuages. Dans cette thèse, ce modèle a été privilégié pour l'étude du motif de polarisation du ciel.
En ce qui concerne la longueur d'onde à privilégier pour l'étude du motif de polarisation, cette question ne peut pas être uniquement considérée à travers le modèle de diffusion simple de Rayleigh. En effet, en considérant ce modèle, le motif de polarisation du ciel est le même quelle que soit la longueur d'onde considéré. Le seul critère pouvant alors être considéré est l'intensité de la lumière polarisée dans le ciel. Le phénomène de diffusion de Rayleigh dépend fortement de la longueur d'onde. Plus la longueur d'onde sera courte, plus l'intensité diffusée sera grande. En considérant le spectre du Soleil, le motif de polarisation du ciel devrait donc être observé de préférence dans les longueurs d'ondes correspondant au bleu ou au vert. Or, il a été observé chez certains insectes, une sensibilité à la polarisation dans l'ultraviolet, dans la zone supérieure de leurs yeux composés, nommée aire dorsale marginale (en anglais DRA pour dorsal rim area), leur permettant d'observer le motif de polarisation du ciel. Cette sensibilité est en apparence paradoxale, lorsque l'on considère le modèle de Rayleigh. Elle parait également paradoxale lorsque l'on considère le motif de polarisation réel. En effet, sous un ciel clair, du fait de la diffusion multiple dans l'atmosphère, le maximum de DoLP dans le ciel est plus faible pour les courtes longueurs d'onde. Or, l'information extraite du motif de polarisation du ciel est plus fiable lorsque le DoLP est proche de 1. Ainsi, l'UV ne semble pas être la gamme de longueur d'onde à privilégier pour l'observation du motif de polarisation du ciel. Ce paradoxe est connu sous le nom de « paradoxe de la perception du motif de polarisation du ciel dans l'ultraviolet », ou UV-pol-paradox. Une explication de ce paradoxe est que le DoLP dans le ciel serait plus élevé en présence de nuages dans l'UV que pour des longueurs d'onde plus longues. La lumière diffusée par les nuages est en général non polarisée ou très faiblement polarisée. La polarisation de la lumière du ciel en présence de nuage serait liée à la diffusion de la lumière du soleil dans la couche d'air située sous les nuages. Le DoLP de la lumière diffusée, en présence de nuages, est faible quelle que soit la longueur d'onde considérée. Chez les insectes, un DoLP minimal est supposé requit pour utiliser l'information provenant du motif de polarisation du ciel. En présence de nuages, un DoLP inférieur à la valeur minimale requise peut être observé, ne permettant pas d'utiliser le motif de polarisation du ciel pour la navigation. Les valeurs de DoLP du ciel dans l'UV étant supérieures aux valeurs de DoLP dans le visible, en présence d'une couverture nuageuse, le motif de polarisation peut être utilisable dans l'UV lorsque cela n'est pas le cas dans le visible.

Lorsque le ciel est totalement dégagé, l'information est toujours utilisable dans l'UV et le visible, la sensibilité à l'UV ne pose donc pas de problème dans ce cas.

Capteur polarimétrique : conception et calibration

Afin de mesurer l'état de polarisation de la lumière, plusieurs méthodes peuvent être envisagées. Ici, uniquement la mesure d'un état de polarisation linéaire est considérée. L'état de polarisation d'une source de lumière polarisée linéairement, peut être obtenue à partir de trois mesures de l'état de polarisation avec différentes orientations de filtres. Ces multiples mesures peuvent être obtenues de manière temporelles ou instantanées. Les polarimètres à division de temps consistent à appliquer une rotation à des filtres polarisants afin d'obtenir plusieurs mesures dans le temps. Afin de déduire l'état de polarisation de la lumière, il est nécessaire que l'état de polarisation de la lumière à analyser ne varie pas dans le temps nécessaire à la mesure, et que le polarimètre reste fixe pendant la mesure. Les polarimètres instantanés peuvent être de deux types. Premièrement, les polarimètres à division d'amplitude nécessitent de diviser un faisceau en de multiples faisceaux dont l'état de polarisation sera analysé. Ces polarimètres ne nécessitent aucune hypothèse particulière mais peuvent être difficile à mettre en place. Deuxièmement, les polarimètres à division de plan focal consistent à mesurer la polarisation à travers de multiples filtres disposés côte à côte. Les propriétés de la source étudiée dans ce cas ne doivent pas varier spatialement sur la surface du polarimètre. Pour la mesure du motif de polarisation du ciel, deux types de capteurs peuvent être distingués, les capteurs non imageants et les capteurs imageants. Ces deux types de capteurs ont des fonctionnements similaires à ceux des polarimètres présentés ci-dessus, mais permettent de mesurer l'état de polarisation en différents points du ciel. Les capteurs non imageants consistent en plusieurs unités de mesure de polarisation, orientées différemment vers différents points du ciel. Leur avantage principal est qu'ils ne nécessitent que très peu de puissance de calcul pour traiter les données associées, car ils sont généralement constitués de peu d'unités, allant de 2 à quelques centaines. Ils peuvent ainsi être compatible avec la navigation en temps réel. Les capteurs imageants fonctionnent sur le même principe que les cameras grand publique. Ils sont constitués d'une lentille est d'un capteur sur lequel est projeté une image. Le traitement de l'information de polarisation est permis par l'ajout de filtres polarisants avant ou après la lentille. Ces capteurs permettent d'acquérir plus de données que les capteurs non-imageants, et ainsi d'être plus robuste aux bruits.
Quel que soit le type de capteur privilégié, afin d'obtenir une information fiable, le capteur doit être calibré. La calibration d'un capteur peut être de trois types. Premièrement, une calibration géométrique peut être réalisée afin de connaitre la direction d'observation de chaque unité ou pixel composant le capteur. Cette calibration peut être divisée en deux étapes, d'abord une calibration intrinsèque, puis une calibration extrinsèque. La calibration intrinsèque consiste à obtenir les propriétés du capteur permettant de déterminer la direction d'observation de chaque pixel relativement

au repère de la caméra. Ensuite, la calibration extrinsèque permet de déterminer l'orientation du capteur par rapport à un repère extérieur, ce qui permet ensuite de déterminer la direction d'observation de chaque pixel par rapport au repère extérieur au capteur. Une calibration géométrique intrinsèque de la caméra a été réalisée dans cette thèse à partir d'un outil de calibration, basé sur une mire, et existant sous Matlab. Une calibration géométrique extrinsèque a été réalisée en se basant sur la trajectoire du soleil observée dans le champ de vision de la caméra comme référence. Deuxièmement, la calibration radiométrique consiste à obtenir la relation entre l'irradiance d'une source lumineuse et la valeur de sortie des photodétecteurs composant un capteur. Alternativement, cette calibration peut également consister à uniformiser la réponse des photodétecteurs à une source lumineuse homogène. Dans ce cas, seule la valeur relative de l'irradiance est nécessaire. En faisant varier l'irradiance d'une source de lumière homogène et non polarisée, ou en faisant varier le temps d'intégration du capteur à calibrer, éclairé par une source de lumière homogène, non polarisée et dont l'irradiance ne varie pas, le gain associé à chaque photodétecteur peut être estimé en supposant, par exemple, une réponse linéaire du capteur à la variation d'irradiance ou de temps d'intégration. Une telle source de lumière peut être générée à l'aide d'une sphère intégrante. Troisièmement, la calibration polarimétrique consiste à déterminer la réponse du capteur en fonction de l'état de polarisation de la lumière. Pour cela, une lumière polarisée, et dont l'état de polarisation est connu, peut servir de référence à la calibration. En mesurant différents états de polarisation avec le capteur à calibrer, les propriétés des filtres composant le capteur, par exemple à travers leur matrice de Mueller, peuvent être déterminées. Une lumière purement polarisée, générée à partir d'un filtre polarisant rotatif, à travers lequel passe une lumière uniforme non polarisée, est généralement suffisante pour calibrer un capteur polarimétrique. Une source de lumière partiellement polarisée, dont le degré de polarisation peut être contrôlé, est plus difficile à mettre en place qu'une source de lumière purement polarisée. Pour cette raison, la majorité des méthodes de calibration sont basées uniquement sur la génération de lumière purement polarisée. Or, la lumière du ciel étant partiellement polarisée, il peut être utile d'évaluer la réponse d'un capteur à une source de lumière partiellement polarisée. Ainsi, une source de lumière partiellement polarisée a été développée dans cette thèse afin de caractériser la réponse d'un capteur polarimétrique à une telle lumière. La source développée ici permet de contrôler indépendamment le degré et l'angle de polarisation, ainsi que l'irradiance. La caractérisation du capteur à travers la mesure du DoLP est particulièrement pertinente ici, car la méthode de géolocalisation développée dans cette thèse, et décrite ci-dessous, est basée sur la mesure du DoLP. La source implémentée génère une lumière UV (385nm), mais peut être aisément adaptée au visible. Afin de générer une lumière partiellement polarisée, la source lumineuse consiste à combiner deux faisceaux de lumière purement polarisés, dont l'état de polarisation est orthogonal. L'intensité relative de deux faisceaux de polarisation orthogonale dépolarise la lumière. Le degré de polarisation de la lumière est alors dépendant de l'intensité relative de chaque faisceau. Si un faisceau a une intensité nulle, le degré de polarisation de la source sera maximal. En effet, l'état de polarisation sera identique à celui du faisceau dont l'intensité est non nulle. Si les

deux faisceaux ont exactement la même intensité, la lumière aura alors un degré de polarisation nul. Enfin, si un des faisceaux a une intensité supérieure à celle de l'autre faisceau, alors la lumière sera partiellement polarisée, et son angle de polarisation sera celui de la source dont l'intensité est la plus grande. En pratique, afin de générer ces deux faisceaux, un séparateur de faisceaux polarisant est utilisé. Ce composant permet de séparer une lumière en deux faisceaux de polarisation orthogonale. Cette séparation dépend de l'état de polarisation de la lumière incidente. Ici, afin de faire varier l'intensité relative des deux faisceaux, un polariseur est placé avant le séparateur de faisceaux polarisant. Les deux faisceaux sont ensuite recombinés à l'aide de miroirs et d'un second séparateur de faisceaux polarisant. Ces composants permettent de faire varier le degré de polarisation uniquement. Afin de faire varier l'angle de polarisation, une lame demi-onde permet de faire tourner la polarisation sans modifier le degré de polarisation. Des moteurs de précision sont utilisés afin de contrôler la rotation des composants optiques. Les composant optiques n'étant pas parfaits, la théorie ne permet pas d'estimer avec précision l'état de polarisation généré en pratique par cette source. Ainsi, une table de correspondance, associant des orientations de filtres avec l'état de polarisation de la lumière, mesurée à l'aide d'un polarimètre considéré parfait, est créée. Grâce à la répétabilité en rotation des moteurs, les différents états de polarisation de la lumière peuvent être générés avec une répétabilité de 0.007° en angle de polarisation et 0.007 en degré de polarisation. Par manque de temps, cette source de lumière n'a pas été utilisée pour la caractérisation d'un capteur. En parallèle de cette source, des capteurs sensibles à l'UV sont en cours de fabrication, et leur caractérisation est prévue à l'aide de cette source.

Géolocalisation

À partir de la mesure de l'état de polarisation de la lumière issue du ciel, diverses stratégies de navigation peuvent être adoptées. La plupart de ces stratégies se basent sur l'estimation de la position du soleil à partir du motif de polarisation du ciel. L'azimut du Soleil permet, par exemple, d'obtenir une mesure de cap. Pour estimer la position du Soleil, plusieurs méthodes ont été proposées. Par exemple, en se basant sur le modèle de diffusion simple de Rayleigh, la direction de polarisation de la lumière diffusée par une particule est orthogonale au plan contenant cette particule, le capteur, ainsi que le Soleil. Par cette propriété, l'azimut du Soleil peut être obtenu directement en estimant la direction de polarisation de la lumière au zénith de la caméra (le point directement au-dessus de la caméra). La position du Soleil peut être obtenue à partir de la mesure de la direction de polarisation en seulement deux points du ciel. La forme du motif de polarisation peut également directement être utilisée pour obtenir la position du Soleil. Les méthodes de géolocalisation développées se basent généralement sur l'estimation de la position du Soleil. La position sur Terre est ensuite déduite à partir d'éphémérides solaires, tables décrivant la trajectoire du Soleil, de la date et de l'heure. La mesure instantanée de position à partir de cette méthode nécessite la fusion de données, avec, par exemple, un compas magnétique.

Certains animaux, comme les oiseaux migrateurs, sont, cependant, supposés capables de déterminer leur position sur Terre sans avoir accès à des éphéméride solaire. La façon dont ces animaux déterminent leur position sur Terre, reste, en revanche, peu comprise. Des études ont montré que certains oiseaux migrateurs utilisent trois types de compas, un compas magnétique, un compas stellaire de nuit ainsi qu'un compas basé sur le motif de polarisation de jour. Leur compas stellaire permet de calibrer leur compas magnétique. Pour cela, ces animaux utilisent la rotation céleste des étoiles, due à la rotation de la Terre sur elle-même, afin de déterminer la position du pôle Nord céleste (pour un observateur situé sur l'hémisphère nord), un point dans le ciel, dont les coordonnées donnent accès, de manière directe, au nord géographique et à la latitude de l'observateur sur Terre. De jour, des études ont montré que le motif de polarisation du ciel était utilisé par des oiseaux migrateurs afin de calibrer leur compas magnétique. Le compas polarimétrique des oiseaux migrateurs reste cependant méconnu. En s'inspirant de la calibration du compas magnétique chez l'oiseau par la rotation céleste des étoiles, une méthode permettant d'obtenir la position du pôle Nord céleste, et ainsi le nord géographique et la latitude de l'observateur, à partir de la rotation du motif de polarisation du ciel, a été développée dans cette thèse. Pour cela, on considère, tout d'abord, que le soleil, vu par un observateur sur Terre, tourne autour du pôle céleste (on néglige ici les variations de déclinaison, c'est à dire le mouvement de la Terre autour du Soleil). Le motif de polarisation du ciel étant, d'après le modèle de diffusion simple de Rayleigh, fortement lié à la position du Soleil dans le ciel, le motif de polarisation varie également lorsque la position du Soleil varie. La méthode développée ici consiste à observer le DoLP dans le ciel à plusieurs instants. Ce DoLP est fonction, d'après le modèle de diffusion simple de Rayleigh, de l'angle entre les vecteurs Observateur-Soleil et Observateur-Point d'observation, qu'on appelle angle de diffusion. Le soleil tournant autour du pôle Nord céleste, l'angle de diffusion est constant au niveau de ce point, et donc le DoLP est aussi constant. Le pôle Nord céleste est le seul point dans le ciel pour lequel le DoLP est constant à tout instant de la journée. Ainsi, pour trouver la position du pôle Nord céleste, une méthode consiste à faire la différence des DoLP entre deux instants quelconques. Cela permet d'obtenir une figure avec deux cercles d'invariance de DoLP sur la demi-sphère céleste, l'un lié à la symétrie radiale de la fonction DoLP, l'autre lié à la symétrie plane de cette fonction. Le pôle Nord céleste est situé sur le cercle d'invariance lié à la symétrie radiale de la fonction DoLP. Sur ces invariances, la différence de DoLP est nulle. En réitérant cette étape à d'autres instants, on obtient à nouveau ces invariances, mais avec une autre orientation. Le pôle Nord Céleste se situera toujours sur l'invariance radiale de la fonction DoLP. Ainsi, à partir de trois observations du motif de polarisation dans le ciel, on peut obtenir la position du pôle Nord céleste. Il suffit pour cela de trouver l'intersection des deux invariances radiales de la fonction DoLP. Pour plus de robustesse, plus de trois observations peuvent être réalisées, et ainsi, le pôle céleste sera localisé à l'intersection de toutes les invariances radiales. Les invariances planes et radiales ne sont pas trivialement distinguables. Il n'est cependant pas nécessaire de distinguer ces deux invariances pour trouver la position du pole céleste car, si suffisamment de mesures sont faites, le pôle céleste sera le seul point localisé à l'intersection d'autant

d'invariances que de paires d'images. Cela nécessite néanmoins des temps d'observation longs. Afin de réduire le temps d'observation nécessaire à l'estimation de la position du pole céleste, un réseau de neurones a été entrainé afin de distinguer l'invariance plane de l'invariance radiale, et permet ainsi de réduire le nombre d'images nécessaires. Une autre manière de réduire le temps d'observation par la réduction du nombre d'images nécessaire, consiste à ajouter l'information de la déclinaison solaire, ce qui est équivalent à la connaissance de la date. En considérant l'intersection des invariances plane et radiale obtenues par la différence de deux images de DoLP, il a été montré dans cette thèse que le pôle céleste se situe sur l'invariance radiale, à une distance de l'intersection des invariances égale à la déclinaison solaire. Ces méthodes permettent d'estimer la position du pole céleste et ainsi la direction du nord géographique et la latitude de l'observateur. Cependant, pour obtenir la longitude, la connaissance de l'heure solaire est nécessaire. Bien qu'aucun algorithme n'ait été proposé dans cette thèse pour estimer la longitude, des méthodes ont été proposées afin d'obtenir l'heure solaire. Une méthode, inventée précédemment, consiste à mesurer la direction de polarisation au niveau du pole céleste. Cela donne un accès direct à l'heure solaire. Une autre méthode proposée dans cette thèse consiste à estimer l'heure solaire moyenne entre deux observations à partir de l'invariance radiale. Mis à part les méthodes d'estimation d'heure, les méthodes de détection du pôle céleste ont toutes été testée expérimentalement. Ces méthodes ont permis d'obtenir la position du pole céleste avec une précision moyenne, en azimut et élévation, de quelques degrés. Bien que les résultats obtenus ne soient pas assez précis pour une grande partie des applications en navigation, les résultats sont prometteurs et nécessiteront des améliorations dans le traitement des données afin d'obtenir de meilleurs résultats. Ces recherches ont également permis de faire émerger des questions sur la navigation des animaux, et notamment au sujet du compas basé sur la polarisation du ciel chez les oiseaux migrateurs.